



City Research Online

City, University of London Institutional Repository

Citation: Williams, M. J. (2004). Control of air-intake lip separation using air-jet vortex generators. (Unpublished Doctoral thesis, City, University of London)

This is the accepted version of the paper.

This version of the publication may differ from the final published version.

Permanent repository link: <https://openaccess.city.ac.uk/id/eprint/30948/>

Link to published version:

Copyright: City Research Online aims to make research outputs of City, University of London available to a wider audience. Copyright and Moral Rights remain with the author(s) and/or copyright holders. URLs from City Research Online may be freely distributed and linked to.

Reuse: Copies of full items can be used for personal research or study, educational, or not-for-profit purposes without prior permission or charge. Provided that the authors, title and full bibliographic details are credited, a hyperlink and/or URL is given for the original metadata page and the content is not changed in any way.

Control of air-intake lip separation using air-jet vortex generators

Matthew J. Williams

Thesis submitted as part of the requirements for the degree of
Doctor of Philosophy

Centre for Aeronautics
School of Engineering & Mathematical Science
City University
Northampton Square
London EC1 OHB

June 2004



Executive Summary

Air vehicle air intakes are required to operate across a range of flow conditions, the design criteria for which are not necessarily complementary. It is proposed that flow control, in particular the novel application of Air-Jet Vortex Generators (AJVGs), can be used to enhance the off-design performance of an air intake system allowing a design focused heavily toward a particular design point.

A review of the open literature suggests a noticeable benefit of flow control in optimising intake performance by improving total-pressure recovery and reducing total-pressure distortion. The practicalities of installation, however, have rendered most studies only of academic interest. Vane vortex generators (VVGs) provide an improvement at only a small range of flows for which they are specifically designed. They also exhibit a large off-design penalty in the form of a parasitic pressure loss in the propulsion streamtube. Tangential blowing requires a relatively large portion of the intake mass-flow and is also inflexible to different operating regimes making it unacceptable. The more traditional form of intake flow control in the form of variable geometry is expensive and heavy but efficient if a Mach 2 plus capability is desired.

In a novel application, AJVGs have been proposed for control of flow separation at the intake lip. The large operating envelope of AJVGs, particularly with regard to local flow direction, small mass-flow requirement and negligible off-design penalty make AJVGs potentially unrivalled in this application. Maximum benefit could be obtained by using an existing intake leading edge, ice-protection system, and this will potentially save installation weight and cost. In this study, *AJVGs have been shown to increase the angle of incidence for which separation occurs on an intake lip by 10 degrees using less than 0.5% of total intake mass flow.*

A computation modelling technique has been developed which saves computational expense in the design of an AJVG installation by using a relatively simple boundary condition at the intake surface to model the jet exit. Wind tunnel tests on an installation designed using this method have validated its applicability. Computational fluid dynamics has been used to expand the test envelope to mass flows not obtainable

experimentally, demonstrating the validity of AJVGs for controlling lip separation at the extremes of the operating envelope.

This demonstration of AJVG technology is applicable to a range of different aircraft and engine types; in particular, modern military air-vehicles driven by low-observable design considerations that are penalised by small radius lip intakes.

The development of a methodology for successful intake flow control comes from the understanding that intake lip separation, certainly for practical applications, is three-dimensional in nature.

Contents

List of Figures	8
Acknowledgements	11
Declaration	13
Nomenclature	15
1. Introduction	19
1.1. Background	19
1.2. Goal and key specific objectives	23
2. Literature review	25
2.1. A historical perspective of intake lip design	26
2.1.1. The external cowling	26
2.1.2. The internal lip	33
2.2. Intake lip separation	34
2.2.1. External separation	35
2.2.2. Internal separation	41
2.3. Leading-edge flow separation	48
2.4. A correlation for internal lip separation	52
2.5. Three-dimensional flow separation	55
2.6. Flow control, variable geometry & novel approaches for eliminating lip separation	56
2.7. Air Jet Vortex Generators (AJVGs) for propulsion applications	65
2.8. Flow control trade-off study	70
2.9. The future for flow control in intake design	72
2.10. Conclusions from literature review	75
2.11. References	94
3. Numerical Methods	107
3.1. Introduction	107
3.2. The Navier-Stokes Equations	108
3.3. The finite volume method	111
3.4. Turbulence closure	115
3.5. Grid Generation	119
3.5.1. SAUNA multi-block mesh	119
3.5.2. Unstructured Prism/tetrahedral mesh	123
3.6. Flow solver	125
3.6.1. FLUENT commercial CFD software	125
3.6.2. SIMPLE	125
3.6.3. Turbulence modelling	126
3.6.4. Near-wall approximations	126
3.6.5. Boundary conditions	129
3.7. Code Validation	132
3.7.1. Grid dependence study	133
3.7.2. Turbulence model study	135
3.8. References	138
4. Experimental Procedures	141

4.1.	Water Tunnel Testing.....	141
4.1.1.	Design & Manufacture.....	141
4.1.2.	Test Procedure.....	143
4.2.	Wind Tunnel Testing.....	145
4.2.1.	Intake model.....	145
4.2.2.	Wind tunnel facility.....	147
4.2.3.	Instrumentation & Data Acquisition.....	148
4.2.4.	Test technique.....	148
4.2.5.	Error analysis & data repeatability.....	149
4.2.6.	Data reduction.....	151
4.2.7.	Flow visualisation.....	154
4.2.8.	Wind tunnel blockage corrections.....	154
4.2.9.	Air Jet Vortex Generator installation.....	156
4.3.	References.....	161
5.	Analysis of air intake lip separation behaviour.....	163
5.1.	Introduction.....	163
5.2.	Validation of CFD techniques at low forward speed.....	163
5.3.	Characteristics of intake internal performance at incidence.....	165
5.3.1.	Pressure Recovery.....	165
5.4.	Determination of internal separation.....	167
5.4.1.	Comparison of methods.....	167
5.4.2.	Increasing incidence at fixed mass flow.....	169
5.5.	Development of three-dimensional internal separation.....	174
5.6.	Determination of external separation.....	179
5.7.	Development of three-dimensional external separation.....	184
5.8.	More appropriate intake mass flows.....	189
5.9.	Higher Mach numbers.....	196
5.10.	Summary of results concerning intake lip separation.....	199
5.11.	References.....	201
6.	Control of lip separation using Air Jet Vortex Generators.....	203
6.1.	Reasoning.....	203
6.2.	System Design.....	204
6.2.1.	Initial thoughts on AJVG system design.....	204
6.2.2.	Ram Air jet vortex generators.....	205
6.3.	Computational modelling of vortex generators.....	209
6.3.1.	Vane Vortex Generator models.....	209
6.3.2.	Modelling of AJVGs.....	210
6.3.3.	Implications of modelling vortices with CFD.....	211
6.4.	Design of an installation for experimental validation.....	211
6.5.	Interactive analysis.....	215
6.5.1.	Experimental results.....	215
6.5.2.	Effects of Intake mass-flow ratio.....	221
6.5.3.	Validation of CFD methods.....	223
6.6.	More Appropriate Intake mass-flows.....	228
6.7.	Off-design performance.....	234
6.8.	Comments regarding further applications and applicability.....	237
6.8.1.	Application to separation type.....	237
6.8.2.	Application to external separation.....	237

6.8.3. Net thrust evaluation	238
6.8.4. Thoughts on physical installation.....	238
6.9. Summary of AJVG results	239
6.10. References	241
7. Conclusions	243
8. Suggestions for future research	245
Appendix A. Glossary of air intake terms	247
Appendix B. Model 742L geometric definition.....	249
Appendix C. Model instrumentation.....	251
Appendix D. Derivation of equations in text	257
D.1. Calculation of jet blowing total pressure ratio(Equation 6.1)	257
D.2. Relationship between jet momentum coefficient and jet pressure ratio (Equation 6.2)	258
Appendix E. Assessment of experimental and numerical errors	259
E.1. Experimental Errors	259
E.1.1. Surface Static pressure coefficients.....	260
E.1.2. Intake dynamic pressure recovery.....	263
E.1.3. Incidence angle.....	264
E.1.4. Intake mass flow.....	265
E.1.5. Errors in measurement introduced by unsteady flow.....	265
E.1.6. Wind tunnel velocity	265
E.1.7. Error Summary	266
E.2. Computational Errors	267
E.2.1. Geometric fidelity and surface finish.....	267
E.2.2. Modelling of AJVGs	268
E.2.3. Transition modelling	270
Appendix F. A note on the correlations of intake lip separation.....	273

List of Figures

<i>Figure 1-1: Vane vortex generators in the intake duct of the F-111 aircraft</i>	20
<i>Figure 1-2: Subsonic intake operating conditions</i>	21
<i>Figure 2-1: Example of pressure distributions on engine cowlings (Robinson & Becker, 1942)</i>	27
<i>Figure 2-2: NACA 1-Series Cowling (Baals et al, 1948)</i>	28
<i>Figure 2-3: Typical civil cowl profile</i>	29
<i>Figure 2-4 : NACA cowl performace (Butler, 1973)</i>	31
<i>Figure 2-5: Reynolds number effects on upper cowl separation (Hoelmer et al , 1987)</i>	37
<i>Figure 2-6 : External cowl separation schematic(Dobson & Goldsmith, 1970)</i>	39
<i>Figure 2-7:Reduction in engine-face turbulence from Tornado cowl redesign (Stocks & Bissinger, 1981)</i>	42
<i>Figure 2-8: Calculated surface flow for F/A-18 at high angle of attack and sideslip (Podleski, 1994)</i>	44
<i>Figure 2-9: Lip flow mechanics at incidence and high mass-flow (Jakubowski & Luidens (1975))</i>	47
<i>Figure 2-10 : Internal flow schematic high incidence $M=0.8$ (Hurd 1976)</i>	47
<i>Figure 2-11: Gault's correlation for aerofoil separation</i>	51
<i>Figure 2-12: Intake data from Table 2.1 Plotted on Gault's correlation</i>	51
<i>Figure 2-13: Correlation of lip separation data</i>	54
<i>Figure 2-14: Effect of VVG location on static intake performance (Hancock & Hinson ,1969)</i>	60
<i>Figure 2-15: VVGs on F-4 Phantom lip (Herzmark and Victor,1970)</i>	61
<i>Figure 2-16: Intake flow control concept (Miller, 1977)</i>	62
<i>Figure 2-17: Lip slot blowing concepts (Cawthon, 1976)</i>	65
<i>Figure 2-18: VVG installation in F-111 aircraft duct (Burcham & Bellman, 1971)</i> ..	65
<i>Figure 2-19 :Comparison of AJVG & VVG in m2129 s-duct, DC60 plotted against throat Mach number, M_{th}. (Anderson & Gibb, 1992)</i>	67
<i>Figure 2-20: Engine-face contours without (left) and with (right) distortion management Philpot (2000)</i>	68
<i>Figure 2-21 Generation of mixing from a pitched and skewed jet Pearcey (1961)</i>	69
<i>Figure 2-22: Trade-off matrix for flow control techniques</i>	70
<i>Figure 2-23: Vortex Breaker fence on F/A-18E/F intake</i>	74
<i>Figure 2-24: NACA Flush Intake (Frick et al, 1951)</i>	75
<i>Figure 3-1: Finite volume notation</i>	113
<i>Figure 3-2: SAUNA nacelle topology (left) and flow domain (right)</i>	120
<i>Figure 3-3: SAUNA Multi-block surface grids on SYM, ODNs and COWL</i>	122
<i>Figure 3-4: Leading edge C-grid detail-Euler grid</i>	122
<i>Figure 3-5: Example ICEM Tetra surface mesh</i>	124
<i>Figure 3-6: Example prism/tet grid around leading edge</i>	124
<i>Figure 3-7: SIMPLE solution procedure</i>	126
<i>Figure 3-8: Boundary layer near-wall region(FLUENT,2001)</i>	128
<i>Figure 3-9: Engine-face pressure calibration</i>	130
<i>Figure 3-10: Air Jet Vortex Generator coordinate system</i>	131
<i>Figure 3-11: Grid study (S-A Turbulence model)</i>	135
<i>Figure 3-12: Comparison of turbulence models on coarse grid</i>	136

Figure 3-13: Total pressure recovery and mass-flow ratio convergence	137
Figure 4-1: Water tunnel model	142
Figure 4-2: Visualisation of attached external flow	144
Figure 4-3: Visualisation of external separated flow	144
Figure 4-4: RAE model 742L geometry description	145
Figure 4-5: Schematic of 3.5 inch engine-face rake	146
Figure 4-6: T2 Low speed wind tunnel	147
Figure 4-7: Data repeatability check example	149
Figure 4-8: Derivation of intake parameters	151
Figure 4-9: Mass-flow ratio blockage on tunnel dynamic pressure	156
Figure 4-10: AJVG Pitch and skew angle definitions	158
Figure 4-11: Repeatability of engine-face total pressure coefficient and DC90 for a blowing pressure ratio of 1.1	159
Figure 5-1: Experimental and CFD distortion comparison for cowl9, $M=0.1$, $A_o/A_c=0.90$. Contour plots, left to right: 5° , 15° , 20° . Experiment top and CFD bottom.	164
Figure 5-2: Intake total pressure recovery with incidence	166
Figure 5-3: Dynamic pressure recovery variation with incidence.	166
Figure 5-4: Pressure coefficient traces at fixed locations with varying incidence, $A_o/A_c=0.9$	168
Figure 5-5: Pressure traces at Tap 26 ($x/D_{max}=0.0098$)	168
Figure 5-6: Windward lip internal and external pressure variation with incidence at fixed mass-flow, $A_o/A_c=0.89$	170
Figure 5-7: Windward lip internal and external pressure variation with incidence at fixed mass-flow, $A_o/A_c=0.65$	170
Figure 5-8: Computed Mach number contours on symmetry plane for increasing incidence at fixed mass-flow, $A_o/A_c=0.89$	172
Figure 5-9: Internal separation at $A_o/A_c=0.89$ Top to bottom, $\alpha=7.5^\circ$, $\alpha=15^\circ$, $\alpha=20^\circ$, contours of pressure coefficient.	175
Figure 5-10: Computed limiting streamlines $\alpha=20^\circ$, $M=0.1$ $A_o/A_c=0.89$	176
Figure 5-11: Schematic of internal flow separation on a ducted body.....	177
Figure 5-12: Pressure distribution at zero incidence for reducing mass-flow ratio	180
Figure 5-13: Different external cowl pressure variation with reducing mass-flow ratio, $\alpha=0^\circ$	181
Figure 5-14: Experimental prediction of external separation for different mass-flow ratios at tap 4.	181
Figure 5-15: Crown pressure coefficient at $A_o/A_c=0.88$ for increasing incidence..	183
Figure 5-16: Crown pressure coefficient at $A_o/A_c=0.4$ for increasing incidence....	183
Figure 5-17: External pressures at $A_o/A_c=0.89$ top to bottom, $\alpha=7.5^\circ$, $\alpha=15^\circ$, $\alpha=20^\circ$, contours of pressure coefficient.	185
Figure 5-18: External pressures at $A_o/A_c=0.4$ top to bottom, $\alpha=2.5^\circ$, $\alpha=7.5^\circ$, $\alpha=15^\circ$, contours of pressure coefficient.	186
Figure 5-19: Computed surface streamlines on cowl side (top) and cowl top (bottom) for $\alpha=10^\circ$ (left) & $\alpha=20^\circ$ (right)	187
Figure 5-20: Schematic of external flow separation at incidence	188
Figure 5-21: Mass-flow demand for assumed engine	190
Figure 5-22: Total pressure recovery and distortion for high-mass-flow computations	190

Figure 5-23 DC90 for range of mass-flows scaled to $Ao/Ac=4.0$	192
Figure 5-24: Symmetry plane Mach number contours for $Ao/Ac=2.15$	194
Figure 5-25: Symmetry plane Mach number contours for $Ao/Ac=4.00$	195
Figure 5-26: Mach number contours at windward lip for $\alpha=0^\circ$ and $\alpha=10^\circ$	196
Figure 5-27: Symmetry plane Mach number contours for $Ao/Ac=0.76$, $M=0.8$	197
Figure 5-28: Change in separation type as incidence increases, $Ao/Ac=0.76$, $M=0.8$	198
Figure 5-29: Low incidence external cowl separation, $Ao/Ac=0.76$, $M=0.8$, showing shock/boundary layer interaction, density contours (left) and Mach number (right)	198
Figure 5-30: Iso-surface of $M=1.0$ enclosing supersonic region on external cowl (contours of density).....	199
Figure 6-1: AJVG blowing requirements.....	206
Figure 6-2: Iso surface of $M=0.07$ coloured by p/H showing separation dominance over AJVGs.....	212
Figure 6-3: Schematic of final AJVG location (viewed from front).....	213
Figure 6-4: Effect of AJVG skew angle on engine-face distortion, $\alpha=20^\circ$	214
Figure 6-5: Comparison between clean (left) and 60-Deg skew (right) - surface limiting streamlines and engine-face contours of Mach number- blue is low, red is high - viewed looking down duct.....	215
Figure 6-6: Effect of blowing pressure on intake distortion	216
Figure 6-7: Effect of blowing pressure ratio on recovery	217
Figure 6-8: Distortion characteristic with engine-face dynamic recovery contours, $Ao/Ac=0.96$	220
Figure 6-9: Blowing performance at $Ao/Ac=0.74$ (left) and $Ao/Ac=0.68$ (right)	221
Figure 6-10: Variation of intake mass-flow ratio at constant blowing pressure, $PR=1.23$	221
Figure 6-11: AJVG performance map	222
Figure 6-12: CFD validation for a range of jet mass-flows, $Ao/Ac=0.96$	223
Figure 6-13: Comparison of CFD and experiment, $Ao/Ac=0.89$, $PR=1.23$	225
Figure 6-14: Symmetry plane Mach contours at $Ao/Ac=0.90$, $\alpha=15.0^\circ$ with(left) and without (right) AJVGs, $PR=1.23$	227
Figure 6-15: Comparison of internal surface pressures, clean (shaded) and $PR=1.23$ (wire) $\alpha=15.0^\circ$, $Ao/Ac=0.89$	228
Figure 6-16: Computed distortion characteristic for $Ao/Ac=2.10$, with blowing ($PR=1.23$) and without blowing, contours of Mach number.	230
Figure 6-17: Computed distortion characteristic for $Ao/Ac=4.0$, with blowing ($PR=1.00$) and without blowing, contours of Mach number	231
Figure 6-18: Symmetry plane Mach contours at $Ao/Ac=2.10$, $\alpha=15.0^\circ$ with(left) and without (right) AJVGs, $PR=1.23$	233
Figure 6-19: Symmetry plane Mach contours at $Ao/Ac=2.10$, $\alpha=17.5^\circ$ with(left) and without (right) AJVGs, $PR=1.23$	233
Figure 6-20: Symmetry plane Mach contours at $Ao/Ac=4.00$, $\alpha=15.0^\circ$ with(left) and without (right) AJVGs, $PR=1.00$	233
Figure 6-21: Comparison of internal surface pressures, clean (shaded) and $PR=1.23$ (wire) $\alpha=17.5^\circ$, $Ao/Ac=2.10$	234
Figure 6-22: Effect of AJVGs during increasing yaw at $\alpha=15^\circ$	236
Figure 6-23: Effect of AJVGs during increasing yaw at $\alpha=17.5^\circ$	236
Figure 6-24: Nacelle ice-protection system (Rolls-Royce, 1986)	238

Acknowledgements

The list of people who have supported me during the course of this research by providing their time, knowledge and experience is long, and to those people I offer my deepest thanks.

Special mention must go to my academic tutor, Professor David Peake who has guided me through this process and provided endless enthusiasm and encouragement. Also to my industrial supervisor Mr. John Hodges who advised me in the preparation of this document.

I am grateful to Mr. Peter Martin who provided me with the opportunity to start this project and has allowed me to pick his brains on all things intakes since that time. I would also like to thank QinetiQ and before that DERA for sponsoring this research programme and providing use of computing facilities.

My experiments could not have been completed with out the assistance of the staff of the Handley Page Laboratory in the Aeronautic department at City. Particularly Mr. Mike Smith, whose extraordinary skills turned nice ideas in to practical components, and of course for the endless supply of tea.

Finally, I would like to acknowledge the support and encouragement given to me by my friends and family, especially my partner Miss Sonya Anson, without whose support and inspiration I could not have completed this study.

Declaration

I grant powers of discretion to the University Librarian to allow my thesis to be copied in whole or in part without further reference to the author. This permission covers only single copies made for study purposes, subject to normal conditions of acknowledgement.

Nomenclature

Abbreviations

A	Area
AIAA	American Institute for Aeronautics and Astronautics
AIP	Aerodynamic interface plane
AJVG	Air-jet vortex generator
ARA	Aircraft Research Association (UK)
ARC	Aeronautic Research Council (UK)
BAES	BAe Systems plc.
CFD	Computational fluid dynamics
CPU	Central processing unit
DERA	Defence Evaluation and Research Agency (Now QinetiQ)
ERCOFTAC	European Research Community On Flow, Turbulence And Combustion
DES	Detached Eddy Simulation
GE	General Electric Company
ISA	International Standard Atmosphere
LEX	Leading-edge Extension
Le	Leading-edge
LES	Large Eddy Simulation
LO	Low-Observable
HARV	F/A-18 High Alpha Research Vehicle at NASA Dryden Research Centre
NACA	National Advisory Committee for Aeronautics (USA)
NAM	Northwest aerodynamic Models Ltd. (UK)
NASA	National Aeronautics & Space Administration (USA)
NGTE	National Gas Turbine Establishment (UK)
NS	Navier Stokes
QCSEE	Quiet, Clean, Short-Haul, Experimental Engine
QQ	QinetiQ
RANS	Reynolds Averaged Navier-Stokes
RAE	Royal Aircraft Establishment (UK)

R-R	Rolls-Royce plc.
RSM	Reynolds Stress Modelling
SIMPLE	Semi-Implicit Method for Pressure Linked Equations
SAUNA	Structured & Unstructured Numerical Analysis (CFD code)
TWT	Transonic Wind Tunnel
UAV	Unmanned Air Vehicle
UCAV	Unmanned Combat Air Vehicle
VG	Vortex Generator
VVG	Vane Vortex Generator
V/STOL	Vertical/Short Take-off & Landing
WT	Wind Tunnel

Symbols

a	Ellipse major axis
a	Local speed of sound
A	Area
b	Ellipse minor axis
C_d	Drag coefficient, $\frac{D}{qA_{MAX}}$
C_p	Static pressure coefficient, $\frac{p - p_\infty}{q}$
CR	Intake contraction ratio, $\frac{A_C}{A_{ef}}$
D	Drag (N)
DC(θ)	Rolls-Royce distortion descriptor, $\frac{(HRA - \bar{H}_{\theta MIN})}{q_{ef}}$
D	Diameter
e	Internal energy per unit mass
H	Total pressure (Pa)
HRA	Area weighted total pressure recovery, $\frac{\bar{H}_{ef}}{H_\infty}$
L	Length (m)
m	Model

\dot{m}	mass-flow rate (kg/s)
M	Mach Number
MAX	Maximum
MIN	Minimum
PR	Jet pressure ratio, $\frac{H_{PLENUM}}{p_{\infty}}$
p	static pressure (Pa)
q	dynamic pressure (Pa)
Re	Reynolds number based on maximum intake diameter, $\frac{\rho V D_{max}}{\mu}$
T	Temperature (°K)
u,v,w	Components of velocity in x,y and z
V	Velocity magnitude (m/s)
WAT	Corrected intake mass-flow, $\frac{\dot{m}\sqrt{T_{ef}}}{AH_{ef}}$
α	Intake angle of incidence (degrees)
β	Intake angle of yaw (degrees)
δ	Relative pressure, $\frac{P}{P_{SL}}$
δ_{ij}	Kroneker delta (logical operator)
γ	Ratio of specific heats
ρ	Density (kg/m ³)
θ	Intake angle of roll (degrees)
θ	Relative temperature, $\frac{T}{T_{SL}}$
ϕ	Angle of pitch (degrees)
σ	Relative density, $\frac{\rho}{\rho_{SL}}$
μ	Viscosity (kg/ms)

Subscript	
c	Highlight
ef	Engine-face
J	Jet
Max	Maximum
Min	Minimum
o	Sea-level or free stream
Plenum	Air-jet plenum
Spill	Spillage
SL	Sea level (ISA)
t	Stagnation
t	Turbulent
th	Throat
WS	Working section
∞	freestream
θ	Angular segment of engine-face (degrees)

1. Introduction

1.1. Background

The design of the air intake for gas turbine powered aircraft is ultimately one of compromise; the design affects not only the engine performance but also the vehicle external aerodynamics. These are often conflicting requirements. To maximise engine performance, the intake is required to deliver air to the fan with minimal total pressure loss and minimal spatial total pressure distortion over a wide range of incidence angles and engine operating points. The fluidic mechanisms generating these losses or distortions are associated with flow separations and/or shock losses within the intake system. Minimising the pressure loss and distortion is critical for take-off conditions, where the engine is at a maximum power setting. The requirement is that the intake should be sized to prevent choking and shock losses at this condition and the lip should be shaped to eliminate flow separation. Designing for take-off, however, introduces complications for the cruise condition; the intake is effectively oversized and operating at a spilling condition; this will induce excessive velocities on the external lip, resulting either in separation or a shock wave on the external surfaces. For high subsonic cruise aircraft, the thick rounded lip that is required for maximum take-off performance might cause shock waves leading to a premature drag divergence. For military combat air-vehicles, the converse is often true. Low-observable or high-speed design requirements result in sharp lip geometry that may penalise the low speed or manoeuvre performance of the vehicle by introducing pressure loss and distortion to the propulsion steam tube, reducing engine thrust and surge margin respectively.

The compromise required between the internal and external aerodynamic design of air intakes provides an ideal opportunity for the use of flow control techniques in addressing any lip flow separation. The intake contour may be designed for cruise efficiency and flow control may be used to improve low speed, high-incidence or high mass-flow operation. Air Jet Vortex Generators (AJVGs) are ideal for this application. The close proximity of the intake lip to the engine compressor means that small quantities of high-pressure air may be taken from the engine with the addition of minimal ducting and its associated weight penalty. AJVGs offer two major

advantages over vane vortex generators (VVGs). Firstly, since they are immersed in the intake surface, they are not at risk of being ingested by the engine in the event of a structural failure. Secondly, there is no 'off-design' penalty as the flow rate may easily be matched to the intake operating conditions by means of a relatively simple control system. When not required the flush exits provide no parasitic pressure-loss in the streamtube.

The use of vortex generators (VGs), both AJVGs and VVGs, has long been established for distortion management within offset intake diffusers. Such systems are installed in the F-111 [see *Figure 1.1*] the F/A-18 military aircraft and the Boeing 727 transport aircraft. However, VGs have only been used to control lip separation as a late design fix, and has not been adopted on production air vehicles. Traditional pod engines for civil transport aircraft, may not have a long enough diffuser for the discrete vortices from the VGs to be sufficiently diffused, resulting in a non-uniform circumferential velocity distribution. This leads to increased load variation on the fan blades reducing the fatigue life. Military aircraft engines have a higher distortion tolerance than civil engines and are often over powered, so that some performance degradation can be tolerated.

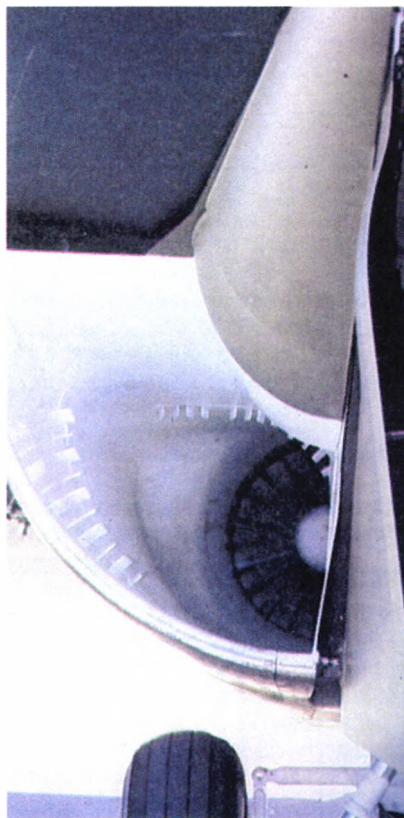


Figure 1-1: Vane vortex generators in the intake duct of the F-111 aircraft

When the flight envelope is too broad to allow compromise in the air intake design, variable geometry such as rotating intakes on the F-15 or vari-cowls (leading edge flaps) on the Eurofighter, may be used to maintain acceptable local flow angles at the cowl lip.

The design space for both military and civil aircraft is changing. The current emphasis with military aircraft design is lightweight, high performance, unmanned combat air vehicles (UCAVs) which are primarily driven by Low Observability (LO) requirements. For this type of configuration, lip flow control is a more attractive option than variable geometry due to the reduction in both weight and mechanical complexity. The prospect of using flow control is also becoming more attractive in civil aircraft design. Acoustic requirements are leading to longer diffusing ducts. Examples of such are negatively scarfed nacelles (in which the upper lip is swept aft leaving a lower lip protruding forward) and buried installations such as those used in blended wing body (BWB) designs or Boeing's sonic cruiser. These types of configuration may allow the use of vortex flow control at the lip without compromising the life of engine components.

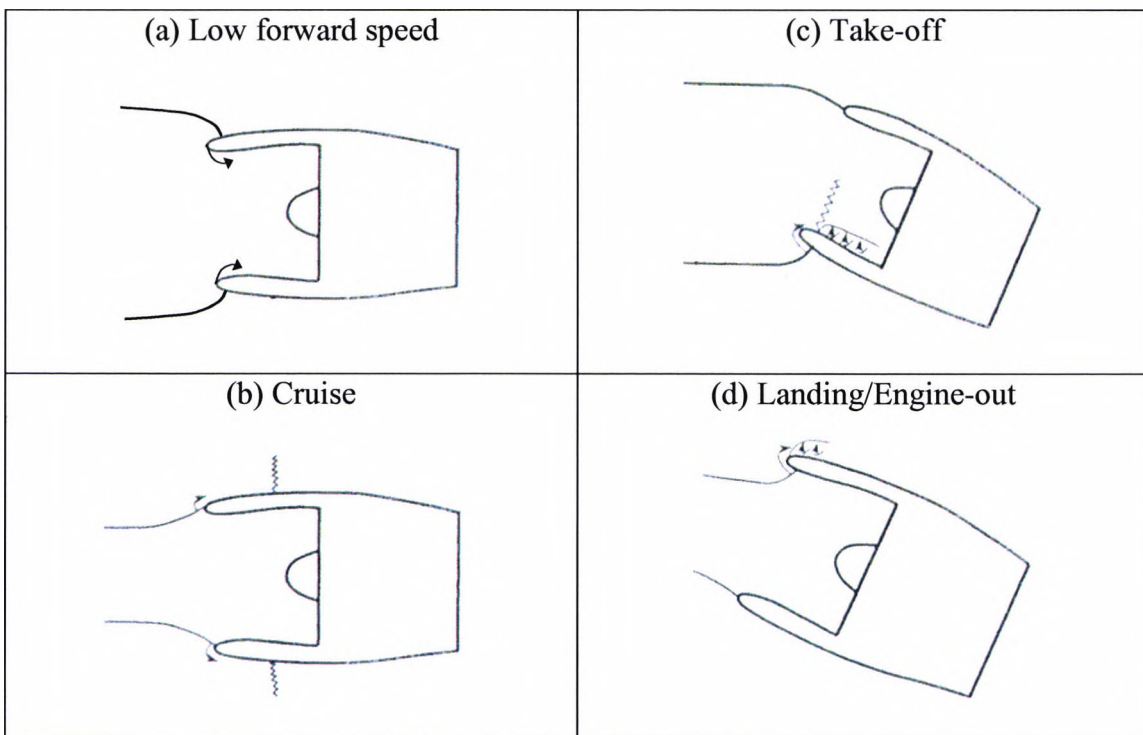


Figure 1-2: Subsonic intake operating conditions

The four principle operating regimes of a subsonic intake are shown in Figure 1.2. This illustrates the potential for lip separation at the different operating conditions. The top two illustrations of the figure show conditions at which internal separation is likely, low-forward speed and take-off, where the entering streamtube is larger than the intake capture area. In the lower pictures, the intake is 'spilling', i.e. the entering streamtube is smaller than the intake capture area. This condition may lead to external lip separation.

The Centre for Aeronautics at City University is well established as the UK's leading authority on AJVGs. QinetiQ (then DERA) has previously supported work at City University on the application of AJVGs to diffusing S-ducts and on swept wings. This piece of research builds upon that partnership by demonstrating the novel concept of using AJVGs to control air intake lip separation.

The intake model used for this piece of research is RAE model 742L. This a series of axi-symmetric pitot intakes that has been tested extensively over the last twenty years over a range of Mach numbers and Reynolds numbers. The wind tunnel model of this intake, along with the necessary flow metering equipment, is readily available, thereby helping to reduce the cost of the experimental procedures.

RAE model 742L consists of eight cowls that differ in both external, and internal lip geometry. The series was designed to extend the database of previous RAE & NASA intake research. The variation in geometry across the series represents both civil (blunt) and military (sharp) intake lips. The simplicity of an axi-symmetric configuration allows the effects of the variation in individual geometric parameters to be isolated.

A glossary of specialist intake and propulsion terminology is provided in Appendix A.

1.2. Goal and key specific objectives

The goal of this research is to demonstrate the novel concept of AJVGs for minimising engine face distortion by controlling the development of flow separation at the intake lip, using an interactive computational and experimental approach. This is to be done whilst considering the practical issues of a real-life installation, to provide maximum benefit to industry. Consequently, we must consider the quantity of air that would need to be taken from the engine, as well as blowing pressures and structural integration. These considerations could well limit the available design space.

The research programme can be split into the following key specific objectives (KSOs):

- Understand the aerodynamic mechanisms responsible for three-dimensional internal air intake lip separation at low speed and high incidence using an interactive computational and experimental approach.
- Use computational and experimental resources to investigate the use of AJVGs to minimise engine-face distortion by controlling the development of flow separation at the intake lip.
- Assess the practicality of a real –life installation.
- Devise an appropriate method for computational modelling of AJVGs installed in an air intake that is cost effective in terms of computing time and numerical accuracy.
- Validate the FLUENT v6.0 computational software for prediction of air intake lip separation and determine the best practice in terms of turbulence modelling and grid density and distribution.

2. Literature review

This chapter presents a review of open literature relating to the problems of air intake lip separation and its control. Where appropriate, documents relating to flow control on different configurations such as high-lift systems or diffusing s-ducts are introduced. This is the case with AJVGs, which have not previously been applied to intake lips.

The problems associated with lip separation have developed alongside the use of the gas turbine engine, although the origin of low-drag intake shapes arises from problems encountered in the piston engine era. The development of modern intake shapes is discussed from podded nacelle type geometry through to modern low-observable shapes.

Traditionally efforts have been made to avoid lip separation on intakes, its presence being determined by a reduction in total pressure recovery and an increase in distortion or external drag. Aircraft and engine manufacturers have developed new intake designs based on their historical databases. For advanced low-observable configurations, particularly UCAVs where the constraint of the pilot is removed, these databases no longer apply.

In recent years, efforts have been made to try to understand the nature of the three-dimensional separations using modern computational techniques. However, in the preceding years, the onset of intake lip separation was seen as analogous to 2-D aerofoil leading edge separation. Aerofoil methods were used to try to understand some of the fluid dynamic mechanisms leading to separation, although this was limited purely to predicting the onset of separation rather than its three-dimensional development.

Flow-control techniques for managing lip separation have been mainly proposed for military aircraft and use blowing, suction or variable geometry techniques. Within the intake-diffuser, VVGs and AJVGs have successfully been used for managing distortion.

This chapter concludes with four tables categorising the most important papers in the open literature. Each table is presented chronologically with three fields representing each entry. Column one holds the author(s) and date, column two details of the configuration and flow conditions and column three, the key findings.

The first table, Table 2.1, catalogues literature on intake research models, which provide data on lip separation; the entries may contain windtunnel or computational results.

The second table, Table 2.2 comprises literature relating to problems arising from lip separation on real aircraft, either prototype or production.

Table 2.3 presents literature on flow control at the intake lip, and, finally Table 2.4 introduces important works on distortion management in diffusing s-ducts and the more general use of AJVGs.

2.1. A historical perspective of intake lip design

2.1.1. The external cowling

Investigations into air intake lip separation have occurred concurrently with the development of the aeroplane. The origins of air intake shapes for gas turbine engines can be traced to the development of engine cowlings for piston engine aircraft. *Jones (1929)*, in his lecture to the Royal Aeronautical Society, was the first in the UK to identify the effect of drag due to the exposed cylinders on early air-cooled radial engine aircraft on performance, particularly in lowering maximum speed. The problem of the drag due to the exposed cylinders was also recognised in the United States and the National Advisory Committee for Aeronautics (NACA) initiated a cowling research programme in 1927. This programme resulted in a series of cowling shapes that not only reduced drag but also maintained cooling performance (*Theodorsen et al, 1937*). *Anderson (1998)* discusses this research in detail.

Towards the end of the Second World War, aircraft speeds had increased to such an extent that another problem was becoming apparent. The external drag of cowlings was seen to rapidly increase as the ‘compressibility burble’ was encountered.

Robinson & Becker (1942) report how this drag rise was related to the peak negative pressure on the external cowl surface. The speed at which the drag increases was found equal to or slightly greater than the flight speed at which the speed of sound was reached locally on the cowling. The criterion proposed for design of the inlet with a high critical speed, is a uniform pressure distribution over the cowl with local velocities as close to the free-stream speed as possible. This reduces the possibility of a sudden compression (shock wave) and the associated drag. From the figures presented in the report, it is evident that cowlings corresponding to this requirement are constructed from shapes that permit a gradual and continuous variation in curvature, such as an ellipse of high finesses ratio. Blunter, more abrupt shapes, such as a circular arc leading edges lead to a rapid increase in suction followed by a marked compression as the circular arc becomes tangent to a parallel section. The difference between these types is shown in Figure 2-1 in which the pressure distributions are plotted normal to the cowl surface for a range of incidence angles.

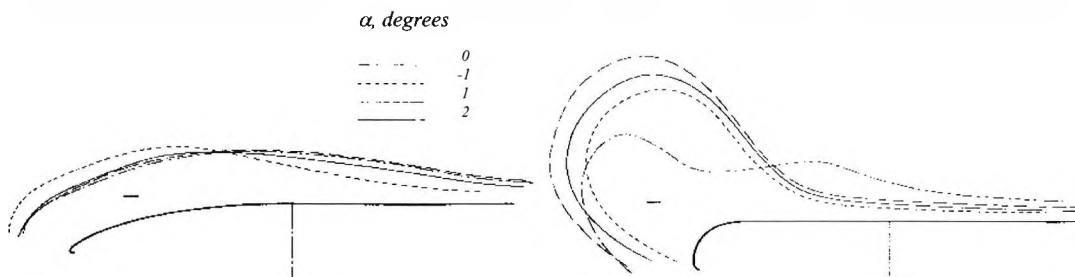


Figure 2-1: Example of pressure distributions on engine cowlings (Robinson & Becker, 1942)

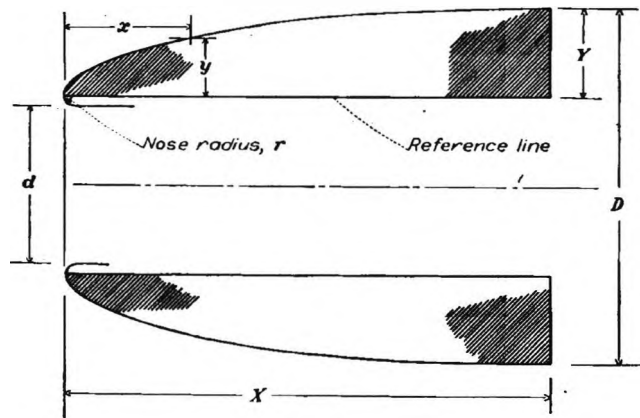
The transonic limitations of cowlings described above led to further experimental studies at NACA. The result was the NACA 1-Series Cowling. This profile is described by a series of non-dimensional ordinates that may be scaled by the intake diameter ratio (d/D_{MAX}) and length ratio (L/D_{MAX}). The performance of NACA 1-Series cowls is a function of these proportions. The NACA 1-series is essentially a super ellipse with an exponent of 1.78. However, slight differences are apparent near the leading edge and the crest as the shape was faired by hand whilst in the wind tunnel to provide the best performance. As a result there are a number of discontinuities in the surface curvature of the cowling which leads to discontinuities in the surface static pressures. Recently, *The Engineering Sciences Data Unit (ESDU) (1994)* provided a mathematical description of the profiles, which removes these anomalies in the surface curvature.

A NACA 1-Series is generally described by a number that defines its proportions; this takes the form:

NACA 1-85-45

The numbers 85 and 45 are percentages that describe the diameter ratio (d/D_{MAX}) and the fineness ratio (L/D_{MAX}) respectively. These dimensions are illustrated in Figure 2.2

TABLE I
NACA 1-SERIES ORDINATES
[Ordinates in percent]



$$X = \left(\frac{X}{D}\right) D$$

$$Y = \frac{D-d}{2} - r$$

$$\text{For } r = 0.025Y: Y = \frac{D-d}{2.05} = \frac{D(1-d/D)}{2.05}$$

s/X	y/Y	s/X	y/Y	s/X	y/Y	s/X	y/Y
0	0	13.0	41.94	34.0	69.08	60.0	89.11
.2	4.80	14.0	43.66	35.0	70.05	62.0	90.20
.4	6.63	15.0	45.30	36.0	71.05	64.0	91.23
.6	8.12	16.0	46.88	37.0	72.00	66.0	92.20
.8	9.33	17.0	48.40	38.0	72.94	68.0	93.11
1.0	10.39	18.0	49.88	39.0	73.85	70.0	93.95
1.5	12.72	19.0	51.31	40.0	74.75	72.0	94.75
2.0	14.72	20.0	52.70	41.0	75.63	74.0	95.49
2.5	16.57	21.0	54.05	42.0	76.48	76.0	96.16
3.0	18.31	22.0	55.37	43.0	77.32	78.0	96.79
3.5	19.94	23.0	56.66	44.0	78.15	80.0	97.35
4.0	21.49	24.0	57.92	45.0	78.95	82.0	97.87
4.5	22.96	25.0	59.15	46.0	79.74	84.0	98.33
5.0	24.36	26.0	60.35	47.0	80.50	86.0	98.74
6.0	27.01	27.0	61.52	48.0	81.25	88.0	99.09
7.0	29.47	28.0	62.67	49.0	81.99	90.0	99.40
8.0	31.81	29.0	63.79	50.0	82.69	92.0	99.65
9.0	34.03	30.0	64.89	51.0	83.36	94.0	99.85
10.0	36.13	31.0	65.97	52.0	84.00	96.0	99.99
11.0	38.15	32.0	67.03	53.0	84.63	98.0	99.99
12.0	40.09	33.0	68.07	54.0	85.25	100.0	100.00

Nose radius: 0.025Y

Figure 2-2: NACA 1-Series Cowling (Baals et al, 1948)

Due to the fine transonic performance of NACA 1-Series cowls, the shape has been extensively used with gas turbine engines and it is still used today as a benchmark in cowl design. The low-speed performance requirement for this type of engine means that the internal part of the lip has to be modified to provide sufficient internal contraction. This is often done by truncating the NACA curve at the leading edge, replacing the original radius with a quarter ellipse of larger dimension. This, however, introduces a discontinuity in curvature at the leading edge that may be remedied by using an additional curve to blend the internal and external lines. In general, intake geometry may be considered to consist of three distinct parts, although these may be constructed from a different number of curves. These are the external cowling, the internal lip and the diffusing duct. A typical cowl constructed in this manner is shown in *Figure 2.3*

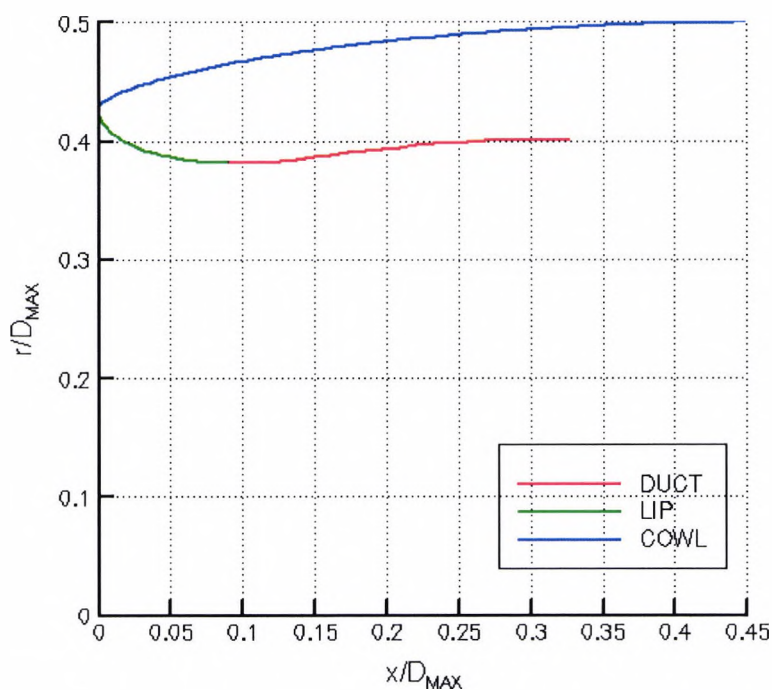


Figure 2-3: Typical civil cowl profile

Gas turbine engines introduced another difficulty to be overcome in the design of an intake profile, namely spillage drag. Spillage drag is not a drag in the traditional sense, but a correction applied to the airframe drag to account for the effects of the propulsion stream tube on the external aerodynamics. Conventional thrust and drag accounting procedures define the propulsion system as the streamtube passing through the propulsion system starting infinitely far upstream and terminating at the nozzle

exit plane (See *ARC CP. No.190*). A variation in the size of the propulsion streamtube will affect the air-vehicle external aerodynamics. As the engine mass-flow is reduced from a datum value, usually a mass-flow-ratio of unity, the propulsion streamtube cross sectional area reduces in size, the stagnation point of the streamline dividing the internal and external flow moves inside the intake and the external flow is accelerated due to the increased turning required to negotiate the cowl lip. This creates a thrust force on the cowl lip. In potential flow, this thrust balances an additional drag force that is generated by the pressure on the streamtube surface as it approaches the intake. This is termed pre-entry drag or additive drag. Under viscous compressible flow conditions, the cowl thrust does not balance the pre-entry drag. The difference between the two is termed spillage drag. As long as the flow remains attached on the cowl, this difference is negligible. When separation does occur on the external cowl at some critical mass-flow-ratio, a rapid increase in spillage drag occurs and continues to elevate as the mass-flow ratio is reduced further.

The NACA 1-Series cowl has been used on a number of aircraft throughout the 1960s and 1970s, such as the Lockheed C-5 Galaxy (*Hancock and Hinson, 1969*). This cowl is often the starting point for a practical design. Both the Jaguar (*Leyland, 1998*) and the Tornado (*Stocks & Bissinger, 1981*) started with NACA 1-Series cowls even though the Mach 2 Tornado's envelope is substantially greater than that originally perceived for the NACA cowling.

As a result of its excellent transonic performance and good low mass-flow performance when used in conjunction with realistic internal geometry, the NACA 1-Series has become the benchmark by which all other cowlings are evaluated. In both the US and the UK, a large amount of data had been collected enabling performance correlations to be made based on the cowl's geometric proportions. Examples are reported by *Stanhope (1968)*, *Hancock and Hinson, (1969)*, *Butler (1973)* and *ESDU (1984)*. These correlations provide a trade-off between transonic cruise performance, primarily a function of the fineness ratio (L/D_{MAX}), and spillage performance, a function of diameter ratio (D_c/D_{MAX}). The correlation by *Butler (1983)* is presented in Figure 2.4. This is based on data originating from Rolls-Royce. The charts are intended to provide data for initial project selection. The upper chart expresses the drag rise Mach number as a function of a geometric parameter that may be considered

equivalent to a thickness/chord ratio of an aerofoil section. The different lines on the graph show the effect of the afterbody curvature in accelerating the flow over the crest and reducing the drag divergence Mach number. The lower plot in the Figure shows the critical mass-flow for spillage onset plotted against a similar geometric parameter; the effect of a moderate incidence angle in lessening the amount of spillage required for the drag can also be seen. Charts such as the pair depicted in Figure 2.4 may be used in an iterative manner to broadly determine the proportions of a cowl to achieve a specified performance. However, the accuracy of such methods is not adequate for detailed design or achieving the strict trade-offs required for some projects. This is mainly because the complex array of variables that may be used to define a modern three-dimensional nacelle such as local camber and profile shape cannot truly be accounted for in such a simple correlation.

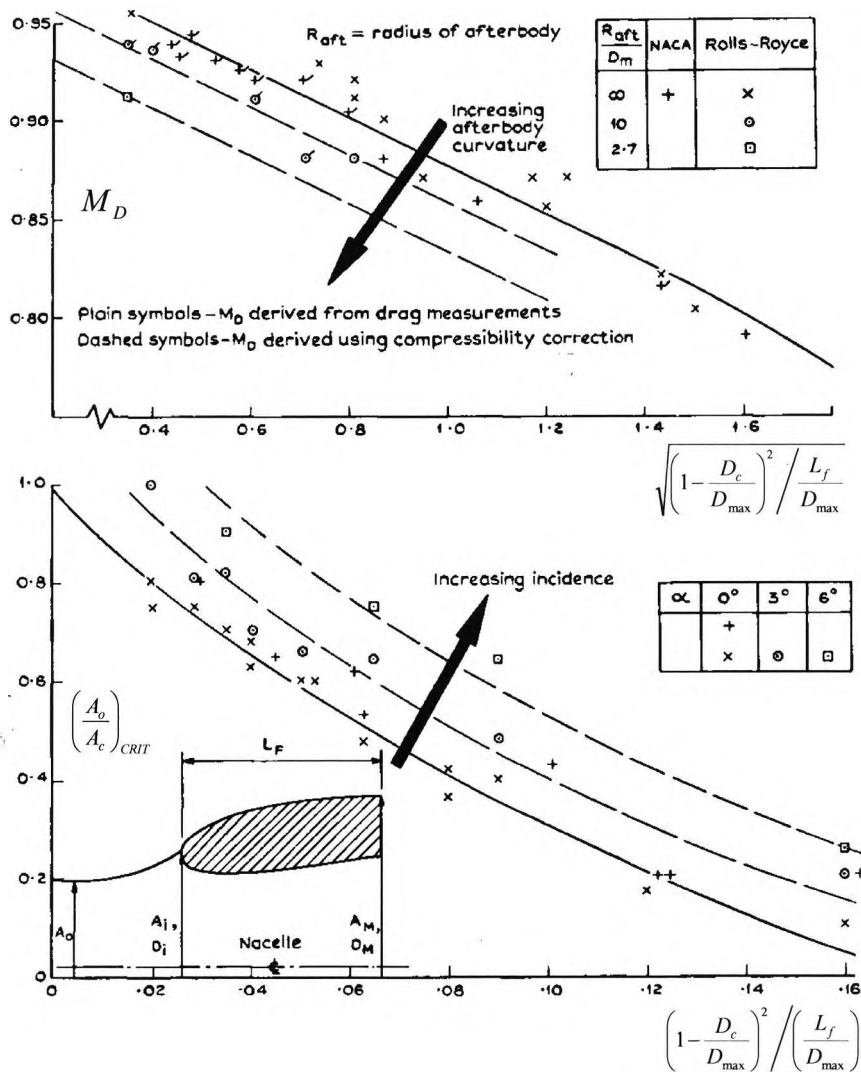


Figure 2-4: NACA cowl performance (Butler, 1973)

The NACA 1-Series may be considered to give good performance across a wide range of mass-flows and Mach numbers. However, the small leading-edge radius may compromise low speed operation: particularly when considering that the D_c/D_{MAX} of modern high-bypass turbofans has increased to values of around 0.9, leading to flat sharp profiles. Modern aerodynamic design tools have been used to generate lip and cowl profiles that eliminate the defects of NACA 1-Series profiles. Current generation profiles can be based on the manipulation of surface curvature to achieve favourable pressure distributions, a technique developed for transonic aerofoil section design by *Pearcey (1960)*. *Langley (1979)*, who used conic sections to devise cowl profiles, has described the application of this technique to achieve better high-speed drag performance than the NACA 1-Series. *Re & Abeyounis (1993)* describe profiles in which the curvature at the leading edge was modified to improve low-speed performance without compromising the drag divergence.

Ultimately, a cowl profile may be generated for a specific application using Design Optimisation (DO). In this technique, a computational analysis tool is coupled with an optimising algorithm. The geometry of the cowl is created parametrically and the effect of each parameter on the pre-defined performance metrics evaluated. The optimiser then recreates the geometry by adjusting the geometric parameters to create what it believes to be the optimum shape. The process continues until some specified convergence criteria are met. The resulting shape is obviously heavily dependent upon the geometric parameters used. *Rodriguez (2002)* has demonstrated DO by adjusting the inclination of the nacelles on a blended wing body (BWB) configuration. *Williams & Jackson (2003)* used a conventional NACA 1-Series geometry definition in conjunction with the QinetiQ DO tool CODAS to design an optimum transonic intake.

In summary, a first iteration of an external profile can be produced by well-known and understood shapes such as the NACA-1 Series. However, the constant search for performance improvement has reduced the design space, meaning configuration specific designs are often used. In this case, the performance may be penalised in one area of the flight envelope in order to achieve acceptable performance in another.

2.1.2. The internal lip

The governing flow regime for the design of the internal lip contour is the low-forward speed or static condition with the engine requiring maximum airflow. This represents take-off or hover in the case of a VSTOL aircraft. For this condition, the stagnation point on the dividing streamline between the internal and external flow, is located on the external cowl surface. The loss associated with the internal lip separation may be regarded primarily as functions of contraction ratio and throat Mach number. Throat length and diffuser geometry have also been shown to have an effect on lip loss (*Seddon & Goldsmith, 1999*).

The focus of early work studying the effect of entry losses originating at the lip was a number of analytical studies using configurations with sharp lips such as that by *Frandenburgh & Wyatt (1954)* and methods described in a chapter entitled 'Lip separation and transonic throat flow' in *Seddon & Goldsmith (1999)*. These methods use a momentum analysis to give values of lip-loss as a function of Mach number and mass-flow ratio assuming the Mach number somewhere within the intake where uniform flow has been re-established is known.

The analytical methods for intakes with sharp lips have been adapted by *Moeckel (1955) & Bore (1993)* to take account of finite thickness lips. These tools provide a methodology by which important intake design requirements, such as contraction ratio, can be determined for proposed operating conditions. They do not provide a method for describing the internal contour but are based purely on lip thickness, or more precisely the difference in area of the lip between maximum thickness and the throat, as areas can be easily inserted into the equations for streamtube flow. Traditionally, a quarter ellipse or super ellipse is used for the internal lip. The choice is dependent upon performance compromise. Typical major to minor axis ratios range from 1.0 (circular arc) to 5.0. These shapes provide an acceptable amount of contraction with minimum infringement on the available diffuser length. Increasing the major-minor axis ratio to larger than 1.0 will reduce shock losses by ensuring a lower surface Mach number but the lip may be prone to earlier separation. *Clark and Vasta (1984)* discuss how the AV-8B Harrier II changed the circular arc lip of the AV-8A for a 2:1 ellipse to reduce lip velocities at the static condition.

Many studies have been conducted looking at the effects of lip geometry at low speed and cruise conditions. For example *Blackaby & Watson (1954)* looked at a range of lip shapes including sharp, elliptical and circular arc. *Goldsmith (1990)*, *Hacker et al (1985)* extended these configurations with the RAE m742L and *Wilmer et al (1981)* with the m2129 series of models.

2.2. Intake lip separation

Lip separation may be split into two categories, internal separation and external separation. Internal separation affects the operation and performance of the powerplant; while external separation influences the vehicle external aerodynamics. For a well-designed intake, the onset of lip separation is directly related to the movement of the stagnation point of the streamline dividing the external and internal flows. For high engine mass flows, the capture stream tube will be larger than the intake area. The stagnation point is situated on the outside surface of the intake, flow entering the intake must pass around the lip (see *Figure 1.2a*), and a critical mass-flow will be reached above which attached flow cannot be maintained. A similar process occurs for external separation except that the upstream area of the propulsion streamtube is being reduced below the intake capture area (see *Figure 1.2b*). As a rule, external separation will not be present during the normal operation of transport aircraft (*Berry, 1994*) but in the event of an engine failure or extreme manoeuvres in the case of a military aircraft, lip separation may be induced (see *Figure 1.2d*). The addition of incidence or sideslip must also be considered as this has an influence on the location of the stagnation point. Positive incidence will move the stagnation point aft on the cowl of the lower lip. In a flight condition, such as take-off when a high engine flow demand is required, an incidence angle will compound the mass-flow effect on the dividing streamline, making the lower lip particularly susceptible to separation (see *Figure 1.2c*). At low forward speeds, crosswind effects can lead to high local flow-angles on the side of the intake enhancing the prospect of separation. Internal and external lip separation are discussed in more detail in the following section.

2.2.1. External separation

Intake external separation is often associated with spillage-drag. When a separation occurs on the external lip, the lip suction force no longer cancels out the force on the pre-entry stream tube. In the case of subsonic transport aircraft with podded nacelle type engine installations, separation can be eliminated for all usual flight conditions. *Berry (1997)* describes the nacelle operating range required for the twin engine Boeing 777 that includes the importance of designing the nacelle for off-design operation particularly with an inoperative engine. An inoperative engine in flight is termed 'windmilling'; under this condition the mass-flow-ratio of the nacelle is reduced to a value of approximately $A_o/A_c=0.3-0.4$. This condition is sketched in *Figure 1.2d*. To be able to achieve certification, in the event of an engine failure during take-off, a twin-engined aircraft must be able to climb away from the airfield. It is, therefore, a design requirement of twin engine civil aircraft that in the event of an engine failure attached flow is maintained on the cowl. This keeps spillage drag to a minimum, which is important, because an increase in drag in addition to the loss of engine thrust will be critical to aircraft performance. An additional requirement in the case of the Boeing 777 was the requirement for Extended Twin-Jet Operation (ETOPS) certification. In the event of an engine failure during cruise, there is a requirement to maintain high-speed operation for extended periods, in order to be able to reach an alternative airfield. The flow conditions experienced by the nacelle during engine failure at cruise are slightly different to those at take-off. The reduction in streamtube area due to the windmilling engine is smaller, but local surface Mach numbers on the cowl are larger due to the higher forward speed. The requirement is still to eliminate external separation, as an increase in spillage drag may affect the fuel usage and, hence, the range.

Difficulties in predicting the behaviour of nacelle upper cowl separation with sub-scale models have been documented by *Younghans, Hoelmer & Stockman (1982)* and *Hoelmer, Younghans & Raynal (1987)*. In a series of tests with different size models in the pressurised F1 low-speed windtunnel at ONERA for General Electric (GE), the dependence of upper cowl separation on Reynolds number is established for civil type cowls. In all cases, the mass flow was fixed to a value representative of engine failure. The angle of attack was then increased until separation on the upper cowl was detected. Two means were used initially to detect separation: these were examining

local cowl static pressures for a sudden increase with increasing incidence and evaluating wake total pressures for a sudden reduction with increasing incidence. Later tests only used cowl static pressures rise as a separation indicator. Variations in tunnel total pressure in conjunction with 15% and 33% scaled models enabled Reynolds numbers up to full scale to be achieved. The results show that the incidence at which separation occurs on the upper cowl is a linear function of Reynolds number up to approximately 1.0×10^7 based on intake capture (highlight) diameter; this is approximately 50% of flight Reynolds number. Above this Reynolds number, the incidence angle for separation is more or less constant. In this case, the critical Reynolds number could only be reached with a 33% scale model in a pressurised tunnel. The results can be seen in *Figure 2-5*.

The implication of sub-scale testing is serious. A cowl that achieves the correct incidence angle for separation at sub-scale will be over engineered for flight scale. This may be interpreted as a lower than necessary diameter ratio (D_c/D_{max}), effectively cowl frontal area. This will obviously have weight and drag penalties for the nacelle itself as well as for the supporting structure of the pylon and wing. The most likely cause of the sudden change in behaviour as Reynolds Number increases is a change in the type of the leading-edge separation. Leading-edge separations will be discussed in more detail in Section 2.3.

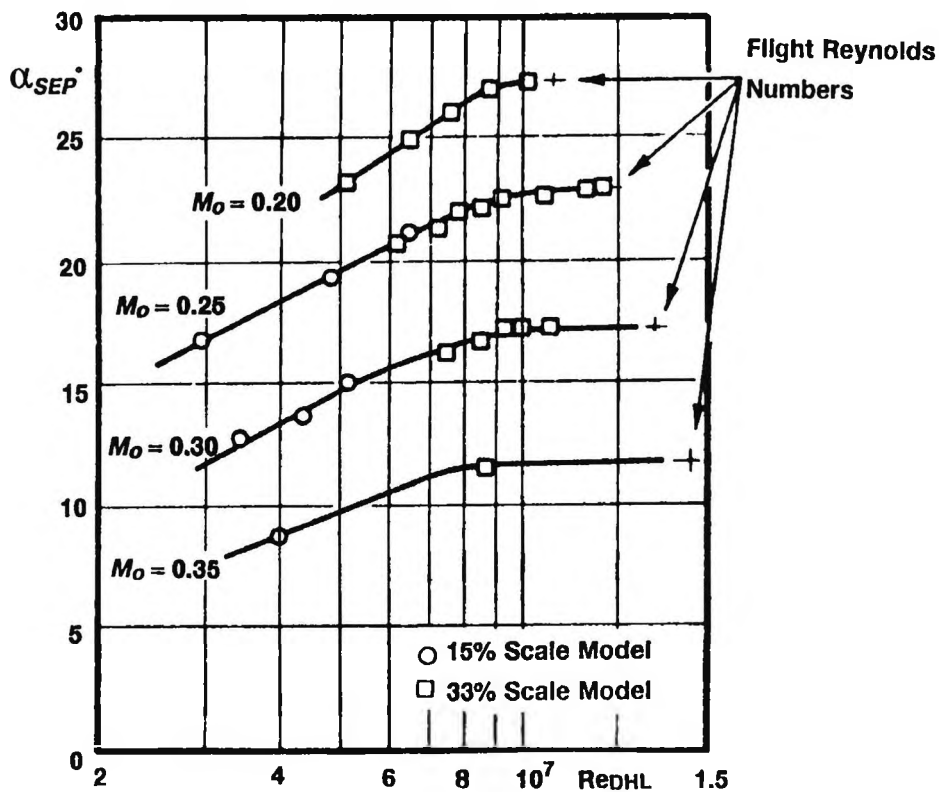


Figure 2-5: Reynolds number effects on upper cowl separation (Hoelmer et al , 1987)

To try to understand the Reynolds number dependence on upper cowl separation the authors applied both empirical theory and computational analysis to the 33% scale model. The computational analysis was based on an inviscid code with coupled boundary layer analysis in which boundary layer transition was applied at a fixed value of momentum thickness Reynolds number of 140. This approach only led to the prediction of turbulent boundary layer separation on the external cowl, although the angle of incidence for separation at low Reynolds numbers was well predicted. However, over the full range of Reynolds numbers, this method predicted a linear variation in incidence angle for separation with Reynolds number, not the ‘dogleg’ curves in Figure 2.5. A further insight into the change in the separation onset dependence with Reynolds number is disclosed by examining the inviscid prediction of surface Mach numbers upon which the boundary layer analysis is based. The surface Mach numbers are under predicted by the computational analysis and this discrepancy increases with Reynolds number. The difference is 0.11 at the highest Reynolds number computed where the peak Mach number is 1.1. The location of the peak Mach number also appears to move forward towards the leading edge as

Reynolds number is increased. The difference is due to neglecting viscous effects in the theoretical calculation of surface Mach numbers. It is perhaps this strong coupling of both compressible and viscous effects, which leads to the over prediction of the separation angle at high Reynolds numbers. This is possibly due to the movement of the separation point towards the leading edge, where it remains fixed as Reynolds number increases further.

Andrew, Lehnig and Rahm (1991) describe an inlet redesign process to achieve higher angle-of-attack requirements for both the internal keel at maximum airflow and upper external cowl (crown) separation during engine out – second segment take-off. The re-design is constrained by maintaining drag divergence Mach number. The design requirement is that no flow separation should occur within the flight envelope. The new cowl design was tested in the ONERA F1 pressurised tunnel having been originally designed with Euler CFD methods. The separation requirements were met; however, the contradictory requirement for maintaining drag divergence Mach number was not achieved, but the shortfall was deemed acceptable.

Much of the data available in the open literature with information on external lip separation is in the form of spillage drag comparisons and the mechanics of the lip separation are not examined in any detail. When comparing spillage drag across the mass-flow range, the points of note are the critical mass-flow-ratio, that mass-flow at which there is a rapid drag rise indicating the onset of lip separation and the gradient of the slope after the drag rise has been initiated.

Data sets provided by *Blackaby and Watson (1954)* focus primarily on the effects of lip radius on spillage drag. Two NASA data sets by *Re (1974,1975)* examine the drag characteristics of isolated axisymmetric NACA 1-Series cowls. Both these sources provide excellent parametric data sets for high-speed pitot intakes. The data sets by *Re* in particular would make excellent CFD validation test cases as all necessary geometric and flow data are presented. However, in both cases, very little information is presented regarding the fluid dynamic mechanisms behind lip separation. *Blackaby and Watson (1954)* make an attempt at flow visualisation for the static case by inserting a splitter plate on the intake symmetry plane, which is coated in a lampblack and kerosene mixture. The photographs indicate separation bubbles inside the leading

edge as well as a shock in the duct. Other features unidentified by the authors most likely relate to the boundary layer on the splitter plate. For example, the flow on the plate appears to undergo transition across the vena-contractor created by the lip separation bubbles.

For more integrated applications such as combat aircraft, the origins and the mechanics of intake external separation are more important, as the separated flow field may interact with the external aerodynamics. *Dobson & Goldsmith (1970)* and *Dobson (1972)* report on some RAE research on the external drag of fuselage side mounted intakes, both rectangular and circular, with and without external compression surfaces. This extensive work presents a series of oil-flow visualisations in which the mass-flow ratio is reduced below unity at a Mach number of 0.6. A schematic interpretation of the surface flow at mass-flow ratios of 0.4 and below is presented for the rectangular intake. This is reproduced in *Figure 2.6*. The separation grows from a small bubble at the lip at mass-flow ratios near unity to encompass most of the cowl as shown the *Figure 2.6*. Although this intake may be considered to be ‘two-dimensional’, the separation is three-dimensional in nature. This is dominated by a pair of spiral nodes located on the cowl, which are bounded by flow coming onto the cowl from the sidewalls. The separation is bounded by a pair of saddle points.

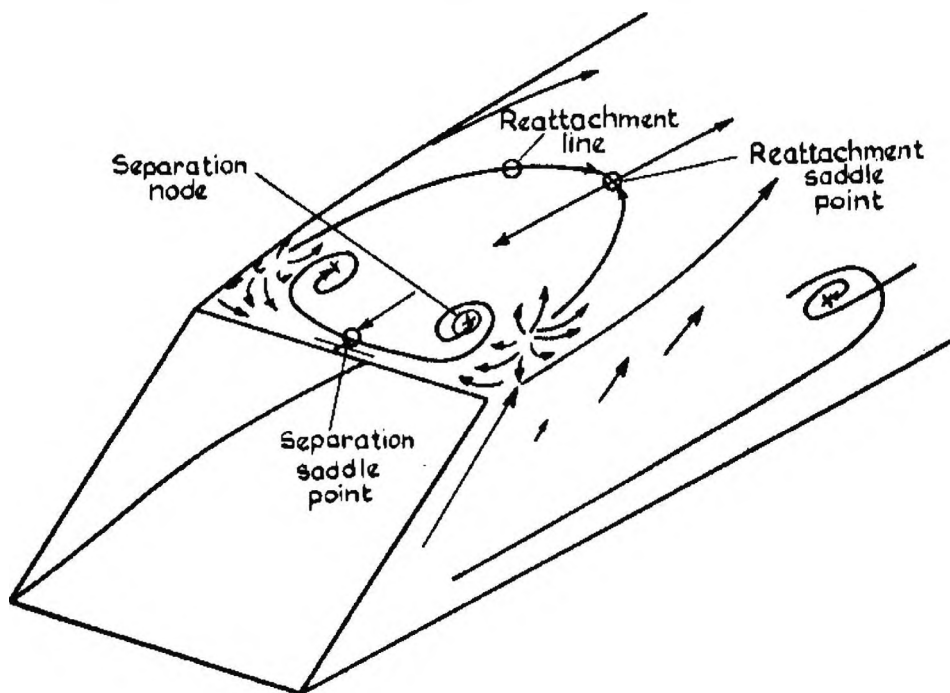


Figure 2-6: External cowl separation schematic(Dobson & Goldsmith, 1970)

There are a number of reported cases of separation originating from the intake, causing problems on production aircraft. *Neuhart & Rhode (1990)* report on water tunnel study of an F-15 aircraft to assess the effects of the intake spillage vortex that originates from the rearmost corner of the cowl, interacting with the fuselage mounted missiles. A similar cowl vortex on the Tornado aircraft has been reported as affecting the stability and control of this aircraft (*Stocks & Bissinger, 1980*). At high incidence, this vortex passes over the wing and breaks down; at low incidence, it passes under the wing and unloads the tailplane, forcing the aerodynamic centre aft. This phenomenon led to the tail-plane planform being redesigned to regain some longitudinal stability. A vortex from the upper corner of the intake may also cause tail buffet problems on twin tail aircraft at high incidence. This has been reported by *Norris (2002)* with regard to the Lockheed Martin F-22 and for the F/A-18, F-15 and F-22 by *Moses (2000)*.

The phenomenon of a vortex originating from the external inlet surface is in some instance desirable and actively promoted. This is the case with the nacelle strake or nacelle chine. This device is a large vortex generator located on the side of the nacelle. At incidence, this vortex passes over the wing enhancing the high-lift system (*Schwetzer, 1994*). Navier-Stokes computations have been performed by *Slotnick et al, 2000* including oil-flow representation showing the flow on the nacelle and the path of the vortex on such a configuration. The strake fixes the nacelle separation providing a much more orderly flow environment at incidence.

In general, external lip separation has been studied in regard to spillage drag for both military and civil aircraft. In the civil aircraft sector, where the airframe is designed to be separation free over the normal flight envelope, much research has been focused on elimination of external separation for a nacelle with an inoperative engine. In this case, the mass-flow ratio may become as low as 0.3. This design criterion produces nacelles with excessively thick lip shapes for cruise performance, which are accepted as drag and weight penalties. Many military aircraft have air intake installations that are essentially three-dimensional, and external flow separations that are focused on the rearmost part of the cowl, are inevitable at some conditions within the broad envelope for which these aircraft are designed. This may lead to interference with weapons and sensors or affect the stability and control of the aircraft. Research has

shown that external separation is three-dimensional, even when the configurations in question may be considered to be notionally two-dimensional.

2.2.2. Internal separation

Internal separation is most likely to occur at high mass flows and low speeds, when the capture stream tube is at its largest due to high engine flow demand. Therefore, a large amount of turning is required for the flow to negotiate the lip and pass into the intake. This problem is compounded by the addition of an incidence or yaw angle, as is often the case during high mass-flow operation. For example, take-off, manoeuvre or static with crosswind. The occurrence of a lip separation when the engine is demanding high mass-flow is highly undesirable. The separation will result in a loss of total pressure at the engine face. Theoretically, this loss has been shown to be as much as 21% of ambient total pressure for intakes with a sharp lip operating at the static condition (*Fradenburgh & Wyatt, 1953*). A more realistic assessment of lip loss for a modern military aircraft is given by *Tindell et al (1982)*, who show the total pressure recovery of the F-14, with its relatively sharp lip, but aided by an auxiliary intake, is approximately 90% during static running. Almost all of this loss can be considered as a direct result of the sharp lip contour. The impact of lip loss on engine thrust is put into perspective by considering that a loss of 1% in total pressure may be translated as approximately 1.5-2% thrust loss for a current generation military turbofan. In extreme cases, the separation bubble may cause a blockage effect, prematurely choking the intake. Perhaps more important, is the generation of total pressure distortion and swirl, which will affect the life of the fan blades, as they are continuously loaded and unloaded passing through a varying pressure field. Ultimately, the distortion may be large enough to cause the fan to stall. Sometimes, particularly for highly manoeuvrable combat aircraft, it may not be possible to completely remove lip separation. There are a number of examples of production aircraft where the lip shape of the original design has been blunted to improve low speed performance. All of the following examples are aircraft with external compression surfaces and the cowls were designed for supersonic performance. The redesigned lip on the F-14 (*Tindell, R.H., Hoelzer & Alexander, 1982*) aircraft produced a total-pressure recovery increase of 3% and a distortion reduction of 15% at the static condition; however, lip separation remained present. The F-111A aircraft was flight tested with a thickened lower cowl to reduce the lip separation at high

incidence (Bellman & Hughes, 1969). The Tornado aircraft was originally designed with a small leading edge radius NACA 1-series cowl. Water tunnel studies indicated that this sharp cowl lip was susceptible to internal separation at large incidence angles. This separation caused an increase in distortion, which effectively lowered the surge margin of the engine. At high incidence, the surge margin is small due to the large power extraction for the hydraulic controls, so further reduction due to intake problems is unacceptable. As a result, the cowl was blunted and de-cambered to unload the lip (Figure 2.7). This reduced the distortion parameter DC60 by 28% at 17 degrees of incidence. A penalty was paid at supersonic speeds for the low speed, high incidence improvement. The blunter cowl leads to a greater shock stand-off distance resulting in reduced pressure recovery, greater wave drag and reduced maximum mass-flow (Stocks & Bissinger, 1981).

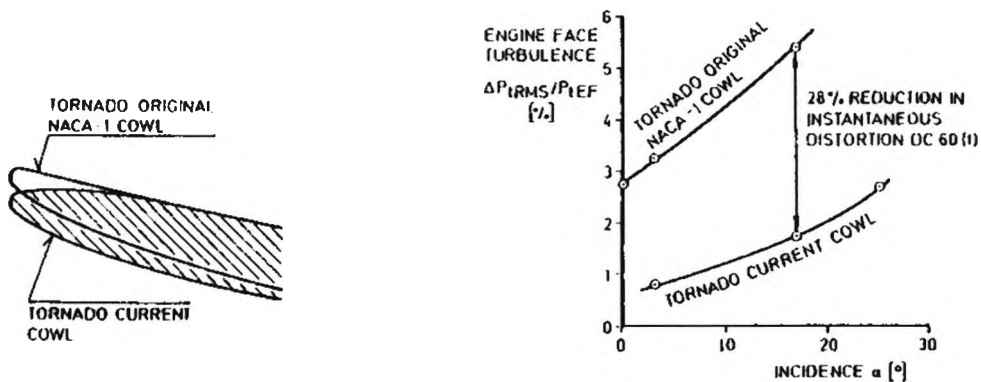


Figure 2-7: Reduction in engine-face turbulence from Tornado cowl redesign (Stocks & Bissinger, 1981)

Many data have been published with regard to the high incidence performance of the F/A-18, particularly because of NASA's 'high alpha technology program'. A highly instrumented F/A-18A termed the High Alpha Research Vehicle (HARV) which utilises thrust vectoring, has been used to analyse steady state and dynamic distortion during high-incidence and manoeuvring flight. Data has simultaneously provided computational fluid dynamics verification and validation. Although the intake on the F/A-18 is a fixed geometry of external compression type, the lip was optimised for manoeuvring in the subsonic high-alpha range of the flight envelope (Walsh, Steenken & Williams, 1998). The results of the HARV flight tests show some important differences between steady state and dynamic distortions, a phenomenon that has

caused engine/airframe compatibility problems for a number of aircraft. During a pitch-up manoeuvre for instance, there is a sudden drop in instantaneous total pressure recovery at 55-degrees angle of attack that is not present in steady state predictions. It is hypothesised that this is a result of a change in intake separation characteristics due to pitch rate.(*Yuh et al, 1997*).

Podleski (1994, 1995) has performed Navier-Stokes calculations on the F/A-18 HARV with the aircraft at 60 degrees incidence and 10 degrees of sideslip. Limiting streamlines for the lip flows are reproduced in Figure 2-8. The intake flow at this condition is highly three-dimensional due to the geometry and flow angle. The direction of sideslip means the intake being studied is on the windward side of the fuselage, so despite interference in the flow from other sources the separation is primarily due to the angle of flow at the lip. The separation line is located inside the lip fairly close to the leading edge. The solution shows the roll-up of the separated flow into a vortex that is ingested by the engine.

Separations from the intake lip can affect the life of components other than those in the engine. *Galea and Callinan (2001)* describe a repair to the Australian fleet of F/A-18 aircraft, which suffered cracking in the nacelle skin as a result of acoustic fluctuations due to flow separation at the lip.

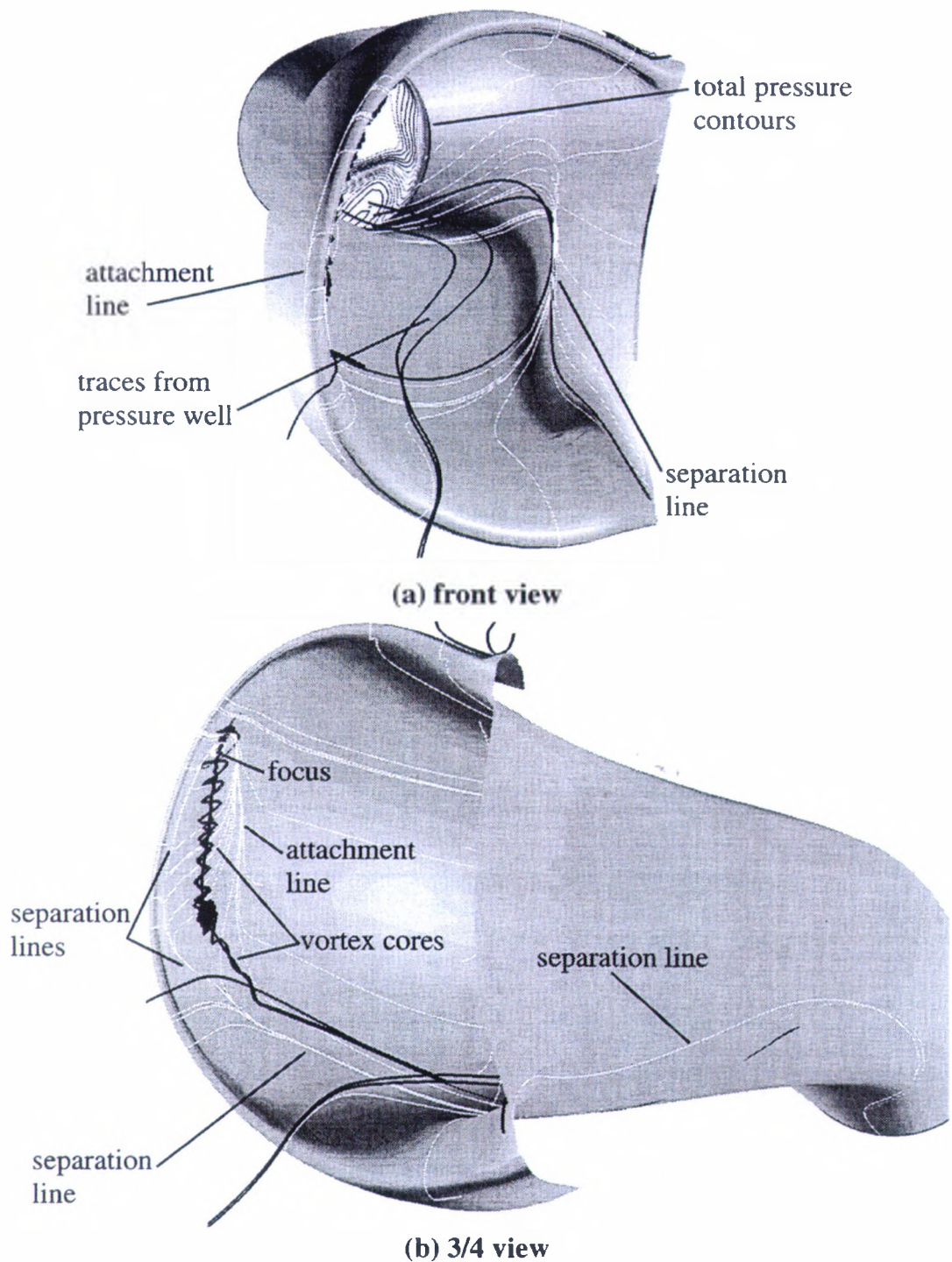


Figure 2-8: Calculated surface flow for F/A-18 at high angle of attack and sideslip (Podleski, 1995)

The American Quiet Clean Short-Haul Experimental Engine (QCSEE) Programme produced a large amount of both experimental data and theoretical calculations relating to lip separation. The QCSEE aimed to develop technology for short take-off

and landing passenger aircraft that would be capable of landing in city centre airports (*Albers, Stockman & Hirn, 1975*). Due to the short take-off requirement, the intake for these aircraft would be exposed to high incidence angles. Lip separation was unacceptable both in terms of aerodynamic performance and for the effect it would have on fan noise. The QCSEE programme provides a lot of information in terms of cowl profile, contraction ratio and internal lip shape on the aerodynamic and acoustic performance of pitot intakes. To reduce noise, a number of variable geometry components such as translating centrebodies (*Abbott, 1974*) and grids (*Miller and Abbott, 1972*) to choke the intake thus restricting the propagation of fan noise were tested. Although some of these arrangements were shown to suppress separation at the lip by effectively increasing the contraction ratio (*Luidens & Abbot, 1976*), the underlying trend of these devices was to reduce the overall pressure recovery.

Albers (1973) validates an axisymmetric potential code with boundary layer analysis against experimental data and finds that the peak-surface Mach number occurs in the highlight region. His results also show how increasing the lip contraction ratio increases the incidence angle at which internal separation occurs. This method predicts the onset of separation, but not the pressure distribution in the bubble. The use of the boundary-layer method shows up the presence of possible laminar separations (*Stockman, 1975*). *Felderman & Albers (1975)* do not predict the lip separation until it is well established at high incidence. The separation is initiated in the diffuser, probably because of the diffusion pressure gradient and moved toward the lip as the incidence angle was increased. The results show a sudden drop in total pressure recovery as the separation reaches the lip. Most of these studies on lip geometry indicate consistent trends, in both the influence of the lip shape, particularly contraction ratio, which is by far the most influential parameter for low speed performance, as well as the manner in which the separation size increases with incidence. *Albers & Miller (1973)*, in an extensive computational study on the effect of lip geometry, found that increasing the contraction ratio (CR) of the windward lip was the most successful modification for reducing surface Mach number. Increasing the CR from 1.3 to 1.42 reduced the peak Mach number by 27%. A major to minor axis ratio of the internal lip of 2 provided the smallest Mach number gradients. As the major to minor ratio is increased, a larger exponent of the super-ellipse is needed to maintain a low surface Mach number. This is done by maintaining the lip shape at the

leading edge. The contraction ratio was found the most influential parameter in improving total pressure recovery and reducing distortion in a crosswind (*Miller & Dastoli, 1975*). These studies highlight a couple of interesting results that are worthy of more attention. Firstly, contraction can be increased locally to eliminate lip separation on a particular fraction of the cowl; it may also be reduced in the region of low lip suction. This philosophy led to the adoption of three-dimensional nacelle shapes. Secondly, the curvature or 'bluntness' of the lip governs the peak surface Mach number. When the lip is stretched by increasing the major to minor axis ratio, it is necessary to increase the exponent of the super-ellipse to maintain the curvature near the leading edge.

Chou et al (1981) use a potential-flow method with compressibility corrections and a boundary-layer analysis modification to calculate the effect of Reynolds number on the incidence angle at which separation occurs on the inside of the lower lip. The boundary-layer modification permits the calculation of laminar and turbulent boundary layers as well as transition. Their calculations indicate that the full size intake has a longer laminar flow run but shorter transition, thereby achieving turbulent flow before the scale model. For throat Mach numbers below 0.6, the full-scale intakes are more tolerant to incidence angle than the sub-scale models. At throat Mach numbers above $M=0.6$, the reverse is true. It is suggested that this is because the flow is separated on the cowl before entering the intake.

Much of the QCSEE work is summarised by *Jakubowski and Luidens (1975)* who provide an insight into the flow mechanics of internal lip separation, albeit in a two-dimensional framework. The contraction ratio provides an increase in performance by reducing the magnitude of the minimum pressure. This reduces the magnitude of the adverse pressure gradient the boundary layer needs to negotiate. The sharpness of the external contour is also shown to have a major effect on the angle at which internal separation occurs. A schematic of the flow in the lip region at high incidence is reproduced in Figure 2-9. This shows a small supersonic region around the highlight terminated by a shock, the strength of which depends on mass flow and incidence. The pressure rise across this shock has a thickening effect on the boundary layer, reducing its tolerance to the adverse pressure gradient in the intake. If the shock is of sufficient strength, it may cause a shock-induced separation on the inside of the lip.

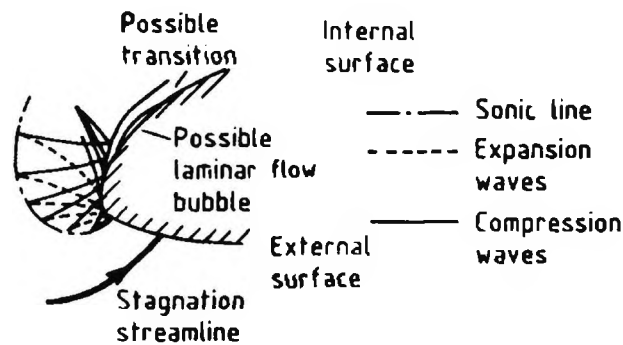


Figure 2-9: Lip flow mechanics at incidence and high mass-flow (Jakubowski & Luidens (1975))

Hurd (1976) provides information on the three-dimensional nature of internal lip separation summarising a series of wind tunnel tests at the Aircraft Research Association (ARA) for Rolls Royce (R-R) on axisymmetric pitot intakes at military flight conditions. The intakes had pitot rakes inside the lip to detect separation. Three 'states' are identified for the internal flow: minimum boundary layer, a thickened boundary layer and separated flow. At moderate incidence angles, the separation is initiated by the expansion/ shock-recompression similar to that described above. At high incidence angles, the separation occurs very close to the leading edge with the flow remaining subsonic. An oil-flow schematic shows the formation of a pair of vortices on the inside of the lip when the separation has occurred (Figure 2-10).

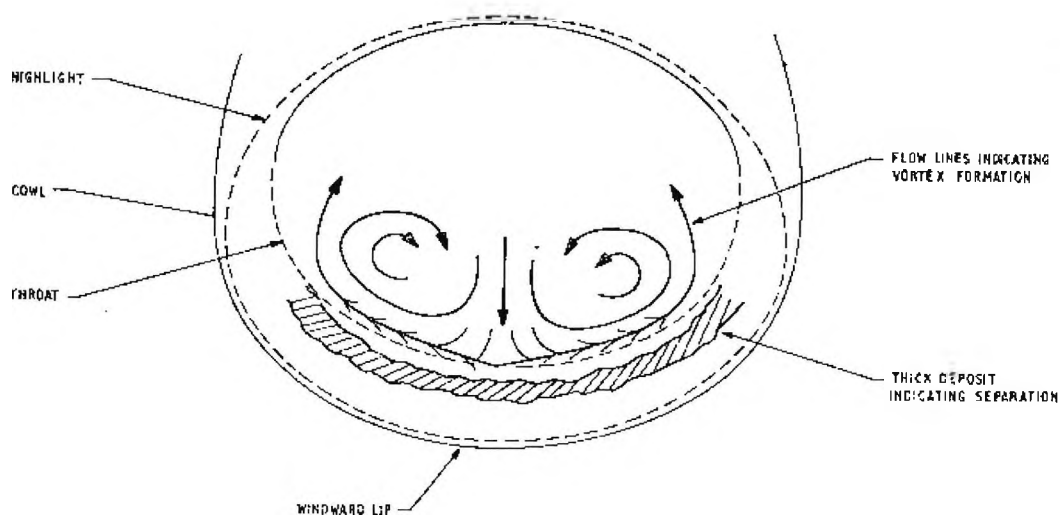


Figure 2-10: Internal flow schematic high incidence $M=0.8$ (Hurd 1976)

At incidence angles above 13° , the relationship between peak surface Mach number and separation onset (that defines a shock-induced separation on the lip) breaks down. At this condition, the flow separates when the surface pressure indicates it is well subsonic. This phenomenon causes *Hurd* to doubt the validity of his higher incidence results and he suggests a further series of studies to verify his findings. However, it is likely that these results are correct and that, at high incidence, the lip separation will occur on the lip before sonic conditions are reached. The flow visualisation shows this is very much a three-dimensional problem. Therefore, factors other than the axial pressure gradient may influence the separation characteristics of the intake.

Flow separations emanating from an intake lip are three-dimensional for almost all practical occurrences, the exception being an axisymmetric nacelle at zero angle of incidence. In reality, intake shapes are three dimensional and operate at some angle of inclination to the freestream flow. These features produce flow separations that are three dimensional in nature and often focused on a particular portion of the intake lip. Attempts to understand the development of lip separation have historically been based around the development of one-dimensional analytical methods or by relating the problem to that of the two-dimensional aerofoil. In conjunction, experimental work, particularly when relating to specific projects, has focused on eliminating lip separation at its first occurrence, usually by increasing the thickness of the lip, with little, if any, attempt to understand and manage the flow. Investigating lip separation in this manner is perhaps outdated in the current environment of integrated design. A step towards understanding the problem on a more global basis may lead to greater integration in design and much improved propulsion system performance.

2.3. Leading-edge flow separation

Hoelmer, Youghans & Raynal (1987) use an analogy of aerofoil stall to explain the dependence of intake leading-edge separation on Reynolds number. An empirical relationship was used which suggests that at full scale, the separation type was fully turbulent rather than laminar. These separation types will be discussed in more detail later in this section. Previously, in some unpublished research at the NGTE, *Flitcroft, Philpot and Ball (1982)* used the same analogy to explain the type of internal lip separation on a full-scale intake tested in a free-jet test cell. They used a correlation proposed by *Gault (1957)*, who related the freestream Reynolds number to the surface

ordinate at 1.25-% chord (effectively an indication of leading-edge bluntness), to provide a map of separation type for aerofoils. This map is shown in *Figure 2-11*. The types of separation described in the figure were proposed earlier by *McCullough & Gault (1951)* who described three primary types of separation and a fourth, that was a combination of two of the previous types. These are:

- Trailing-edge stall
- Leading-edge stall
- Thin-airfoil stall
- Combined stall

Trailing-edge stall is characterised by the movement of a turbulent separation forward from the trailing edge. For aerofoils, this type of stall must be dependent upon achieving a satisfactory trailing-edge condition. This condition must be different for intake flows, as there is no coupling of this manner. For integrated propulsion systems, the external cowl will fair into the aircraft lines, while for nacelle type intakes, the flow conditions at the cowl crest are heavily coupled with the afterbody geometry and flow conditions (*Neale, 1968*). For the internal flow, a more identifiable constraint is the downstream pressure set by the engine mass-flow demand. Variation of this pressure with throttle setting and the corresponding movement of the stagnation point of the dividing streamline is the analogue of incidence variation on an aerofoil. In addition, incidence may be varied for the intake that will have a compound effect on the stagnation point location. *Felderman & Albers (1975)* describe a turbulent separation in the diffuser on a QCSEE inlet that moved towards the lip as incidence is increased. We may hypothesise that this is the intake equivalent of trailing-edge separation.

Leading-edge stall is associated with an abrupt separation near the leading edge of moderately thick aerofoil sections. This category can be further sub-divided into two groups, the boundary between which is governed by the behaviour of the boundary layer during the stall. The first group suggests that the stall will occur due to the bursting of a short laminar separation bubble. The second suggests that the flow reattaches after the separation as a turbulent boundary layer and re-separates almost

immediately. Much work has been completed on characterising laminar separation bubbles for aerofoils. A detailed discussion is beyond the scope of this document, but such information can be found in *Haines (1994)*, who presents an in-depth review of the topic. However, the salient points will be extracted as an aid to understanding potential mechanisms in intake lip separation. *Young & Horton (1967)* summarise work at Queen Mary College on laminar bubbles. Of particular note is Gaster's parameter, which separates short and long bubbles as a function of Reynolds number based on momentum thickness at the separation point. This parameter uses the inviscid velocity gradient over the length of the bubble that was suggested by *Crabtree (1957)*.

The change in separation type from the turbulent reattachment to a bursting laminar bubble occurs as the Reynolds number is reduced. This reduction in Reynolds number causes an increase in the length of the laminar bubble forcing the turbulent portion to higher levels of diffusion to maintain the correct pressure at reattachment. Eventually, under the bubble, the suction peak is reduced, thereby reducing the pressure gradient over the bubble and allowing the turbulent shear layer to reattach. In the event of a further reduction in Reynolds number, the bubble increases in length until reattachment is no longer possible. *Roberts (1979)* characterises the two forms of bubble with regard to the inviscid pressure distribution. The short bubble only has a slight effect on the suction peak and circulation, while for the long bubble or 'burst' bubble, there is a substantially reduced suction peak and circulation.

Van den Berg (1981) argues using an analytical approach, that turbulent re-separation downstream of reattachment is the normal mechanism except for very low Reynolds number cases. The final criteria using Gaster's relationship already described and Thwaites' expression for momentum thickness leads to the momentum thickness Reynolds number at the separation point being less than 140 for the separation to be of bubble type.

Thin-airfoil stall is characterised by the progressive rearward movement of the attachment point as incidence is increased. This type of separation is of laminar type and has a gradual effect on the pressure distribution and loading, in contrast to the bubble burst described above.

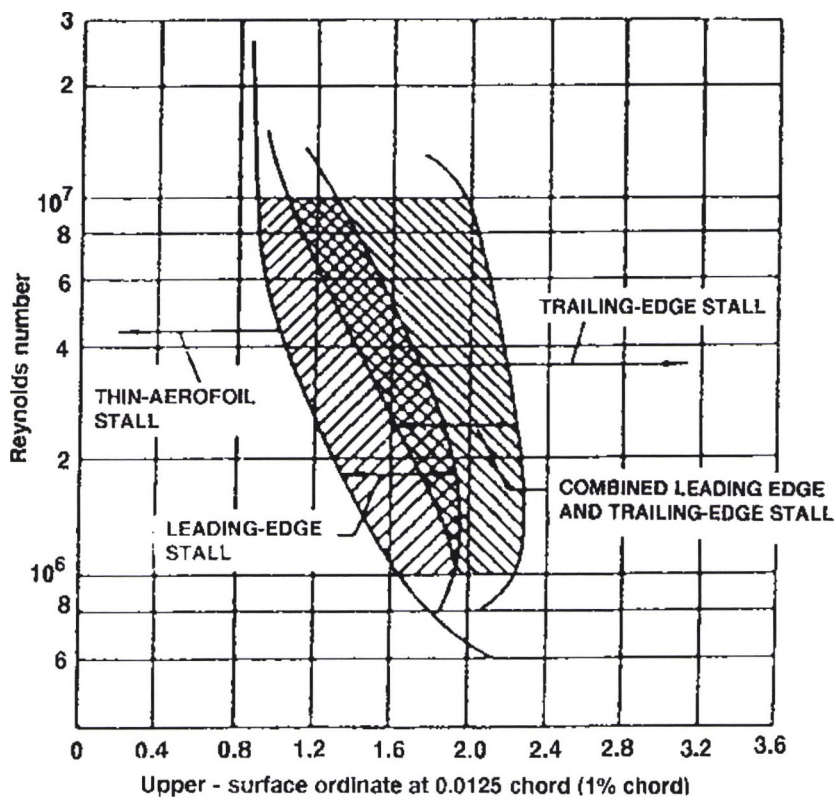


Figure 2-11: Gault's correlation for aerofoil separation

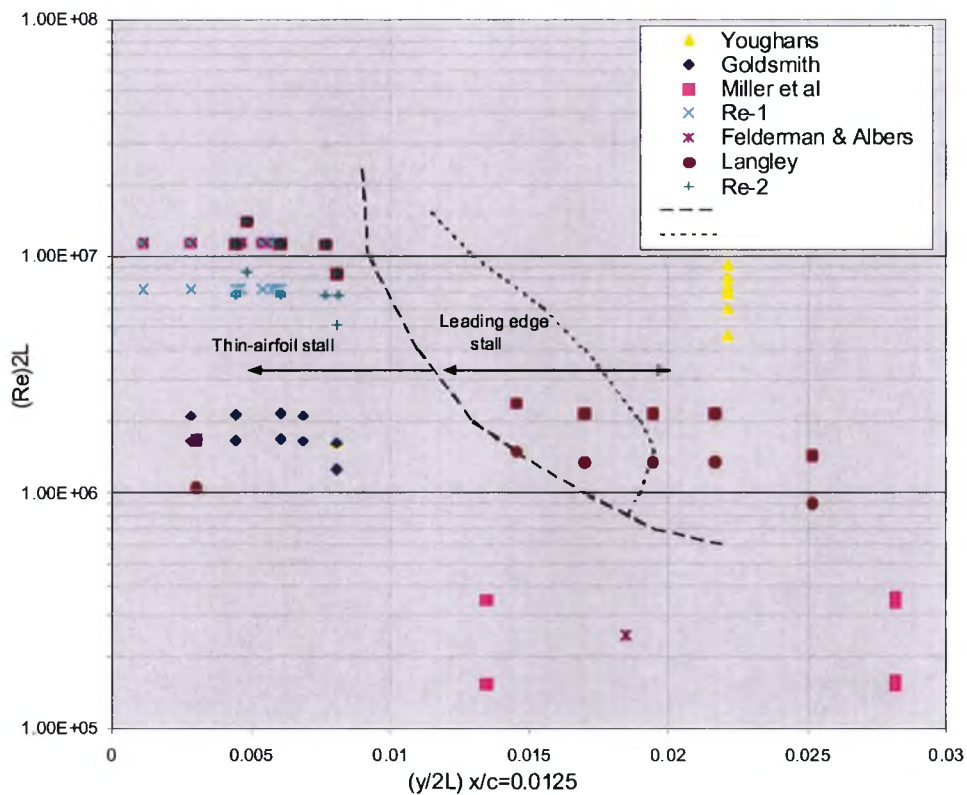


Figure 2-12: Intake data from Table 2.1 Plotted on Gault's correlation

Gault's correlation (Figure 2.11) which relates aerofoil nose 'bluntness', in the form of an upper-surface ordinate near the leading edge and Reynolds number to separation type can be used as the basis an intake correlation (Figure 2.12). Using the suggestion of *Nangia(1993)* that the intake 'chord' is twice the distance between the leading-edge and the crest to form an equivalent aerofoil, a number of cowls reported in the open literature can be plotted to give an impression of the dependence of external separation on Reynolds number and lip cowl geometry. Although the boundary lines between types perhaps require re-computing for intake cowls, it is evident from Figure 2.12 that lip separation type can vary as Reynolds number is changed, particularly from thin airfoil stall to a laminar bubble type separation. This has obvious implication for sub-scale tests as has been shown by *Hoelmer, Youghans & Raynal (1987)*.

2.4. A correlation for internal lip separation

Many researchers have provided correlated information relating to lip separation. With the exception of that by *ESDU(1984)*, the reports on such work focus on a particular test or series of tests relating to the author's experience. Correlated intake data is often configuration dependent and may be presented in a number of forms indicating performance; for example: spillage drag (*Stanhope, 1968*) or total pressure loss (*Wilmer, Brown & Goldsmith, 1981*). The most appropriate form for a lip-separation correlation for this study must be the angle of attack or mass-flow ratio at which separation occurs.

The main problem with correlating data from the open literature is determining a consistent form of intake mass-flow and separation indicator. For example, the results may be presented in the form of distortion plotted against throat Mach number. In this case, it may be possible to determine the onset of internal lip separation by looking for the throat Mach number at which the distortion increases. This will only provide an approximation that will depend on the distribution of the experimental data. The other problem is converting throat Mach number to the chosen measure of mass flow. This requires the knowledge of other pressures and/or Mach numbers in the diffuser as well as the geometric area ratios of the model. As a result, some assumptions have been made to display the following data in the correct form for correlation.

To correlate the internal lip separation data from the literature it is necessary to identify the key parameters that affect the onset of lip separation. We can divide these into three groups.

- Group I – Lip geometry
- Group II – Streamtube size and location
- Group III -Throat flow conditions
- Group IV- Scale

Group I describes the geometry, the most readily available data being the lip contraction ratio and major to minor ellipse ratio. In addition, the super-exponent of the ellipse may be considered but the effect of this is likely to be small with respect to the data accuracy. *Bore (1993)* used bellmouth area (the forward projected area of the lip) in a pressure loss correlation for VSTOL intakes. However, lip contraction ratio was chosen for this study as the use of bellmouth area introduces additional variables describing the external cowl shape. The Group I variables chosen, which describe the bluntness of the lip are:

- a/b – major to minor ellipse ratio of internal lip
- $\sqrt{\left(\frac{CR-1}{CR}\right)}$ - Scaling factor for the lip ellipse

Where CR is the lip contraction ratio, $CR = A_c/A_{th}$

The Group II parameters chosen are the mass-flow ratio (A_o/A_c) and the cosine of the incidence angle. These parameters in conjunction describe the location of the stagnation point of the streamline dividing internal and external flow. The product of the cosine of the incidence angle and the mass-flow ratio gives the mass flow in the streamtube referenced by the forward projected capture area of the intake at incidence.

- A_o/A_c
- $\cos \alpha$

Group III relates the free-stream Mach number to the throat Mach number.

- M_o
- M_t

This indicates the type of flow in the throat and the type of lip separation such as shock induced or due to the lip adverse pressure gradient

Finally, Group IV has been neglected, as experimental studies such as those by Goldsmith (1990) have indicated that the effect of Reynolds number on internal lip separation is small.

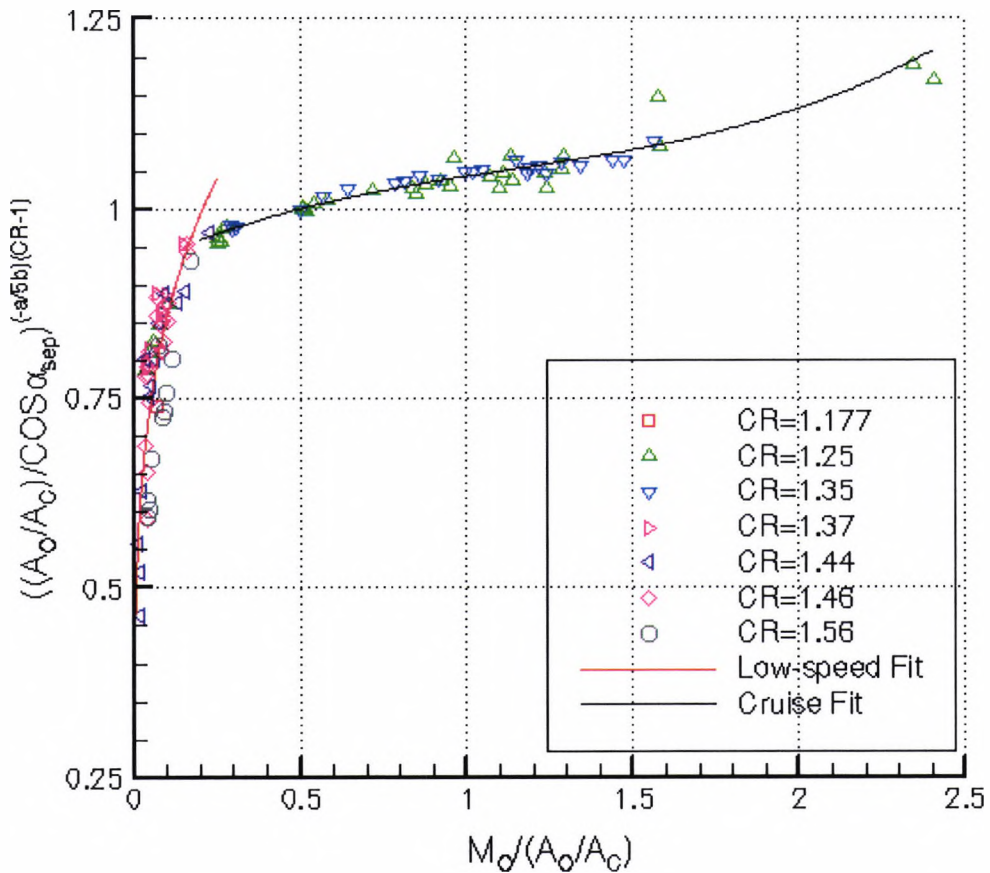


Figure 2-13: Correlation of lip separation data

Figure 2.13 shows a correlation for intake internal separation onset. The parameter on the x-axis, $\frac{M_o}{A_o/A_c}$, is similar to the $\frac{M_o}{M_t}$ parameter used by Wilmer et al (1981) for

the correlation of lip loss at low forward speed to combine the effect of stream tube size and throat conditions. In this case, the mass-flow ratio rather than the throat Mach number is used. The throat Mach number may be calculated from the mass-flow ratio using the streamtube equation. Mass-flow ratio is used here as this quantity is presented in most of the literature, as the parameter describing the intake flow condition. The conversion to throat Mach number, if not presented, requires the knowledge of geometry and scale factors not always available, as well as the assumption of total pressure loss due to the lip flow. The plots in Figure 2-13 use different colours to indicate the different contraction ratios of the available data. The different locations of the contraction ratios along the axis are an indication of the inlets use. Low speed intakes of high contraction ratio are located predominately near the origin of the x-axis. However, the contraction ratio of 1.25, a suitable value for transonic pitot intakes, spans the whole range of the configuration which gives rise to the validity of the correlation. The data may be considered to collapse to a single line, which in identifiable parameters takes the form:

$$\left(\frac{\frac{A_o}{A_c}}{\cos \alpha_{SEP}} \right)^{\frac{a}{5b}(CR-1)} = f \left(\frac{M_o}{\frac{A_o}{A_c}} \right) \quad \text{Equation 2-1}$$

This function may be split into two principle regions that may be considered linear in nature. The first portion covers the range: $0 < x < 0.2$, which is high-mass flow and low forward-speed operation. In this region, the incidence angle at which separation occurs is very sensitive to contraction ratio. The second linear region at $x > 0.2$ corresponds to cruise operation, high subsonic Mach number and unity mass-flow. Here, the separation incidence is much less sensitive to the lip geometry.

Although in theory, a correlation such as this could be used for concept assessment, the exponent needed to collapse the vast data set reduces the detail when used inversely. Details of the complex interactions between these variables and some simpler correlations are shown in the Appendix.

2.5. Three-dimensional flow separation

Further complications are raised when three dimensionality of the flow is introduced, either by modification of the local flow angle or by the type of geometry, such as a

swept intake. An example of this can be seen in the previous section in *Figure 2.10*. The topology and development of three-dimensional flow is a subject in its own right. *Peake & Tobak (1980)* provide a detailed treatise on the subject including a set of rules for determining the flow topology.

We have seen that the key to understanding and manipulating lip separation lies with accepting the three-dimensional nature of the problem. Traditionally, the aim has been to remove lip separation from the flight envelope, and to this purpose, using two-dimensional methods to predict the onset of lip separation, either internal or external, has been the rule. In retrospect, however, this approach does not appear to have been particularly successful as a proportion of modern combat aircraft have undergone lip redesign late in their development programmes.

2.6. Flow control, variable geometry & novel approaches for eliminating lip separation.

The aircraft air intake will experience a wide envelope of operating conditions. This presents an excellent opportunity for using boundary-layer flow control techniques to bias the design aggressively toward a particular operating point and compensate at other conditions by using flow control. *Lord, MacMartin and Tillman (2002)*, in a paper looking at future opportunities for flow control, suggest the benefit of using a thinner cruise oriented lip. Flow control could then be used to obtain take-off performance, although they do not suggest possible ways of achieving this.

Traditionally, intake designers have used two approaches. The first is a fixed geometry intake that provides a compromise across all design points: for example, the pitot intake on the F-16 (see *Hawkins, 1974*) or the fixed ramp, external compression intake on the F/A-18 (*Walsh et al, 1998*). An alternative approach is the use of variable geometry. This is almost exclusively used for aircraft with a Mach 2.0 capability for reasons that will now be discussed. Variable geometry takes two main forms often used in conjunction. These are movable compression surfaces and auxiliary intakes. Movable compression surfaces such as translating cones (F-111) and movable ramps (Concorde, F-14, Tornado) allow the compression surface angle

to change as a function of flight Mach number. This enforces maximum pressure recovery by adjusting the strength of the terminal shock. In addition, the movement of the compression surfaces may also reduce the intake capture area as Mach number increases, so reducing spillage drag. Alternatively, movement in the other direction, increases the capture area at low forward speeds to increase the contraction and hence pressure recovery. Auxiliary intakes or blow-in doors are used to improve the low-speed performance of intakes with sharp lips by providing extra intake area without increasing the capture area. Auxiliary intakes are also used on the subsonic Harrier aircraft to aid hover performance. Most supersonic variable geometry intakes utilise complex bleed arrangements to stabilise shock/boundary-layer interactions although on some aircraft, the bleed systems may be integrated with the auxiliary intake system.

A more specific form of auxiliary intake is the slotted lip. In its simplest form, an annular slot exists around the circumference of the intake, which exits internally in the vicinity of the throat. A spring-loaded door closes off the slot. Under normal conditions, the slot is closed, but at high mass flows or at incidence, the pressure difference between the internal and external flows opens the slot providing additional intake area and unloads the lip. RAE research on slotted lips [*Wilmer et al (1981)*, *Ross et al (1981)*] has shown that a slot provides a noticeable benefit on pressure recovery at incidence angles above 30 degrees, but with an accompanying increase in total pressure distortion. This is probably because of the mixing of the two streams.

A unique variable lip geometry was used on the Hawker-Siddeley P1127, a predecessor to the Harrier, to cope with the differing high and low-speed requirement encountered by this vertical take off aircraft. The leading edge was manufactured from a rubber compound. The default sharp leading edge shape was inflated at low speed to provide a bellmouth entry to the intake. This concept was dropped after the rubber was repeatedly torn by oscillating shock waves on the cowl at cruise operation (*Bore, 1993*).

The major problem with variable geometry is the weight and maintenance cost, which must be traded against the performance loss without variable geometry. Intake complexity reached a peak in the 1960s with aircraft such as the F-111. However, the complex engine/intake compatibility problems (*Burcham & Bellman, 1971*)

experienced during flight test have led to a trend of decreasing complexity in modern aircraft intake systems. Modern military aircraft constrained by additional low-observability requirements are limited in the use of variable geometry, as surface discontinuities and cavities between ramps and auxiliary inlets are not compatible with the management of radar returns (*Howe, 1998*).

The requirement for performance at high angle of attack has led to another form of variable geometry, the so-called vari-cowl. This is a flap on the cowl leading edge, which may be rotated to align the cowl with the local flow direction, as well as sizing the intake capture area for different mass-flow ratios. This is a very versatile technique across a wide range of Mach numbers, from the static condition at which the vari-cowl can be used to increase the capture area, to supersonic speeds, where reducing the capture area reduces spillage drag. *Lotter & Malefakis (1978)* have demonstrated the vari-cowl on a post-stall fighter concept, up to angles of attack of 70 degrees. Its performance and compatibility in terms of both pressure recovery and distortion exceeded alternative variable-geometry designs including leading-edge slats and auxiliary doors. A derivative of this design was used on the Eurofighter Typhoon aircraft.

Cawthon (1976) tested a similar vari-cowl arrangement for a highly manoeuvrable aircraft concept and found the vari-cowl beneficial in reducing lip separation. Further improvements were found by using tangential blowing at the cowl 'knee', the surface discontinuity at the cowl hinge. *Leyland (1988)* conducted a computational analysis of this region on a configuration similar to that studied by *Lotter & Malefakis (1978)* and concluded that the hinge discontinuity was not of concern. The difference between the opinions of *Leyland (1998)* and *Cawthon (1976)* can firstly be put down to the test conditions. *Cawthon's* test was at higher Mach number and higher angle of attack than *Leyland's* computation and the chord of the vari-cowl appears to be smaller in proportion to the intake height. In addition, particularly when considering specific applications, different levels of distortion may be tolerated by different engines, so a small local separation may be a problem for one aircraft and not another. A further factor to be considered is the influence of the diffusing duct connecting the intake to the engine as the pressure gradients here may further reduce the quality of the flow delivered to the engine.

The ultimate variable-geometry intake for LO purposes is the Smart Aircraft and Marine Project System Demonstration (SAMPSON) adaptive intake lip project in the US. This utilises shape memory alloys (SMA) and consists of a vari-cowl flap which has a variable radius leading edge (*Pitt et al, 2001*). The shape and orientation of the cowl can be varied depending upon flight conditions. The SMAs are covered by a flexi-skin leaving no discontinuities in the surface during operation. Aerodynamic results or comparative weights are not available in any detail for this configuration. It can be suggested that this form of intake will have unrivalled aerodynamic performance across a large Mach number range, whilst still achieving radar cross section (RCS) targets. In fact, it may be considered the ultimate evolution of *Bore's* inflatable lip intake that has already been discussed. This design may well be the future standard for expensive manned aircraft, although ultimately, its weight and complexity may limit its progress.

Boundary-layer flow control methods applied to intakes to control lip separation may be separated into the usual two groups of passive or active flow control systems or perhaps, more appropriately, powered or un-powered. Passive flow control research has mainly focused on Vane Vortex Generators (VVGs) or suction/blowing powered by pressure differentials in the flow. Active flow control in this sense uses powered blowing or suction techniques.

Hancock & Hinson (1969) reported an example of the use of Vane Vortex Generators (VVGs) for intake flow control. VVGs were tested in a variety of locations within an intake to improve the low speed performance of the Lockheed L-500 propulsion system. The results are shown in Figure 2-14. The authors comment that the VVG location on the lip in a favourable pressure gradient, was best for improving the pressure recovery. No results are presented for corresponding distortion levels.

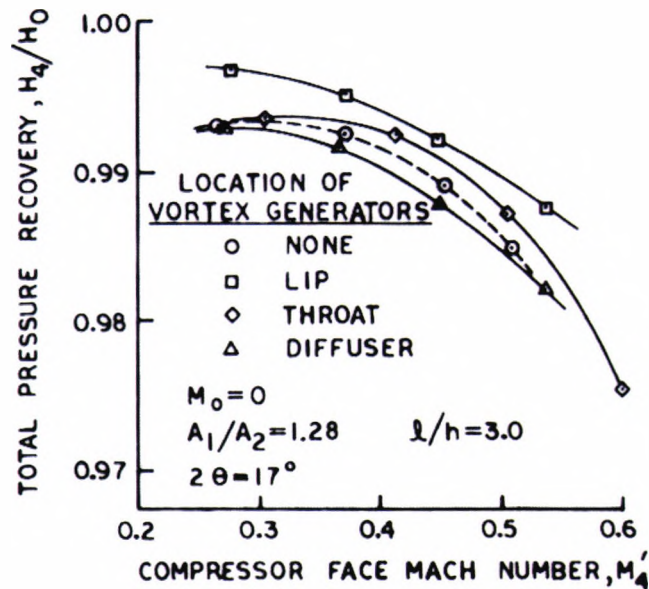


Figure 2-14: Effect of VVG location on static intake performance (Hancock & Hinson, 1969)

The result of this study, shown in Figure 2.14, is quite remarkable when considering that VVGs are not used in this manner on aircraft. Nor does this study appear to be built on in any form in the open literature. The particular region of interest in Figure 2.14 corresponds to compressor face Mach numbers in the region of 0.5 to 0.55, which covers the likely take-off design range. At these values of compressor face Mach numbers, the total pressure loss is halved by installing VVGs on the clean intake lip. It can only be assumed that the reason that this research has not been progressed further is due to the off-design penalty, for example at cruise, where a parasitic pressure loss will be present in the streamtube.

Herzmark and Victor (1970) describe how the McDonnell F-4 Phantom II experienced distortion-induced engine flameouts during low speed, high angle-of-attack manoeuvres. In an attempt to stop this problem, VVGs were flight tested on the lower intake lip. No benefit was found from the VVG installation. Post flight, it was believed that the VVGs were mounted downstream of the separation line. The Phantom has a complex propulsion system utilising a bypass system with an ejector nozzle. Manipulating the bypass scheduling to adjust the engine surge margin solved the problem and the VVGs were not tested again in a more suitable location. The VVGs can be seen on the lower lip near the leading edge in Figure 2-15.

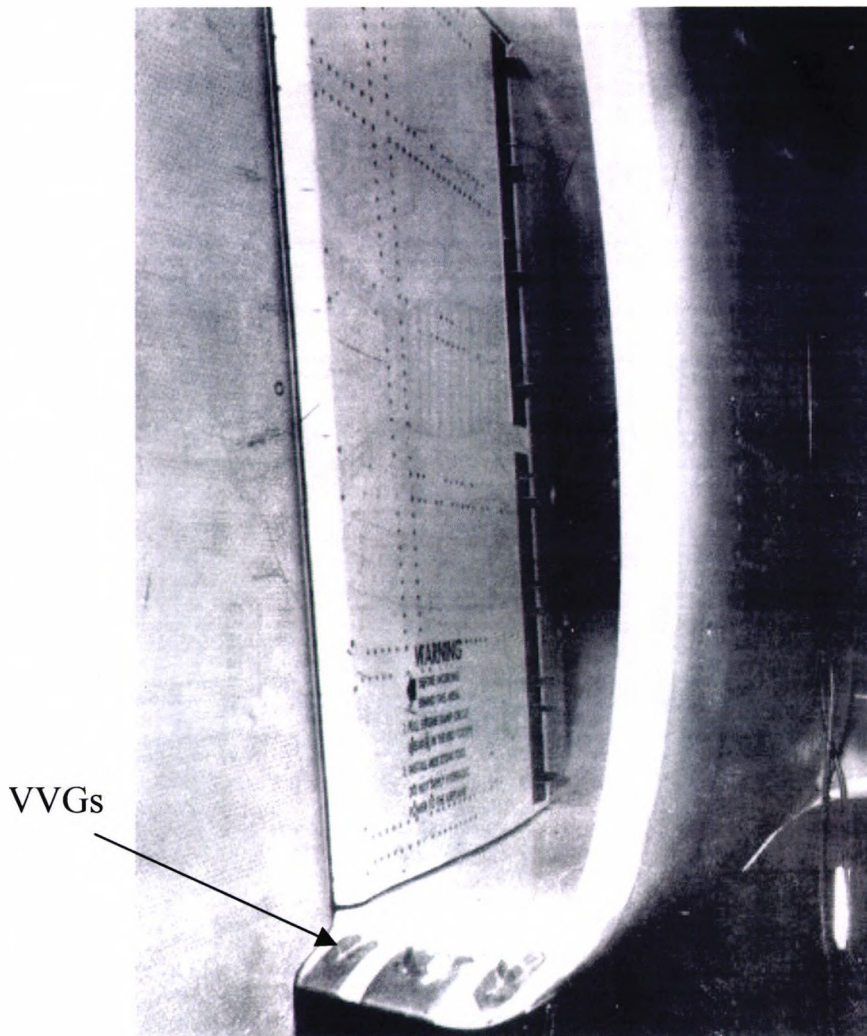


Figure 2-15: VVGs on F-4 Phantom lip (Herzmark and Victor, 1970)

The use of VVGs on the intake lip seems to be considered undesirable. The reasons for this are most likely as follows: firstly, there is the prospect that the VVGs could work loose and be ingested by the engine. In addition, they induce an off-design pressure loss and hence thrust loss. There must also be enough mixing length downstream of the VVGs so that the vortex core has sufficient length over which it can be dissipated, and does not reach the fan. The cyclic loading on the fan due to discreet vortices may generate noise as well as potentially reduce blade fatigue life.

Miller (1977) presents a novel passive control system for pitot intakes at incidence. This intake uses a suction slot downstream of the throat at the start of the diffuser where the local static pressure is reasonably high. The circumferential extent of the slot is small. The suction slot is “powered by” two rows of holes located either side

of the slot at approximately 45% from the keel, and connected to the slot via a plenum chamber. The porous regions are located in the region of high suction, when the intake is at incidence. The pressure difference between the low pressure porous region and the high pressures in the vicinity of the slot enable the low energy boundary layer on the throat wall to be removed. This system provides nearly 4% increase in pressure recovery at 60 degrees incidence and reduces DC60 to about 1/7th of that recorded for the clean intake. The layout is shown in *Figure 2-16*.

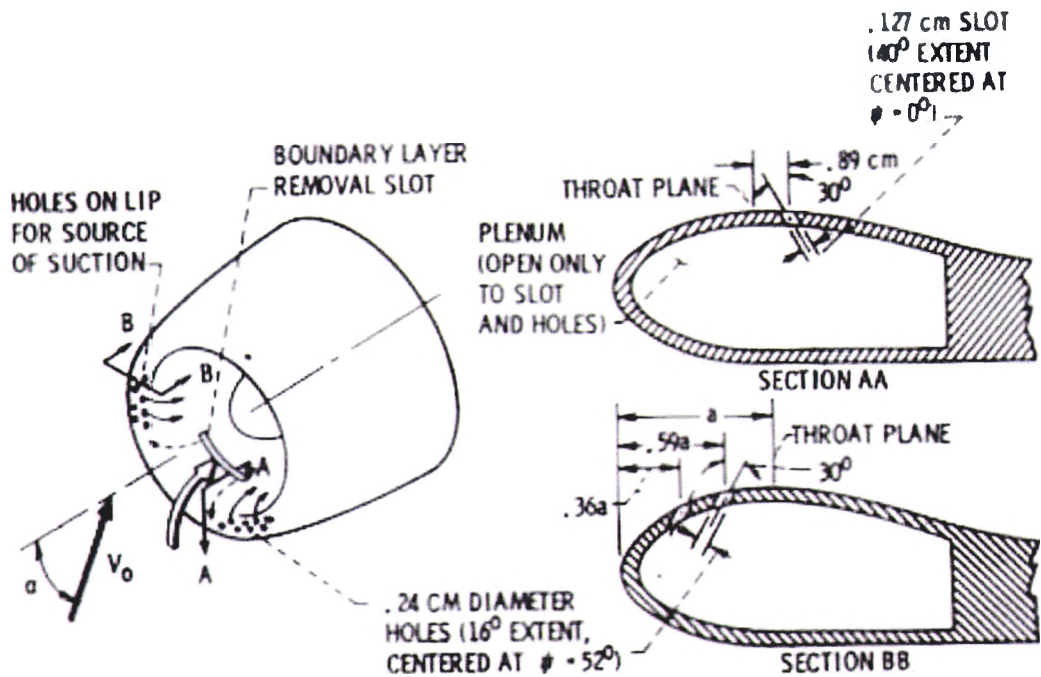


Figure 2-16: Intake flow control concept (Miller, 1977)

One favoured form of active control for use in air intakes is blowing a thin jet of air out of a slot tangential to the local surface. The added momentum of the jet re-energises the boundary layer by cancelling out the momentum deficit in the immediate near-wall region. This is a well-known principle and has been researched in depth and applied for high-lift flow control on wings (*Lachmann Vol.1, 1961*). Slot blowing has been proposed for a number of intake applications, but installation on any production aircraft has not been published. *Peake (1963)* demonstrates the value of slot blowing for boundary-layer control and suggests possible performance improvements for a supersonic intake. *Patilla (1972)* uses an oil-flow technique to determine the location of a lip separation in crosswind on an isolated Lockheed L.1011 intake with a thought to determining the appropriate location of a slot for

blowing. The most appropriate location of the slot was 1.68% of the highlight diameter downstream of the highlight plane. Unfortunately, any further studies progressing this work are not available in the open literature.

One of the prime design points for application of flow control to intake lips is at the static condition, where the propulsion streamtube is much larger than the intake capture area. *Gregory (1971)* analytically defines two types of lip separation at this condition. The first is due to the development of an adverse pressure gradient at the lip. The second arises as a requirement of satisfying the momentum equation, whereby, in order to stay attached at the lip, the flow must reach pressures lower than vacuum; and as this cannot be obtained, the flow separates. The use of blowing is suggested to try to eliminate the first type of separation. A convergent/divergent nozzle is used to inject flow into the throat across the full span of a two-dimensional intake. This proves successful in improving the pressure recovery of intake with contraction ratios of 1.25 and 1.50, but unsuccessful at the lower contraction ratio of 1.12. However, to control the flow separation on the 1.25 contraction intake, the blowing mass flow was 6-8% of total intake mass-flow, an unacceptably high level. This research raises several points worth considering further. Firstly the location of the slot at the throat is, perhaps, too far downstream to prevent separation on the thinner (lower contraction ratio intakes) by re-energising the boundary layer. In addition, the slot does not appear to be angled tangential to the surface as in the work of *Peake (1963)*. If this were the case, this would undoubtedly affect the performance of the blowing. Finally, this report shows how much mass flow can be required for a poorly performing slot-blowing system. Discrete air jets would require much less mass flow, primarily because of the small exit area of the installation and, therefore, induce a much smaller penalty on the propulsion unit.

McGregor (1971) provides detail of a series of tests using slot blowing on semi-circular side mounted intakes on a VSTOL type configuration. Four different slot configurations were tried; forward and aft of the throat, with sizes of 0.5mm and 1.0mm. The size of the model was not disclosed. In this case the blowing was not on the lip, but on the diffuser wall opposite the lip. DC60 reduces as blowing pressure is increased. At the maximum blowing total pressure ratio ($P_j/P_\infty=1.88$), DC60 was 0.08;

with no blowing the DC60 value was 0.25. It is stated that this blowing pressure would be available from the engine fan. The blowing mass-flow ratio was 2.5% of total engine demand. This paper also provides a useful thrust analysis whereby the effect of removing high-pressure air from the compressor to achieve improved pressure recovery with blowing, is compared to the clean intake with no blowing. A net thrust increase of up to 1.7% is produced when blowing is used in the intake. This analysis is important in showing the net affect that an active flow control system can have on improving the installed engine performance.

Cawthon (1976) has demonstrated slot blowing in several locations around the lip for controlling separation. A two-dimensional horizontal ramp intake was used with the slot blowing applied to the lower cowl. Incidence angles were up to 56 degrees (*Figure 2-17*). The two locations for the slot were just downstream of the leading edge, but upstream of the throat. The second configuration used a vari-cowl type arrangement with slot blowing at the knee. The slot blowing was effective in eliminating the lip separation, thus reducing the distortion and turbulence levels and improving the manoeuvre capability of the intake. The critical jet momentum blowing coefficient that can provide the best performance is influenced by surface shape and local flow incidence. Effective blowing is accomplished with less than 1% engine airflow. In the second configuration, the blowing improved the performance of the cowl flap at very high incidence angles.

Suction may also be used for intake flow control. *Gerthold et al (2002)* describe an integrated experimental and computational approach using suction through a porous region to reduce distortion on a civil intake with negative scarf. The improvements obtained from the experiment were not as large as was predicted from CFD.

The use of any form of powered flow control technique requires a thrust-drag balance to be performed to determine the true effectiveness of the technique. The increase in thrust due to the improved total pressure recovery that occurs because of removing the lip separation needs to be traded against the thrust loss due to the removal of the bleed air from the engine. If distortion and manoeuvrability are the prime drivers, then some degree of power loss may be tolerated to increase the engine surge margin.

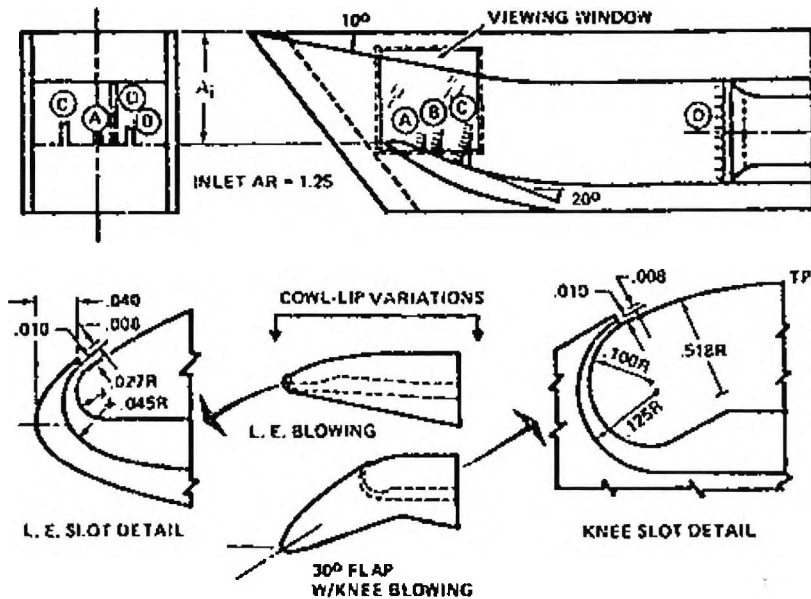


Figure 2-17: Lip slot blowing concepts (Cawthon, 1976)

2.7. Air Jet Vortex Generators (AJVGs) for propulsion applications

Vane Vortex Generators have long been established for improving the performance of diffusing air-intake ducts. Both the F-111 (Burcham & Bellman, 1971) shown in Figure 2-18 and the F/A-18 (Yugas et al, 1997) have VVGs installed in the diffuser for suppression of separation.

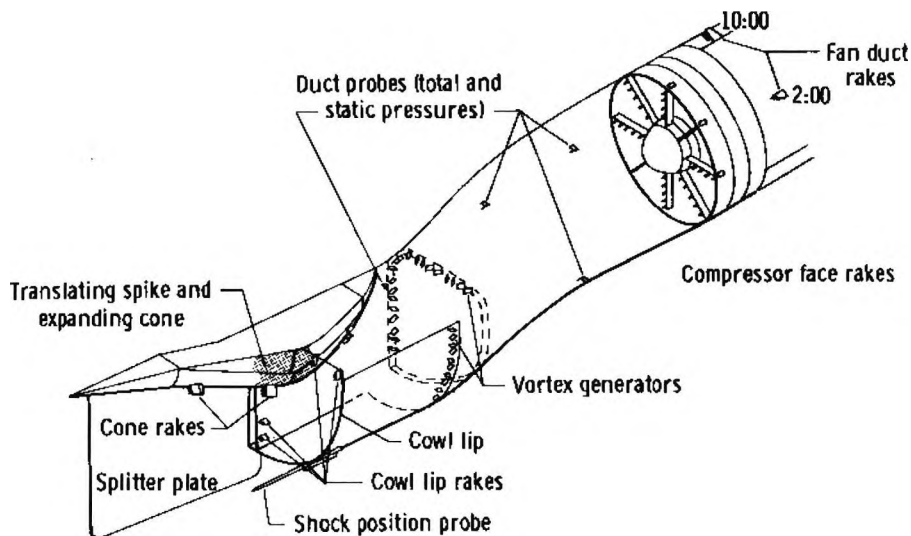


Figure 2-18: VVG installation in F-111 aircraft duct (Burcham & Bellman, 1971)

Anderson & Gibb (1992) describe the principle of using VVGs for 'distortion management'. This paper introduces a shift in the strategy of vortex generators. Traditionally, VVGs have been used locally to prevent boundary-layer separation. The philosophy of distortion management is a global one, where the VGs are used to restructure the secondary flow to reduce engine face distortion. The results can be seen in *Figure 2-19*. *Anderson & Levy (1991)* specify that for distortion management, a co-rotating array of vortex generators has several significant advantages over counter rotating set-ups. The induced vortices from co-rotating arrays remain closer to the wall leaving a "cleaner" core flow. *The induced vortices will counteract the strong secondary flows that may develop.*

Computational models have been developed such as that by *Kunik (1986)* whereby the effect of VVGs is modelled by using a source term in the Navier-Stokes equations to replicate the vortex shed from the generator. These models have been used extensively for computational evaluation of VVGs in S-ducts. *Figure 2-20*, taken from *Philpot (2000)* shows engine-face contours for the m2129 duct with and without flow control. This figure shows the redistribution of the secondary flow around the circumference, removing the region of low total pressure present at the bottom of the fan face on the clean duct.

Possible problems resulting from using VVGs in close proximity to the engine, such as ingestion, in the event of a vane structural failure, have already been discussed. In addition, for military aircraft, the use of VVGs may compromise the low observable advantages of using an S-type diffuser to shield the engine-face. AJVGs are particularly appealing for the use of intake flow control, despite the engine power loss and additional weight associated with the blowing. The reduced risk of a foreign object damage (FOD) source in addition to a smooth surface finish is also advantageous.

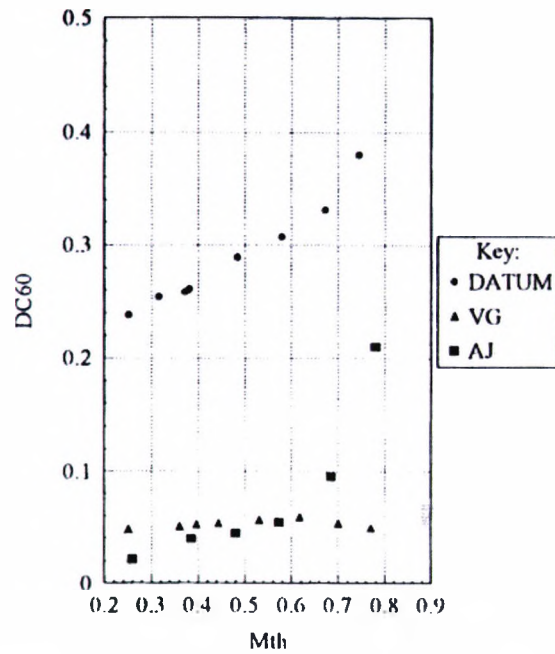


Figure 2-19: Comparison of AJVG & VVG in m2129 s-duct, DC_{60} plotted against throat Mach number, M_{th} . (Anderson & Gibb, 1992)

Gibb & Anderson (1995) present further distortion management results on the RAE m2129 diffusing S-duct. These results show a comparison between VVGs and AJVGs for reducing engine face distortion. Figure 2-19 shows that AJVGs provide a marginally higher reduction in distortion for throat Mach numbers below $M_{th}=0.65$; above this value, there is a sharp increase in DC_{60} . VVGs provide an approximately constant value of DC_{60} across the full mass-flow range. For the AJVGs, blowing pressures up to 4 bar in the plenum were used, this maximum blowing pressure provides maximum distortion reduction. Hamstra *et al* (2000) compare microvanes and microjets in a highly offset diffuser. The jets provided the highest pressure-recovery but the corresponding DC_{60} values fell in between the clean duct and the duct with vanes. The jets used approximately 1% of engine airflow. The configurations that were tested were selected using a design of experiments (DOE) approach based on CFD simulations using a VVG model, in a Navier-Stokes solver, to simulate the microvanes. The microjet arrays were designed using Anderson & Gibb's vorticity signature equivalency principal. This states that 'the key element of secondary flow control is the overall vorticity strength, distribution and secondary flow field interaction created by an effector array within the boundary layer.' The source of this vorticity, AJVG or VVG is unimportant. Experiments were then conducted to validate the CFD.

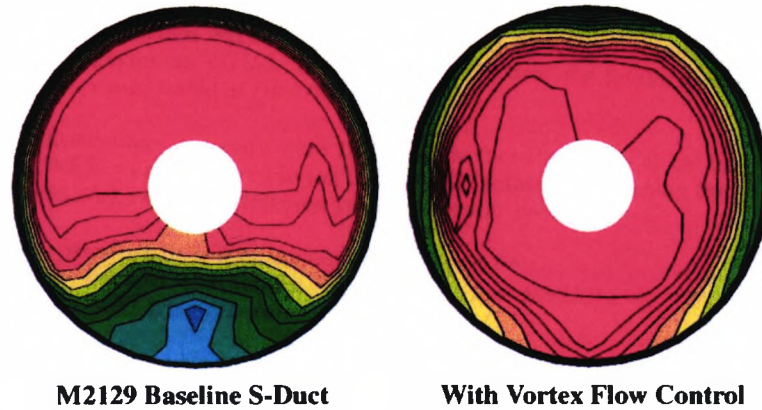


Figure 2-20: Engine-face contours without (left) and with (right) distortion management Philpot (2000)

Computations have been performed by *Currie and Syms (2000)* on the AJVG configuration described by *Gibb and Anderson (1995)* using both the SST variant of the $k-\omega$ model and the realizable $k-\epsilon$ variant. Both models over predicted total pressure recovery and under predicted DC60 for the clean duct case. The $k-\epsilon$ model was more accurate at high mass flows and the $k-\omega$ more accurate for the low mass-flow case. The lip and the duct were calculated separately with the lip results being used as the inflow condition for the duct calculation. The calculations were performed on a prism/tetrahedral mesh that included the plenums and air-jet ducts. A comparison is not made with experimental data for the AJVG calculations.

Wallis (1952) first proposed the use of AJVGs to control leading-edge flow separations on thin wings. He demonstrated the benefits of increasing the maximum lift and reducing drag at high incidence. He identified the mechanism of momentum transport to the boundary layer to be different from other blowing concepts of the time. Wallis also identified the engine intake and ducts as areas that will potentially benefit from this technology. Wallis describes further potential benefits of AJVGs in that they could be switched off for normal operation during which they contribute zero parasitic drag.

The mechanisms behind AJVGs have since been studied in detail. *Pearcey (1961)* describes a pair of counter rotating vortices formed about the pitched and skewed jet, which are of unequal strength (*Figure 2-21*).

Peake *et al* (1998) provide a more detailed description of the mechanisms of pitched and skewed jets as well as reviewing work carried out at City University. The authors provide a detailed experimental and computational analysis of the workings and applications of AJVGs (See also Peake, Henry & Pearcey, 1999). The work at City University includes a large database of AJVG parametric variation, including jet spacing, size, jet exit shape and blowing pressures. These have been demonstrated for a wide range of configurations such as multi-element aerofoils (including racing car wings) wind turbines, helicopter rotor blades and S-ducts.

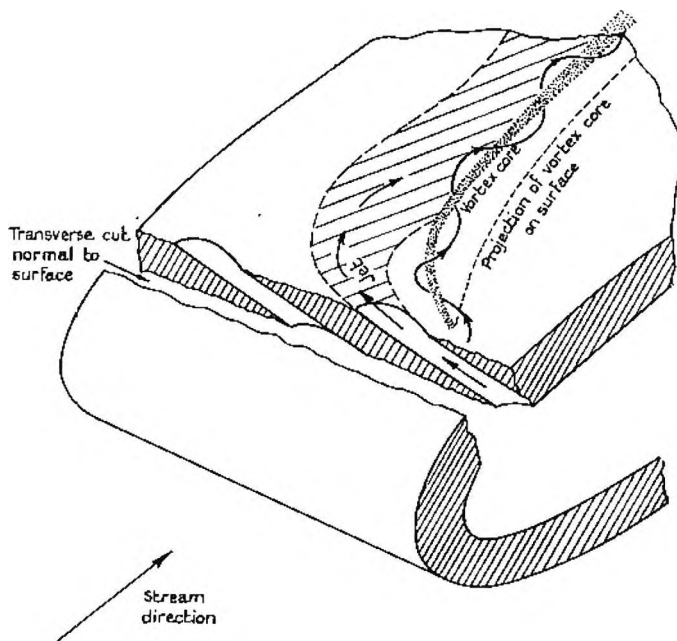


Figure 2-21: Generation of mixing from a pitched and skewed jet Pearcey (1961)

Much research has focused on validation of CFD methods for prediction of AJVG flows. Akanni & Henry (1995) describe calculations on a single AJVG on a flat plate with the standard $k-\epsilon$ two-equation turbulence model. These calculations show good prediction of the spanwise shear-stress distribution downstream of the AJVG. Küpper & Henry (2002) expanded this study using a sector model to represent a circular intake duct without offset. The results are similar to those previously shown for a flat plate and suggest that this is because the vortex is small compared to the diameter of the duct. The peak pitch and skew angle of the jet in relation to the surface that provided maximum flow enhancement was 30-degrees and 75-degrees respectively.

2.8. Flow control trade-off study

To assess the feasibility of using flow control concepts, a weighted decision matrix was constructed containing various types of flow control and variable geometry devices, as well as the solution using no flow control. This is shown in Figure 2-22.

	Low Observability	Lightweight	Design Performance	Off-Design Performance	Control System Simplicity	Failure Mode	Power Requirement				
Military weighting	3	1	2	1	1	1	1				
Civil weighting	0	2	2	2	1	2	2	Military		Civil	
								Score	Rank	Score	Rank
No Flow Control	3	3	4	3	5	5	3	36	4	41	4
VVG	2	5	5	1	5	2	5	34	6	41	4
Suction	4	3	4	2	3	3	2	33	7	31	7
Slot Blowing	2	3	4	1	2	3	2	25	8	28	8
AJVG	5	4	5	5	3	3	3	43	1	43	2
Vari-cowl	3	4	5	4	3	2	3	35	5	39	6
Blow in Doors	3	3	4	5	5	3	5	38	3	45	1
Variable L.E. Radius	5	3	5	5	3	4	3	43	1	43	2

Figure 2-22: Trade-off matrix for flow control techniques

The seven different flow control types were evaluated for seven different design criteria that are likely to affect the overall performance of the vehicle in which the flow control system is to be installed. Each of these seven factors has been weighted between 0 and 2 for both civil and military applications, with one exception described below. A rating of '0', implies no relevance, for example low-observability for civil aircraft. A rating of '2' implied high importance. For the military weightings, low observability has been set as '3' due to its exceptional importance above that of more traditional vehicle performance metrics. For each performance category, the flow control devices have been awarded a score between '1' and '5' where '1' is poor performance and '5' good performance. The scores have been awarded based on engineering judgement and the literature study. Of the seven performance categories, most are self-explanatory. Further explanation follows for failure-mode and power requirement. Failure mode describes what happens in the even of failure of the flow

control system. A low rating is safety critical for example, ingestion of components by the engine or an increase in distortion causing engine failure. Higher scores represent loss in range, or manoeuvrability without compromise in survivability or safety. Power requirement describes the off-take required from the engine, either in terms of high-pressure air or shaft power. If we consider the internal drag of active air flow control systems, as well as the exit drag of suction or bleed systems, power requirement may be assumed to be an overall assessment of thrust minus drag.

The overall weighted scores have been calculated for flow control type with respect to both civil and military applications. The flow control types have then been ranked in order of desirability. The first point of note for both civil and military configurations is that the option of not using flow control is more desirable than using four of the flow control types evaluated. The same three options surpass the overall performance of the clean intake for both military and civil aircraft. For military aircraft, the variable radius lip and the AJVG solution are equally the most desirable. These are followed by the blow-in doors option. These results provide a good representation of the current state of the art in production aircraft and indicate why flow control has not been previously applied to intake flows. The variable lip discussed in the literature study is still at the concept stage. Currently, its limitation is related to the engineering design rather than the aerodynamics. This is next generation technology. AJVGs have been proved for distortion management in offset ducts, but have not been used yet in production vehicles. The blow-in doors (auxiliary intakes) option has the highest technology readiness level (TRL) of the three concepts that out performed the clean intake. They are used on a number of current generation low-observable aircraft for example F-22 and B-2.

The assessment for civil aircraft indicated blow-in doors to be the favoured option. The main driving factor is the simplicity: these devices are controlled by the natural pressure gradients in the intake and their reasonable performance both on and off design.

Although this study is relatively simplistic, it does appear to correspond to what has been seen in production aircraft intake design. It is only the relatively new technology, using smart materials with a variable radius lip, along with the new application of

AJVGs to intake lips, that can provide a better solution across the flight envelope than the 'clean' intake. The main reasons for this are the off-design performance of the flow control system in the case of VVGs or the high power off-take needed for suction or slot blowing.

2.9. The future for flow control in intake design

At the current time, there are major changes occurring in the platform and layout of both military and civil air vehicles. Much current research in the civil aircraft market is focussed on blended wing body (BWB) configurations. Many proposed configurations have intakes mounted at the top and to the rear of the airframe. This maximises passenger carrying potential as well as providing an element of acoustic shielding. Some of these configurations ingest the fuselage boundary layer (*Rodriguez, 2002*) which has been shown theoretically to provide a benefit in terms of overall thrust minus drag (*Davidson, 1968*). Choosing to ingest the boundary layer may introduce intake-sizing problems. The boundary layer causes a blockage effect that reduces the effective area of the intake, the result being additional losses at the static or low-speed condition. The other option is to enlarge the intake, which will induce weight and external drag penalties, as well as making it susceptible to the pre-entry separation problem at low mass-flow (*Seddon & Goldsmith, 1999*). The ingestion of the fuselage boundary layer may be the source of other potential problems: a thick boundary layer on the inside wall of an S-bend diffuser will seriously deteriorate performance and increase distortion at the engine-face. It is, therefore, of primary interest that the intake flow is well behaved so as to not adversely influence the diffuser performance.

Opportunities exist within the future civil aircraft market for the use of intake flow control, which will allow the intake system to be designed for a particular point of the flight envelope. The use of a thinner conventional podded nacelle will reduce weight and cruise-drag and increase ground clearance, allowing a larger diameter fan. The low speed performance could then be improved by using AJVGs. Similarly, for a BWB configuration, AJVGs could be used to help alleviate the sizing problem.

As has already been mentioned, current and future generations of military fighters are driven by low observable constraints. For the intake, this may take the form aligning the leading edge with the wing sweep and limiting the size of the lip leading edge radius (*Bingman, 1992*).

Aligning the intake capture plane with the dominating vehicle sweep lines has been achieved with the caret intake on the F/A-22 and F/A-18E/F. This results in potentially high areas of local lip loading which may provide opportunities for the use of AJVGs. The F/A-18E/F in particular has suffered with a vortex generated from the highly swept cowl and sidewall surfaces at the aftmost corner of the intake. A 'vortex breaker fence' is installed on the outboard internal lip to reduce the distortion for low-speed, high mass-flow operation. This was found more effective than re-contouring the lip (*Hall et al, 1993*). The vortex breaker fence can be seen in Figure 2-23. It can be imagined that AJVGs would provide a more appropriate form of flow control for this problem. A number of measures were taken to reduce the radar signature of the F/A-18E/F in comparison with its previous incarnation. The single-ramp external-compression intakes were replaced with caret form external-compression intakes to allow edge alignment of the intakes with the wing leading edge. A blocking device (essentially additional engine inlet-guide-vanes) is also present to obscure the fan from forward observation. It appears strange to add a non 'low-observable' device, such as the vortex breaker to the shape. It can only be hypothesised that the extent of the distortion problem due to the intake sweep only became apparent late in the design stage. A more low-observable solution could not be evaluated without major change to the intake.

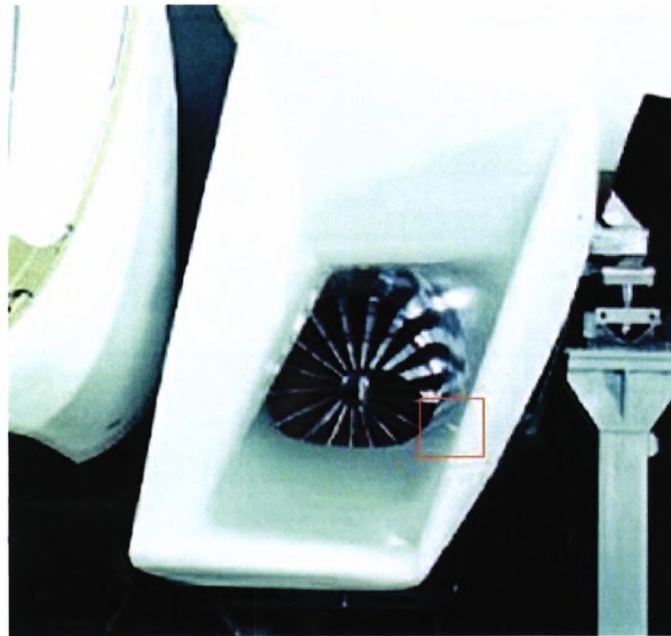


Figure 2-23: Vortex Breaker fence on F/A-18E/F intake

Flush intakes such as the classical NACA style shown in *Figure 2-24 (Frick et al, 1951)*, although potentially advantageous from the low-observable point of view when submerged on the upper surface of a vehicle, are prone to bad static performance. This is especially true when they are used in conjunction with a lip of limited leading edge radius: again, this is an area of potential application of AJVGs.

Martin (2002) proposes several research topics for UCAV intake lips and suggests research needs to be conducted into the lip aerodynamics of such configurations, with particular regard to methods of improving the low speed and static performance of sharp lip intakes.

For AJVGs generators to be used in military vehicles, research may be needed into the effect of AJVG holes and ducts on radar signature. A general rule of thumb, however, is that if the holes are much smaller than the wavelength of the illuminating radar, their presence is insignificant. (*Laruelle, 2002*)

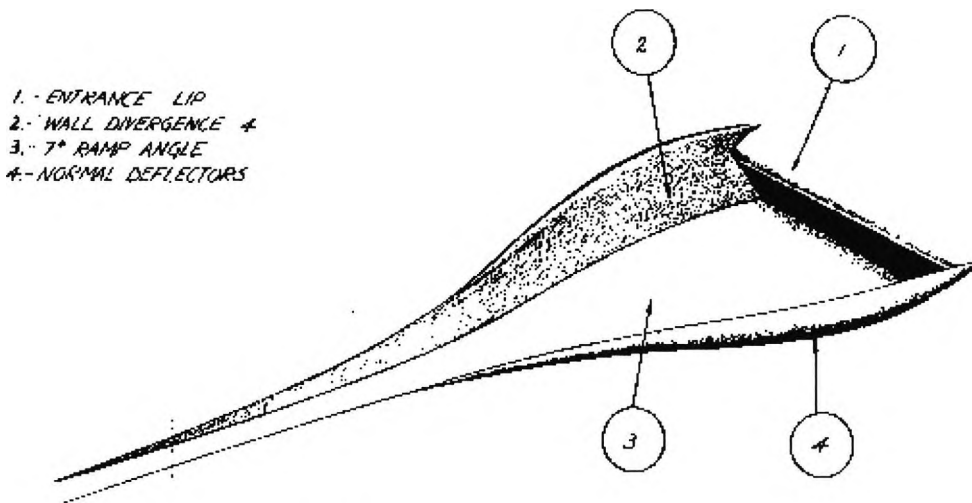


Figure 2-24: NACA Flush Intake (Frick et al, 1951)

2.10. Conclusions from literature review

The following tables (Table 2.1-Table 2.4) present a summary of some of the important contributions to the subjects of intake lip flows and the application of flow control to air induction systems. The summary is colour coded, important findings are highlighted in blue, first discoveries and innovations are highlighted in red. In general, we can draw the following conclusions from the tables and the preceding discussion:

Lip geometric design

- Increasing the contraction ratio may be used to increase low-speed, high-incidence performance by increasing the angle of attack or mass flow at which separation occurs.
- Increasing the ellipse major/minor axis ratio, or using a super ellipse for the internal lip, may be used to sharpen the lip. This reduces the peak surface Mach number.

Lip separation type

- Intake external flow separation is sensitive to Reynolds number. Internal separation is not.

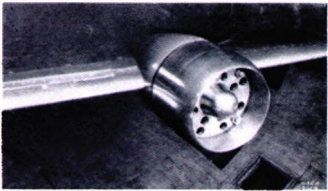

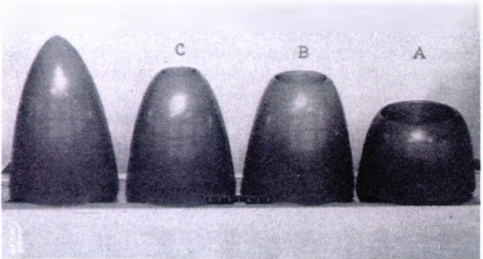
- For high-contraction ratio intakes, lip separation is influenced by compressibility and may be shock induced for a moderate incidence range.
- For low contraction-ratio intakes, lip separation is a function of the ability of the onset flow to negotiate the curvature of the lip.
- Intake flow separation is three-dimensional in nature, but most attempts to analyse its development have been based on two-dimensional analogies.

Flow control

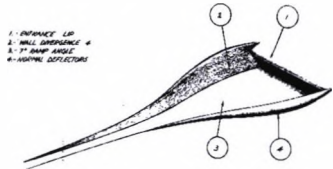
- VVGs have been shown to work well when correctly located on the intake lip; but have not been researched in depth.
- Auxiliary inlets increase pressure recovery but the mixing is detrimental to distortion at the engine face.
- Co-rotating VVGs are best in intake ducts.
- For intake ducts, the goal is to reduce distortion; this does not necessarily mean eliminate separation.
- Slot blowing is effective on thin lips, but not so on higher contraction lips; the required mass flow can be excessive.
- AJVGs have the potential to provide the benefits of VVGs and slot blowing, but across a larger range of flow conditions and at a smaller mass flow

Table 2.1 Intake Lip flows and separation

Simple configurations

Date, Author	Intake type and flow conditions	Summary of findings
<p>1942, Robinson & Becker</p> 	<p>8 Radial engine cowlings WT tested with different leading edge radii and mid-body sections (skirts). Determination of best design practice for maximum critical speed. $0.1 < M < 0.75$</p>	<p>Criterion for high critical speed intake is maintaining uniform pressure distribution over lip</p> <p>Lowest drag transonic cowls were also lowest drag at low speed and had best incidence performance.</p> <p>Thus low speed drag (separation) characteristics may be used as an indicator of high speed performance</p>
<p>1948, Baals, Smith & Wright</p> 	<p>NACA 'B' cowling from Robinson & Becker, 1942 further developed. Into NACA-1.</p> <p>Range of l/D and d/D tested.</p> <p>$0.3 < M < 0.4$ $\alpha \leq 4^\circ$</p>	<p>Performance similarity of shapes with the same non-dimensional profiles, difference in critical speeds due to geometric proportions.</p> <p>NACA 1-series ordinates presented</p> <p>l/D primary dimension governing critical speed. d/D governs mfr for critical speed.</p>
<p>1951, Becker</p> 	<p>Nose inlets integrated into streamline axisymmetric body.</p> <p>Parametric variation of intake geometry.</p> <p>$4 \times 10^6 \leq Re_D \leq 20 \times 10^6$</p> <p>$0.1 \leq M \leq 0.6$</p>	<p>Inlet/outlet may be included in a streamline body without increasing the external drag.</p> <p>Intake may be shaped to provide pressure distributions similar to the body containing no inlets.</p> <p>Transition location moved toward leading edge with increase in Re_D.</p>

1951, Frick, Davis, Randall & Mossman



Parametric investigation of NACA flush intakes including 7 different lip configurations.

Modified leading edge radius with variations of internal and external profile curvature.

$$0.7 \leq M \leq 1.15$$

$$0.4 \leq V/V_\infty \leq 3.2$$

$$0^\circ \leq \alpha \leq 8^\circ$$

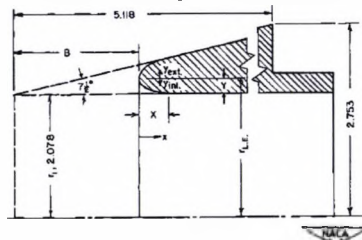
Lip local angle of attack dependent on wall divergence and ramp angle.

Submerged lip that is tangent to the external surface at its crest is potentially the best design from drag perspective.

Adding camber to internal profiles reduces stalling at high V/V_∞ .

Most benefit in internal performance from increasing camber in conjunction with nose radius.

1954, Blackaby & Watson



Nose intake in body of revolution
1 sharp lip, 5 circular lips, 2 elliptic lips
Fore cowl slope 7.5°

$$1.0 \leq CR \leq 1.33$$

$$M \leq 0.330$$

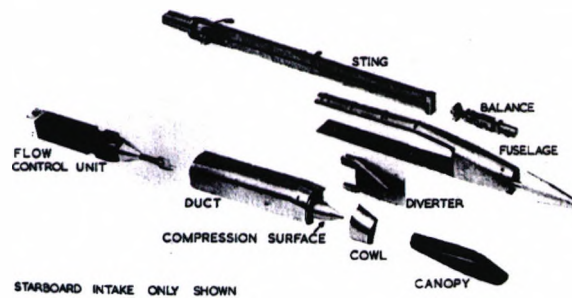
$$0 \leq A_o/A_c \leq \text{crit}$$

Elliptic lip provides better internal performance.

Choked flow in the duct induces an oscillation of 15% H_o in amplitude at a frequency of 20Hz.

External drag matches potential flow when no external separation is present.

1970, Dobson & Goldsmith,
1972, Dobson,
1973, Dobson



Extensive parametric study of intake configurations for strike fighter aircraft.

Rectangular and semi-circular intakes with and without compression surfaces and diverters.

Lip leading edge radius varied.

$$0.6 \leq M \leq 2.00$$

$$A_o/A_c < 1.0$$

$$0.52 \times 10^6 \leq Re \leq 0.78 \times 10^6 \text{ varies with } M$$

Subsonic:

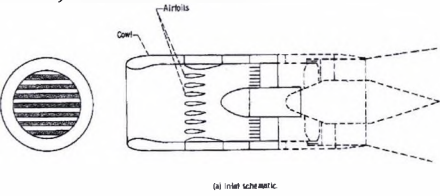
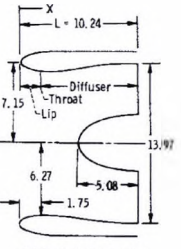
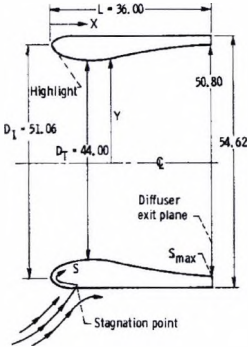
Drag is dependant on lip radius for pitot intakes

External separation increase in extent as mfr is reduced.

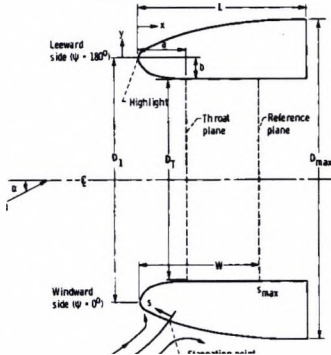
A conical compression surface reduces separation onset sensitivity to lip radius.

Supersonic:

Drag increases with lip radius (except for pitot intakes which are in lower speed flow due to the strength of the normal shock)

<p>1972, Miller & Abbott</p>  <p>(a) Inlet schematic.</p>	<p>Measurements of aerodynamic and acoustic performance of choking intakes. Choking obtained by translating centrebody and airfoil grid.</p> <p>Fan diameter 13.97cm</p> <p>$M = 0.0$</p>	<p>Lip pressure distributions and surface Mach numbers.</p> <p>Reduction in pressure recovery when intake is choked due to separation downstream of throat.</p> <p>Fan noise reduced by 29 decibels with centrebody choking at the expense of pressure recovery.</p>
<p>1973, Albers</p>  <p>(a) Centerbody retracted.</p>	<p>Incompressible potential flow calculations compared with experiment for centrebody forward and contracted</p> <p>Fan diameter 13.97 cm</p> <p>$V_{\infty} = 0, 24, 32, 45 \text{ m/s}$</p> <p>$0^{\circ} \leq \alpha \leq 50^{\circ}$</p>	<p>Large circumferential variation in static pressure at the highlight and throat with incidence. This reduces along the length of the diffuser.</p> <p>Increasing free stream speed forces the stagnation line toward the highlight.</p> <p>Transition based on minimum pressure is not an adequate criteria for boundary layer calculations.</p>
<p>1973, Albers</p> 	<p>Axisymmetric potential flow with boundary layer analysis.</p> <p>Fan diameter 51.0 cm</p> <p>$V_{\infty} = 45 \text{ m/s}$</p> <p>$0^{\circ} \leq \alpha \leq 50^{\circ}$</p>	<p>Internal intake lip separation as a function of incidence angle is identifiable from changes in static pressure distribution.</p> <p>Pressure distribution under the separation bubble not predicted well.</p> <p>Increasing contraction ratio increased attached flow alpha range.</p> <p>For large incidence angle, peak surface Mach number occurs in the highlight region.</p>

1973 Albers & Miller



Incompressible potential flow calculations corrected for compressibility

$V_\infty=0$ & 42.6 m/s, $M=0.8$

$0^\circ \leq \alpha \leq 50^\circ$

CR 1.3, 1.34, 1.42

Internal a/b 1.5, 2.0, 2.5

Internal lip super exp. 1.75, 2.0, 2.25, 2.5

External lip super exp. 1.78, 1.95, 2.15

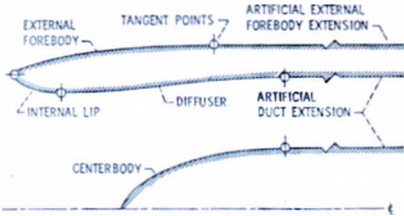
CR had largest effect on surface Mach number distribution that was greatest on the windward lip at large incidence. (27% reduction in M as contraction ratio increases from 1.3 to 1.42 at $\alpha=40^\circ$)

Smallest CR inlet had the largest circumferential Mach number distribution. – Higher cross-flow pressure gradients.

a/b=2 produced smallest surface M and M gradient.

The larger a/b the larger super exponent is needed to reduce surface M gradients. I.e. maintains lip bluntness.

1975, Stockman



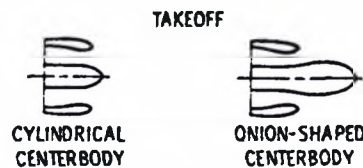
Incompressible potential flow calculations with viscous and compressibility corrections.

Demonstrated for lift fan and QCSEE intakes.

Description of the method used in *Albers & Miller(1973)*.

Shows possible laminar separation in the lip regions and turbulent separation in the diffuser by analysis of skin friction coefficient.

1974, Abbot



Aerodynamic and aeroacoustic tests of single and multiple passage sonic intakes in take-off and landing configurations.

Fan diameter 13.97 cm

CR 1.3, 1.44

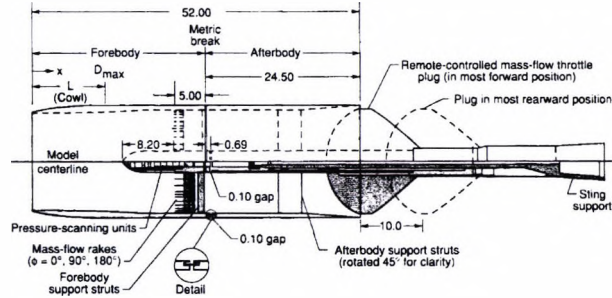
a/b 2.0, 2.9

$\alpha = 0^\circ, 20^\circ, 30^\circ, 40^\circ$

Increasing lower lip local CR increases incidence angle at which separation occurs.

Increasing internal lip a/b increases curvature causing a small bubble separation, which reduces noise suppression.

1974, 1975, Re



Experimental investigation of NACA 1-series cowls.

$$0.81 \leq (d/D_{\max}) \leq 0.89$$

$$0.75 \leq (L/D_{\max}) \leq 1.25$$

$$0.40 \leq M \leq 1.29$$

$$A_o/A_c < 1.0$$

$$3.40 \times 10^6 \leq Re \leq 5.60 \times 10^6 \text{ varies with } M$$

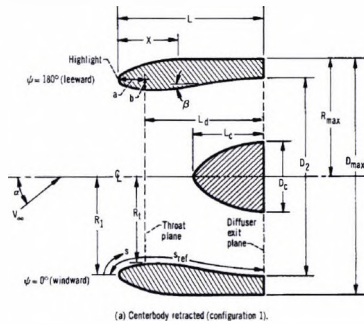
Increasing lip thickness by contraction ratio or lip radius reduced critical Mach number. (external flow)

Blunt lip cowls produced the least flow separation. As mfr is reduced.

The smallest diameter ratio inlet exhibits the lowest value of axial force. (thinnest cowl)

Large database recommended for CFD validation.

1975, Felderman & Albers



Comparison between experimental and theoretical separation positions.

Centrebody extended and retracted 2 diffuser lengths and thickened lower lip.

Fan diameter 13.97 cm
 $CR=1.3$ $a/b=2.0$
 NACA external contour, $L/D=0.3$
 $M=0.17$
 $0^\circ \leq \alpha \leq 50^\circ$

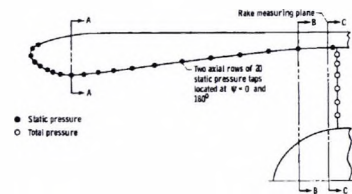
Good agreement for attached flow.

Separation location moves up diffuser toward lip as incidence is increased.

Separation predicted at high incidence in lip region. Not well predicted at lower incidence angles when separation is not as well defined.

Loss in total pressure recovery increased as separation moved forward toward lip.

1975, Miller & Dastoli



Experimental studies of the effect of lip design on high throat Mach number V/STOL intakes.

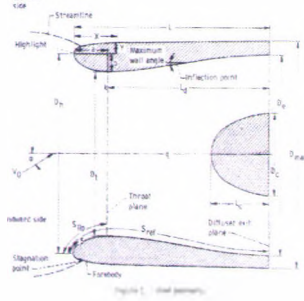
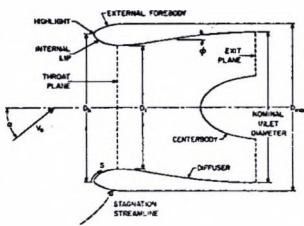
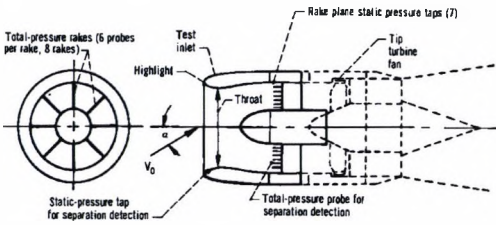
CR 1.37, 1.46, 1.56.
 DAC & NACA external contours.
 $L/D \approx 1.0$
 $V_\infty = 41, 61 \text{ m/s}, 10 \text{ m/s cross wind}$
 $0^\circ \leq \alpha \leq 50^\circ$

Highest contraction ratio produced highest total pressure recovery and lowest distortion.

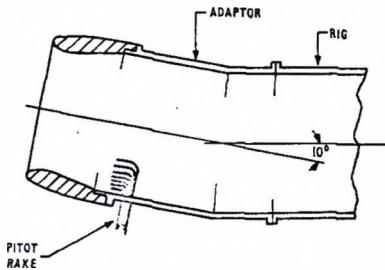
At low M_{th} crosswind separation occurs is reduced as M_{th} is increased. Larger contraction ratio inlets have best crosswind performance.

Larger D_c/D_{\max} reduce incidence performance.

Shock b.l. interaction occurs at high mass flows.

<p>1975, Albers, Stockman & Hirn</p> 	<p>Analytical investigation of internal and external surface Mach numbers on the nacelle for QCSHEE.</p> <p>CR 1.37, 1.46, 1.56. Bi-super ellipse external contours. $p=1.76, 1.78, 1.90, q=1.78, 1.90, 2.25, 2.26$ $L/D=0.175, 0.2, 0.218, 0.335$ $M_\infty=0.0, 0.05, 0.12, 0.18$ $\alpha = 0^\circ, 44^\circ, 50^\circ, 90^\circ$ (crosswind)</p>	<p>Bluntness parameter introduced based on geometry.</p> <p>Internal lip surface M gradients are reduced by blunting the external lip, most effective on the lowest CR.</p> <p>Minimum lip M, f(bluntness)</p> <p>Take off condition ($\alpha=50^\circ, M=0.05$) produced the largest peak surface Mach numbers.</p> <p>For fixed bluntness M decreased with increasing CR</p>
<p>1975, Jakubowski & Luidens</p> 	<p>Examination of six experimental configurations.</p> <p>$1.26 \leq CR \leq 1.56$ DAC & NACA external contours $D_c/D_{max} = 0.905, 0.933$ $7.5 \text{ m/s} \leq V_\infty \leq 65 \text{ m/s}$ $0.65 \leq M_t \leq 0.70$</p>	<p>Incidence angle at which separation occurs increases with M_t until $M_t \approx 0.65-0.7$, then decreases until throat choking.</p> <p>Increasing CR will delay increase separation incidence, sharpening of the external contour will cause a decrease.</p> <p>Mechanisms for low and high throat Mach number separations proposed.</p>
<p>1976, Luidens & Abbott</p> 	<p>Experimental investigation to establish procedure for determining lip separation.</p> <p>With centrebodies, non axisymmetric</p> <p>Fan diameter 13.97 cm $CR=1.3, 1.44:a/b=2.0, 2.9$ NACA external contour, $L/D=0.3$ $M=0.17$ $0^\circ \leq \alpha \leq 90^\circ$</p>	<p>A pressure orifice near the lip may be used to indicate lip separation.</p> <p>For $M_t < 0.43$, incidence angle for internal separation may be generalised by intake velocity ratio. Larger values of M_t may decrease separation incidence.</p> <p>Extending the centerbody into the throat increases the separation angle.</p>

1976 Hurd



Experimental investigation to establish attached internal flow envelopes and investigate the flow mechanics.

CR = 1.25, 1.35
 $a/b = 2, 3$
 $0.60 \leq M \leq 0.90$
 $0^\circ \leq \alpha \leq 19^\circ$

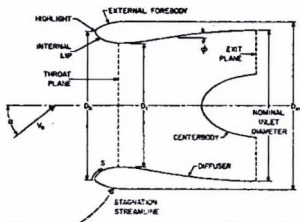
Three types of boundary layer inside intake at incidence were noted; minimum, thickened & separated.

For $\alpha^\circ < 13$ losses are based on throat Mach number and become apparent as this rises to 0.6 and above.

When $13 \leq \alpha \leq 19^\circ$ a fall in separation free mass-flow was apparent at high M. The source remained unidentified.

At high α separation occurred with no shock.

1977, Chow, Luidens & Stockman



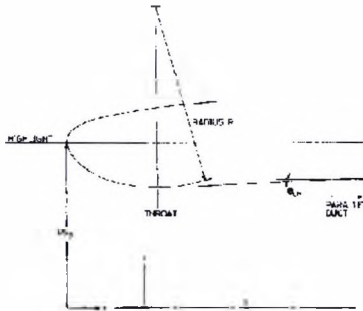
Theoretical description of the boundary layer development on the lip and diffuser for a subsonic intake.

Scale effect and roughness effect calculated
 CR = 1.46
 $D_c/D_{max} = 0.905$
 $L/D = 0.75$

Increasing scale delays diffuser separation. At larger scale laminar flow in lip region is closer to separation.

Roughness increases skin friction coefficient on the lip but promotes earlier separation in the diffuser. In the limit, the turbulent separation in the diffuser moves up to the lip.

1979, Langley



Experimental investigation of six cowls for spill drag onset and gradient. Drag measure by external rake

CR = 1.25
 Circle-conic profiles
 $D_c/D_{max} = 0.85, 0.9$
 $L/D_{max} = 0.45, 0.35$

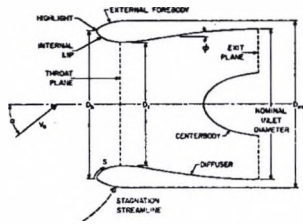
Variation in leading edge radius

Using a larger lip radius than NACA 1-series reduces lip peak velocities, reducing spillage drag at the expense of high Mach number performance.

Flattening profile aft of the lip and increasing curvature near the crest improves performance as long as the shock sits ahead of the high curvature region.

Drag divergence can be related to particular shock strength.

1981, Chou, Baek, Luidens & Stockman

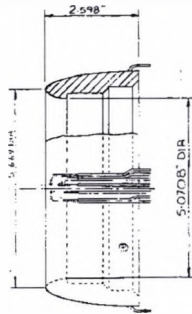


Numerical analysis of viscous flow around V/STOL intakes at high incidence including scale effects. Compared to experiment.

CR=1.46
 $D_c/D_{max}=0.905$
 $L/D=0.75$

Identification of a 'cross over scale effect' at low M_t (< 0.6) a more favourable separation incidence is obtained at full scale. When $M_t > 0.6$, the full scale model tolerates a small incidence before separation. This is due to separation being fixed at the highlight.

1981, Wilmer, Brown & Goldsmith



Experimental investigation of circular section pitot intakes at low speeds.

CR=1.25, 1.177, 1.078
 $a/b = 2, 5, p=q=2.4$
 NACA 1-85-35 external contour
 $0.0 \leq M \leq 0.21$
 $0^\circ \leq \alpha \leq 40^\circ$
 $0.0 \leq Re \leq 6.18e5$

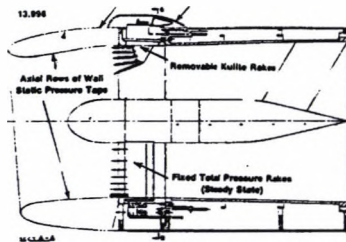
Loss coefficient separated into lip and diffuser components.

Increasing contraction ratio or using a lip slot (10% additional throat area) reduce losses.

An aft extension reduces DC60

Transition fixing has a negligible effect for $CR < 1.2$ and a small effect for larger CR. Transition strips compromise the intake geometry.

1982, Younghans, Hoelmer & Stockman



Experimental investigation in a pressurised WT to determine geometry and Reynolds number effects on external separation (Take-off engine out)

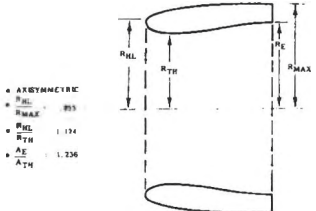
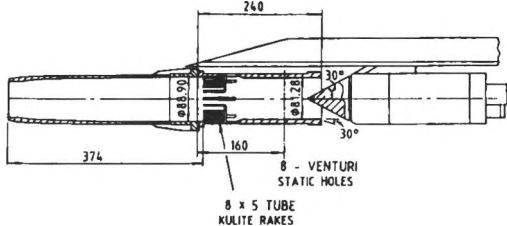
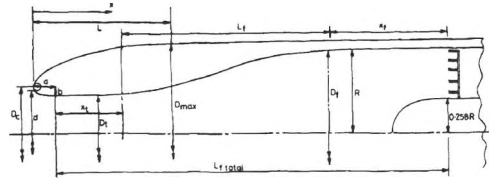
Axi-symmetric & non-axisymmetric intakes
 $D_c/D_{max} = 0.8298, 0.855, 0.860$
 $0^\circ \leq \alpha \leq 35^\circ$
 $3.94e6 \leq Re \leq 6.47e6$

Upper cowl separation is dependent on Re and D_c/D_{max}

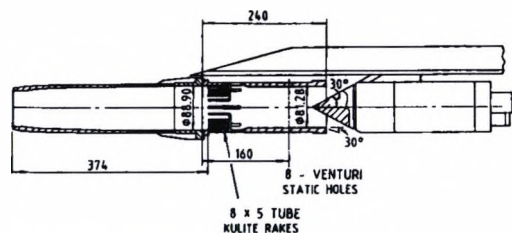
Sub-scale experimental data cannot be extrapolated to full-scale (external separation)

Separation incidence angle increases with Reynolds number.

Separation incidence angle increase with reducing D_c/D_{max}

<p>1984, 1987 Hoelmer, Younghans, Raynal</p> 	<p>Experimental investigation in a pressurised WT to determine geometry and Reynolds number effects on external separation (Take-off engine out) 15% & 33% model to provide additional variation of Re up to full scale $D_c/D_{max} = 0.855$, $CR=1.26$ $0^\circ \leq \alpha \leq 35^\circ$ $3.94e6 \leq Re \leq 6.47e6$</p>	<p>Incidence angle for separation presented over a full range of Reynolds numbers.</p> <p>At full scale, the probable type of external lip separation is a turbulent boundary layer separation.</p>
<p>1985, Hacker, Hirst, Hayward, Hyde & Goldsmith</p> 	<p>WT test of RAE model m742L, all 8 cowls.</p> <p>$CR=1.078, 1.117, 1.25$ $a/b = 2,5$ $d/D_{max} = 0.83, 0.85, 0.89, 0.93$ $L/D_{max} = 0.75, 1.0, 1.25$</p> <p>$0.21 \leq M \leq 2.0$ $0^\circ \leq \alpha \leq 40^\circ$</p>	<p>Large database, extensively instrumented models</p> <p>Recommended and used for CFD validation in this thesis.</p> <p>See Goldsmith (1990) for results</p>
<p>1986, Forsey & Billing</p> 	<p>Axisymmetric invicid, Euler and fully viscous 3D calculations performed on the RAE model 742L series.</p>	<p>Review of computer codes used at ARA in support of RAE research, some results presented spillage drag curves and pressure distributions.</p> <p>See Goldsmith (1990) for results</p>

1990, Goldsmith



WT test of RAE model m742L, all 8 cowls.
Some calculations.

CR=1.078, 1.117, 1.25
a/b = 2,5
 $d/D_{max} = 0.83, 0.85, 0.89, 0.93$
 $L/D_{max} = 0.75, 1.0, 1.25$

$0.21 \leq M \leq 2.0$
 $0^\circ \leq \alpha \leq 40^\circ$

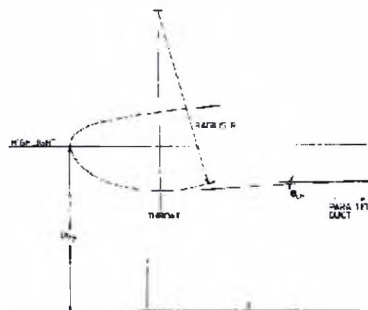
Internal contraction has a small effect on pre-entry drag, lip blunting produces a slightly larger effect, this is cancelled by additional cowl suction.

Spill drag is predicted well until separation occurs.

The rate of decrease of cowl drag with decrease in A_o/A_c is increased by increasing d/D_{max} (cowl projected area) and by a decrease in L/D_{max} (cowl fineness ratio)

Method proposed for calculating spill drag by pressure integration.

1990, Shmilovich



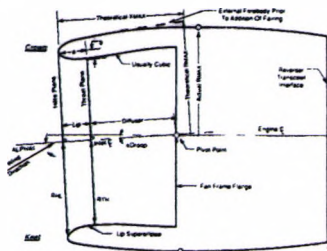
Method for calculating transonic separated flow past intakes at incidence and yaw. -.

M=0.8, NACA 1-85-100
M=0.775, $Re = 6.67 \times 10^6$ GE LFN
M=0.85, $Re = 2.4 \times 10^6$ ARA cowl
M=0.78, $Re = 3.9 \times 10^6$ DC10 Intake

Potential finite volume multi-grid with inverse boundary layer formulation.

Technique provides insight into the development of separation bubbles in the lip region and their interaction with compression waves.

1991 Andrew, Lehnig & Rahm



Existing configurations modified to achieve higher angle of attack for external separation whilst maintaining cruise drag performance and distortion limits. High Re experiment and CFD used in design process.

No specific geometric details given.

Engine-out take-off configuration

External separation requirement was met, spillage drag performance was better than the requirement whilst the drag divergence Mach number fell slightly short.

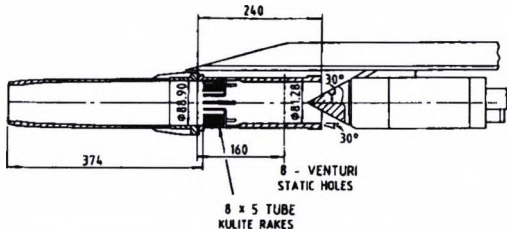
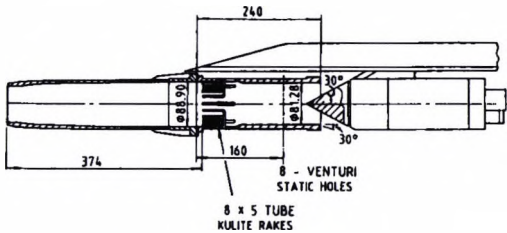
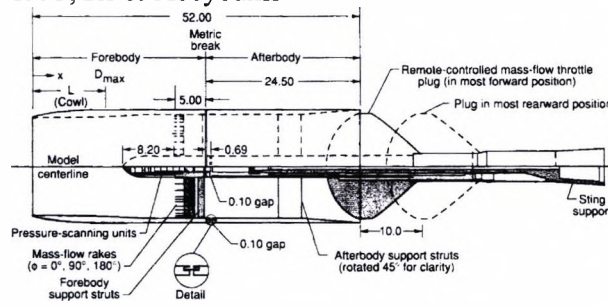
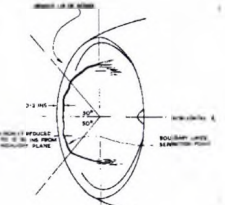
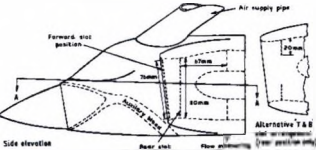
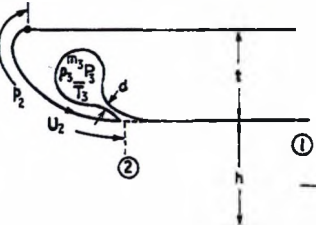
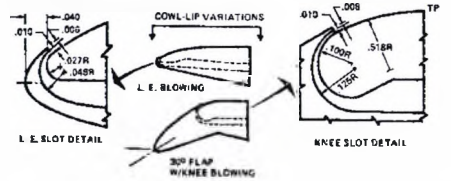
<p>1991 Mackrodt, Goldsmith, McGregor, Leynaert, Garcon & Brill</p> 	<p>RAE m742L cowl 2 tested in European wind tunnels to compare distortion.</p> <p>CR = 1.177 a/b=5 NACA 1-85-100 external contour</p> <p>$M_\infty \leq 0.8, 1.8$ $0^\circ \leq \alpha \leq 40^\circ$ $0.80 \times 10^6 \leq Re \leq 1.90 \times 10^6$</p>	<p>Different size models with different instrumentation produced broadly similar results. The most marked differences were in steady state and dynamic distortions (DC60)</p> <p>Differences are due to slight variations in lip shape, different transition strips and method for calculating DC60</p>
<p>1993, Palmer & Nangia</p> 	<p>RAE m742L series, cowls 2,5,9</p> <p>CR = 1.177, 1.078, 1.177 a/b = 2, 2, 5 NACA 1-85-100, 1-83-100, 1-85-100</p> <p>$M_\infty = 0.45, 0.6, 0.8$ $\alpha = 0^\circ, 2.5^\circ, 5.0^\circ, 7.5^\circ, 10.0^\circ$ Tunnel $H_o = 32, 64''$ Hg</p>	<p>External Flow separation correlated with $C_{p_{min}}$</p> <p>Differences in values of M_t with ARA (Goldsmith, 1990)</p> <p>Test database reduced by predicting separation points analytically.</p>
<p>1993, Re & Abeyounis</p> 	<p>Experimental investigation of three cowls of differing forecowl length but same non-dimensional geometry. External transition fixed</p> <p>CR=1.25 $D_c/D_{max} = 0.85$ $L/D_{max} = 0.337, 0.439, 0.547$</p> <p>$0.60 \leq M \leq 0.92$ $0^\circ \leq \alpha \leq 4.1^\circ$ $3.20 \times 10^6 \leq Re \leq 4.2 \times 10^6$ With M</p>	<p>Short cowl experienced the lowest negative pressures as mass flow was reduced.</p> <p>Increasing Mach number caused the short cowl to lose the uniformity in its pressure distribution (flatness) as shocks developed. The longer cowls behaved better at high Mach number.</p> <p>Large NASA data release</p>

Table 2.2 Specific air craft configurations and problems relating to intake separation

Date, Author	Aircraft and intake type	Summary of findings
1969, Hancock & Hinson	Lockheed L-500 Pitot	Analytic analysis on inlet including low speed and static conditions. Experimental data including vortex generators, lip location shows the best results.
1970, Herzmark & Victor	McDonnell F-4B Phantom II	Separation from lip during extreme low speed manoeuvres causes compressor stall. VG applied unsuccessfully to lip. Flight test.
1974, Hawkins	General Dynamics YF-16 Pitot/Normal shock	Inlet operating envelopes presented, effect of shielding, lip blunted during development to improve internal performance.
1975, Grotz	Boeing YC-14 Over wing Pitot (VSTOL)	2.5:1 super ellipse, exponents, p and q=2.2 effective in increasing angle of attack capability of subsonic intakes. Reduces Maximum surface Mach number compared to ellipse.
1980, Stocks & Bissinger	Panavia Tornado External Compression with variable geometry	Water tunnel visualisation of internal cowl separation. Original NACA-1 design blunted and de-cambered to improve distortion at expense of a reduction in max mass flow and wave drag increase. This is due to shock stand-off distance from the lip being increased by blunt lip.
1982, Tindell, Hoelzer, & Alexander	F-14 3 variable ramps, external compression	Lip 'blunted' to improve low speed performance, lip separation present at low forward speed. 'Lip' separation on internal bleed diffuser ramp lip.
1984, Clark & Vasta	McDonnell Douglas AV-8B Pitot with auxiliary intakes	Original lip changed from circular to elliptical to improve distortion characteristics by reducing peak surface Mach No. DC-10 external cowling.
1988, Leyland	Panavia Tornado/Sepecat Jaguar External Compression with variable geometry/Pitot normal shock	Tornado -Vortex from intake upper corners provides destabilising interaction with the fin at high α . At low α spillage vortex induces throttle dependent variation in pitching moment.

1992, Murman, Rizk & Schiff	Boeing F/A-18 HARV External compression	Effects of engine mass-flow on external aerodynamics presented. Intake spillage effects cause change in axial and rotational momentum of the LEX vortex resulting in the vortex breakdown point moving forward.
1994 Podleski	Boeing F/A-18 External compression	CFD calculation at $\alpha=60^\circ$, $\beta=10^\circ$ Oil flow visualisations presented including lip separation topology. Flow is highly configuration and attitude dependant being affected by fuselage boundary layer and separation on the diverter surface.
1994 Berry	Boeing 777 Podded Nacelle Installation	General integration of the nacelle with flight safety requirements is discussed as well as requirements for engine failure during take-off and ETOPS. WT results for nacelle separations during engine-out flight conditions are presented.
1995 Schwetzler	Airbus A321 Podded Nacelle Installation	The reduction in maximum lift coefficient due to the slat 'cut-out' to accommodate the nacelle pylon is shown. Use of nacelle chine to generate vortex over the top of the wing recovers loss.
1997 Yuhas, Steenken, Williams & Walsh	Boeing F/A-18A High Alpha Research Vehicle (HARV) Fixed geometry external compression	Differences between steady state and dynamic distortions during manoeuvres are primarily due to hysteresis in lip separation.
1998 Hamstra <i>et al</i>	Lockheed Martin JSF Diverterless	Patent application describing how flow diverted by the bump compression surface is spilt around the lip region abutting the fuselage.
2000, Slotnick, An, Mysko, Yeh, Rogers, Roth, Baker & Nash	Boeing 777 Podded nacelles	Calculated oil flow pictures showing effects of nacelle chines on external nacelle three-dimensional separation.
2001, Galea & Callinan	Boeing F/A-18 (Australian Air force) Fixed geometry external compression	Aircraft suffer cracking in the lower, external nacelle skin as result of elevated sound pressure levels from aerodynamic disturbance at the cowl lip.
2002, Flight International	Lockheed Martin F/A-22, Caret Intake	Vortex generated from intake causes a fin buffet problem.

Table 2.3 Intake lip flow control

Date, Author	Intake and flow control type	Summary of findings
<p>1971, Patilla</p> 	<p>Pitot intake in 30Kts crosswind conditions.</p> <p>Slot blowing.</p>	<p>Basic separation spans a 50° angular extent on the side wall</p> <p>Slot positioned at 1.68%Dc from highlight plane. Just ahead of separation point.</p>
<p>1971, McGregor</p> 	<p>Intake at static conditions, fuselage intake at high subsonic speed and lift fan installation.</p> <p>Tangential slot blowing on centre body</p>	<p>Slight increase in net thrust(1-2%), reduction in distortion sensitivity of intake to incidence reduced. Blowing pressure could be accommodated by LPC. Blowing pressure ratio 1.85, 0.7% engine demand.</p>
<p>1971, Gregory</p> 	<p>Slot blowing at lip. 2-D intakes</p> <p>M=0.</p>	<p>Some success but intakes of large contraction. Blowing rates are high, up to 8% of intake flow- not realistic.</p> <p>No assessment of distortion</p>
<p>1976, Cawthon</p> 	<p>2 Ramp, external compression intake.</p> <p>Leading edge tangential blowing. Knee blowing with cowl flap</p> <p>$0.7 \leq M \leq 1.04$</p> <p>$0.0^\circ \leq \alpha \leq 56^\circ$ $0.0^\circ \leq \beta \leq 15^\circ$</p>	<p>Effective blowing can use less than 1% of engine demand. The use of a cowl flap (or vari-cowl) is more beneficial, this further improved by the use of blowing at the flap knee.</p>

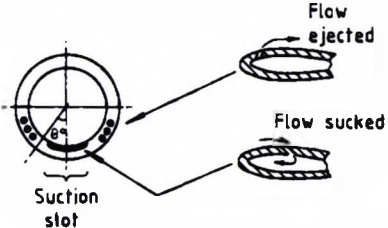



<p>1977, Miller</p> 	<p>Pitot Intake, High incidence.</p> <p>Suction slot in throat, blowing holes either side closer to the lip.</p>	<p>Major improvement between 25° and 60° incidence.</p>
<p>1978, Lotter & Malefakis</p> 	<p>Shielded rectangular strike fighter intake.</p> <p>Variable geometry, cowl slat and tangential blowing.</p> <p>$0.0^\circ \leq \alpha \leq 100^\circ$</p>	<p>Rotating cowl lip (vari-cowl) shows most promise in terms of improving high incidence performance. In addition, allowing capture area to be varied reduces spill drag.</p>
<p>1981, Ross, McGregor & Priest</p>  <p>Symmetrical CR = 1.35</p> <p>Thickened lower lip, CR = 1.25</p> <p>Cambered lower lip, CR = 1.25</p>	<p>Fuselage side mounted rectangular Pitot, Lip slot</p> <p>$0.6 \leq M \leq 1.8$</p> <p>$-8.0^\circ \leq \alpha \leq 36^\circ$</p>	<p>Thickening and cambering lower lip is the method for improving performance at incidence. The use of lower lip slot enhances positive effect of increasing contraction ratio i.e. larger incidence range but at expense of increase in DC60</p>
<p>2002 Gerhold, Clark & Biedon</p> 	<p>Scarfed Pitot Intake</p> <p>Boundary layer suction, via perforated plate inside lip.</p>	<p>Suction intended to reduce inflow distortion and hence noise.</p> <p>Less than 1% of engine flow withdrawn.</p> <p>Only small effect seen experientally.</p>

Table 2.4 AJVG & Diffuser Flow Control		
Date, Author	Configuration	Summary of findings
1986, Kunik	S-duct, VVG	Empirical model is derived for use in CFD tools to remove need to physically model geometry.
1992, Anderson & Gibb	M2129 s-duct, VVG	VG arrangement designed using CFD. Identified need to minimise distortion rather than attach flow.
1995, Gibb & Anderson	M2129 S-duct, VVG, AJVG	Jets or vanes produce an increase in stable flow range by reducing distortion, similar performance from VVG and AJVG.
2000, Hamstra, Miller, Truax, Anderson & Wendt	Ultra-compact serpentine intake duct, Micro vanes, Microjets	Microvanes sized on momentum thickness gave 50% DC60 reduction Microjets 1% of primary flow, not as effective.
2001, Currie & Syms	M2129 S-duct, AJVG computations	AJVG shown to reduce engine face distortion.
2001, Küpper & Henry	Simulated intake duct, AJVG	AJVGs 30° pitch 75° skew - most effective in terms of thinning of boundary layer, no difference between co and counter rotating arrays.
2002, Jenkins, Althoff Gorton & Anders	Submerged BWB intake. Micro VVG, synthetic jets, micro bumps.	Micro-VG's most effective control in adverse pressure gradient, even in the presence of secondary vortical flows. Control by re-energising boundary layer
AJVG		
1995, Akanni & Henry	Flat plate, AJVG inc. ducts. CFX computations.	Jet forms core of vortex, jet produces two vortices of unequal strength, stronger one persists, weaker one decays. Co-rotating hypothesised to be better as they maintain spacing further downstream.

1995, Innes, Pearcey & Sykes	High-lift 3-element aerofoil, WT test.	AJVG show better performance than vanes. One configuration tried (on main element) at two chord stations.
1998, Peake, Henry, Lush & Pearcey. 1999, Peake, Henry & Pearcey	Multi-element airofoil, wind turbines, helicopter rotors.	Review Paper, AJVG elevate Skin friction over most of aerofoil.
1999, Johnston	WT diffusers, AJVGs	Review paper
1999, Küpper	Flat plate & Intake duct, AJVG	Predicted velocity profiles agree well with experiment. AJVG cores located at approximate quarter boundary layer height so provide better mixing than VVG. AJVG and VVG provided similar shear-stress distributions for co-rotating. Increasing skew angle and decreasing pitch provides best enhancement.
2001, Lewington	3-element high lift aerofoil, AJVG, computations and experimental work.	VR>6.0 needed to provide noticeable enhancement of surface pressures. Optimal array provided a 25% increase in normal force coefficient. Attached flow up to 30° incidence

2.11. References

Abbott, J.M., 'Aeroacoustic performance of scale model sonic inlets', NASA TM-X-71637, 1975.

Akanni, S.D., Henry, F.S., 'Numerical calculation of Air Jet Vortex generators in turbulent boundary layers', Paper 16, Proceeding of the RAeS High-Lift and Separation Control Conference, Bath, UK 1995.

Albers, J.A., 'Theoretical and experimental internal flow characteristics of a 13.97-centimeter-diameter inlet at STOL takeoff and approach conditions', NASA TN D-7185, 1973.

Albers, J.A., 'Comparison of predicted and measured low-speed performance of two 51-centimetre-diameter inlets at incidence angle', NASA TM X-2937, 1973.

Albers, J.A., Miller, B.A., 'Effect of subsonic inlet lip geomery on predicted surface and flow Mach number distributions.', NASA TN D-7446, 1973.

Albers, J.A., Stockman, N.O., Hirn, J.J., 'Aerodynamic analysis of several high throat Mach number inlets for the quiet clean short-haul experimental engine', NASA TM X-3183, 1975.

Anderson, B.H., Levy, R., 'A design strategy for the use of vortex generators to manage inlet-engine distortion using computational fluid dynamics', AIAA-91-2474, AIAA/SAE/ASME 27th Joint Propulsion Conference, Sacramento, USA, June 1991.

Anderson, B.H., Gibb, J., 'Application of computational fluid dynamics to the study of vortex flow control for the management of inlet distortion', AIAA-92-32177, AIAA/ASME/SAE 28th Joint Propulsion Conference, Nashville, USA, 1992.

Anderson, John D. 'A History of Aerodynamics', pp330-341, Cambridge University Press 1998.

Andrew, T.L., Lehnig, T.R., Rahm, S.G., 'Inlet/fan cowl design for increased angle of attack requirements of transport aircraft - methodology and test results', AIAA-91-2481, AIAA/ASME/SAE/ASEE 27th Joint Propulsion Conference, Sacramento, USA, 1991.

Baals, Donald D., Smith, Norman F., Wright, John B., 'The development and application of high-speed nose inlets', NACA Report No. 920, 1948.

Becker, John V., 'Wind tunnel investigation of air inlet and outlet openings on a streamline body', NACA Report 1038, 1951.

Bellman, D.R., Hughes, D.L., 'The flight investigations of pressure phenomena in the air intake of an F-111A airplane', AIAA 69-488, Colorado, USA, 1969.

Berry, D.L., 'The Boeing 777 Engine/Aircraft integration aerodynamic design process', ICAS-94-6.4.4, 19th Congress of the International Council of the Aeronautical Sciences, Anaheim, USA 1994.

Bingman, D.C., 'Performance study for inlet installations', NASA CR 189714, 1992.

Bore, C. L., 'Some contributions to propulsion theory – the stream force theorem and applications to propulsion', Aeronautical Journal, pp 138-144, April 1993.

Bore C.L., 'Intakes for vertical landing aircraft' in "Practical Intake Aerodynamic Design" - Ed. Goldsmith & Seddon, pp286-308, Blackwell Scientific Publications, 1993.

Burcham Jr., F.W., Bellman, D.R., 'A flight investigation of steady state and dynamic pressure phenomena in the air inlets of supersonic aircraft', Paper 24, AGARD-CP-91-7. "Inlets and Nozzles for Aerospace Engines", 1971.

Butler, S.F.J., 'Aircraft drag prediction for project appraisal and performance estimation, Paper 6, AGARD CP-124, "Aerodynamic Drag", 1973.

Cawthon, J.A., 'Design and preliminary evaluation of inlet concepts selected for manoeuvre improvement', AIAA-76-701, AIAA/SAE 12th Joint Propulsion Conference, Palo Alto, USA, 1976.

Chou, D.C., Baek, J.H, Luiden, R.W., Stockman, N.O., 'Scale effects on turbulent boundary layer development and flow separation around V/STOL inlets at high incidence' AIAA-91-0014, AIAA 19th Aerospace Sciences Meeting, St. Louis, USA, 1981.

Clark, R.S., Vasta, S.K., 'Development of the AV-8B propulsion system', AIAA-84-2426, AIAA/AHS/ASEE Aircraft Design Systems and Operations Meeting, San Diego, CA, USA, 1984.

Crabtree, L.F., 'Effects of leading-edge separation on thin wings in two-dimensional incompressible flow.', Journal of the Aero. Sciences, Vol.24, pp597-604, 1957.

Davidson, I.M., 'Some notes on propulsion by wake regeneration', International Congress on Subsonic Aerodynamics, Annals of the New York Academy of Sciences, Vol. 154, Art.2, pp245-1117, 1968.

Dobson, M.D., Goldsmith, E.L., 'The external drag at subsonic and supersonic speeds of fuselage-side air intakes for strike-fighter aircraft', RAE Tech. Memo. Aero. 1259.

Dobson, M.D., 'The external drag of fuselage side mounted intakes: rectangular intakes with compression surfaces vertical', Aeronautical Research Council CP 1269, 1972.

Dobson, M.D., 'The external drag of fuselage side intakes: semi-circular configuration both with and without half cone compression surfaces', RAE TR 72203, 1972.

Engineering Science Data Unit Item 94013, 'Transonic data memoranda, NACA 1-Series geometry representation for computational fluid dynamics', June 1994.

Engineering Sciences Data Unit Item 84004, 'Estimation of spillage drag for a wide range of axisymmetric intakes at $M < 1$ ', June 1984.

Felderman, J.F., Albers, J.A., 'Comparison of experimental and theoretical boundary-layer separation for inlets at incidence angle at low speed conditions', NASA TM X-3194, 1975.

Flitcroft, J.E., Philpot, P., Ball, G.J., Unpublished work at NGTE, 1982.

Frandenburgh, E.A., Wyatt, D., 'Theoretical performance of sharp lip intakes at subsonic speeds', NACA Report 1193, 1953.

Frick, C.W., Davis, W.F., Randall, L.M., Mossman, E.A., 'An experimental investigation of NACA submerged-duct entrances', NACA ACR. 5120, 1951.

Galea, S.C., Callinan, R.J., 'An analytically validated highly damped repair for acoustically induced cracking on the F/A-18 nacelle skin.' Defence Science & Technology Organisation (Australia) Technical Report, DSTO-TR-1162, 2001.

Gault, D.E., 'A correlation of low-speed, airfoil-section stalling characteristics with Reynolds number and airfoil geometry', NACA TN 3963, 1957.

Gerhols, C.H., Clark, L.R., Biedon, R.T., 'Control of inflow distortion in a scarf inlet.' AIAA 2002-2432, 8th AIAA/CEAS Aeroacoustics Conference, Colorado, USA, 2002.

Gibb, J., Anderson, B.H., 'Vortex flow control applied to aircraft intake ducts', Paper 14, Proceeding of the RAeS High-Lift and Separation Control Conference, Bath, UK 1995.

Goldsmith, E.L., 'Forces and pressure distributions at subsonic and supersonic speeds on circular section pitot intakes', ARA Report 75, 1990.

Grotz, C.A., 'Development of the YC-14 propulsion system', AIAA-75-1314, AIAA/SAE 11th Propulsion Conference, Anaheim, CA, USA, 1975.

Hall, G.R., Hurwitz, W.M., Tiebens, G.S., Norby, W.P., Singhsinsuk, P, Wilt, C.E., 'Development of the F/A-18E/F air induction system', AIAA-93-2152, AIAA/SAE/ASME/ASEE 29th Joint Propulsion Conference, Monterey, USA 1993.

Haines. A.B., 'Scale effects on aircraft and weapon aerodynamics', AGARDograph AGARD-AG-323, 1994.

Hacker, I.G., Hirst, W., Hayward, R., Hyde, D., Goldsmith, E.L., 'Results from tests on a series of axisymmetric, isolated pitot intakes at Mach numbers from 0.21 to 2.00', ARA Model Test Note M163, 1985.

Hamstra, J.W., Miller, D.N., Truax, P.P. Anderson, B.A., Wendt, B.J., 'Active inlet flow control technology demonstration', ICAS-2000-6112, 22nd International Congress of the Aeronautical Sciences, Harrogate, UK, 2000.

Hawkins, J.E., 'YF-16 inlet design and performance', AIAA-74-1062, AIAA/SAE 10th Propulsion Conference, San Diego, CA, USA, 1974.

Herzmark, R.A., Victor, I.W., 'Propulsion compatibility considerations for engine transients during extreme manoeuvres', Proceedings of the Air Force Airframe-Propulsion Compatibility Symposium, AFAPL-TR-69-103, Ohio, USA, 1970.

Hancock, J.P., Hinson, B.L., 'Inlet development for the L-500', AIAA-69-488, AIAA 5th Propulsion Joint Specialist Conference, Colorado, USA, 1969.

Hoelmer, W., Younghans, J.L., Raynal, J.C., 'The effect of Reynolds number on upper cowl flow separation', Journal of Aircraft, Vol.24, No.3, pp161-169, March 1987

Howe, D., 'Influence of stealth requirements on aircraft design - *Aircraft Stealth Technology – course notes*' Cranfield University, 1998.

Hurd, R., 'Subsonic pitot intakes – high speed performance', Rolls-Royce (Bristol) Report PD 2029, 1976.

Hurwitz, W.M., Witcomb, K.G., 'Flight test validation of B-2 inlet/engine compatibility: a risk management approach' AIAA-97-3157, AIAA/ASME/SAE/ASEE 33rd Joint Propulsion Conference, Seattle, WA, USA, 1997.

Imfield, W.F., 'The development program for the F-15 inlet', AIAA-74-1061, AIAA/SAE 10th Propulsion Conference, San Diego, CA, USA, 1974.

Innes, F. Pearcey, H.H., Sykes, D.M., 'Improvement in the performance of a three element high lift system by the application of air jet vortex generators', Paper 25, Proceeding of the RAeS High-Lift and Separation Control Conference, Bath, UK 1995.

Jakubowski, A.K., Luidens, R.W., 'Internal cowl separation at high incidence', AIAA-75-64, 13th Aerospace Sciences Meeting, Pasadena, CA, USA, 1975.

Jones, B.M., 'The streamline aeroplane', *Journal of the Royal Aeronautical Society* Vol 33, pp.358-85, 1929.

Kuchemann, D., Weber, J., 'Aerodynamics of propulsion', pp59-98, McGraw-Hill, 1953.

Kunik, W.G., 'Application of a computational model for vortex generators in subsonic internal flows', AIAA-86-1458, AIAA/ASME/SAE/ASEE 22nd Joint Propulsion Conference, Huntsville, USA 1986.

Küpper, C., Henry, F.S., 'Numerical simulation of flow in a circular duct fitted with air-jet vortex generators', *Int. J. Numer. Meth. Fluids* 2002; 38:919-943, 2002.

Langley, M.J., 'The design of axisymmetric cowls for podded nacelles for high bypass ratio turbofan engines', ARA Report 54, 1979.

Laruelle, G., 'Air intakes: role, constraints and design', ICAS-2002-643, 23rd International Congress of the Aeronautical Sciences, Toronto, Canada, 2002.

Leyland, D.C., 'Jaguar/Tornado Intake design', VKI Lecture Series 1988-04 "Intake Aerodynamics", von-Karman Institute for Fluid Dynamics, 1988.

Leyland, D.C., 'Intake for high angle of attack', VKI Lecture Series 1988-04 "Intake Aerodynamics", von-Karman Institute for Fluid Dynamics, 1988.

Leyman, C.S., Morris, D.P., 'Concorde powerplant development', AGARD-CP-91-71, "Inlets and Nozzles for Aerospace Engines", Norway, 1971.

Lotter, K.W., Malefakis, J., 'Intake design and intake/airframe integration for a post-stall fighter aircraft', AGARD-CP-247 "High Angle of Attack Aerodynamics", Norway, 1978.

Luidens, R.W., Abbott, J.M., 'Incidence angle bounds for lip separation of three 13.97 centimetre diameter inlets', NASA TM X-3351, 1976.

McCullough, G.B., Gault, D.E., 'Examples of three representative types of airfoil-section stall at low speeds', NACA TN 2502, 1951.

McGregor, I., 'Some applications of boundary layer control by blowing to air inlets for V/STOL aircraft.' AGARD-CP-91-71, "Inlets and Nozzles for Aerospace Engines", Norway, 1971.

Martin, P.G., 'Air intakes for subsonic UCAV applications – some design considerations', Workshop on Aerodynamic Issues of Unmanned Air Vehicles, University of Bath, UK, 2002.

Miller, B.A., Abbott, J.M., 'Aerodynamic and acoustic performance of two choked flow inlets under static conditions', NASA TM X-2629, 1972.

Miller, B.A., Dastoli, B.J., Wesoky, H.L., 'Effect of entry-lip design on aerodynamics and acoustics of high throat Mach number inlets for the Quiet, Clean, Short-Haul Experimental Engine', NASA TM X-3222, 1975

Moeckel, W.E., 'Estimation of lip forces at subsonic and supersonic speeds', NACA TN 3457, 1955.

Moses, R.W., 'Fin buffeting features of an early F-22 model', AIAA-2000-1695, AIAA/ASME/ASCE/AHS/ASC Structures, Structural Dynamics and Materials Conference, Atlanta, GA, USA, 2000.

Neale, M.C., 'Aerodynamic problems of power plant installation (Part B) – mainly concerning the isolated nacelle', NGTE Misc. 185, 1970.

Neuhart, D.H., Rhode, M.N., 'Water tunnel investigation of concepts for alleviation of adverse inlet spillage effects with external stores', NASA TM 4181, 1990.

Norris, G., 'US Air Force searches for F/A-22 fin buffeting fix', *Flight International*, pp16, 15-21 October 2002.

Patilla, R.G., 'Use of a boundary layer blowing slot to improve the cross-wind performance of a pod intake.' Rolls-Royce Installation Research Report IAR.08126, 1972.

Peake, D.J., 'The use of air injection to prevent separation of the turbulent boundary layer in supersonic flow', NGTE Report R. 256, 1963, also ARC CP 890, 1966.

Peake, D.J., Tobak, M., "Three dimensional interactions and vortical flows with the emphasis on high speeds,' AGARDograph No. AG-252., 1980.

Peake, D.J., Henry, F.S., Lush, P.A., Pearcey, H.H., 'Flow control with air-jet vortex generators', Paper No. 10, RAeS Conference on Passive and Active Flow Control, London, UK, 1998.

Peake, D.J., Henry, F.S., Pearcey, H.H., 'Flow control with air-jet vortex generators', AIAA-99-3175, AIAA 17th Applied Aerodynamics Conference, Norfolk, Va, USA 1999.

Pearcey, H.H., 'The aerodynamic design of section shapes for swept wings', "Advances in Aeronautical Sciences (Vols 3-4)", pp 277-321, Pergamon Press, 1961.

Pearcey, H.H., "Shock induced separation and its prevention by design and boundary-layer control", "Boundary Layer and Flow Control", Ed. Lachmann, pp1166-1343, Pergamon Press, 1961.

Philpot, M.G., 'Future challenges for powerplant aerodynamic integration in combat aircraft', ICAS-2000-6.11.1, 22nd International Congress of the Aeronautical Sciences, Harrogate, UK, 2000.

Pitt, D.M., Dunne, J.P., White, E.V., Garcia, E., 'SAMPSON Smart Inlet SMA powered adaptive lip design and static test' AIAA-2001-1359, 42nd Structures, Structural Dynamics and Materials Conference, Seattle, WA, USA, 2001.

Podleski, S.D., 'F/A inlet calculations at 60-deg angle of attack and 10-deg sideslip.' *Journal of Propulsion and Power*, Vol.10, No.6, pp 845-854, Nov.-Dec.1994.

Podleski, S.D., Smith, C.F., Barankiewicz, W.S., 'Comparison of the F/A-18A high alpha research vehicle inlet flow analysis results with flight data: Part II (with sideslip)', AIAA-95-2756, 31st AIAA/ASME/SAE/ASEE Joint Propulsion Conference and Exhibit, San Diego, CA, USA, 1995.

'Report of the Definitions Panel on the definitions of the thrust of a jet engine and of the internal drag of a ducted body', Aeronautical Research Council, CP 190, 1955.

Re, R.J., 'An investigation of several NACA 1-Series axisymmetric inlets at Mach numbers from 0.4 to 1.29', NASA TM X-2917, 1974.

Re, R.J., 'An investigation of several NACA 1-Series inlets at Mach numbers from 0.4 to 1.29 for mass-flow ratios near 1.0', NASA , TM X-3324, 1975.

Re, R.J., Abeyounis, W.K., 'Wind tunnel investigation of three axisymmetric cowls of different lengths at Mach numbers from 0.6 to 0.92', NASA TM 4488, 1993.

Roberts, W.B., 'Calculation of laminar separation bubbles and their effect on airfoil performance', AIAA-79-0285, 17th AIAA Aerospace Science Meeting, New Orleans, La, 1979.

Robinson, Russell G., Becker, John V., 'High speed tests of conventional radial-engine cowlings', NACA Report. 745, 1942.

Rodriguez, D.L., 'A multidisciplinary optimization method for designing boundary layer ingesting inlets', AIAA 2002-5665, Symposium on Multidisciplinary Analysis and Optimisation, Atlanta, GA, USA, 2002.

Ross, J.A., McGregor, I., Priest, A.J., 'Some RAE research on shielded and unshielded fuselage mounted intakes at subsonic and supersonic speeds.' Paper 3, AGARD-CP-301 " Aerodynamics of Powerplant Installation", 1981.

Schwetzler, D., 'Improvement of maximum lift in flight by optimisation of vortex flow', Paper 4, Proceeding of the RAeS High-Lift and Separation Control Conference, Bath, UK 1995.

Slotnick, J.P., An., M.Y., Mysko, S.J., Yeh, D.T., Rogers, S.E., Roth, K., Baker, M.D., Nash, S.M., 'Navier-Stokes analysis of a high wing transport high-lift configuration with externally blown flaps', AIAA-2000-4219, AIAA 18th Applied Aerodynamics Conference, Denver, CO, USA, 2000.

Seddon, J., Goldsmith, E.L., 'Intake Aerodynamics', pp66-102,307-335, 2nd Edition, Blackwell, 1999.

Stanhope, F.W., 'The performance of NACA 1 intakes', Powerplant Research Report IAR 85002, Rolls-Royce, 1968.

Stockman, N.O., 'Potential and viscous flow in VTOL, STOL or CTOL propulsion system inlets', AIAA-75-1186, AIAA/SAE 11th Propulsion Conference, Anaheim, CA, USA, 1975.

Stocks, C.P., Bissinger, N.C., 'The design and development of the Tornado engine air Intake', Paper 10, AGARD-CP-301 "Aerodynamics of Powerplant Installation", 1981.

Theodoresen, T., Brevoort, M.J., Stickle, G.W., 'Full-scale tests of NACA cowlings', NACA Report 592.

Tindell, R.H., Hoelzer, C.A., Alexander, D., 'F-14 inlet development experience', ASME Paper 82-GT-5, ASME Gas Turbine Conference, Wembley, London, UK 1982.

Tokaty, G.A., 'A history and philosophy of fluid mechanics', pp82-85, Dover Publications, Inc., 1971.

Van den Berg, B., 'Role of laminar separation bubbles in airfoil leading edge stalls', AIAA Journal, Vol.19, pp553-556, No.5, 1981.

Wallis, R.A., 'The use of air jets for boundary layer control' Aeronautical Research Laboratory, Australia, Aerodynamics Note 110, 1952.

Walsh, K., Steenken, W., Williams, J., 'Summary of inlet characteristics of the F/A-18A high alpha research vehicle', AIAA-98-3713, AIAA/ASME/SAE/ASEE 34th Joint Propulsion Conference, Cleveland, OH, USA, 1998.

Wilmer, A.C., Brown, T.W., Goldsmith, E.L., 'Effects of intake geometry on circular pitot intake performance at zero and low forward speed', Paper 5, AGARD-CP-301 "Aerodynamics of Powerplant Installation", 1981.

Williams, M.J., 'Propulsion integration aerodynamic technology for buried engines', Presentation to Rolls-Royce (Derby), 2003.

Young, A.D., Horton, H.P., 'Some results of investigations of separation bubbles', Queen Mary College Report, University of London.

Youghans, J.L., Hoelmer, W., Stockman, N.O., 'Low speed effects of Reynolds number and lip geometry on high bypass ratio inlet performance', AIAA-82-0059, 20th Aerospace Sciences Meeting, Orlando, FL, USA 1982.

Yuhas, A.J., Steenken, W.G., Williams, J.G., Walsh, K.R., 'F/A-18A inlet flow characteristics during manoeuvres with rapidly changing angle of attack', NASA TM-104327, 1997.

3. Numerical Methods

3.1. Introduction

Computational fluid dynamics provides an approximation to the analytical solution of the governing equations of fluid motion, the Navier-Stokes equations. The integral or differential terms, depending on the form of the equations used, are replaced with discretised algebraic forms that are solved to obtain values for the flow variables at discrete points in time and space. In addition, the effects of turbulence, which are too complex to be solved mathematically at an appropriate scale, are modelled using statistical techniques. These approximations may lead to inaccuracies in the solution. The quality and fidelity of the computational mesh on which the solution is to be obtained may introduce further errors or uncertainties. In general, many of these uncertainties may be considered problem specific and it is important to validate the computational model against experimental data to try to remove as many possible sources of error. In some cases, it may not be possible to achieve absolute accuracy at an affordable cost. It is therefore necessary to balance the expected solution accuracy with the resources required and use further models to enhance the numerical solution. This is the case for determining dynamic (time-dependent) intake distortion. In this case, an unsteady solution would be required, ranging over a minimum of one period of the lowest frequency distortion source with a time step small enough to achieve accurate resolution of the required high frequency source. This would lead to an enormous requirement of CPU time and data storage. In reality, it is often easier to infer dynamic data from a single RANS solution (*Benek, Kraft & Lauer, 1998*).

At other times, the prediction of trends or increments, rather than absolute values, may be acceptable; for example, during design trade off studies or for obtaining throttle dependent drag effects (*Williams, 2003*).

A further consideration is choosing a solution method or algorithm that is appropriate for modelling the expected flow physics. This may be interpreted in several ways. A potential flow solver assuming steady, inviscid, irrotational and isentropic flow will be wholly unsuitable for modelling the highly separated flow over a swept wing military aircraft at incidence. The expected flow physics is not compatible with the

assumptions made in the solver. At a different level, a full Reynolds-averaged Navier-Stokes (turbulent) model will be inappropriate for determining the correct level of viscous drag on a laminar flow nacelle, if no information is available about the transition location. This is currently beyond the scope of practical turbulence models.

With the continued and rapid development in computer hardware, as well as the reduction in relative cost of the computing power required to obtain a solution, RANS CFD analysis is becoming more affordable and available. In Europe, there is currently a drive towards achieving accepted quality standards. The European Research Community on Flow Turbulence and Combustion (ERCOFTAC) has completed a treatise on CFD best practice (*ERCOFTAC, 2000*). In this document, possible sources of error and uncertainty in CFD methods are discussed and it is recommended to the reader for further information. Relevant sources of error will be discussed within this thesis in the appropriate sections.

3.2. The Navier-Stokes Equations

The governing equations of fluid motion are referred to as the Navier-Stokes equations. This set of coupled second-order partial differential equations is based on the three fundamental principles of mass conservation, Newton's second law in three directional components and the conservation of energy. In modern technical literature, the complete set of governing equations of fluid motion are termed the Navier-Stokes equations, although, historically, it is only the equations based on Newton's second law that are named after their co-originators.

The equations may be derived by considering a finite control-volume located within the fluid that is enclosed by a control surface. If this control volume is fixed in space allowing the fluid to pass through it, the derivation leads to the 'conservation' form of the equations. If the control volume is considered to move in space, such that the same fluid particles are always contained within it, the derivation leads to the non-conservation form of the equations. In both examples, the three principles stated above are applied to the fluid within the control volume and the fluid passing through the bounding surface. The conservation form of the Navier-Stokes equations is the most widely used in modern aeronautical CFD. This is because all of the equations

may be expressed in the same generic form in terms of flux vectors, where the dependent variables are combinations of the primary variables. This approach is particularly advantageous to high-speed computations, as the flux variables are continuous across shock waves. Full derivations of the Navier-Stokes equations may be found in *Anderson (1995)*. For discussion purposes, the Navier-Stokes equations will be written in the following form, starting with continuity of mass:

$$\frac{\partial \rho}{\partial t} + \nabla \cdot (\rho V) = 0 \quad \text{Equation 3-1}$$

The momentum equations, in three Cartesian components, are:

$$\frac{\partial(\rho u)}{\partial t} + \nabla \cdot (\rho u V) = -\frac{\partial p}{\partial x} + \frac{\partial \tau_{xx}}{\partial x} + \frac{\partial \tau_{yx}}{\partial y} + \frac{\partial \tau_{zx}}{\partial z} + \rho f_x \quad \text{Equation 3-2}$$

$$\frac{\partial(\rho v)}{\partial t} + \nabla \cdot (\rho v V) = -\frac{\partial p}{\partial y} + \frac{\partial \tau_{xy}}{\partial x} + \frac{\partial \tau_{yy}}{\partial y} + \frac{\partial \tau_{zy}}{\partial z} + \rho f_y \quad \text{Equation 3-3}$$

$$\frac{\partial(\rho w)}{\partial t} + \nabla \cdot (\rho w V) = -\frac{\partial p}{\partial z} + \frac{\partial \tau_{xz}}{\partial x} + \frac{\partial \tau_{yz}}{\partial y} + \frac{\partial \tau_{zz}}{\partial z} + \rho f_z \quad \text{Equation 3-4}$$

Here τ represents the viscous stresses acting on the fluid element and f the body forces per unit mass.

Finally, conservation of energy may be expressed as:

$$\begin{aligned} \frac{\partial}{\partial t} \left[\rho \left(e + \frac{V^2}{2} \right) \right] + \nabla \cdot \left[\rho \left(e + \frac{V^2}{2} \right) V \right] &= \rho \dot{q} + \frac{\partial}{\partial x} \left(k \frac{\partial T}{\partial x} \right) + \frac{\partial}{\partial y} \left(k \frac{\partial T}{\partial y} \right) + \frac{\partial}{\partial z} \left(k \frac{\partial T}{\partial z} \right) - \frac{\partial (up)}{\partial x} \\ &- \frac{\partial (vp)}{\partial y} - \frac{\partial (wp)}{\partial z} + \frac{\partial (u\tau_{xx})}{\partial x} + \frac{\partial (u\tau_{yx})}{\partial y} + \frac{\partial (u\tau_{zx})}{\partial z} + \frac{\partial (v\tau_{xy})}{\partial x} + \frac{\partial (v\tau_{yy})}{\partial y} + \frac{\partial (v\tau_{zy})}{\partial z} + \frac{\partial (w\tau_{xz})}{\partial x} \\ &+ \frac{\partial (w\tau_{yz})}{\partial y} + \frac{\partial (w\tau_{zz})}{\partial z} + \rho f \cdot V \end{aligned}$$

$$\text{Equation 3-5}$$

This equation may be considered to consist of three separate components, where the left-hand side is the rate of change of energy inside the fluid element. The right-hand side consists of terms relating to the net flux of heat into the element (those containing the thermal conductivity k , and the volumetric heat addition per unit mass \dot{q}) and terms relating to work done on the element due to body and surface forces.

For a Newtonian fluid, the shear stress in a fluid is proportional to the velocity gradient. Hence, all the shear stress terms may be written in terms of the velocity components.

$$\tau_{xx} = \lambda(\nabla \cdot V) + 2\mu \frac{\partial u}{\partial x} \quad \text{Equation 3-6}$$

$$\tau_{yy} = \lambda(\nabla \cdot V) + 2\mu \frac{\partial v}{\partial y} \quad \text{Equation 3-7}$$

$$\tau_{zz} = \lambda(\nabla \cdot V) + 2\mu \frac{\partial w}{\partial z} \quad \text{Equation 3-8}$$

$$\tau_{xy} = \tau_{yx} = \mu \left[\frac{\partial v}{\partial x} + \frac{\partial u}{\partial y} \right] \quad \text{Equation 3-9}$$

$$\tau_{xz} = \tau_{zx} = \mu \left[\frac{\partial w}{\partial z} + \frac{\partial u}{\partial x} \right] \quad \text{Equation 3-10}$$

$$\tau_{yz} = \tau_{zy} = \mu \left[\frac{\partial w}{\partial y} + \frac{\partial v}{\partial z} \right] \quad \text{Equation 3-11}$$

where λ is the second viscosity coefficient and for gases is approximated as:

$$\lambda = -\frac{2}{3}\mu \quad \text{Equation 3-12}$$

The equations form a coupled system of non-linear partial differential equations. As there are more variables than equations, it is necessary to introduce two equations of state for pressure and internal energy, assuming thermodynamic equilibrium.

The ideal gas equation:

$$p = \rho RT \quad \text{Equation 3-13}$$

Calorific equation of state:

$$e = c_v T \quad \text{Equation 3-14}$$

Due to the complex nature of these equations, no closed form solution is possible for practical applications. For CFD purposes, the equations must be discretised, a process whereby the partial derivatives are replaced by numerical expressions. This implies the problem relating to the exact continuous solution has been replaced by one at discrete points. FLUENT, the CFD software used in this study uses a finite volume discretisation. This method is discussed in the next section.

3.3. The finite volume method

The finite volume method is based around the integration of the governing equations over a finite control volume to yield discretised equations at its nodal points (*Versteeg & Malalasekera, 1999*). The nodal points are then related using a suitable interpolation procedure.

Because of the similarities of all the governing equations, it is possible to consider the Navier-Stokes equations in general transport form, in which the unknown variable ϕ is used to represent either u, v, w or e for the energy equation, with the remaining terms enclosed within the source term S . This takes the form:

$$\frac{\partial(\rho\phi)}{\partial t} + \frac{\partial(\rho u\phi)}{\partial x} + \frac{\partial(\rho v\phi)}{\partial y} + \frac{\partial(\rho w\phi)}{\partial z} = \frac{\partial}{\partial x} \left[\Gamma \frac{\partial\phi}{\partial x} \right] + \frac{\partial}{\partial y} \left[\Gamma \frac{\partial\phi}{\partial y} \right] + \frac{\partial}{\partial z} \left[\Gamma \frac{\partial\phi}{\partial z} \right] + S$$

$$\text{Equation 3-15}$$

Γ is the diffusion coefficient used in the equation under consideration. Alternatively, using the velocity vector V , to shorten the expression:

$$\frac{\partial(\rho\phi)}{\partial t} + \nabla \cdot (\rho V)\phi = \nabla \cdot (\Gamma \nabla \phi) + S \quad \text{Equation 3-16}$$

Integrating the general transport equation over a control volume of surface area, S , and volume, Ω , and using the divergence theorem to relate volume integrals to surface integrals, we have:

$$\frac{\partial}{\partial t} \int_{\Omega} (\rho\phi) d\Omega + \oint_s (\rho V)\phi \cdot d\vec{S} = \oint_s (\Gamma \nabla \phi) \cdot d\vec{S} + \int_{\Omega} S d\Omega \quad \text{Equation 3-17}$$

The four terms in this transport equation relate to four different physical processes by which a variable at the control volume may change, the first term being the transient change due to the other three terms. The second term from the left-hand side is the convection through the face of the control volume. The third term is the diffusion across the face of a volume and the final term is the generation or destruction within a volume. This formulation has the advantage that it allows a different numerical algorithm to be used for each of the processes being represented (*Rubini, 1996*). The Fluent finite volume approach uses a cell-centred formulation, where the volume integrals are constructed using the average property values located at the cell centre. Face values, required for the convection term, must be interpolated from the cell centre values. Fluent accomplishes this using an upwind differencing scheme that may be selected by the user. In this study, second order upwind differencing has been used. The diffusion term is always modelled using a second order accurate central difference formulation.

Figure 3.1 shows the terminology used in the following description of the finite volume method. For simplicity, a one-dimensional approach is presented. The nodal point of the control volume or ‘cell’ under scrutiny is P. The nodal points to the left (West) and right (East) are W and E respectively. The control volume faces are located at e and w.

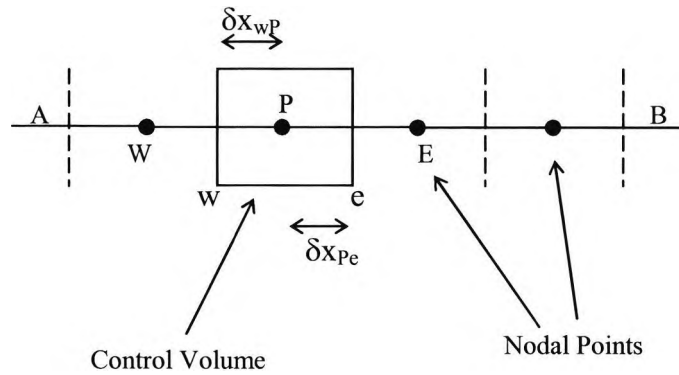


Figure 3-1: Finite volume notation

The physical interpretation of the finite difference method based on Equations 3-16 and 3-17 equates the change of a property within a volume to the convection and diffusion across the volume surface. For a one-dimensional problem, such as that illustrated in Figure 3.1, the surface of the volume may be considered as two discrete faces, east (e) and west (w) of the volume central point (P). To illustrate the technique, the one-dimensional steady-flow convection/diffusion equation for an arbitrary transport variable ϕ is used.

$$\frac{\partial}{\partial x}(\rho u \phi) = \frac{\partial}{\partial x} \left(\Gamma \frac{\partial \phi}{\partial x} \right) \quad \text{Equation 3-18}$$

Integrating this equation over the control volume in Figure 3-1 yields:

$$(\rho u A \phi)_e - (\rho u A \phi)_w = \left(\Gamma A \frac{\partial \phi}{\partial x} \right)_e - \left(\Gamma A \frac{\partial \phi}{\partial x} \right)_w \quad \text{Equation 3-19}$$

Here A represents the area of the cell face. In finite volume notation, it is traditional to represent the convective mass flux and diffusive flux as two distinct variables for simplicity. Here, they will be referred to as G and D respectively.

$$G = \rho u \quad \text{Equation 3-20}$$

$$D = \frac{\Gamma}{\delta x} \quad \text{Equation 3-21}$$

The property ϕ and the diffusion coefficient are defined at the cell centre nodal points, E, P, W. To calculate the property spatial gradients at the cell faces for the diffusion terms, first order central differencing (linear interpolation) is used here to minimise the number of cells required for illustration. First-order central differencing between the nodal points is also used to evaluate convective terms across the cell faces. Substituting the central difference expressions into Equation 3-19 and assuming the faces are of equal area gives:

$$\frac{G_e}{2}(\phi_E + \phi_P) - \frac{G_w}{2}(\phi_P + \phi_W) = D_e(\phi_E - \phi_P) - D_w(\phi_P - \phi_W) \quad \text{Equation 3-22}$$

This expression may be rearranged into a form relating to the central nodal point, P,

$$a_P \phi_P = a_W \phi_W + a_E \phi_E \quad \text{Equation 3-23}$$

The coefficients are:

$$a_W = D_w + \frac{G_w}{2} \quad \text{Equation 3-24}$$

$$a_E = D_e - \frac{G_e}{2} \quad \text{Equation 3-25}$$

$$a_P = a_W + a_E + (G_e - G_w) \quad \text{Equation 3-26}$$

The expression in Equation 3-22 is then constructed for all nodal points within the domain to provide a set of algebraic equations that describe the variation of the transport variable ϕ within the domain.

The use of finite-difference schemes for approximating the fluid properties at a point in space or time, as shown above, raises three primary concerns. The first is accuracy, the second is stability, and the third validity, to the flow physics being approximated.

For use in CFD, the accuracy of a differencing scheme is a trade-off between solution fidelity and run time (and, hence computational cost). A higher-order scheme may provide a more detailed solution, for example, shock clarity in supersonic flows. However, a higher order scheme will be more computationally costly, as more information is required to calculate the variables at each node. Second-order spatial accuracy has become the accepted standard in most applications (Anderson, 1995).

The stability of a difference scheme is a measure of the propagation of numerical errors throughout the course of the calculation. If the errors increase in magnitude, then the calculation will become unstable. If the errors are damped out, the calculation is stable. The two main sources of errors in CFD calculations are truncation errors and round-off errors. Truncation errors arise due to the differencing scheme being of insufficient accuracy; and round-off errors, as the name suggests, are due to the rounding of numbers within the calculation.

The third factor affects the applicability of differencing schemes to certain flow types and relates to the stability. This can be considered as how the nodal point receives computational information referenced to the characteristic directions in the flow field. For example, in supersonic flow, information can only be passed downstream. An upwind scheme in which the nodal point uses upstream values to calculate the variable is more appropriate than a central difference scheme in which downstream information is also required. Further information on different types of differencing schemes and stability analysis is presented by *Anderson (1995)* and by *Versteeg & Malalasekera (1999)*.

3.4. Turbulence closure

Most flows of engineering importance, particularly those of high Reynolds number experienced in aeronautics, are turbulent. Turbulence is a chaotic and random state of

motion in which the velocity and pressure vary continuously with time (*Versteeg & Malalasekera, 1999*). Direct numeral simulation (DNS) of the time dependant Navier-Stokes equations using time intervals small enough to resolve velocity fluctuations of all frequencies in the flow is extremely computationally expensive and impractical for any realistic engineering configuration. In most cases, however, the mean flow properties are more than adequate for engineering analysis and an alternative approach is adopted, whereby the Navier-Stokes equations are replaced by time-averaged versions. This form of the equations is known as the Reynolds-Averaged Navier-Stokes (RANS) equations. The Reynolds decomposition, which uses a time averaging procedure, replaces the time dependent variable with the sum of two components, a mean steady state value and a time dependent fluctuating component with a mean value of zero. For example, the three velocity components become:

$$U = \bar{U} + u', \quad V = \bar{V} + v', \quad W = \bar{W} + w' \quad \text{Equation 3-27}$$

The time average of the fluctuating component must be zero, so assuming the period of integration large compared with the period of the random fluctuations of the property, we have using the first velocity component:-

$$\bar{u}' = \frac{1}{t} \int_{t_0}^{t_0+t} u' dt = 0 \quad \text{Equation 3-28}$$

Applying this procedure of replacing the flow variables by a mean and fluctuating component to the Navier-Stokes equations results in six unknown terms. These terms are turbulent stresses containing the fluctuating velocity components and are termed Reynolds Stresses. These comprise three normal stresses and three shear stresses. The normal stresses are:

$$\tau_{xx} = -\overline{\rho u'^2} \quad \tau_{yy} = -\overline{\rho v'^2} \quad \tau_{zz} = -\overline{\rho w'^2} \quad \text{Equation 3-29}$$

The shear stresses are:

$$\tau_{xy} = \tau_{yx} = -\overline{\rho u'v'} \quad \tau_{xz} = \tau_{zx} = -\overline{\rho u'w'} \quad \tau_{yz} = \tau_{zy} = -\overline{\rho v'w'} \quad \text{Equation 3-30}$$

In order to close the RANS equations, a turbulence model is needed to approximate the Reynolds stresses. Wilcox (2001) categorises 4 types of turbulence model for closure of the RANS equations. They are

- Algebraic models
- One-Equation models
- Two-equation models
- Stress transport models

Algebraic models are based on the Boussinesq assumption that expresses the Reynolds stresses as a product of the turbulent viscosity and the velocity gradients (strain rates). This is analogous to the interpretation of the viscous stresses in laminar flow, which uses the fluid viscosity. An extended form is used in some two-equation models, in which an additional term on the far right hand side incorporates the Kronecker delta, δ_{ij} , and is used to make the expression valid for normal shear stress. δ_{ij} takes a value of zero unless the Reynolds stress in question is normal, *i.e.* $i=j$, when its value is unity.

$$-\overline{\rho u_i' u_j'} = \mu_t \left(\frac{\partial \overline{U}_i}{\partial x_j} + \frac{\partial \overline{U}_j}{\partial x_i} \right) - \frac{2}{3} \delta_{ij} \rho k \quad \text{Equation 3-31}$$

k is the turbulent kinetic energy.

Using dimensional considerations, the turbulent viscosity, μ_t , may be expressed as proportional to the product of the density, a characteristic length scale based on the size of the larger turbulent motions and a turbulent viscosity scale:

$$\mu_t \propto \rho l V_t \quad \text{Equation 3-32}$$

Algebraic turbulence models calculate V_t and l based on flow parameters such as the velocity difference across a shear layer (V_t) or a fraction of the hydraulic diameter for pipes flows (l). Although these methods are relatively simple, they have a number of major limitations: they are only valid for attached flows and the calculation of turbulence parameters is entirely local. *i.e.* the state of turbulence is not related to the

flow's upstream history. In addition, the extraction of the parameters needed for the calculation of V_t and l is not particularly easy for Navier-Stokes codes. No algebraic models were used in this study.

One-equation models are again based upon the Boussinesq hypothesis. However, V_t and l are determined separately. The turbulent velocity scale, V_t , may be related to the turbulent kinetic energy, k , resulting in a transport equation for k , in which the Reynolds stresses are again replaced using the Boussinesq procedure. This allows a historical element of the flow to be accounted for. The one equation model of *Spalart & Allmaras (1992)* which solves a transport equation for the turbulent viscosity was used exclusively in this study. It will be discussed in the next section.

Two-equation models solve an additional transport equation, to determine the length scale in addition to the velocity scale. In the case of the k- ϵ model, this is for ϵ , the rate of dissipation of turbulent kinetic energy. Many forms of two equation model have been proposed, the primary difference between them being the formulation of ϵ or ω . The k- ω model solves for ω in addition to k. ω is the rate of dissipation per unit turbulent kinetic energy (ϵ/k). The standard form of k- ϵ model suggests:

$$\epsilon = C_\mu \frac{k^{3/2}}{l} \quad \text{Equation 3-33}$$

Here C_μ is a constant. Several forms of two-equation model were evaluated (see section 3.7) but were not used in the study. Two equation models do not require any geometric or flow regime dependent input (*ERCRAFTAC, 2000*).

Stress transport or second moment closure models solve a transport equation for each Reynolds stress component rather than using the eddy-viscosity formulation. This introduces a further six coupled equations into the Navier-Stokes set as well as an additional equation for ϵ . As a result, calculations based on these methods are very computationally expensive. Although a model of this nature was available in Fluent, it was not evaluated for this reason.

The reader is recommended to read the book by Wilcox (2001) for a detailed description of a number of turbulence models and Talapurkara (1996) for a review including validation studies of models with particular application to aeronautical flows.

The *Spalart-Allmaras* turbulence model is a one-equation model based around a transport equation for a modified form of turbulent kinematic viscosity. This is identical to the normal form of kinematic viscosity except in the near-wall region.

The model includes eight closure coefficients and three damping coefficients. For this class of model, it is not necessary to calculate the length scale related to the thickness of the local shear layer as is the case with other one-equation models. The model has been designed with aerospace, particularly aerofoil applications in mind. For these types of flow, the model demonstrates unrivalled performance. However, it has been shown to be lacking with regard to some types of flows, for example predicating the spreading rates of jets (Wilcox, 2001). The original form of the model was published by the AIAA (*Spalart & Allmaras, 1992*). The interpretation used by the Fluent code, which contains modifications to counter highly skewed meshes, is described in the user manual (Fluent, 2000).

3.5. Grid Generation

3.5.1. SAUNA multi-block mesh

Multiblock grid generation was conducted using the SAUNA grid generation system (*QinetiQ, 2001*). This enables multiple grids to be generated for a single topology, whilst preserving block structure, overall grid dimensions and point spacing. New grids are created by changing the number of points within the individual blocks. The relationship of the relative positions and orientations of the blocks in a multi-block mesh is governed by the topology. The SAUNA topology generation program, *topgen*, describes geometric components as a series of topological entities such as planes, cubes and nacelles (Figure 3.2).

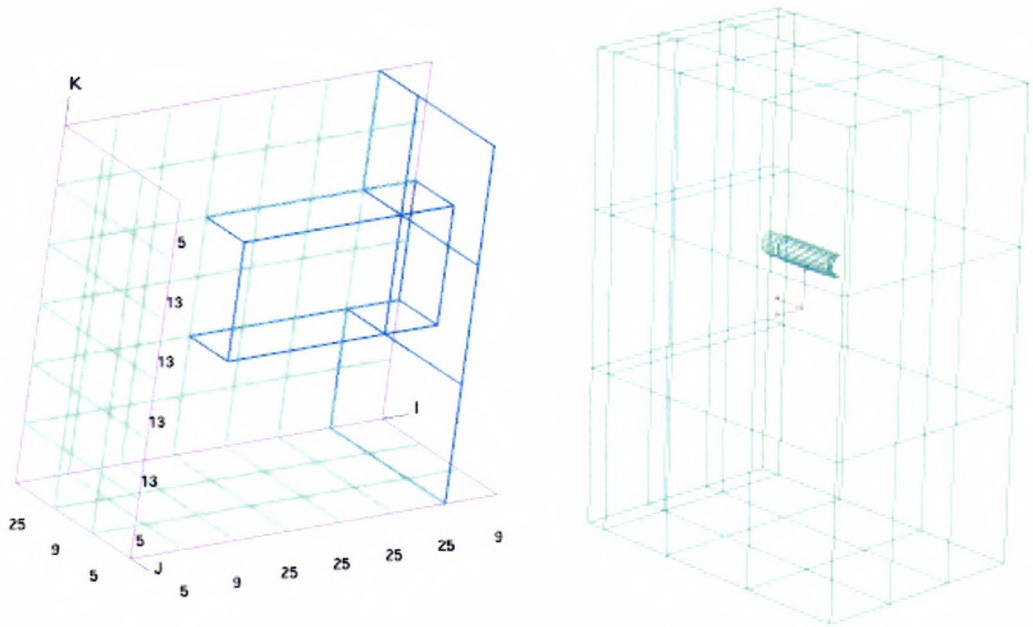


Figure 3-2: SAUNA nacelle topology (left) and flow domain (right)

For computational efficiency, only half the intake was modelled. The half intake was mounted on a symmetry plane with the duct extending out the exterior flow domain. The far-field boundaries were located sufficiently far away from the intake in topological space. Physical locations of components are fixed in the surface grid generation. The far-field boundaries were located approximately ten maximum intake diameters from the entry plane. A geometric extension was added downstream of the engine face, a single engine-face diameter in length to remove boundary-condition interference effects from the engine face. The half-nacelle geometry was split into three individual nacelle components, comprising external surface, internal surface and internal extension. These three components were each split into three further components, representing the top, side and bottom of the topological nacelle.

A major benefit of the multi-block technique is the ability to create grids local to each component of a complex configuration in a curvilinear nature to form ‘O’ or ‘C’ grids around the component. This is known within the SAUNA system as component adaptive topology. This technique leads to higher quality meshes by following the geometric surface, thus maintaining grid lines parallel and normal to the surface. The component adaptive topology for the intake model uses a C-grid, which extends from the external downstream boundary around the lip and on to the internal downstream

boundary. The C-grid follows the intake spanwise curvature in an O-grid form (Figures 3.3 & 3.4).

The SAUNA grid generation procedure requires a surface mesh to be generated on all geometric and boundary components. A field grid is then generated from the surface grids. Grid refinement for use with Navier-Stokes is then implemented by a third program.

The surface grids are generated by solving a coupled set of non-linear, elliptic, partial differential equations. These equations provide natural clustering towards convex surfaces, such as rounded leading edges. Source terms are used to further enhance mesh distribution. These are calculated from the point distributions on the edges of the surfaces that are defined by user input. The elliptic partial differential equations are solved using a multi-grid technique with line relaxation employed as a smoother. The internal block boundaries and line distributions may be edited manually if sufficient quality is not achieved. The block-structured volume grid generator (FGRID) solves a further set of partial differential equations to obtain the field grid. Finally, the Navier-Stokes grid generator, NSGRID, solves algebraic equations to refine blocks within the field grid, which lie on specified components.

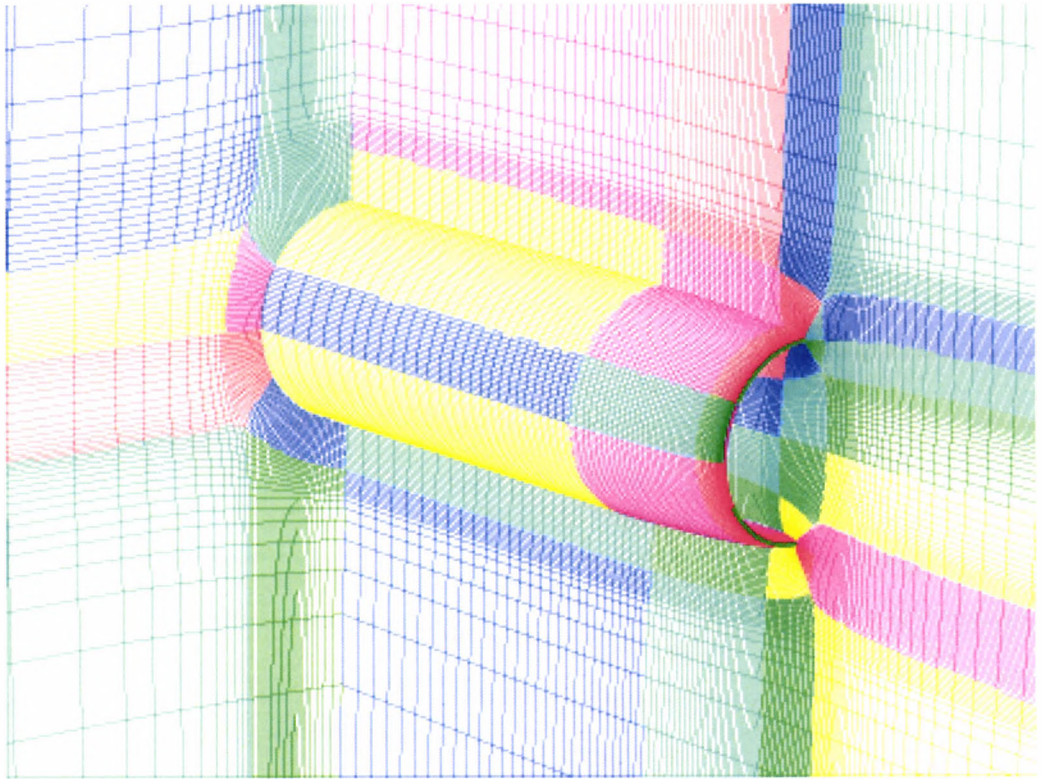


Figure 3-3: SAUNA Multi-block surface grids on SYM, ODNS and COWL

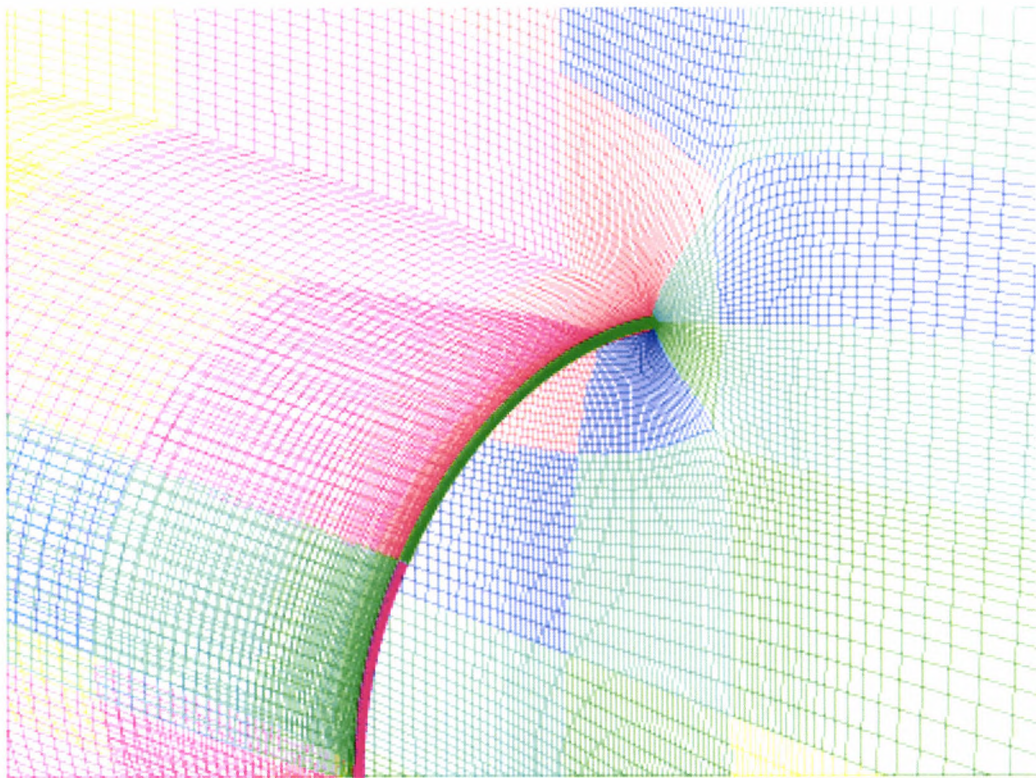


Figure 3-4: Leading edge C-grid detail-Euler grid

3.5.2. Unstructured Prism/tetrahedral mesh

Fully unstructured grids were used to model AJVG configurations. Tetrahedral meshes were generated which used prism layers on the model surfaces to capture viscous effects. For this purpose, ICEM was chosen (*ICEM CFD, 1999*). ICEM is a suite of commercial CFD pre-processing software that enables the generation of multi-block hexahedral or unstructured tetrahedral meshes on complex geometry. A geometry source may be generated within the software, or imported from an external CAD system. In this study, geometry was imported from the SAUNA pre-processor to ensure continuity. The geometry is then manipulated within the ICEM mesh editor (MED) and an external domain defined. To generate a tetrahedral mesh, tetrahedral sizes are specified on the surfaces and curves defining the model geometry. To enable efficient grid clustering in regions of interest, it may be necessary to split the surfaces into sub-components, specifying the size on each. Specifying volumes within the domain and assigning them a maximum tetrahedral size may provide additional control of grid density. A tetrahedral size is also specified for the main domain volume. The tetrahedral mesh is generated by ICEM specifying a single tetrahedron that encloses the whole geometry; this is then repeatedly split until all surface size constraints are met. Nodes are rounded to curves and surfaces to make the mesh conformal with the geometry. The unwanted mesh, for example that enclosed within solid bodies, is cut away and discarded. Finally, the mesh is smoothed by moving or merging nodes and deleting poor quality elements. As a result of this process, the surface mesh is generated. An example surface mesh is shown in Figure 3.5.

To enable resolution of surface boundary layers, prismatic layers can be grown from the surface mesh, using ICEM PRISM. The user specifies the number of layers, first cell height, expansion ratio and an expansion function. As prism layers are grown from the surface, the existing tetrahedral volume mesh is squashed, which can reduce the grid quality. Although the tet/prism process is semi-automated, intelligent-user input is required to generate a grid of high quality. The final prism layer needs to be matched in size to the local tet size for continuity. An example of this type of grid around an intake lip is shown in Figure 3.6.

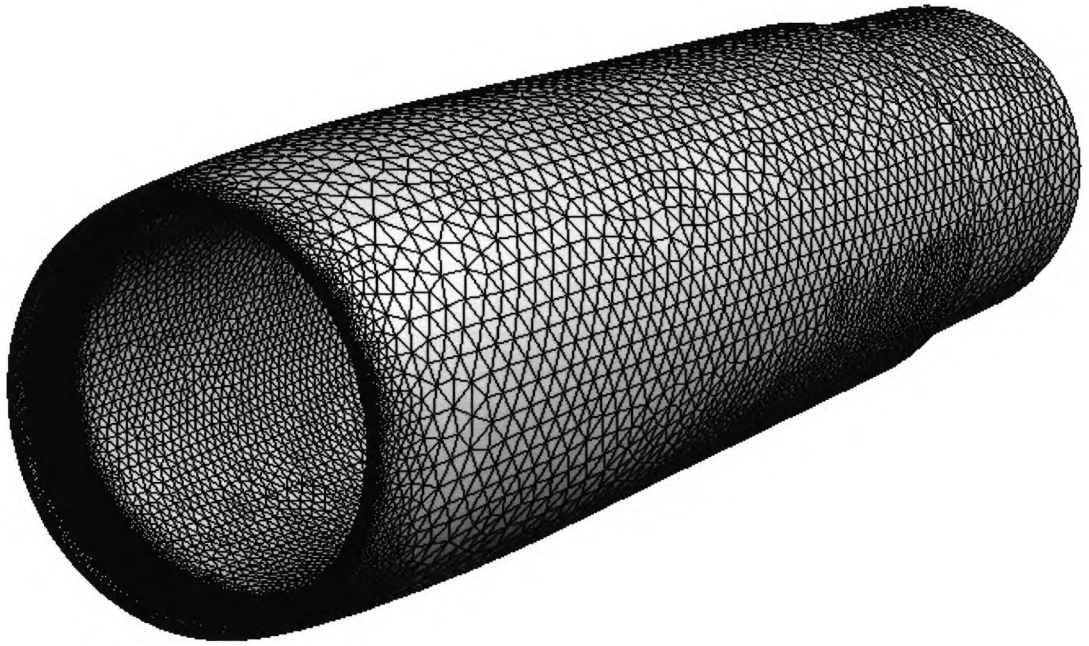


Figure 3-5 : Example ICEM Tetra surface mesh

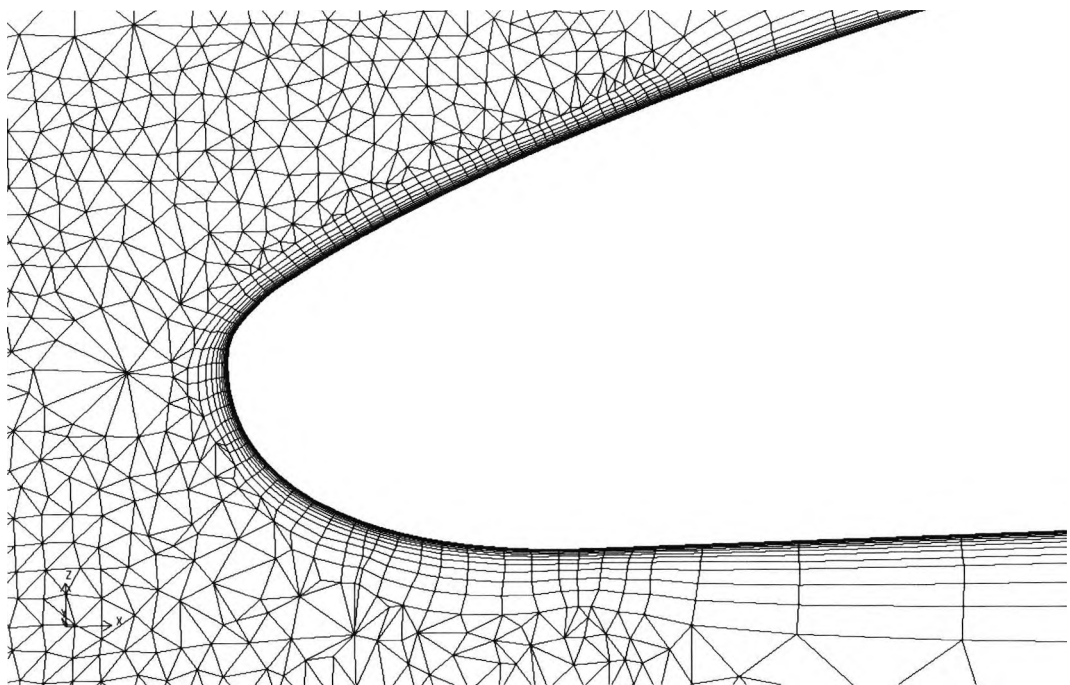


Figure 3-6: Example prism/tet grid around leading edge

3.6. Flow solver

3.6.1. FLUENT commercial CFD software

FLUENT Version 5.0 (*Fluent, 2001*) and onwards consists of an amalgamation of two different solver types, a coupled solver and a segregated solver, within one graphical user interface (GUI). The segregated solver was used for this study because of its faster convergence and its greater suitability to the low Mach number flows that will be encountered (*McGuirk & Page, 1994*).

3.6.2. SIMPLE

The Fluent code is a collection of solvers that have been amalgamated into a single package. Consequently, it is possible to choose the type of solver to suit a particular application. The coupled solver solves the continuity and momentum equation together and is based on a scheme similar to Roe's (Prince, Williams & Edwards, 2001). These equations can then be solved in either an implicit or an explicit manner. Alternatively, a segregated solver is available which solves the continuity and momentum equations separately. This solver has been demonstrated to be at least as accurate as the coupled solver for transonic aeronautical applications, when a second order density discretisation is used (Fluent News, 2002).

The primary segregated solver used in Fluent is based on the SIMPLE (Semi-Implicit Method for Pressure Linked Equations) algorithm described by Patankar (1980). The SIMPLE algorithm uses an iterative process based on guessed velocity components to compute the convective fluxes through the cell faces. A guessed pressure field is then used to solve the momentum equations and the continuity equation, in the form of a pressure correction equation. This is then used to determine a pressure correction field that is used to update the pressure and velocity fields (Versteeg & Malalasekera, 1999). A flow chart for the SIMPLE solution procedure is displayed in Figure 3-7. Second-order discretisation schemes were used for all equations.

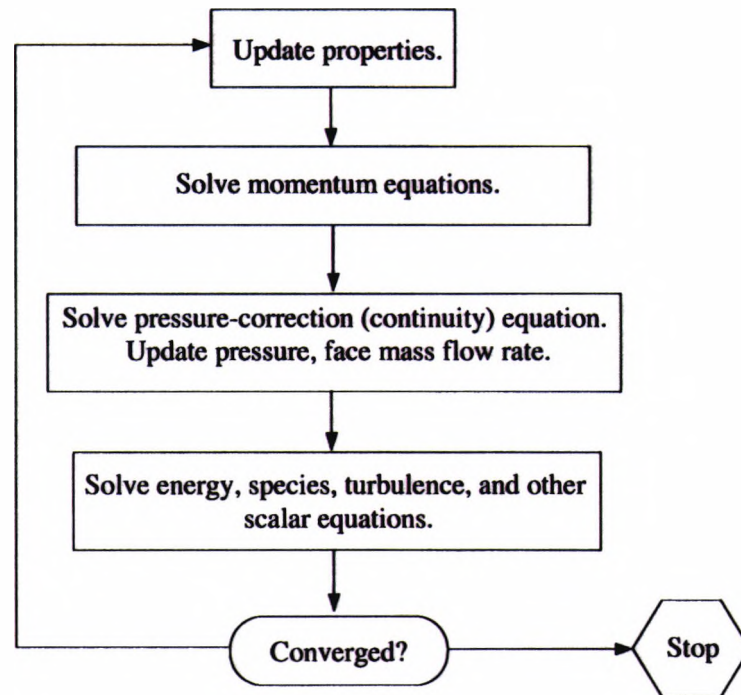


Figure 3-7: SIMPLE solution procedure

3.6.3. Turbulence modelling

A number of turbulence models were evaluated in this work; the results are discussed in Section 3.7, Code Validation. The model that performed with the best results on the validation test case was the Spallart-Allmaras model. The Fluent interpretation of this model that includes a number of ‘fixes’ to aid with convergence difficulties due to poor grid quality will not be discussed in this document. Details are available in the Fluent Users Manual (FLUENT, 2001).

3.6.4. Near-wall approximations

Accurate resolution of boundary-layer flows, especially when considering separation, relies heavily on the fidelity of modelling in the near-wall region. The no-slip boundary condition on the wall implies large velocity gradients. The importance of this region is amplified by a change in the dominating flow physics. It is well known that a turbulent boundary layer may be regarded as three individual layers (Fluent, 2001). The region in the immediate vicinity of the wall is termed the ‘viscous sub-layer’ and in this region momentum, heat and mass transfer are dominated by the molecular viscosity. Away from the wall, in the outer layer, momentum and mass

transfer are dominated by turbulence of the fluid. An intermediate region known as the 'log layer' separates these two regions. In the log layer, the streamwise velocity varies logarithmically with the distance from the surface: this relationship is known as the 'law of the wall'. *Wilcox (2000)* states that the log layer is not a true layer, but a region of overlap, where the sub layer and outer layer merge. These three regions can be seen in Figure 3.8 extracted from the Fluent User Manual (Fluent, 2001), which plots the dimensionless velocity against the dimensionless distance from the wall. An additional layer, called the buffer region, is also shown, which Fluent uses in matching near-wall modelling. This is discussed later in the section. The question of near-wall treatment arises as some turbulence models assume that molecular viscosity is insignificant with respect to the turbulent viscosity ($k-\epsilon$ for example). This is not true in the viscous sub layer where the logarithmic relationship is not valid. There are three approaches for dealing with the viscous sub layer in this situation:

- Wall functions
- Low-Reynolds number model
- Two-layer model

Wall functions bridge the gap between the fully turbulent portion of the boundary layer and the near wall region. Wall functions for Fluent comprise law-of-the-wall equations for the main flow properties plus formulas for near-wall turbulent quantities. Wall functions are known to be inadequate for flow with large pressure gradients, separation and three-dimensional boundary layers, as these conditions are contradictory to the underlying assumption of wall functions. The primary advantage of wall functions as a near-wall treatment, nevertheless, is that only a single grid point is needed within (or on the edge) of the viscous sub-layer.

The Low-Reynolds number model in Fluent uses a coefficient to dampen the turbulent viscosity in the sub layer. Many forms of low Reynolds number models have been published, a detailed review being provided by *Tulapurkara (1999)*.

The Two-Layer model completely resolves the viscous sub layer all the way to the wall. The solution domain is defined into two distinct regions, a viscosity affected

region and a fully turbulent region. In the fully-turbulent region, the turbulence model is used in the normal way. In the viscosity-affected region, a one-equation turbulence model (for k) is used in which the turbulent viscosity is calculated directly from the flow parameters. The switch between the two regions is made using a turbulent Reynolds number based on distance from the wall. A blending function is then applied to smooth the transition between the two techniques.

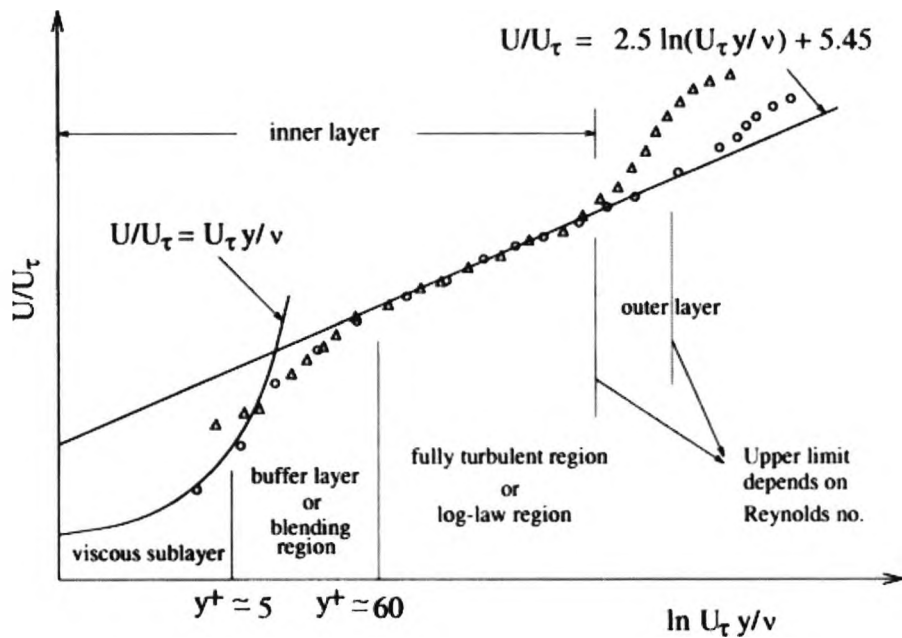


Figure 3-8: Boundary layer near-wall region(FLUENT,2001)

The spacing of the first point away from the wall is often specified using a non-dimensional parameter, y^+ , which is derived from dimensional analysis. For low Reynolds number models, a y^+ value of the order of unity is desirable. For wall functions, the values should be between 30 and 60, which corresponds to the start of the log-law region. The definition of y^+ in Fluent is:

$$y^+ = \frac{\mu_t \rho y}{\mu} \quad \text{Equation 3-34}$$

Where μ_t is the turbulent viscosity, y , the distance of the first point from the wall and μ and ρ , the fluid viscosity and density, respectively. When generating computational grids, it is necessary to make some assumptions regarding the flow parameters in the

y^+ expression. It is possible to approximate y^+ with the following expression (SAUNA, 2001)

$$\frac{y}{L} \approx \frac{y^+}{\text{Re}_L \sqrt{\frac{C_f}{2}}} \quad \text{Equation 3-35}$$

The additional parameters are, L , the representative length scale; Re_L , the Reynolds number based on that length scale; and C_f , the skin friction coefficient at the axial coordinate in question. The skin friction may be ‘guessed’ using a flat plate assumption.

3.6.5. Boundary conditions

In order for the simulations of the Navier-Stokes equations to converge to a desired solution, it is necessary to specify the conditions at the domain boundary from which the flow parameters within the volume of interest may be calculated. The number and type of boundary conditions required to construct a ‘well-posed’ problem is dependent upon the characteristics of the form of Navier-Stokes equations under consideration. Boundary conditions are applied in three forms: the Dirichlet type where the dependent variables are specified; the Neumann type where derivatives of the dependent variables are specified; or, a mixture of the two types. The following boundary conditions were used in this study. The inputs types are set by Fluent.

Engine-face - Pressure Outlet

The pressure-outlet boundary condition in Fluent requires the specification of a static pressure at the boundary for subsonic flow. All other flow quantities are extrapolated from within the domain. In case of reversed flow at the boundary ‘back-flow’, conditions are specified for temperature and turbulence. A function is available in Fluent to adjust the boundary pressure to achieve a specific mass-flow rate. This facility was not used as it greatly increased convergence time. The engine face static pressure may be estimated from isentropic streamtube relations, but it is dependent upon total pressure recovery, which itself is a function of throttle setting. The engine-face pressure was calibrated against mass-flow ratio across the likely mass-flow range using CFD. This can be seen in Figure 3.9. The best-fit polynomial describes the engine face pressure as a function of mass-flow ratio.

$$\frac{P_{ef}}{P_{\infty}} = -0.0077 \left(\frac{A_o}{A_c} \right)^2 + 0.0021 \left(\frac{A_o}{A_c} \right) + 1.0066$$

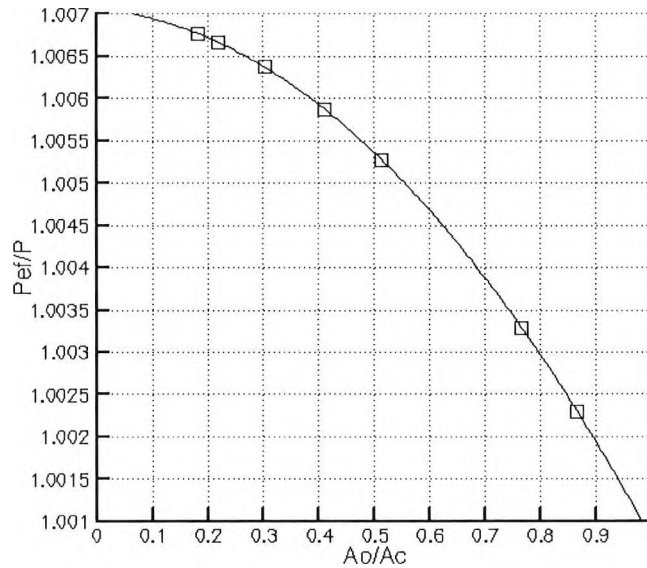


Figure 3-9: Engine-face pressure calibration

Cowl surface - Wall

The cowl surface is defined as a wall with the no-slip condition enforced at the boundary. The shear-stress and heat transfer are calculated based on the local flow field.

Symmetry plane - Symmetry

To reduce the number of cells in the computational grid, a symmetry plane was implemented at the plane $y=0$. The symmetry boundary condition assumes a zero flux of all quantities across the boundary and, thus, the normal velocity component is zero as well as the normal gradients of the variables.

Far field boundary - Pressure far-field

All freestream boundaries were modelled using the pressure far-field boundary type. This specifies the free-stream Mach number and the static conditions. These boundaries are located at a distance of 10 intake diameters away from the cowl where the effect of the intake flow is negligible.

Down stream boundary - Pressure outlet

The pressure-outlet boundary condition for the downstream boundary external to the cowl was given by the freestream value of static pressure. This boundary was located far downstream from the intake crest, so as not to affect the flow in the lip region. The pressure outlet boundary permits the passing of flow with non-uniform velocity, such as that which may be encountered when a lip separation is present.

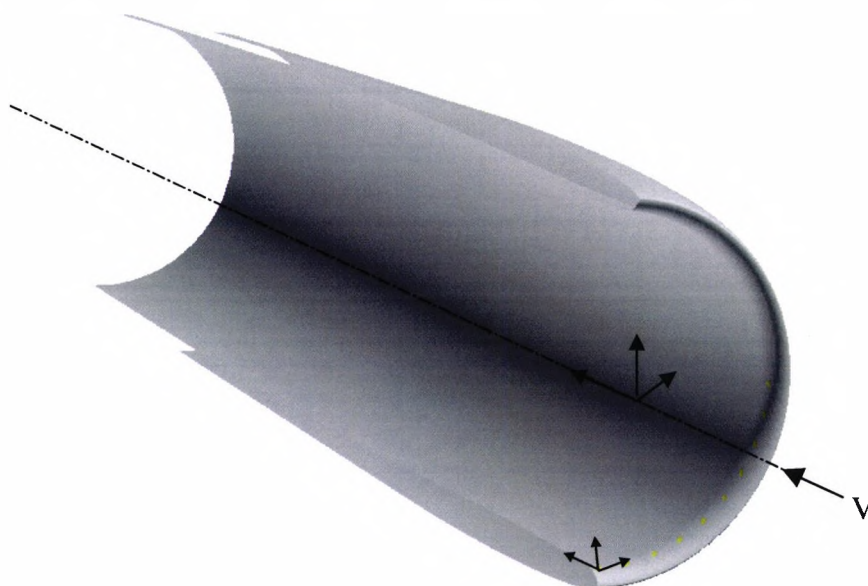


Figure 3-10: Air Jet Vortex Generator coordinate system

Air Jet vortex generators - Pressure inlet

The air jet vortex generators were modelled using the Fluent pressure-inlet boundary condition. The AJVG exits were created in the geometry as discrete surfaces for which a surface mesh was created. The pressure-inlet boundary condition requires the specification of the stagnation properties. This can be considered to be the AJVG plenum conditions that relate directly to the jet performance. In addition, a flow vector is required, that can be used to define the AJVG pitch and skew angles. For ease of calculating and entering the jet vector angle, a cylindrical co-ordinate system was used, in which the origin is located on the cowl centreline, as shown in Figure 3.10. For an axisymmetric cowl, the vector components to define pitch and skew angles are then independent of circumferential location.

3.7. Code Validation

In order to determine any shortcomings with the flow solver, or unknown errors or uncertainties, it is necessary to validate the model against data of known accuracy for a similar configuration. This is usually experimental data obtained either in the wind tunnel or in similar flow rigs. This can provide the user with a rough assessment of accuracy or indication of likely problems. A number of organisations have defined test cases for CFD validation such as AGARD. For aircraft intake and duct flows, the accepted standard has been defined by the AGARD Fluid Dynamics Panel (*AGARD Advisory Report 270, 1991*) where cases are presented for intakes and S-duct flows. These cases are concerned primarily with internal intake flows. In addition QinetiQ uses the experimental data obtained in the former DERA 8ft x 8ft high speed pressurised wind tunnel (*Palmer and Nangia, 1993*) for external and internal intake validation.

The data to be used for CFD validation are those of Nangia and Palmer, which have been used extensively for code validation by DRA and its successors (*Murgatroyd, 1997*). The data were collected in 1992-93 in the then DRA 8ft x 8ft wind tunnel. This facility is a pressurised closed-circuit, continuous operation wind tunnel with a Mach number range of $0.13 < M < 0.87$ and $1.3 < M < 2.5$. The tunnel stagnation pressure may be increased up to 4 atmospheres at subsonic conditions. The tests concerned the R.A.E. model 742L series, in particular cowls, 2,4,5 and 9. The tests were conducted at two Reynolds numbers corresponding to working section total pressures of 32 and 60 inches of mercury at three Mach numbers 0.45, 0.6 and 0.8 at incidences of 0, 2.5, 5.0, 7.5 and 10 degrees. The mass-flow-ratio was generally around separation onset, as the test was aimed at validating an inlet separation prediction method (although a number of full mass-flow sweeps are present).

The collected data consisted of internal performance integrated from a 12 arm, 6 tube engine face rake. Surface static measurements were taken from a primary meridian, with additional taps located at varying azimuth angles, to enable complete coverage in the lip region. The intake model instrumentation is described in more detail in Chapter 4. The chosen data point was particularly demanding, being at zero incidence. The free stream Mach number is $M=0.45$ and the mass-flow ratio is $A_0/A_C=0.34$. At this

condition, the flow is well separated on the external cowl. Good prediction of attached flow at higher mass flows is fairly independent of turbulence model and grid density (Williams, 1999 or Murgatroyd, 1997) and has been assumed to be deliverable by tools validated for more demanding computations. The purpose of this exercise was to determine the best turbulence model and required grid density for the prediction of separated flow in the absence of specific high incidence data. The complete validation matrix is shown below, details of the grid densities and the turbulence models and modifications will be discussed in the following sections.

	rk- ϵ	k- ω	low Re k- ϵ	S.A	S.A _{0.12}	S.A _{0.11}	S.A _{0.10}
Coarse	✓		✓	✓	✓	✓	✓
Medium	✓	✓		✓			
Fine	✓	✓		✓			

Table 1: Matrix for computational validation

3.7.1. Grid dependence study

Grid dependence can appear in a number of forms in CFD. Its general meaning is that a solution obtained on a particular configuration for specific flow conditions would differ, if the number or distribution of mesh points in the computational domain were changed. The implication is usually that the mesh contains insufficient points for a correct resolution of the flow field. In general, the more mesh points, the more accurate the solution; although some numerical schemes may introduce a discretisation error, if the mesh spacing is excessively small. There is a trade-off between mesh size and computational efficiency, which may be considered in terms of CPU time, memory and storage space. Insufficient mesh points can induce other errors, such as poor representation of the underlying geometric model, which may be considered as a computational scale-effect.

The SAUNA CFD system requires that the number of points allocated to blocks must be in multiples of four points, plus one additional point i.e. 5,9,13 etc. The first grid, called GRID1, was defined using a block structure, which previous experience had

shown to be effective, both in controlling and preventing ‘bowing’ of block boundaries, particularly with regard to maintaining an axi-symmetric O-grid around the nacelle and locating the 5-point singularities supporting the lip C-grid. The grid density of this mesh was similar to that which had been shown acceptable in similar studies (*Williams, 2000*). The density of this mesh was then used to derive GRID2 and GRID3. This process was achieved by increasing the number of points in all blocks bounding the inlet, by 4 points. In the direction normal to the cowl surface, the number of points in the boundary layer was kept constant at 33 for GRID1 and GRID2 but increased to 41 for GRID3. The total number of points in the mesh, as well as the points distributed circumferentially around the cowl and those in the leading-edge region of the lip are recorded in the table below.

	Lip	Circ	b.l	Euler	NS
coarse	17	52	33	230528	331904
medium	25	72	33	517248	729216
fine	33	92	41	886528	1351168

Table 2: Point distribution for grid study (half model)

The results of computation for the data point discussed can be seen in Figure 3.11. This shows a comparison of the model surface pressures for both the internal and external cowl. The external crest is located at $x/D_{max}=0.035$. All the calculations displayed in this figure are for the default settings of the Spalart-Allmaras turbulence model, which will be discussed in more detail in the next section.

At this mass-flow condition, the stagnation streamline is located well inside the intake very close to the throat. The internal flow is fully attached and all three grids provide impeccable solutions. The external flow shows a noticeable dependence on grid density. At this mass-flow, the external flow is separated over a large extent of the forecowl. The experimental pressure distribution is reminiscent of a laminar separation with turbulent reattachment as described in detail by *Haines(1994)*. For the experiment from which the data originates, transition was only fixed for the internal flow. From Figure 3-11, it is clear that the coarse grid solution neither defines the constant pressure plateau under the bubble nor the reattachment well. The medium and fine grids provide almost identical solutions for the external flow. The pressure plateau is defined excellently but the reattachment process not as well. This is,

however, a function of turbulence modelling and will be discussed in the next section. As a result of this study, it was decided to use the medium density grid for further computations, as no additional accuracy was achieved by using the fine grid, which would have entailed a substantial increase in running cost.

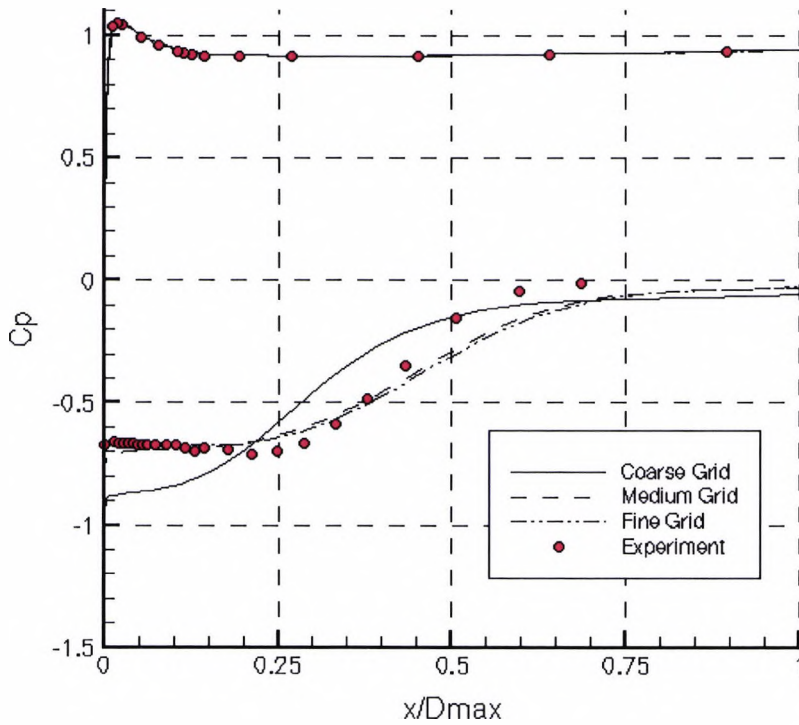


Figure 3-11: Grid study (S-A Turbulence model)

3.7.2. Turbulence model study

An assessment of the turbulence models available in the FLUENT CFD suite was initiated on the medium grid using the same experimental data point that was used for the grid study. Turbulence models that were deemed inappropriate from previous studies, for example, the standard $k-\epsilon$ model (Murgatroyd, 1997), or too computationally expensive to be of practical use for this project, such as Large Eddy Simulation (LES) or Reynolds Stress Modelling (RSM), were not investigated. Figure 3.12 shows a comparison between the different turbulence models tested, by plotting the centreline pressure distributions for the internal and external surfaces of the cowl.

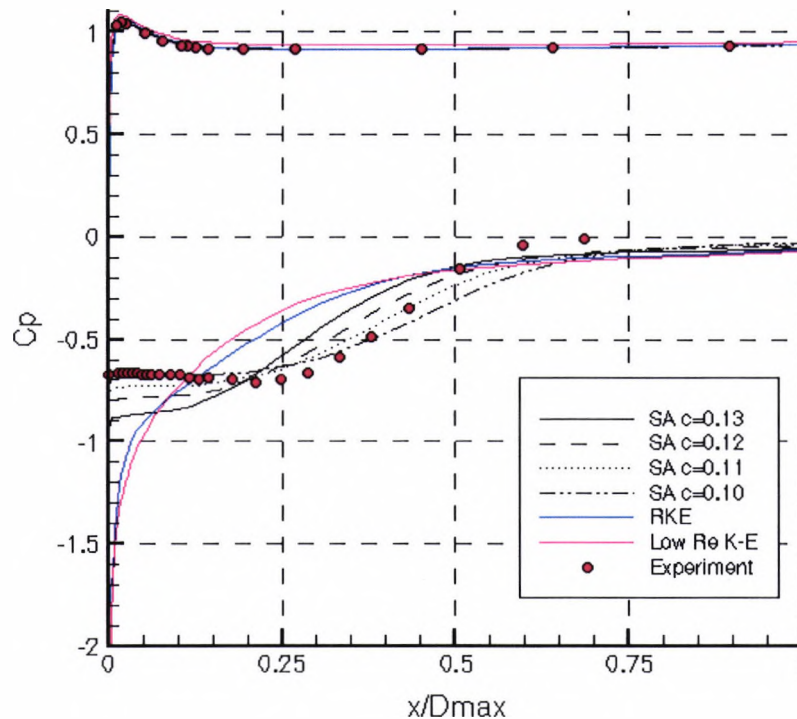


Figure 3-12: Comparison of turbulence models on coarse grid

The fully attached turbulent internal flow is excellently predicted by all the tested models. The more challenging separated external flow shows up noticeable differences between the models. The pair of two-equation models tested, the realizable $k-\varepsilon$ model and the low Reynolds number version of the standard $k-\varepsilon$ model, both predict the flow incorrectly over the lip region. These two-equation models use different techniques for modelling the near-wall region. The realizable $k-\varepsilon$ model uses Fluent's two-layer model which utilising a single equation model in near the wall. Alternatively, the low Re model users modified coefficients which are dependent upon the distance from the wall. These models predict very large leading-edge suction with an almost immediate recompression. The primary reason for this is a mis-match in the flow physics. The models are based on the assumption of fully turbulent flow, and hence, a turbulent separation is predicted. As has already been discussed, the external surface of the model allows free transition and the experimental data implies an initial laminar separation. The Spalart-Allmaras model provides a much better replication of the pressure distribution in the separated region and appears to cater, to an extent, for a laminar-type separation. The original paper by

Spalart & Allmaras (1992) suggests that laminar flow could be replicated in the model by suppressing the production of turbulence. The additional subscripted S-A curves in Figure 3-12 represent the gradual reduction of the turbulence production coefficient in the model from the default value of 0.13 down to 0.1. For the coarse grid, this was shown to better replicate the laminar portion of the separation. However, this increase in accuracy is traded against reduced accuracy for the turbulent part of the separation. For further calculations, the default version of the model is used, as its behaviour is well known and has been validated for a range of flow problems. [FLUENT Users Guide, 2001].

The criterion for convergence, recommended by Fluent, was a reduction in the residuals of all equations by three orders of magnitude. This was found insufficient for this problem and additional convergence criteria were set based on the total pressure recovery and mass-flow ratio measured at the engine face (upstream of the pressure outlet boundary). The solution was deemed to be converged, when both these parameters had converged to 5 significant figures, for 500 iterations. Figure 3.13 shows a convergence history for mass-flow-ratio and total pressure recovery.

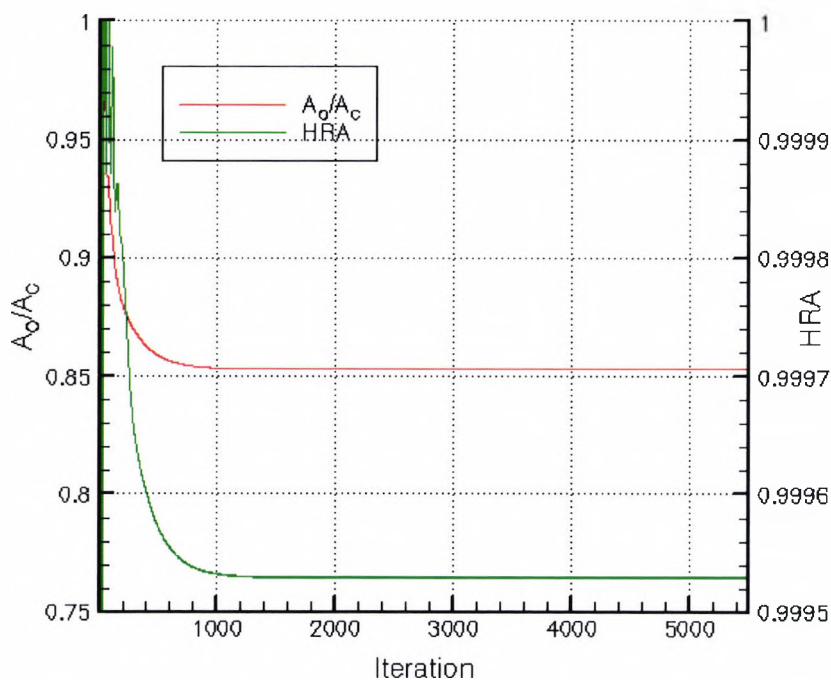


Figure 3-13: Total pressure recovery (HRA) and mass-flow ratio (A_o/A_c) convergence

3.8. References

'Air Intakes for High Speed Vehicles' AGARD Advisory Report 270, Fluid Dynamics Working Group 13, September 1991.

Anderson, B.H., Towne, C.E., 'Application of computational fluid dynamics to inlets', In 'Practical Intake Aerodynamics' Ed. Goldsmith E.L., Seddon, J. Blackwell 1993.

Anderson Jr., John D., 'Computational fluid dynamics, the basics with applications', McGraw-Hill 1995.

Benek, John A., Kraft, Edward M., Lauer, Rodney F., 'Validation issues for airframe engine integration', AIAA Journal, Vol. 36, No.5, pp759-763, May 1998.

DRA Services and Facilities, Wind Tunnel Brochure, Defence Evaluation and Research Agency.

ERCRAFTAC (European Research Community On Flow, Turbulence and Combustion), 'Special interest group on quality and trust in industrial CFD, best practice guidelines – Version 1', January 2000.

FLUENT Training Course Notes, FLUENT Inc. 1998.

FLUENT 6 - User's Guide, FLUENT Inc., December 2001.

Haines, A.B., 'Scale effects on aircraft and weapon aerodynamics', AGARDograph 323, 1994.

ICEM CFD, 'ICEM training course notes', November 1999.

McGuirk, J.J., Page, G.J., 'Total pressure loss and drag predictions for a supersonic circular pitot intake', *European Forum – Recent developments and applications in aeronautical CFD*, RAeS, London, 1993.

Murgatroyd, J.D., 'An evaluation of the RAMPANT commercial CFD code applied to intake model 742L. (U)' *DRA/AS/HWA/TR96096/1*, March 1997.

Palmer, M.E., Nangia, R.K., 'Circular model 742L inlet, subsonic tests in the DRA 8ft x 8ft wind tunnel for separation onset prediction, incidence and Reynolds number predictions', *RKN/AERO/Report/93-30/Issue 1*, February 1993.

Prince, Simon A., Williams, Matthew J., Edwards, John A., 'Application of a parabolised Navier-Stokes solver to some problems in hypersonic propulsion aerodynamics', *AIAA Atmospheric Flight Mechanics Conference, Montreal, Canada August 2001*.

QINETIQ, 'SAUNA Manual', 2001

Rubini, R., 'Numerical methods for turbulent flows' *MSc.Lecture Notes*, Cranfield University, 1996.

Spalart, P., Allmaras, S., 'A one-equation turbulence model for aerodynamics flows', *AIAA 92-0439*, 30th *AIAA Aerospace Sciences Meeting & Exhibit*, Reno, NV, USA, 1992.

Tinoco, Edward N., 'The changing role of computational fluid dynamics in aircraft development', *AIAA-98-2512*, *AIAA 16th Applied Aerodynamics Conference*, Albuquerque, NM, USA, 1998.

Tulapurkara, E.G., 'Turbulence models for the computation of flow past airplanes', *Progress in Aerospace Sciences Vol. 33 pp 71-165*, 1997.

Uenishi, K., Person, M.S., Lehnig, T.R., Leon, R.M., 'CFD-based 3d turbofan nacelle design system', AIAA-90-3081, AIAA 8th Applied Aerodynamics Conference, Portland, OR, 1990.

Versteeg,, H.K., Malalashera, W., 'An introduction to computational fluid dynamics, the finite volume method', pp 85-154, Longman 1999.

Wilcox, David C., 'Turbulence modelling for CFD', Second Edition, DCW Industries, Inc. 2000.

Williams, Matthew J., 'The mechanics of air intake lip separation at a wide range of Reynolds numbers – Progress Report, Year I.' DERA/MSS/MSF2C/WP00280, 2000.

Williams, Matthew J., 'Evaluation of cross section shaping techniques on offset diffuser performance', QinetiQ/FST/TR024594, 2002.

Williams, Matthew J., Unpublished work on the use of CFD for spillage drag prediction, 2003.

4. Experimental Procedures

This chapter describes the experimental techniques used in this study, for both evaluation of intake separation and the application of AJVGs for managing air intake flow separation. Most data were collected from two wind-tunnel entries. The first was concerned with gathering pressure data to analyse the onset and development of lip separation. The second entry was concerned with testing and validating an AJVG that had been designed using a computational modelling approach. Prior to the wind tunnel testing, at the genesis of the programme, a preliminary water-tunnel test was performed to aid in the assessment of the development of three-dimensional flow separation.

4.1. Water Tunnel Testing

As part of the initial problem assessment, a small-scale water-tunnel test was conducted at City University. The primary aim of this investigation was to use flow visualisation to provide a basic understanding of the flow physics and fluid dynamic mechanisms that contribute to lip separation, for both internal and external flow. Due to the relatively sharp nature of the lip, it was assumed that initial separation onset and the resulting three-dimensional separation, would largely be representative of that experienced at higher Reynolds numbers.

The City University water tunnel facility is effectively a water channel. A weir located at the downstream end of the facility provides stream movement. Fluid passing over the weir is collected in a tank and pumped upstream to a 'settling' tank ahead of the channel. It re-enters the channel and passes through a series of flow straightening honeycombs before entering the working section.

4.1.1. Design & Manufacture

The water tunnel model was designed in modular form to fit into the existing high-incidence quadrant in the water tunnel facility. The model consists of three separate interchangeable axisymmetric intake cowls based on the RAE m742L series. The cowls could be attached to a metering section, fitted to which was a translating cone to throttle the mass-flow through the model. The model was built under subcontract to DERA by Northwest Aerodynamic Models Ltd. (NAM) of Stockport, Lancashire. The

model was sized around a three-and-one-half-inch engine face diameter, to allow a degree of compatibility between these models and existing components that would be used in a planned wind-tunnel test.

The three cowl models were machined from transparent acrylic that was later coated with primer to enhance the flow visualisation. The three cowls were chosen from the RAE model 742L series to provide a systematic variation of two different geometric parameters. These were lip contraction ratio and lip internal ellipse major to minor-axis ratio. The cowls were attached via push fit to the metering section. The metering section consisted of a parallel portion upstream of a venturi nozzle designed in accordance with BS1042 (*Ower & Pankhurst, 1977*).

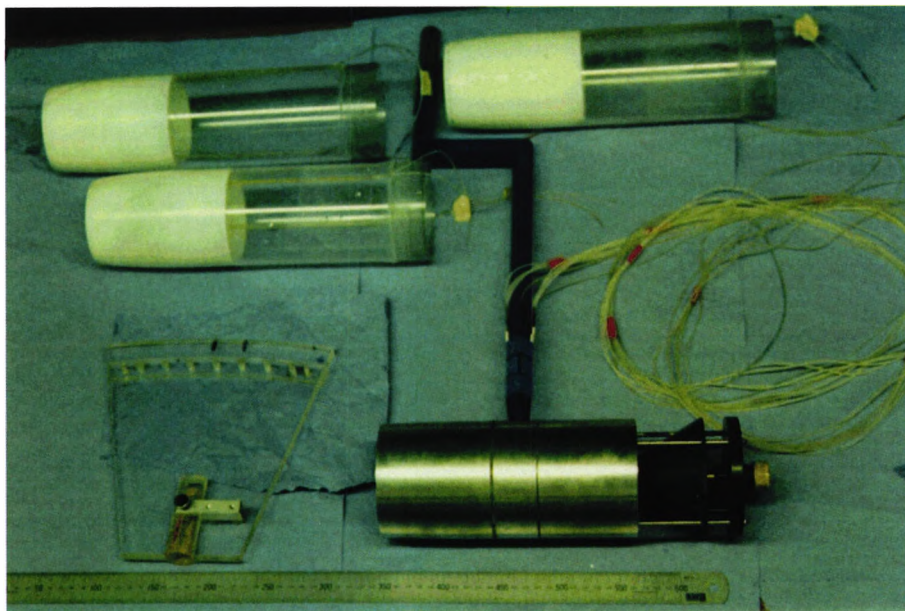


Figure 4-1: Water tunnel model

The mass flow through the duct was varied by means of a thirty-degree half-angle cone that could be translated manually into the venturi exit. The model was supported from the existing high incidence quadrant of the water tunnel by means of a quarter inch plastic coated bar. The rig permitted incidence and yaw ranges of plus or minus 30 degrees. A number of plastic tubes were inlaid into the model to provide dye release into the stream. These tubes were located close to the cowl leading edge and along the side of the intake. The model assembly is shown in *Figure 4.1*. Dye was supplied to the model from a number of reservoirs located externally to the water-

tunnel. Constricting the flexible dye tubes or adjusting the height of the dye reservoirs could vary dye flow rate.

4.1.2. Test Procedure

Each particular model was tested through a range of incidences and yaw angles. A mass flow sweep was made at each model attitude. The mass flow control cone was adjusted manually after each data point and time was then allowed for the flow to settle after the disturbance, before the data point was recorded. The throttling cone was always driven inwards to reduce mass flow ratio, thus always moving the circumferential stagnation line downstream in the duct, with the aim of avoiding hysteresis in the flow. A VHS video camera and 35mm still camera were used to record the flow visualisation. The channel freestream speed was measured on the centre line by timing the progress of a dye streak injected into the flow. Typical speeds were approximately 3.0 cm/second, with a Reynolds number of the order of 10^3 based on maximum diameter.

Following the poor quality of flow visualisation in the first phase of testing, it was decided to return to the facility with improved models to obtain some better images. It was decided that the dye distribution system in the model was insufficient. The existing flexible tube was removed, as it was believed it that might have become blocked. It was replaced with brass hypodermic tubing. The extent to which the tubing circumferentially covered the leading edge was increased from 240-degrees to 360-degrees.

The water tunnel programme provided interesting results in terms of qualitative visualisations of the flow physics, which are useful in providing some validation for the CFD, particularly at high incidence, where no experimental data were available. The general unsteadiness of the flow, particularly at high incidence, made it impractical to determine separation criteria for the different configurations with respect to mass-flow or incidence. Examples of attached and separated external flow are shown in Figures 4.2 & 4.3.

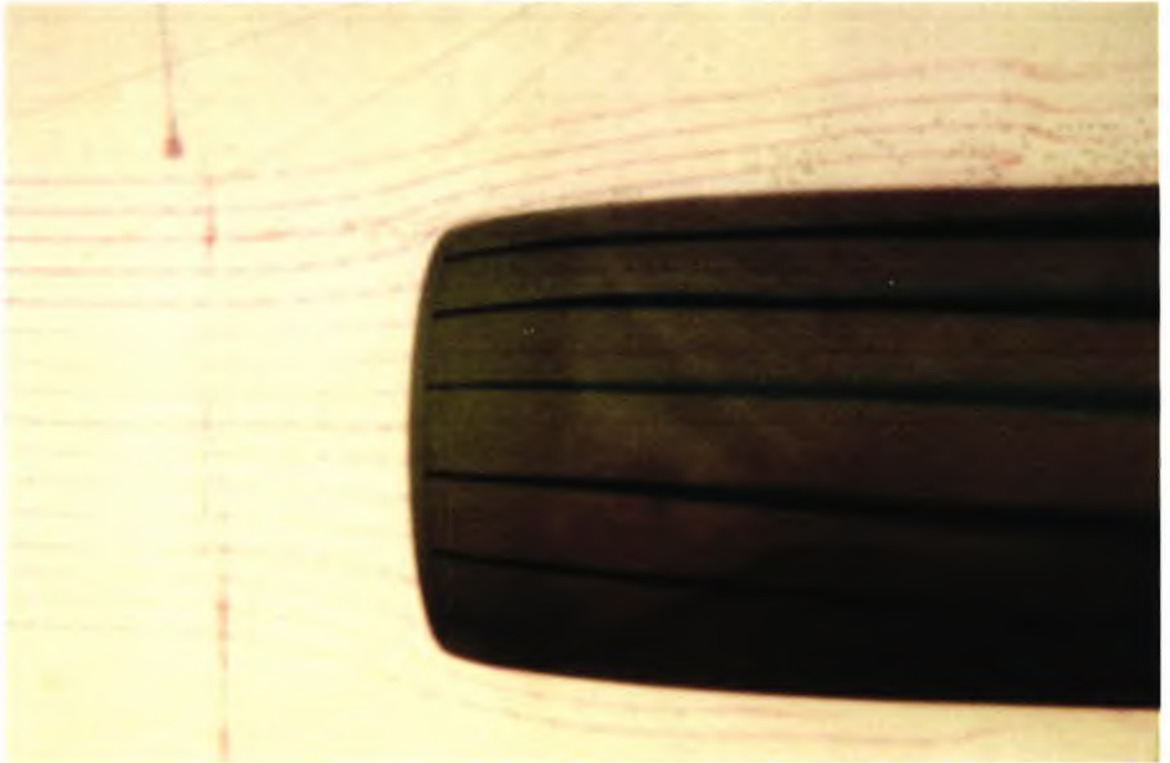


Figure 4-2: Visualisation of attached external flow

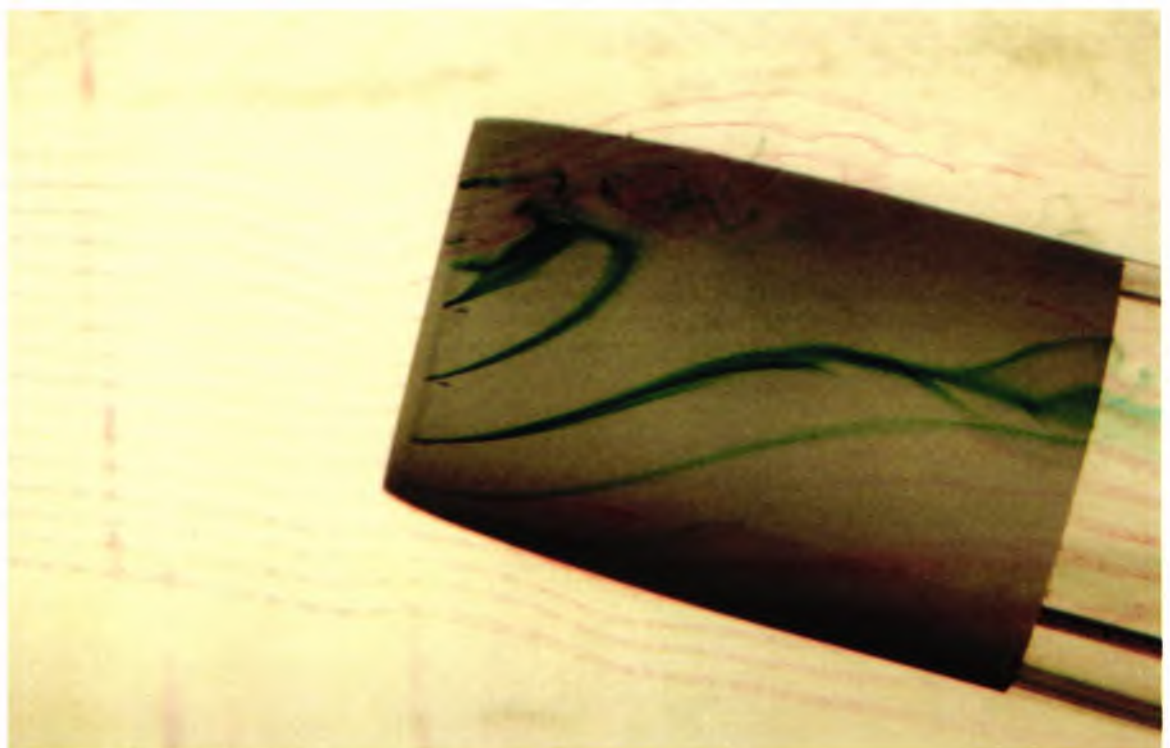
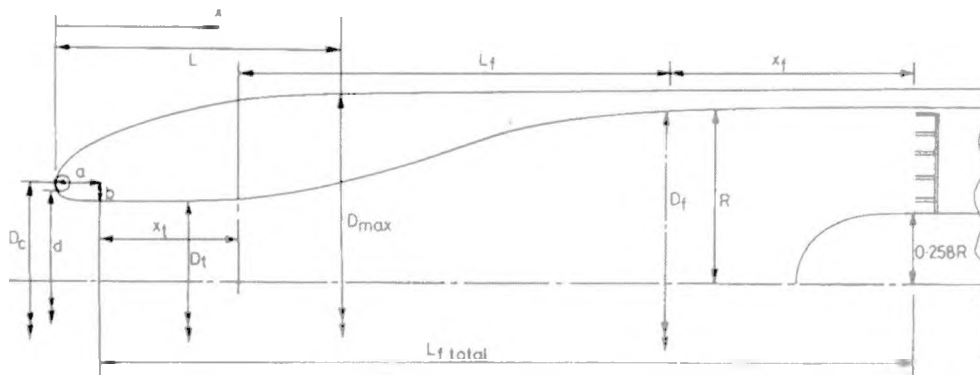


Figure 4-3: Visualisation of external separated flow

4.2. Wind Tunnel Testing

4.2.1. Intake model

The intake model chosen for this study was the RAE model 742L. This is a series of eight axisymmetric pitot intakes, which provide a parametric variation in a range of geometry descriptors. This series of models was designed to complement NACA research into intake geometry effects that were available at the time of design. A full description of the geometry for each of the cowls in the series may be found in *Goldsmith (1990)*. The three cowls used in the experimental part of this study are summarised in Figure 4.4 below. This model was chosen, partly because it was already in existence, which eliminated the need for the potentially costly design and manufacture process. Secondly, the geometry is representative of high-speed, fixed-geometry, military pitot intakes, with low supersonic speed capability, such as that used for the Jaguar (*Hacker & Hirst, 1978*). Intakes of this type may be susceptible to non-compressibility affected lip separation at high incidence and thus may reap the most benefits from lip flow control.



cowl	d/D_{max}	L/D_{max}	A_c/A_{max}	Lip CR	a/b	L_f/D_t	X_t/D_t	A_t/A_t
2	0.85	1.00	0.729	1.177	5	3	0	1.4
5	0.825	1.00	0.696	1.078	5	3	0	1.4
9	0.825	1.00	0.729	1.177	2	3	0	1.4

Figure 4-4: RAE model 742L geometry description

The m742L models consist of an external NACA profile, a quarter ellipse internal lip and a diffusing section aft of the throat. The primary reason for choosing this model was that it, as well as the associated flow measuring equipment, was available. The

physical size of the model, 3.5-inch diameter engine-face, means that it was compatible with several of the wind tunnels in City University's Handley-Page Laboratory.

Due to time and cost constraints, only one configuration could be tested. The configuration tested was Cowl 9, for which the external contour is described by a NACA 1-85-100 profile. The internal lip is a quarter ellipse with a major/minor axis ratio of 2.0. The throat section is of zero length and the down stream duct is defined by a fourth order polynomial:

$$\frac{D - D_t}{D_f - D_t} = 3 \left[1 - \frac{x}{L_f} \right]^4 - 4 \left[1 - \frac{x}{L_f} \right]^3 + 1 \quad \text{Equation 4-1}$$

D_f and D_t are the engine-face and throat diameters respectively, L_f is the length of the duct and x the distance along the duct. The internal contraction ratio is 1.177. The original cowl was extensively pressure tapped on one primary generator with 25 external tappings and 16 internal tappings plus one on the highlight. Additional taps are located near the leading edge, radially around the cowl to provide detailed coverage. Details of the cowl and rake pressure tappings are presented in the Appendix.

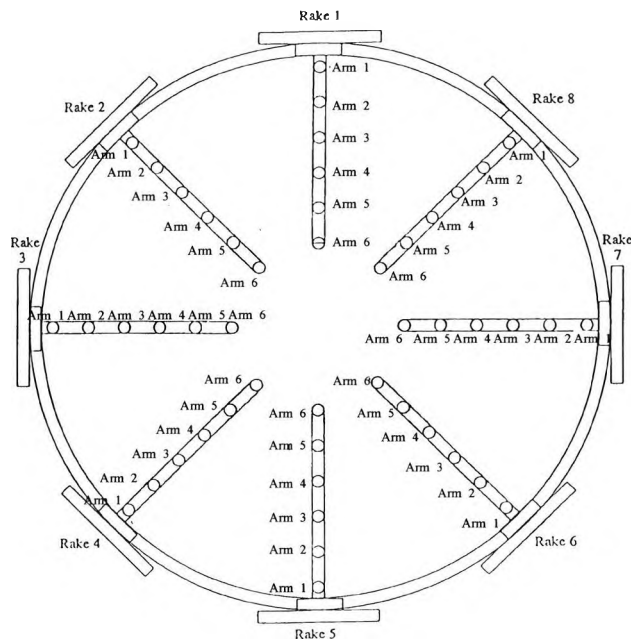


Figure 4-5: Schematic of 3.5 inch engine-face rake

The cowl attaches to a constant area section adapter that in turn attaches to a QinetiQ flow metering section. The adapter, manufactured at City University, enables the cowl section to be rotated while the metering section remains at the same orientation. (In tests in the QinetiQ 8ft tunnel, the sting was rotated). The metering section allows the model to be mounted to the wind tunnel external 6-component balance. The flow metering section is similar to the RAE type 'a' described by *McGregor (1971)* and consists of eight six-arm total pressure rakes located at equal intervals around the circumference. The arms on the rakes are located at the centre of annuli of equal area. A schematic of the rake is presented in Figure 4.5. Downstream of the engine-face rake is a venturi section with eight static pressure tapings in the main duct and eight in the contraction. The mass flow through the duct is varied by translating a 30-degree half angle cone into the exit of the metering section. This was mounted at the rear of the assembly and driven remotely by an electric motor.

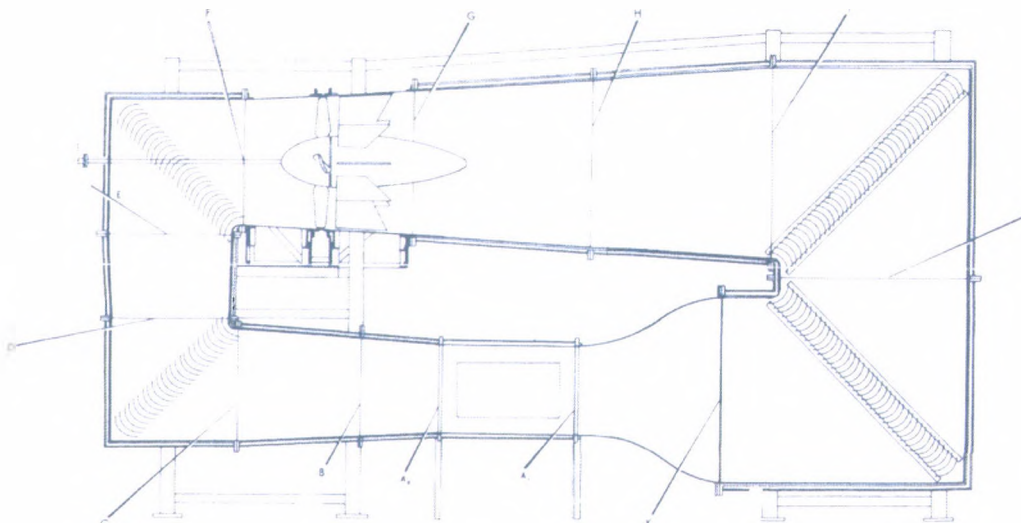


Figure 4-6: T2 Low speed wind tunnel

4.2.2. Wind tunnel facility

The wind tunnel test was conducted in City University's T2 low speed wind tunnel. This is a closed return tunnel with a working section measuring 1.2 metres wide by 1.0 metres high and with a length of 3m. The tunnel has a top speed of approximately 45 metres per second ($M_\infty=0.13$) and is equipped with a 6-component external balance. The circuit is shown in Figure 4.6. The test Reynolds number based on intake maximum diameter was $Re_{D_{MAX}}=0.25$ million.

4.2.3. Instrumentation & Data Acquisition

The pressure measurement offices on the cowl and metering section were connected to three D-Type scani-valve pressure-scanning units, which were located outside the tunnel working section. The connecting tubing was sheltered within the strut shroud. The scani-valve units were fitted with 1.5psi differential pressure transducers. Signal to the transducers was provided by power-packs passing through low pass filters set at 50Hz before being amplified and fed into a Cambridge 1401 analogue/digital converter control unit. Transducer output was converted into pressures via City University's online data analysis system described by *Innes (1993)* and loaded into a Microsoft Excel workbook for on-line analysis. Details of the procedure for calculating intake parameters from the existing data reduction routine are described in the Appendix. The arrangement of pressure tubes on the scani-valve was designed to allow an expected smooth variation of pressure from tube to tube to aid transducer response. Where this was not possible, a pressure tube was spliced to allow the reading to be taken twice. In this instance, the second measurement was used in calculations.

4.2.4. Test technique

The aim of the test was to build up a detailed picture of external nacelle flow. Due to time constraints, a number of specific points was chosen to closely replicate critical aircraft design points in terms of model attitude and throttle setting. Critical mass-flow-ratios were chosen as $Ao/Ac=0.88$ (representative of cruise), $Ao/Ac=0.43$, (engine out) and $Ao/Ac=0.30$ (engine idle). Additionally, $Ao/Ac=0.5$ was included in the test matrix, to provide an even distribution of throttle settings across the applicable range. This value would also provide insight into the development of the separated flow topology. Incidence was varied from 0-degrees to a maximum of 25-degrees. Above this incidence angle, the flow became unsteady. An experimental run consisted of a variation in incidence for a fixed throttle setting. This enables a direct measurement of the incidence angle for which separation onset occurs. This is an important parameter usually set as a specific target for engine out/take-off performance (*Youghans, Hoelmer & Stockman, 1982*). The cowl was rotated at thirty degree intervals over 180 degrees to provided detailed pressure data for the progression of the separated region on the cowl surface. Repeatability was verified at the start of each day of running by a check on mass-flow-ratio and cowl surface

pressures at the zero incidence condition. The position of zero incidence and side-slip angle of the model in the working section was achieved by manual adjustment to provide equality of pressure coefficients at constant axial stations.

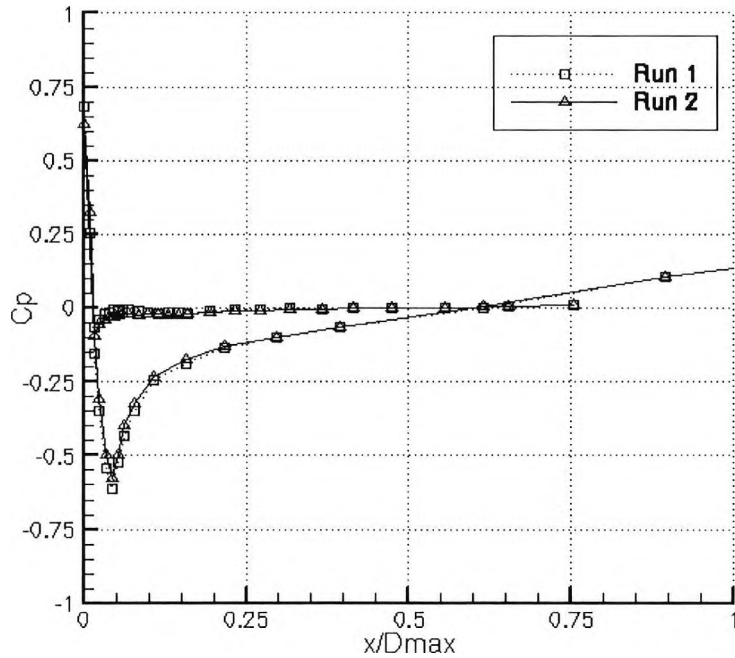


Figure 4-7: Data repeatability check example

4.2.5. Error analysis & data repeatability

When conducting an experiment, it is necessary to obtain an estimate of the accuracy of that experiment. The AIAA standard concerning uncertainty in wind tunnel testing, AIAA-S-071A-1999, defines accuracy as an indication of the closeness of an experimentally measured value and its true value. The difference between the experimentally measured value and the true value is called error.

The error in a measurement can be considered to consist of two components: a precision or random error and a bias or systematic error. Systematic errors are those that are the same for all measurements and can be accounted for by calibration or correction. Precision errors arise from non-repeatable sources that contribute to scatter of the data.

Considering the chain of components in a measurement system, each of which is a source of error, for example: the pressure tap orifice, the transducer and the data reduction process, may all provide errors that will propagate through the measurement system to the final result. An overall assessment of accuracy may be obtained either statistically, if repeat measurements were taken, or by analysing the error or combination of errors within the measurement system for single sample measurements. The AIAA standard provides a definitive guide to sources of error in wind-tunnel measurement, as well as some component values of uncertainty. A simpler but often used uncertainty analysis for single sample measurements is described by *Kline & McClintock(1953)*. This method has been demonstrated for wind-tunnel surface static-pressure measurements by *Mange (1996)*, who used the manufacturer's stated uncertainty for the pressure transducer to approximate the overall uncertainty in pressure coefficient.

In the experiment described here, a number of data repeatability checks were taken at the same flow conditions. This can be used to provide an indication of the uncertainty in the experimental results. The repeat points are taken over the span of the test so providing a variation in the random error sources: for example, model build and Reynolds number variation due to temperature change due to tunnel running time.

The configuration-to-configuration variation of mass-flow ratio was checked at zero incidence and $A_o/A_c=0.74$. The mean value of A_o/A_c was found to be 0.7399 with a standard deviation of 0.0045. That is less than a half percent of full flow. An example of the variation of cowl pressure for a number of these cases is displayed in Figure 4-7. Further analysis on the magnitudes of errors in the measured variables is presented in the Appendix.

During continuous wind-tunnel running, two factors were seen to have an effect on the tunnel speed. Firstly, the tunnel total temperature would rise as a consequence of wall friction and the continuous addition of energy via the fan. Secondly, increasing the incidence of the model increased the tunnel blockage. Theoretically a further blockage, similar to what is traditionally called wake blockage may be present due to the large separated region at low mass-flow-ratios. Variation in tunnel total temperature is accounted for by entering the correct value at each data point. The

variation in Reynolds number due to these phenomena is deemed insignificant to cause a change in the flow physics. The change in tunnel speed, similarly provided an insignificant change in Mach number. However, the effect of the blockage would be to prematurely overload the lip causing the flow to separate early; a separate correction is required to correct the pressure coefficient values to those appropriate to unconstrained freestream flow.

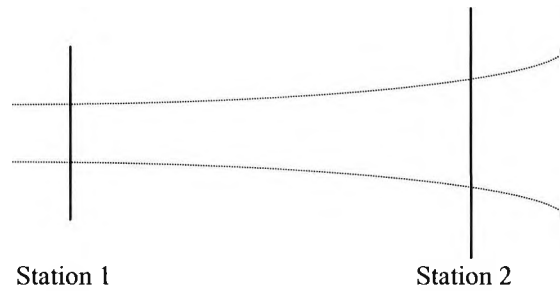


Figure 4-8: Derivation of intake parameters

4.2.6. Data reduction

The data from the City University data reduction program was loaded into a Microsoft Excel spreadsheet for on-line analysis. The existing data reduction program was designed for use with high-lift aerofoils, consequently a number of modifications had to be made to the data to calculate specific intake parameters. Initially the data were converted from static pressure coefficients to static pressure normalised by free-stream total pressure (calculated from flow speed and working-section static pressure). This would be used, for example, in total-pressure distortion. For calculations of the intake performance parameters, total pressures are measured at the engine face as well as the wall static pressures. The intake parameters are calculated by considering a stream tube of varying cross sectional area, as shown in Figure 4.8. The engine-face rake is installed at Station 2. The total pressure recovery is the mean engine-face total-pressure normalised by the freestream total pressure:

$$\eta = \frac{H}{H_\infty} = \frac{1}{A_{EF} H_\infty} \int H dA \quad \text{Equation 4-2}$$

In this case, the rake consists of m arms of n tubes located at the centres of equal area sections, A_{ij} , and the integral becomes a summation:

$$\eta = \frac{1}{H_\infty n} \sum_{i=1}^n \sum_{j=1}^n H_{ji} A_{ij} = \frac{1}{nm H_\infty} \sum_{i=1}^n \sum_{j=1}^m H_{ji} \quad \text{Equation 4-3}$$

Alternatively, the dynamic pressure coefficient is:

$$\frac{(\bar{H} - p_\infty)}{q_\infty} = \frac{1}{nm} \sum_{i=1}^n \sum_{j=1}^m \left(\frac{H - p_\infty}{q_\infty} \right) \quad \text{Equation 4-4}$$

The mass-flow ratio through the duct is calculated from continuity of mass between the two stations:

$$\dot{m}_1 = \dot{m}_2 \quad \text{Equation 4-5}$$

Using Bernoulli's equation, the incompressible mass-flow ratio is:

$$\left(\frac{A_O}{A_C} \right)_{INC} = \frac{A_{ef}}{A_C} \sqrt{\frac{q_{ef}}{q_\infty}} \quad \text{Equation 4-6}$$

The compressible form can be derived from a useful form of the continuity equation appropriate to stream tube flows using the sonic area, A^* :

$$H_1 A_1^* = H_2 A_2^* \quad \text{Equation 4-7}$$

Using the definitions of A^*/A and calculating the engine-face Mach number from the static and total pressures at the rake:

$$\frac{A^*}{A} = \left\{ \frac{\gamma + 1}{2} \right\}^{\frac{\gamma+1}{2(\gamma-1)}} M \left\{ 1 + \frac{\gamma-1}{2} M^2 \right\}^{\frac{\gamma+1}{2(\gamma-1)}} \quad \text{Equation 4-8}$$

$$M_{ef} = \sqrt{\frac{2}{\gamma-1} \left[\left(\frac{H}{p} \right)^{\frac{\gamma-1}{\gamma}} - 1 \right]} \quad \text{Equation 4-9}$$

The mass-flow ratio becomes:

$$\frac{A_{\infty}}{A_C} = \left(\frac{\eta A_{ef}}{A_C} \right) \frac{M_{ef} \left\{ 1 + \frac{\gamma-1}{2} M_{ef}^2 \right\}^{\frac{\gamma+1}{2(\gamma-1)}}}{M_{\infty} \left\{ 1 + \frac{\gamma-1}{2} M_{\infty}^2 \right\}^{\frac{\gamma+1}{2(\gamma-1)}}} \quad \text{Equation 4-10}$$

Distortion is evaluated using the Roll-Royce distortion descriptor DC θ where because of the 45° spacing of the rake arms, θ becomes 90°. DC90 is defined as:

$$DC90 = \frac{(\bar{H}_{ef} - \bar{H}_{90MIN})}{q_{ef}} \quad \text{Equation 4-11}$$

Where \bar{H}_{90MIN} is the mean total-pressure in the worst 90° angular segment of the engine-face. This is determined by calculating the average total pressure in the 90° segment starting at each rake arm. Thus there are eight 90° segments in the engine-face. The minimum segment is then selected for use in calculating the distortion. For each segment, the mean total pressure is calculated using the data from three rake arms, at the start end and mid locations. Several methods can be used to determine the average total based on these readings from the rake. These are described by *McGregor & Clark (1986)*. For this test, a Simpson's rule approximation was used to give:

$$\bar{H}_{90} = \left[\frac{1}{6} (H_i + 4H_{i+1} + H_{i+2}) \right] \quad \text{Equation 4-12}$$

The intake performance has been calculated by replacing the integrals in the expressions for area weighted pressure recovery and mean duct static pressure by the summation of pressure values at discrete points. Consequently, it is necessary to provide a mass-flow calibration factor, k_f , which relates actual mass flow through the duct to the measured mass flow. The QinetiQ mass flow metering cells are calibrated

regularly, as a matter of course. The calibration factors are QinetiQ proprietary information and are not reported in this document.

4.2.7. Flow visualisation

To aid in the understanding of the three-dimensional flow on the intake cowl at incidence, the oil-dot surface flow visualisation technique was used (*Merzkirch, 1987*). For this purpose, the acrylic water tunnel model of Cowl 9 was modified to fit the wind tunnel rig. This was so as to not damage the high quality wind tunnel model by contaminating the pressure orifices with oil. For the oil-dot visualisation, a matrix of discrete dots of an oil/pigment mixture is placed on the model surface. When air is blown past the model, the oil is carried with it leaving behind deposits of the pigment. The patterns left behind by the pigment mark directly the local flow directions at the surface and thus imply the structure of the off surface three-dimensional flow (*Maltby, 1962*). In this case, kerosene was used as the oil base with lampblack as a thickening pigment. The viscosity of the oil pigment mixture is carefully chosen, as the oil streaks generated must be sufficiently thin so as not to interfere with the aerodynamics and modify the surface flow. To ensure this, the ratio of the viscosity of the air, to that of the oil, should be small. Merzkirch (1987) suggests a value of the order 10^{-2} to 10^{-4} . It should be noted that in some circumstances, pressure and gravitational forces may affect the direction of the indicated surface streamlines. This effect is in most cases small (*Maltby, 1962*). In addition to external visualisation with the oil-dot technique, the oil dots were also used on a splitter plate at the model symmetry plane to determine the state of the internal flow with and without AJVGs. Limited internal flow visualisation was performed using a mixture of kerosene and Dayglow 17, but because of the small physical size of the model, these images could only be recorded manually.

4.2.8. Wind tunnel blockage corrections

The walls of the wind tunnel working section have a constraining effect on the flow around the model. If the model could be tested in free air, as is the case in flight, disturbances in the flow induced by the model would have a large lateral distance to return to the freestream conditions. When the model is tested in a wind tunnel, the presence of the walls constrains the flow by forcing the velocity vector of the flow to

align with the wall. The presence of the wall can have a number of effects on the pressures and forces and moments experienced by the model. These effects are categorised by *Pope & Harper (1966)*. Of particular interest is the solid blockage effect. This is an increase of the dynamic pressure in the working section due to the constraining effect of the walls. This correction takes the form of a modification to correct the speed and pressure to the values that will be experienced if the working section is empty and is independent of model attitude (*Thompson, 1948*). It may be considered as a reduction in working section area due to the presence of the model. A similar blocking effect due to the wake may be present if the wake is particularly large and this may be the case at large angles of attack. The forward projected area of the intake model is very small in comparison with the tunnel working-section cross sectional area, 0.27%, and it was felt that no correction was needed.

In addition to the usual forms of wall correction described above, it is hypothesised that an additional form of correction may be required for propulsion applications. This is proposed due to the variation in stream tube size with model throttle setting. Far upstream where the flow is uniform across the working section, the capture stream tube area may be considerable larger or smaller than the intake highlight area. As the streamtube approaches the intake, its area must change to pass through the intake aperture. Therefore, the flow inside the tunnel, but outside the stream tube, will undergo a velocity change, due to the constrained tunnel area and the continuity requirement. The effect of this additional blockage is presented in Figure 4-9 for a range of working section/model area ratios including that of m742L. The effect is very small for this model across the full mass flow range, less than 0.15% of freestream dynamic pressure.

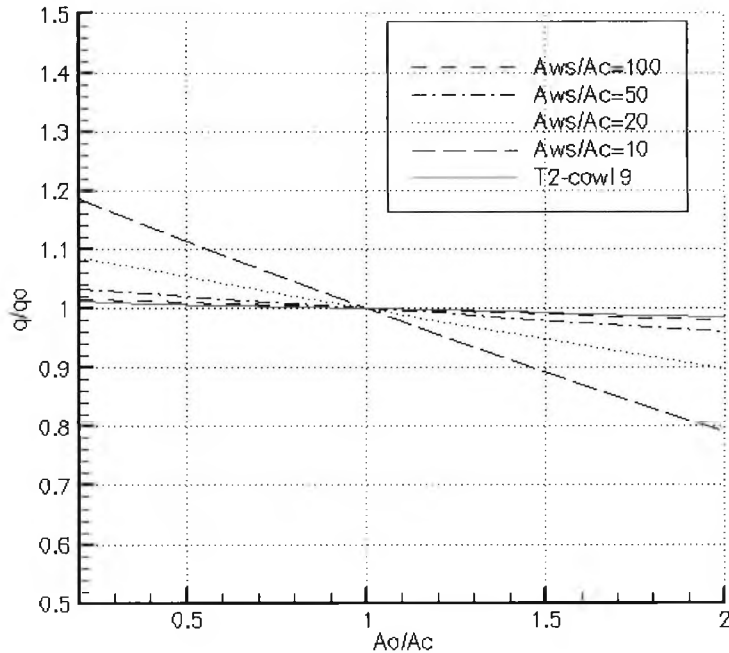


Figure 4-9: Mass-flow ratio blockage on tunnel dynamic pressure

4.2.9. Air Jet Vortex Generator installation

Due to the apparent success of computational predictions using AJVGs to control the internal flow separation at the lip (see Chapter 6), it was decided to install a comparable AJVG system in one of the intake models. The aim was to validate the computational analysis and hence gain confidence in using the computational tools to further expand the design envelope.

The AJVG system was installed in the acrylic copy of model 742L, Cowl 9. The acrylic model was originally designed for use in the initial water tunnel test and was then modified so as to be attachable to the wind-tunnel flow metering rig for flow visualisation studies.

A deep groove was cut into the outside of the intake cowl near the leading edge. The groove was then covered to make a plenum chamber in the lip. The plenum cover maintained the external cowl geometry. Eight supply lines located in pairs at 90-degree increments around the cowl circumference fed the plenum from the house high-pressure air supply. Two pairs of the supply lines were created from a modification to the existing dye supply lines used in the water-tunnel experiment.

Two additional grooves were cut into the cowl surface to house the other four air-supply lines.

Holes were drilled into the lip plenum chamber from outside of the cowl to form the AJVG apertures. The plenum cover was then attached. This ensured that the air-jets were not blocked by waste material during the drilling process. The air-jets were drilled at the chosen angles with a drill bit of 0.75mm diameter. This created an individual jet exit area of $2.5 \times 10^{-6} \text{ m}^2$.

The chosen pitch and skew angle settings of the jets illustrate the nature of the computational and experimental interaction within this project. Computationally, several different jet angles were evaluated. However, the small physical nature of the cowl model, along with its relative fragility of being manufactured from acrylic only a few millimetres thick, made the drilling of compound pitch and skew angles a complicated and delicate procedure. To reduce the risk of damaging the model during this modification, the easiest angle to drill would be a pure jet pitch angle (skew angle is 90-degrees). Here the jet direction is normal to the cowl centreline. This configuration was evaluated computationally and found adequate in comparison with other AJVG configurations evaluated. Therefore, the 30-degree pitch and 90-degree skew angle was the configuration tested experimentally. Of course, these angles only describe the pitch and skew with regard to the local surface geometry, which is curved. The aerodynamic skew angles are dependent on the local flow direction; at incidence, this varies around the circumference of the cowl and, therefore, so do the aerodynamic skew angles. This perhaps explains the relative insensitivity of the AJVG performance to the jet geometric skew angles.

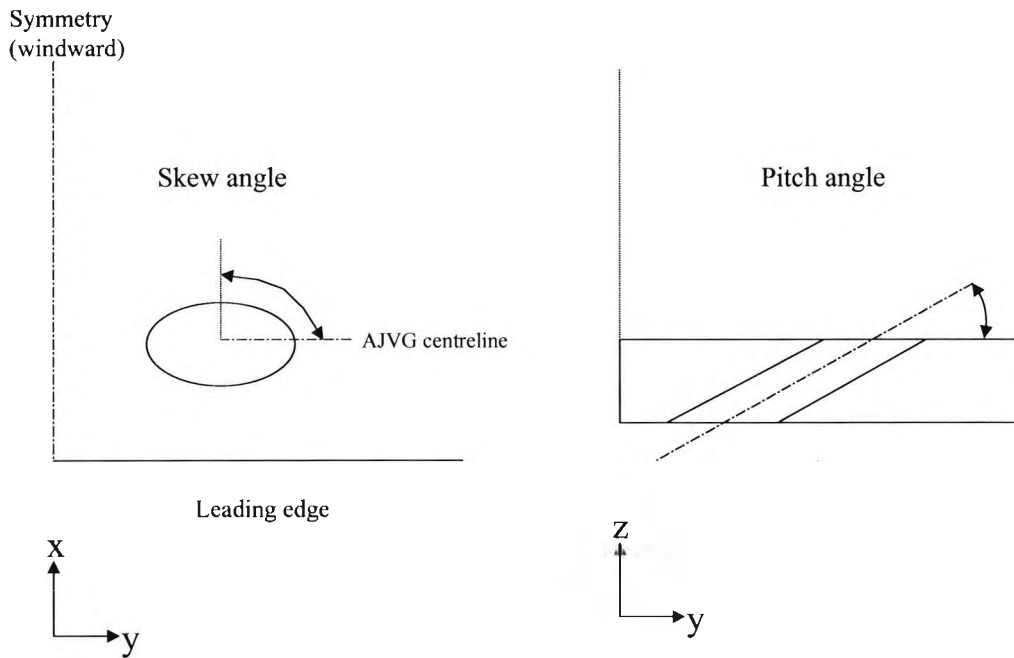


Figure 4-10: AJVG Pitch and skew angle definitions

The supply of high-pressure air to the model was regulated by a valve with a pressure indicator located next to the tunnel control panel. Large pressure losses were expected in the air supply between this valve and the model, so a more accurate measure of the lip blowing pressure needed to be determined. A GFM Mass Flowmeter (Aalborg, 2003) was installed downstream of the pressure control valve. This provided two functions. Firstly it provided the measurement of the high-pressure air mass flow entering the model; secondly, it permitted the single line from the house system to be spliced into the eight model supply lines.

A pressure tapping was installed into the lip plenum chamber to determine the blowing pressure at the lip. A transducer mounted on the model assembly was used to measure this pressure. The transducer was calibrated directly against a known pressure source and against the pressure reading on the indicator at the control valve to aid in the setting of the lip pressure during testing. The mass-flow used by the intake model AJVG installation was small compared to the requirement from the larger scale aerofoil models tested in T2. Consequently, the pressure measured at the control valve was unstable. This instability was not maintained at the lip plenum, most likely due to the large pressure loss in the supply system damping the fluctuations.

Repeatability runs were conducted over the duration of the test. The upstream pressure fluctuation had no influence on the performance of the AJVG system. Repeat points were taken during every session to check the instrumentation and the integrity of the pressurised components. Data repeatability for distortion and loss-coefficient are plotted in Figure 4-11. The recovery curves are almost identical but differences can be seen in the distortion curves at high incidence. This is not a cause for concern, because at this condition, the flow is massively separated. The important parameter is the onset of separation.

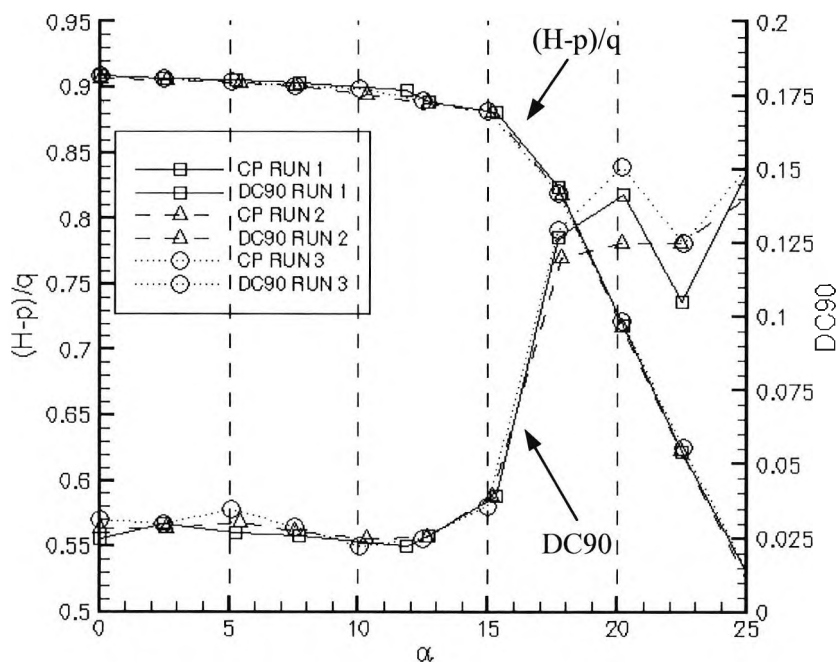


Figure 4-11: Repeatability of engine-face total pressure coefficient and DC90 for a blowing pressure ratio of 1.1

As the acrylic model was used for the AJVG installation, the presence of lip separation must be judged by engine-face data. The presence of an internal lip separation could be ascertained either by a drop in the total pressure measured at the engine-face, or by an increase in total pressure distortion. An increase in distortion could be measured directly using a total pressure distortion descriptor, or by viewing contours of total pressure at the engine face. During the test, the Rolls-Royce distortion descriptor $DC\theta$ was used, where the angular extent, θ was 90 degrees. Simpson's rule was used to integrate the total pressure in the eight 90-degree segments given by the rake. It would be possible to use a more complex hybrid

interpolation and integration method such as those discussed by *McGregor & Clark (1986)*, to obtain the more often used DC60. This was not done as the distortion descriptor was being used primarily as an indication of internal separation rather than a direct indicator of intake/engine compatibility.

4.3. References

American Institute of Aeronautics and Astronautics, 'Assessment of experimental uncertainty with application to wind tunnel testing', AIAA Standard S-071A-1999, 1999.

AGARD Ad Hoc Committee, 'Engine-Airplane interference and wall corrections in transonic wind tunnel tests', AGARD Advisory Report No.36, 1971

Bryer, D.W., Pankhurst, R.C., 'Pressure probe methods for determining wind speed and flow direction', National Physical Laboratory, HMSO, 1971.

Hacker, I.G., Hirst, W., 'Preliminary transonic tests to investigate the effects of lip shape on the internal performance of pitot intakes at very high incidence', ARA Model Test Note M110/1, 1978.

Doebelin, E.O., 'Measurement systems – application and design' 4th Edition, McGraw-Hill, pp58-73, 1996.

Innes, F, 'An experimental investigation into the use of vortex generators to improve the performance of a high lift system,' Ph.D. Thesis, City University, 1995.

Kline, S.J., McClintock, F.A., 'Describing uncertainties in single sample experiments', Mech. Eng., Vol 75, p3, 1953.

Maltby, R.L., 'Flow visualisation in wind tunnels using indicators' AGARDograph 70, April 1962.

Mange, R.L., 'Aerodynamics of a chined forebody oscillating in pitch' Ph.D. Thesis, University of Illinois at Urbana-Champaign , 1996.

McGregor, I., 'The characteristics and calibration of two types of airflow metering device for investigating the performance of model air intakes', RAE TR 71212, 1971.

McGregor, I., Clark, R., 'A note on the calculation of the Rolls-Royce flow distortion parameter $DC\theta$ ', RAE Technical Memorandum Aero 2086, HMSO, 1986.

Merzkirch, W., 'Flow visualisation' Second Edition, Academic Press, 1987.

Ower, E., Pankhurst, R.C., 'The measurement of airflow', 5th Edition, Pergamon Press, 1977.

Pope, A., Harper, John, J., 'Low-speed wind tunnel testing', John Wiley & Sons, 1966.

Simmons, M, - QinetiQ product manager experimental aerodynamics- Private communication regarding application of error analysis standards in major wind tunnel facilities, 1st February, 2004.

Thompson, J.S., 'Present methods of applying blockage corrections in a closed rectangular high speed wind tunnel.' RAE Report Aero. 2225, 1948.

Younghans, J.L., Hoelmer, W., Stockman, N.O., Low speed effects of Reynolds number and lip geometry on high bypass ratio inlet performance', AIAA-82-0059, AIAA 20th Aerospace Sciences Meeting, Orlando, Fl, USA, 1982

5. Analysis of air intake lip separation behaviour

5.1. Introduction

This chapter presents an analysis of the separation characteristics of a relatively sharp pitot intake under low speed operation. An integrated computational and experimental approach has been used whereby validated computational methods are employed to analyse combinations of design variables not accessible in the wind tunnel. A full description of the experimental arrangements and techniques is described in Chapter 4.

5.2. Validation of CFD techniques at low forward speed

To successfully use an interactive study using computational fluid dynamics and wind tunnel testing, it is first necessary to validate the CFD tools to determine how well the governing flow features are predicted. In Chapter 3, the Fluent CFD predictions were compared to experimental results at zero incidence and higher freestream Mach number than achieved in the tests of this study, but at appropriate mass-flow ratios. External and internal pressure coefficients were predicted well even under separation, leading to confidence in this software for intake flows. The experiments described in Chapter 4 provided the opportunity to further validate the CFD code particularly against intake performance and compatibility, such as recovery and distortion.

Figure 5.1 shows a comparison between computed and experimental values of DC90 with three engine-face contour plots for each curve. The engine-face plots correspond to incidence angles of 5° , 15° and 20° . It can be seen that the overall value of distortion is predicted reasonably well. It should also be noted that the values of DC90 are calculated for the CFD data by interpolating on to a rake matching that used experimentally. The experimental contours are constructed from these discrete rake locations, while the CFD contours use the full range of mesh points at the engine-face plane. This is responsible for some of the differences between the two sets of plot plots, particularly as the flow separates. Generally, the CFD predictions at low speed can be considered good, although as the separation becomes large the prediction of the complex three-dimensional motion is beyond RANS techniques. Our main interest is the prediction of separation onset and the initial flow mechanics of this separation rather than the highly separated flow itself.

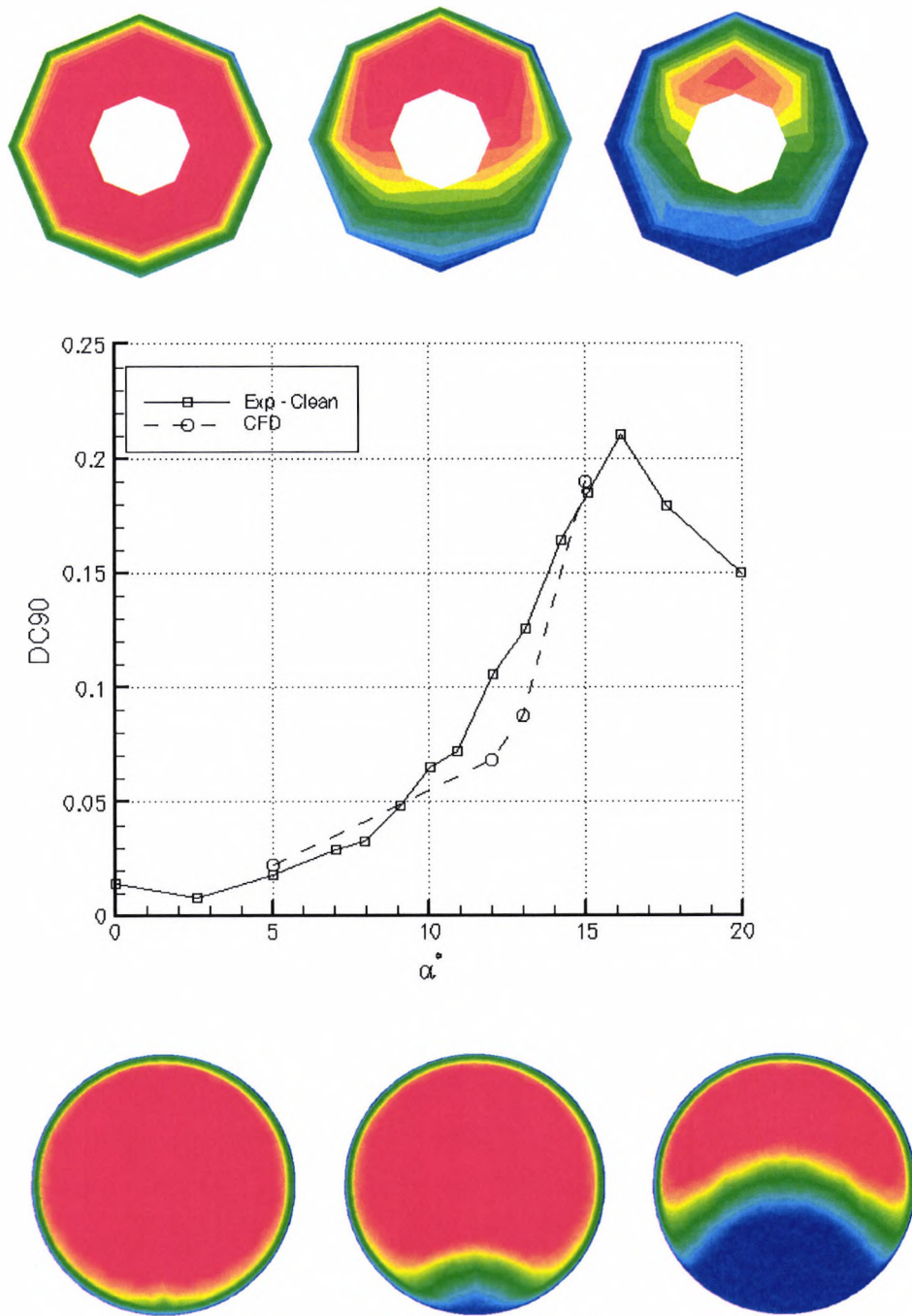


Figure 5-1: Experimental and CFD distortion comparison for cow19, $M=0.1$, $A_O/A_C=0.90$. Contour plots, left to right: 5° , 15° , 20° . Experiment top and CFD bottom.

5.3. Characteristics of intake internal performance at incidence

5.3.1. Pressure Recovery

The measured total-pressure recovery variation with incidence for a number of different intake mass flows is presented in *Figure 5.2*. Due to the low engine-face Mach number, the values of total pressure recovery are high and the fractional variation across the range is small. It is often more appropriate to use either total-pressure loss coefficient:

$$\frac{\Delta H}{q_\infty} = \frac{(H_\infty - H_{ef})}{q_\infty} \quad \text{Equation 5-1}$$

or the dynamic pressure recovery, which for incompressible flow may be assumed to be:

$$1 - \frac{\Delta H}{q_\infty} = \frac{(H - p_\infty)}{q_\infty} \quad \text{Equation 5-2}$$

Both these forms of performance indicator are advantageous for low speed work in that they stretch the performance variable over a larger range than total pressure recovery. This permits differences between performance characteristics to be easily identified. The dynamic-pressure recovery form is plotted in *Figure 5-3*. This will be used throughout this document as the primary indicator of internal performance at low freestream Mach number. The difference between the curves representing the different mass flow ratios, along with the variation in performance with incidence, are more readily identifiable in *Figure 5-3* than the total pressure recovery plot of *Figure 5-2*.

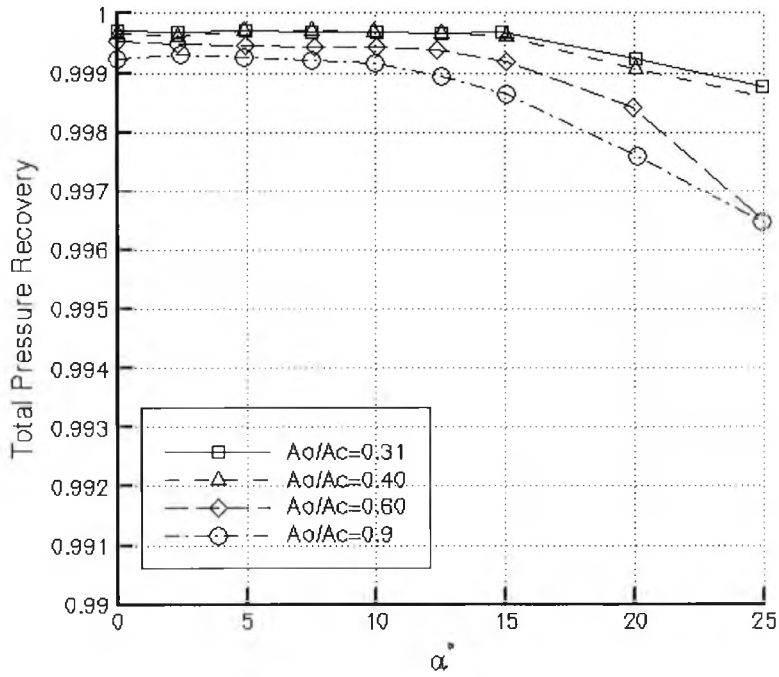


Figure 5-2: Intake total pressure recovery with incidence

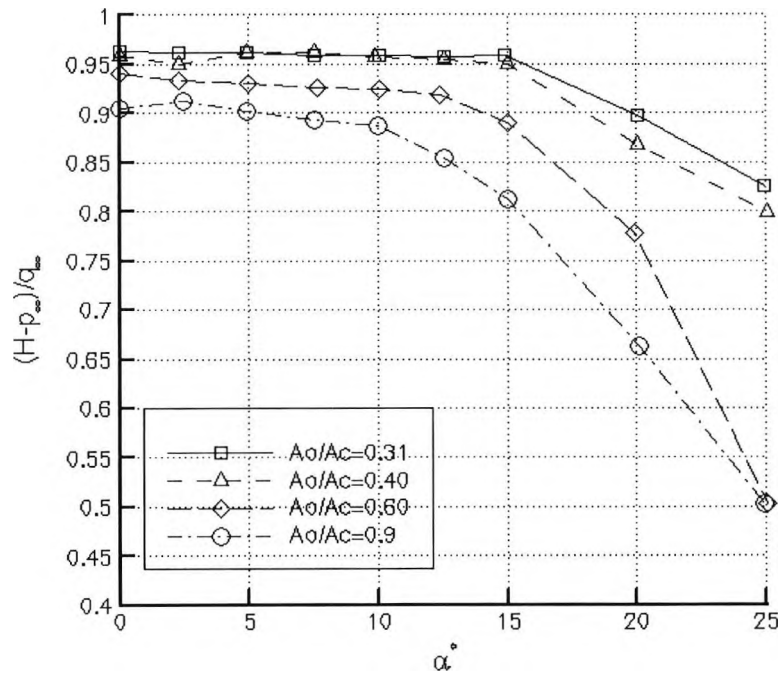


Figure 5-3: Dynamic pressure recovery variation with incidence.

The curves for these flow conditions may be divided into two components: an almost constant recovery as incidence increases, followed by a rapid decline in dynamic recovery with further increase in incidence. The first portion of the curve shows a very gradual decline in dynamic recovery as incidence is increased. This is due to the thickening of the boundary layer on the leeward side of the windward lip, resulting from the adverse pressure gradient around the lip. This is amplified by a further adverse pressure gradient due to the diffusion in the duct. The rapid decline of recovery with incidence that follows is due to the occurrence and growth of separation on the leeward side of the windward lip. The prediction and analysis of this separation will be discussed in detail in the following sections. Increasing mass flow has a detrimental effect on recovery. This is partly due to an increase of dynamic pressure in the duct and partly because increasing mass flow forces the stagnation line further around on to the windward lip at incidence, thereby increasing turning losses. The effect of increasing mass flow in moving the stagnation line is also responsible for reducing the incidence at which the rapid drop in recovery is initiated, i.e. the incidence at which appreciable separation is first seen to occur. For example, in Figure 5.3, the effect of separation is first seen at around 15° for the lowest mass flow, but at 10° for the highest mass flow.

5.4. Determination of internal separation

5.4.1. Comparison of methods

Hoelmer et al (1987) have shown the onset of external separation may be determined in the wind tunnel by monitoring the pressure in the vicinity of the intake-lip leading edge. Results collected in this manner complemented spillage drag measurements, which indicated the onset of appreciable external lip separation with a sudden increase in the external drag. This is because the cowl thrust does not balance the force on the pre-entry streamtube after separation occurs at the lip. This method has been applied to determine the onset of internal separation and is compared to other likely indicators of internal separation for validation. Figure 5-4 shows the variation of static pressure at a number of fixed locations on the leeward side of the windward lip as incidence is increased for a fixed intake mass-flow. The pressure tap locations described in the key should be cross-referenced with the instrumentation layout described in the Appendix for detailed descriptions of the tap locations.

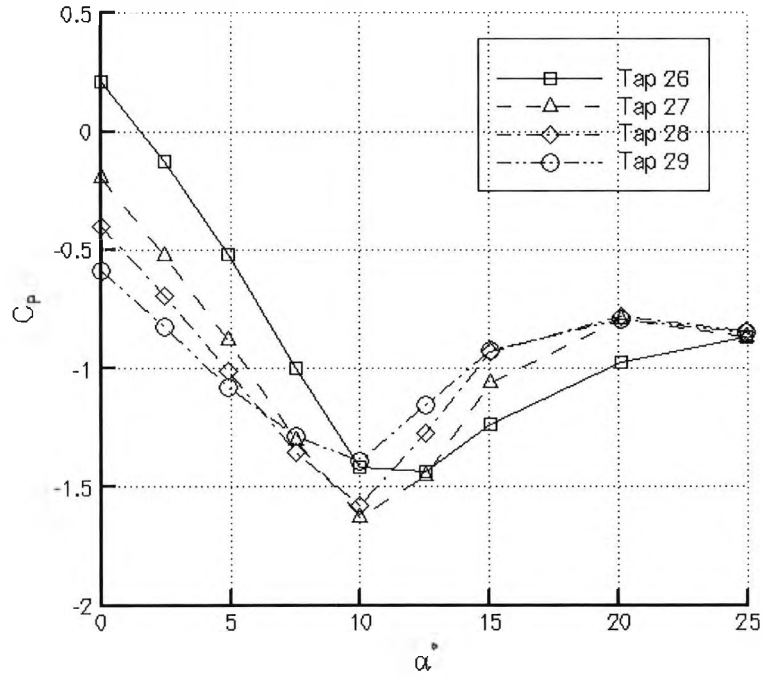


Figure 5-4: Pressure coefficient traces at fixed locations with varying incidence, $Ao/Ac=0.9$.

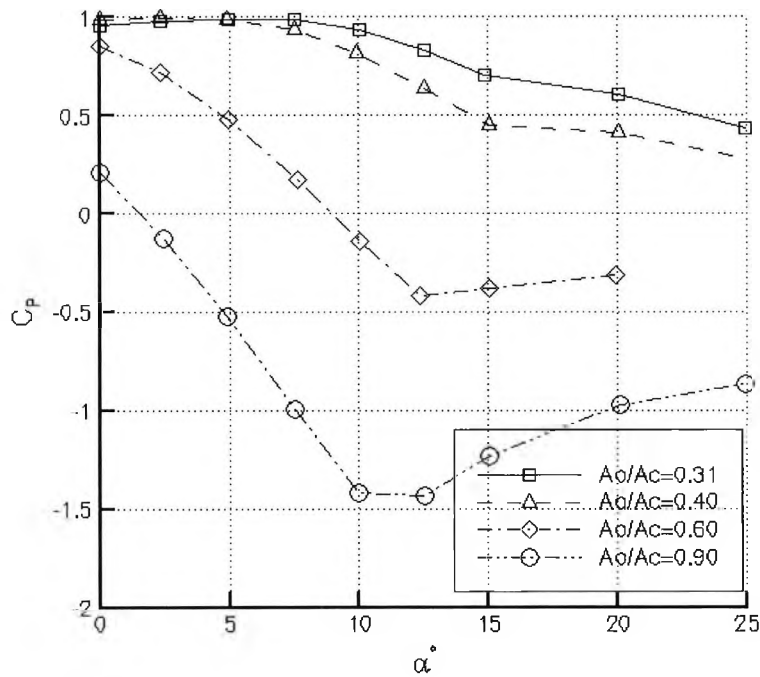


Figure 5-5: Pressure traces at Tap 26 ($x/D_{max}=0.0098$)

The pressure taps that span a x/D_{\max} range from 0.0098 to 0.0343 initially indicate a near-linear increase in magnitude of suction, as the incidence is increased. A critical incidence angle is then reached at which the suction can no longer be maintained and the flow around the lip separates. As the incidence increases beyond this point, the magnitude of the suction at first decreases linearly, as the separation bubble inside the lip develops. When the separation inside the lip becomes very large, at high incidence angles, the reduction in suction with incidence becomes more gradual. From Figure 5.4 may be determined that separation occurs between 10° and 12.5° for all the pressure tap locations plotted. The assumption can be made that when the loss of suction representing lip separation occurs, the extent of the separated region increases almost instantly as the suction loss occurs over the whole vicinity of the lip at the same time. This implies a bubble bursting separation type.

The pressure coefficient at the pressure tap located at $x/D_{\max}=0.0098$ has been plotted for four different mass-flows in Figure 5.5. As mass-flow ratio is decreased, the critical incidence angle at which separation occurs increases in value. The method for predicting the onset of separation can be cross-referenced to the dynamic pressure recovery shown in Figure 5.3. The inflection points in the two sets of curves correspond, linking the reduction in pressure recovery to the wall static pressure near the lip.

5.4.2. Increasing incidence at fixed mass flow

The influence of increasing the angle of incidence for a fixed mass flow on the cowl windward centreline static pressure distribution can be seen in Figures 5.6 and 5.7 for mass-flow ratios of approximately 0.89 and 0.65 respectively. The external surface has been plotted in the negative axial sense for clarity. The higher mass-flow case in Figure 5.6 shows that the stagnation point close to the leading edge moves fractionally aft along the external cowl as the incidence is increased. In contrast, the peak suction experienced on the internal lip moves forward toward the leading edge. In almost all of the pressure distributions on the internal surface, there is a discontinuity in pressure gradient at approximately $x/D_{\max}=0.066$. This location is the geometric throat and corresponds to a discontinuity in surface curvature. Only the tangents of the lip and the diffuser lines are continuous at this station.

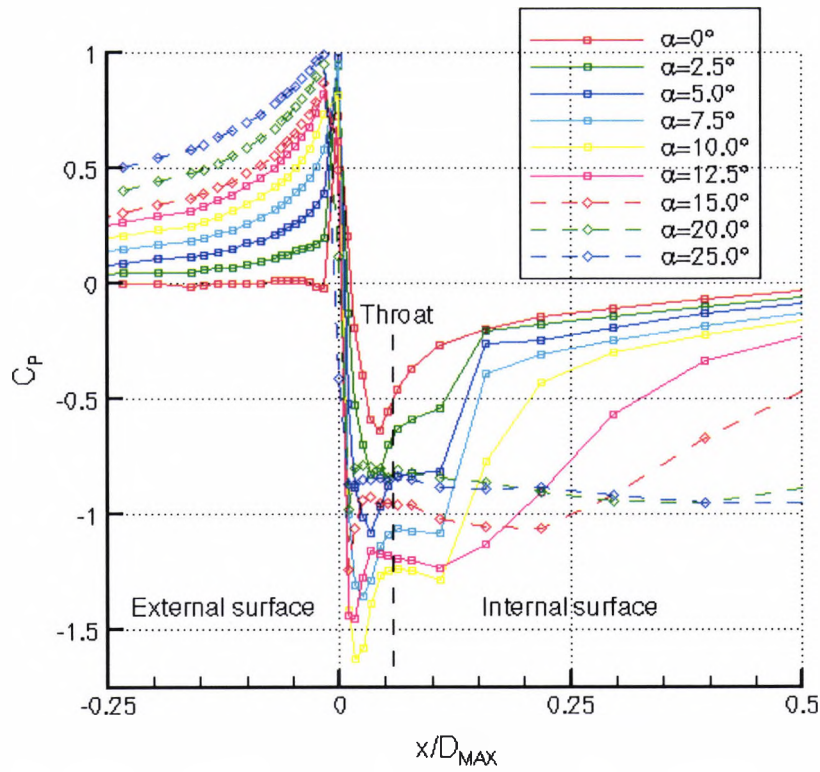


Figure 5-6: Windward lip internal and external pressure variation with incidence at fixed mass-flow, $A_0/A_C=0.89$.

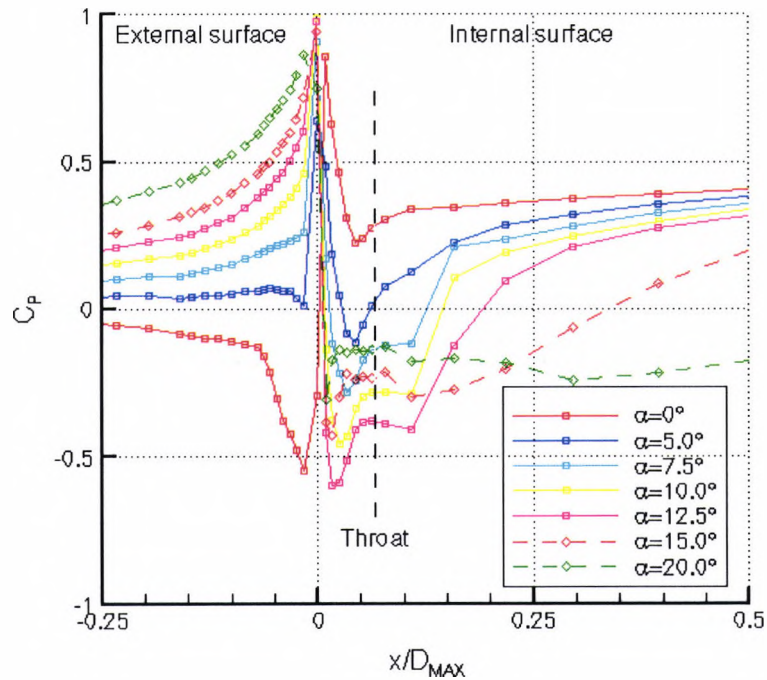


Figure 5-7: Windward lip internal and external pressure variation with incidence at fixed mass-flow, $A_0/A_C=0.65$

The length of the throat is zero. This results in an interaction between the lip and the duct. The discontinuity leads to a flat section in the pressure distribution, that at incidences lower than the separation onset indicated by Figure 5.4, is terminated at approximately $x/D_{MAX}=0.13$. It may be possible that the discontinuity at the throat is causing a small separation, but this anomaly is most likely due to the interaction of the diffuser with the accelerating flow approaching the throat. This phenomenon is noticeable on results presented by *Hacker et al (1985)*, for this cowl at the higher Mach number of $M=0.4$. The low speed of this test may serve to amplify this feature. This is further discussed in Section 5.4 with regard to the global development of separation within the cowl.

When the incidence angle has exceeded 10° , the angle above which the dynamic-pressure recovery plot (Figure 5.3) and the lip static pressure (Figure 5.4) indicate separation has occurred, there is a noticeable change in the internal pressure-coefficient at the lip. Firstly, the magnitude of the peak suction starts to reduce. Then the compression does not occur immediately after the throat, but is stretched out, reaching the downstream pressure in the duct over a larger axial extent and, therefore, at a reduced pressure gradient. As the incidence angle is further increased, the extent of the implied separation becomes larger, passing downstream of the throat; the pressure gradient in the diffuser becomes shallower still.

A qualitative insight into the development of the separation may be obtained from Figure 5.8. This shows computed Mach number contours on the symmetry plane for a mass-flow ratio $A_O/A_C=0.89$. The pressure distribution of Figure 5.6 corresponds to the lower lip. At this low Mach number, the exact prediction of the onset of lip separation by RANS methods, such as those presented here, may not be obtainable. However, the 2.5° difference between data points should mean the predicted flow physics are a reasonable indication of the development of the physical features within the data point spread. The calculations for values of incidence above which large-scale separation has occurred should be considered as illustrative only, as RANS methods are not appropriate for dealing with a large separation such as is present, which is most likely unsteady.

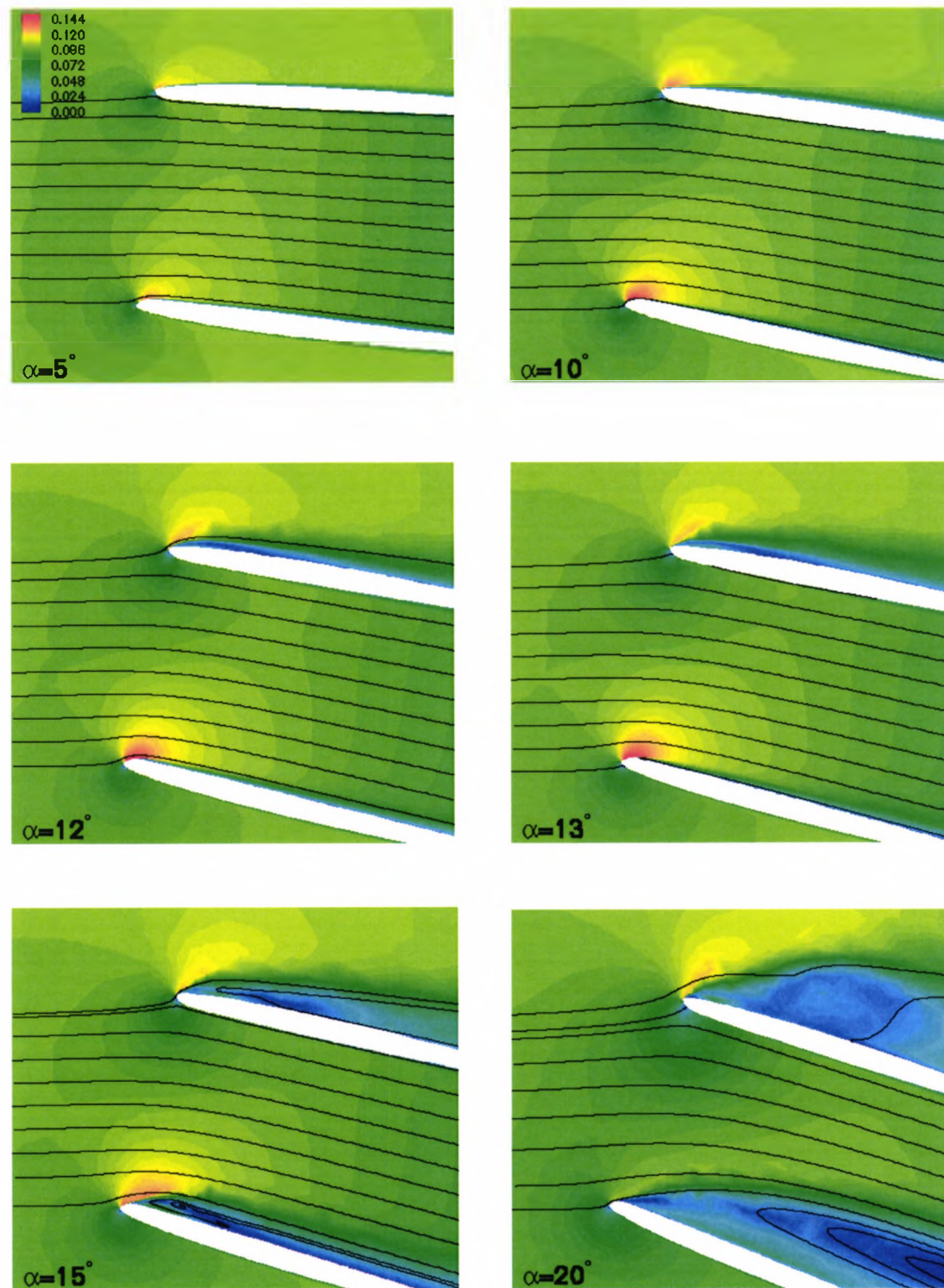


Figure 5-8: Computed Mach number contours on symmetry plane for increasing incidence at fixed mass-flow, $A_0/A_C=0.89$

The selected incidence angles presented in Figure 5.8 show how increasing the incidence angle causes the local velocity to rise on the leeward side of the windward lip. The acceleration around the leading edge of the lip creates the suction, thus increasing the amount of diffusion required in the duct. The static pressure downstream in the duct is fixed by the engine demand, or exit throttle setting in the wind tunnel. This may be considered similar to the Kutta condition in aerofoil theory. At $\alpha=12^\circ$, there is a noticeable thickening of the boundary layer aft of the throat. By 15° incidence, there is a noticeable separation; the flow leaves the lip surface between the leading edge and the throat. The re-circulating region extends into the throat and most likely reattaches, leaving a low Mach number region to develop along the lower cowl. A further increase in incidence shows the separation line has moved forward and the reattachment line has moved further aft.

For the lower mass-flow ratio shown in Figure 5.6, a similar pattern is evident except that the reduced mass-flow ratio through the duct subdues the tendency towards leading-edge separation. The peak suction is reduced, leading to a smaller pressure gradient and thus separation occurs at a higher incidence angle.

5.5. Development of three-dimensional internal separation

Experimental data representing the variation of the pressure coefficient on the internal surface of the intake as the angle of incidence increases is shown in Figure 5.9, as a series of carpet plots, for $A_O/A_C=0.89$. The axis labelled θ , is the angular variation around the cowl. The top (crown) of the intake is at 0° and the bottom (keel) or windward lip is at 180° . The iso-contour lines are of pressure coefficient. The plots are constructed by rotating the intake model in the wind tunnel at thirty-degree intervals over 180° to build the surface. The upper graph in the Figure represents $\alpha=7.5^\circ$. At this small incidence angles a cross flow pressure gradient has been established, $\left(\frac{\partial p}{\partial \theta}\right)$. The pressure gradient is sinusoidal in form as the stagnation line moves from the external cowl at the keel to the internal lip at the crest. This is also evident (but not shown) in the computations of Figure 5.8.

Away from the lip, near the maximum plotted value of x/D_{MAX} , the circumferential pressure gradient has been reduced, giving an almost constant value of pressure coefficient. This is evident at all angles of attack, with the three-dimensional separation controlling the magnitude of the pressure gradients. As the incidence is increased above 7.5° , the minimum pressure region on the keel increases in extent. This results in an increase in the axial pressure gradient aft of the throat, because the downstream pressure must be fixed by the engine demand (throttle setting). In addition, in the circumferential direction, the pressure gradient is increased because the stagnation point remains at the same axial station on the crown, thus fixing the location of the maximum value of pressure coefficient. The increase of incidence forces the flow on the windward lip to require additional turning to follow the surface contour. The additional turning and the circumferential pressure gradient lead to the onset of flow separation at the lip. This is maintained by the axial pressure gradient in the duct. At the maximum incidence angle presented, 20° , the separation at the lip extends over a sixty-degree sector of the half intake and a large axial extent.

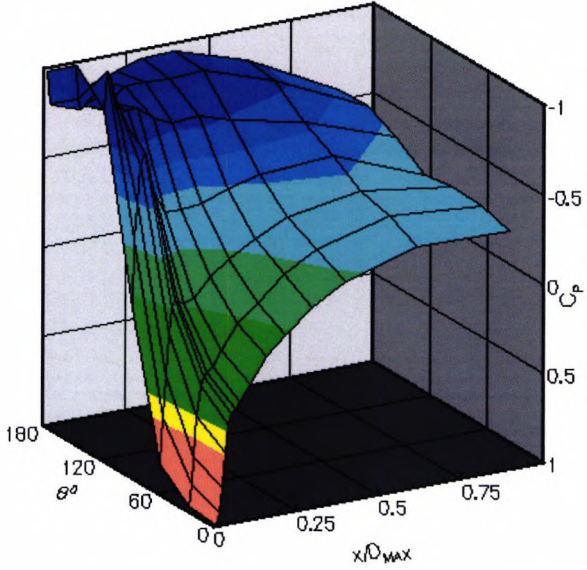
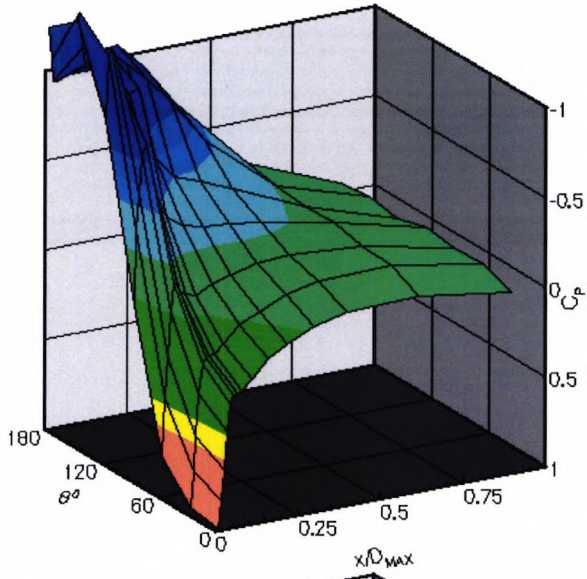
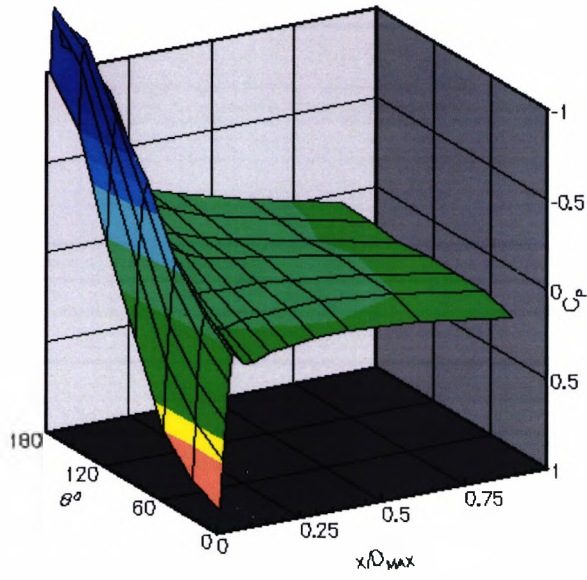


Figure 5-9: Internal separation at $Ao/Ac=0.89$ Top to bottom, $\alpha=7.5^\circ$, $\alpha=15^\circ$, $\alpha=20^\circ$, contours of pressure coefficient.

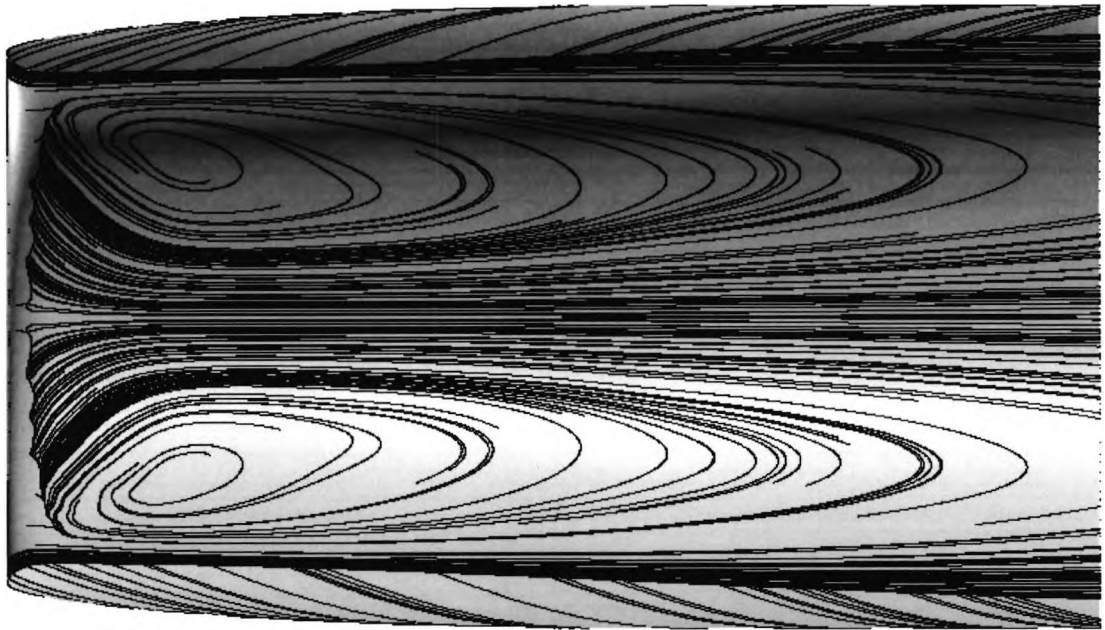
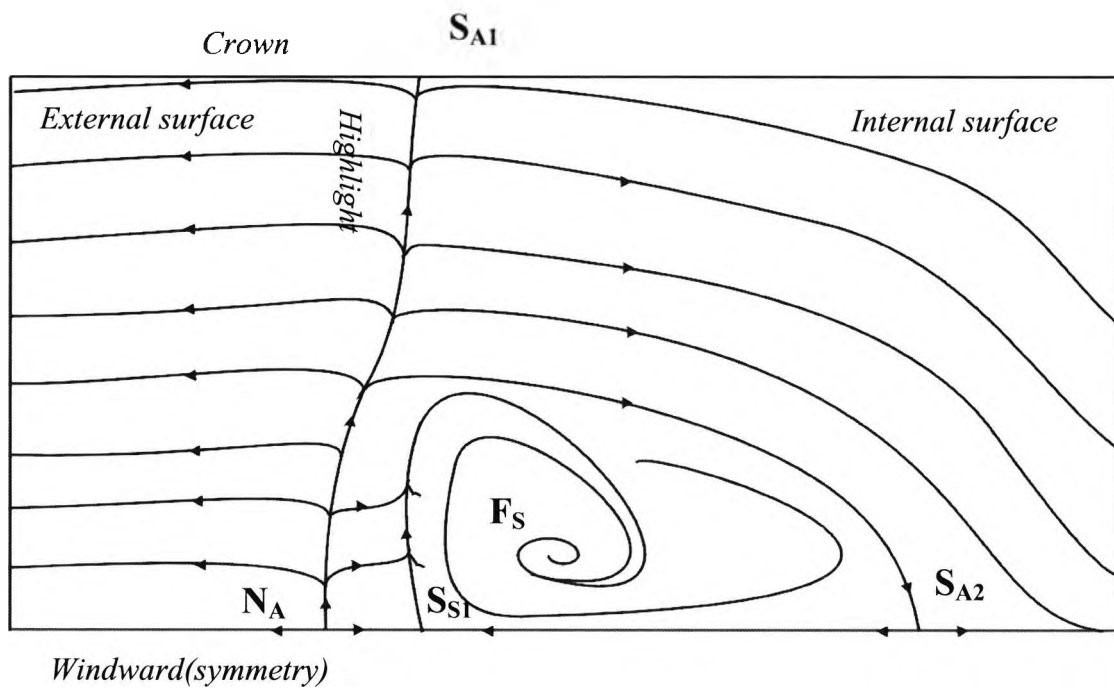


Figure 5-10: Computed limiting streamlines $\alpha=20^\circ$, $M=0.1$ $Ao/Ac=0.89$

The discontinuity in pressure at the throat has already been discussed (see Figure 5.6) is also evident on the carpet plot, Figure 5.9. This discontinuity shows up as ridge in the surface that runs the full circumferential extent of the throat. This is evident at all incidence angles.

Figure 5.10 shows computed surface limiting streamlines for the 20° case of the forward section of the cowl viewed from above, with the top half removed to provide viewing access. The computation was performed for the half-model only, using a symmetry plane, and has been reflected. The reader's attention is drawn to Figure 2-10 in the literature review, taken from Hurd (1976), which shows the same flow features recorded at a higher Mach number in a larger scale facility, ARA's TWT. Primarily a pair of large spiral nodes are situated immediately aft of the throat with the separation occurring at the lip. Hurd (1976) noted that, at incidence angles greater than 16° , there was no identifiable indicator of imminent separation, as the suction peak on the windward lip was well subsonic, and separation was occurring in the presence of less severe recompressions that, in other lower incidence cases, maintained attached flow. He hints at the three-dimensional nature of the windward

lip flow as a possible source of this anomaly. The surface plots of Figure 5.9 confirm this hypothesis by displaying the circumferential pressure gradient that may serve to drive the separation as much as the axial-flow development. In his experiment, Hurd only had pressure instrumentation on the windward and leeward lips and thus could not develop an insight into the full nature of the circumferential pressure gradients.



- | | | | |
|-------|----------------------------|-------|----------------------------|
| N_A | Node of attachment | F_S | Focus of separation |
| S_A | Saddle point at attachment | S_S | Saddle point at separation |

Figure 5-11: Schematic of internal flow separation on a ducted body

From flow visualisation analysis conducted in the wind tunnel or from CFD computations, it is possible to construct the topology of three-dimensional separated flow by analysis of the surface skin-friction vector-field, with particular regard to the singular points contained within. Figure 5.11 shows a sketch of the dominant skin-friction lines. It is constructed using observations made in the wind-tunnel experiment coupled with CFD calculations. The Figure shows a symmetric half of the cowl, the symmetry plane being the windward generator. The model is split on the leeward side and unrolled about the model centreline. It is then unfolded at the leading edge to present a planar representation of the three-dimensional intake shape. The singular

points denoted by N , S and F correspond to nodal points, saddle points and foci, respectively. The subscripts S and A imply a relationship with an attachment or separation. In Figure 5.11, a pitot intake is considered at a positive incidence and a corresponding mass-flow ratio large enough to cause a separation inside the windward lip. The external flow attaches to the body by means of a nodal point of attachment (N_A) located on the external surface of the windward lip on the symmetry plane. Emerging from the nodal point of attachment, the attachment line, the dividing line between external and internal flow, follows the circumference of the intake lip in the leading-edge region. The annular nature of the intake means that the two opposite paths followed by the attachment line around the lip must meet at the crown of the intake, the external leeward side. This point must therefore be a saddle point. In Figure 5.11, this is termed a saddle point of attachment, S_{A1} . Although not pictured in Figure 5.11, it is hypothesised that the flow must leave the body in an opposite but similar manner, which is with a node of separation accompanied by a saddle point of separation on the opposite surface. If the reader's attention is briefly turned from Figure 5.11 to a more trivial lower incidence case in which the flow remains attached over the entire surface of the body, the only singular points will be the nodes of separation and attachment and their accompanying saddle points. This hypothesis leads to the proposal of an additional rule to those presented by *Peake & Tobak (1980)*, and that is that for ducted bodies, the number of nodal points equals the number of saddle points.

$$\sum N - \sum S = 0 \quad \text{Equation 5-3}$$

In the case of Figure 5-11, we have four nodes. The attachment node (N_A) and one foci (F_{S1}) which are shown, in addition, not pictured, we have one foci from reflection in the symmetry plane (F_{S2}) and the node of separation at the downstream end of the body (N_S). We also have four saddle points; shown are the saddle point of separation (S_{S1}) and attachment (S_{A2}) which enclose the separation along with the saddle point of attachment (S_{A1}) for the stream tube. Not shown is the saddle point of separation as the flow leaves the duct (S_{S2}).

The internal flow of Figure 5-11, is dominated by a focus of separation, F_S . In the region of the windward lip, the streamlines originating at the attachment line on the

external surface pass over the leading edge and converge on a separation line running nearly parallel to the leading edge. The strength of the cross-flow pressure gradient forces the dividing surface emanating from the separation line to spiral up into the focus of separation, F_S , in the manner described by *Peake & Tobak (1980)*. The pair of spiral nodes is enclosed by a further pair of saddle points located on the symmetry plane. The saddle point of separation, S_{S1} , is the midpoint of the separation line. The saddle point of attachment, S_{A2} , is located downstream, at the termination of the separated region. This is consistent with equation 5.3. The combination of a pair of spiral nodes enclosed by a pair of saddle points is also present in other internal flow applications. For example, the spiral node/saddle point combination is present in classical s-duct flow in which separation is forced on the inside bend by the cross-flow pressure gradients.

5.6. Determination of external separation

Reducing the mass-flow ratio for a fixed incidence angle moves the streamtube attachment line further inside the cowl. This results in the flow requiring more turning to negotiate the lip, leading, in turn, to lower pressures and larger adverse pressure gradients. Figure 5.12 shows the pressure distributions on the external surface, as the mass-flow ratio is reduced at $\alpha=0^\circ$. As the leading-edge suction can no longer be maintained, the flow separates from the cowl, noticeable by the pressure plateau near the leading edge in the pressure distributions. In all cases, when separation occurs, it is very close to the leading edge. When the mass-flow ratio has been reduced to 0.48 the flow separation becomes fixed at the leading edge. The extent of the separation increases in magnitude with reducing mass flow so that nearly half of the external cowl is in separated flow at the lowest mass-flow condition.

At the lowest mass flow, the Mach number and mass-flow-ratio are representative of that expected for a windmilling engine at take-off: a case for which twin-engine, civil aircraft engine intake cowls are designed to achieve attached flow. This cowl, which is notably sharper in comparison, separates well before this design point.

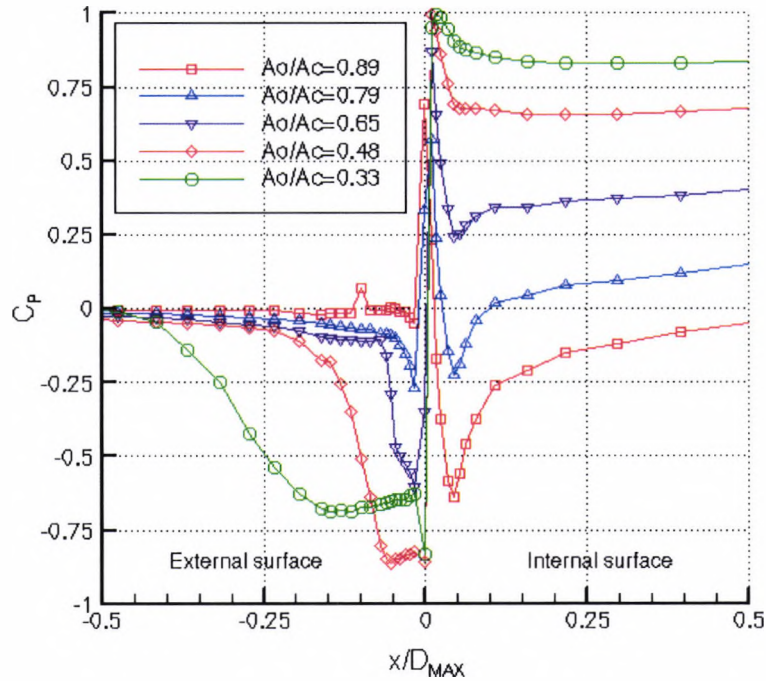


Figure 5-12: Pressure distribution at zero incidence for reducing mass-flow ratio

The method of using lip static pressure variation to indicate the onset of separation has been validated in this study for indicating internal separation by comparing with the engine-face performance and compatibility parameters, recovery and distortion. This method has been shown to indicate external separation by a corresponding cowl drag rise (Hoelmer et al ,1987).

Figure 5.13 shows the variation in static pressure coefficient at a number of pressure measurement stations on the external cowl at zero incidence for reducing mass-flow ratio. The most aft location (tap 15) indicates a change in gradient at a slightly lower mass flow, but this tap is somewhat back on the cowl and is not affected by the separation, until the mass flow is substantially reduced. All the taps in the leading-edge region indicate separation occurs at the same mass-flow ratio. This suggests a sudden change in the flow, rather than a gradual increase in separation size, although there is quite a range in mass flow between the data points.

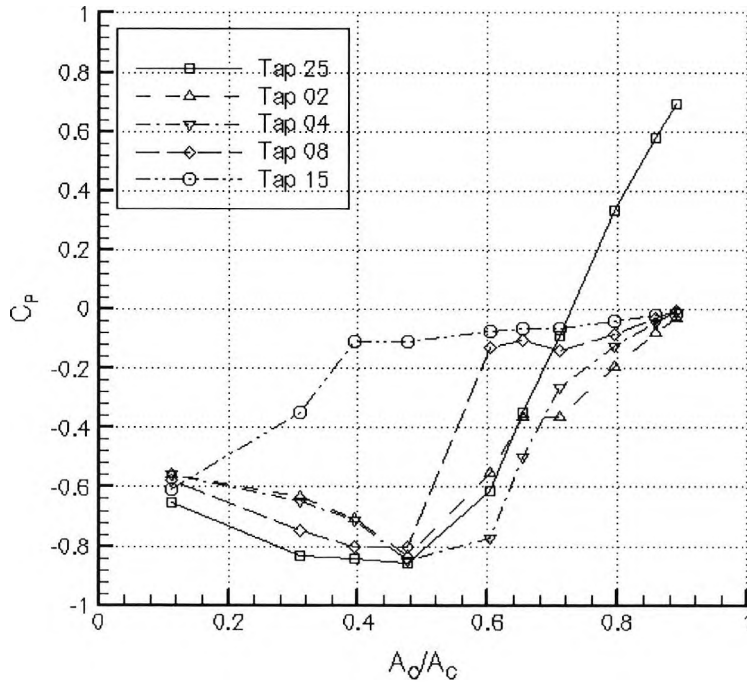


Figure 5-13: Different external cowl pressure variation with reducing mass-flow ratio, $\alpha=0^\circ$.

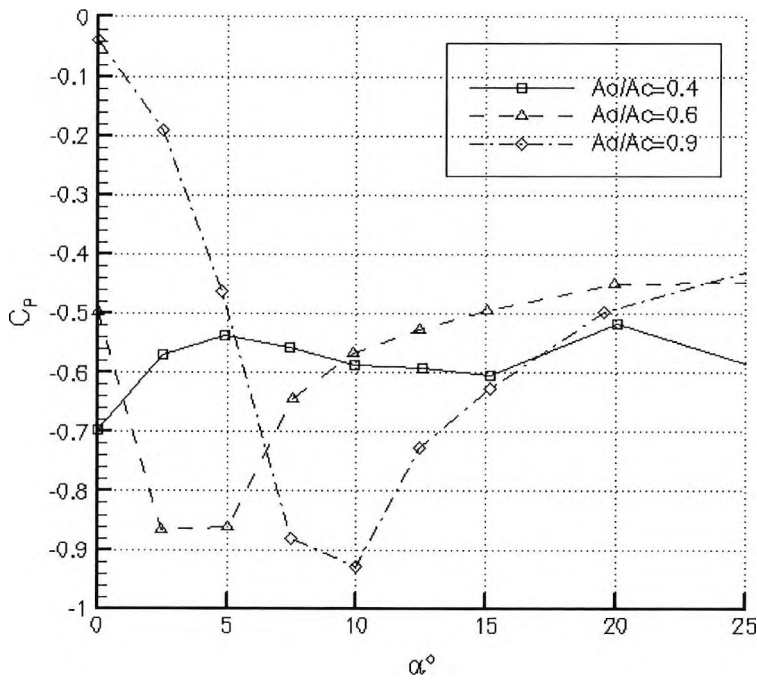


Figure 5-14: Experimental prediction of external separation for different mass-flow ratios at tap 4.

Figure 5.14 shows the change in pressure coefficient on the external cowl at tap 4, (located at $x/D_{MAX}=0.039$) as the incidence angle is increased at fixed mass flow. For the mass-flows of $A_O/A_C=0.6$ and 0.9 the external flow separates as the positive incidence is increased. As would be expected at positive incidence, the flow on the cowl separates at lower incidence for lower mass-flows. In fact, the lowest mass flow plotted on Figure 5.14 is separated at all conditions. After separation has occurred, the curve takes the form of a gently decreasing slope, which corresponds with the reduction in the suction peak at the leading edge, as the extent of the separation grows with incidence. This can be seen in more detail in Figure 5-15, which shows the development of the external pressure distribution as incidence is increased for a fixed mass-flow ratio of approximately $A_O/A_C=0.9$. Initially the pressure distribution takes the form of an expansion from the attachment point inside the cowl, around the lip to the suction peak. A smooth recompression, followed by a gradual decline, returns the cowl pressure to freestream conditions. For incidences above which separation occurs on the external cowl at approximately $\alpha=10^\circ$, the magnitude of the suction peak reduces as incidence increases further. The symmetry plane cuts (extracted from a 3-D calculation) shown in Figure 5.8 may be used to qualitatively aid in the visualisation of the separation. Of course, this is only a two-dimensional view of a three-dimensional problem. As has already been shown for the internal separation, these calculations agree well with the experiment, as would be expected from a validated CFD method. At 10° , the boundary layer has undergone a noticeable thickening due to the adverse pressure gradient aft of the leading edge. By 12° , a separation is evident on the forecowl, which grows in magnitude as the incidence is increased up to 20° . The extent of the separation at 20° and above was such that convergence difficulties were encountered. Solutions were not obtained above 20° incidence, because the 3-D separation is most likely unsteady. Evidence of this can be seen in some of the experimental pressure distributions at 25° , which show 'bumpy' pressure distributions, evidence that the pressure is fluctuating with time. In addition, at large incidence angles, the separated shear-layer is no longer located within the refined areas of the computational mesh that are intended to capture such features. Even at smaller incidences, the separated shear layers are not always aligned with curvilinear 'c-grid' around the lip, although efforts were made to keep the cell aspect ratio close to unity to nullify this problem.

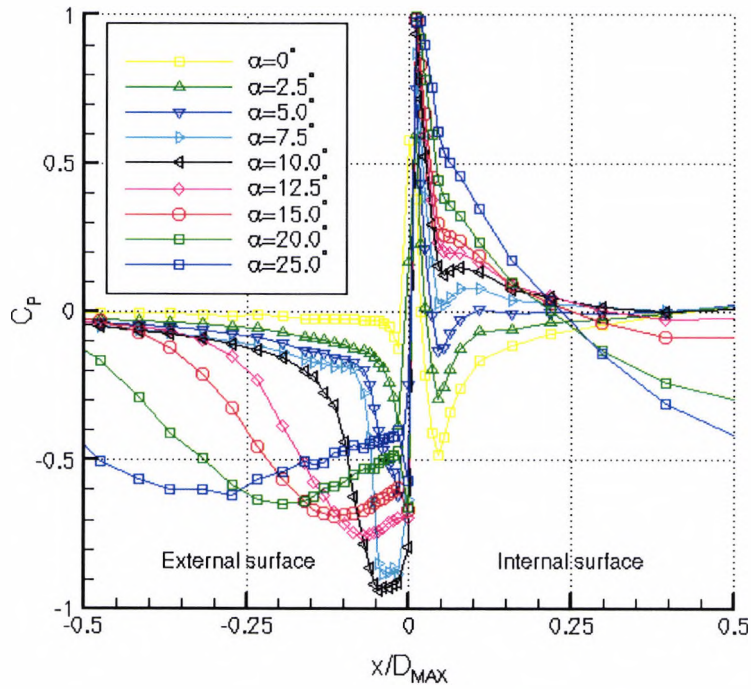


Figure 5-15: Crown pressure coefficient at $A_o/A_c=0.88$ for increasing incidence

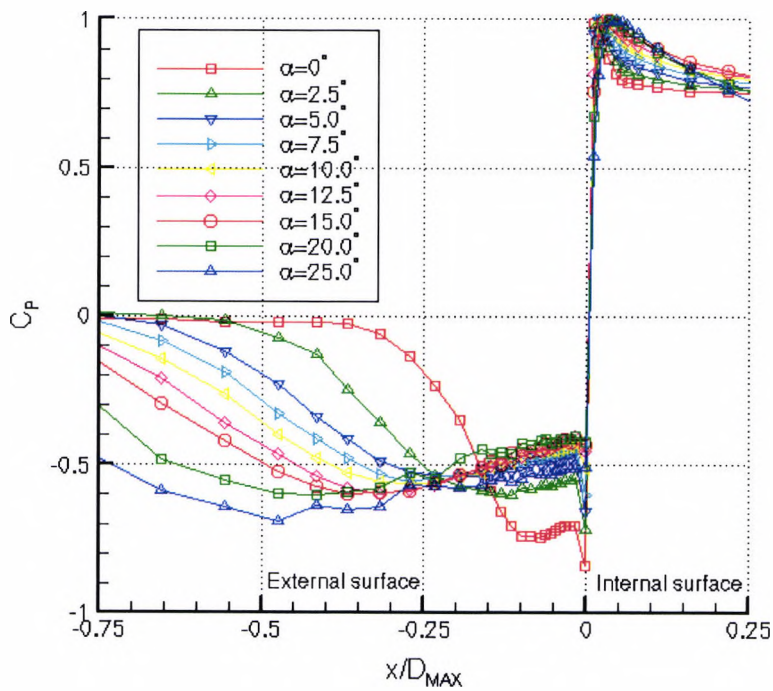


Figure 5-16: Crown pressure coefficient at $A_o/A_c=0.4$ for increasing incidence

Figure 5.16 is a similar plot to Figure 5.15, with the exception being that this is for a much smaller mass-flow-ratio, $A_O/A_C=0.4$. Note the translation of the scale on the x-axis to show a larger extent of the external flow. This mass-flow ratio and Mach number combination is representative of engine failure during take-off. From Figure 5.14, it can be seen that this mass flow at zero incidence angle, is sufficient to cause external separation. The addition of incidence compounds the low mass-flow ratio effect, increasing the extent of the separation on the cowl. Due to the sharp nature of cowl 9 (large L/D_{MAX}), it would not be appropriate for civil aircraft applications, particularly twin engine aircraft, despite its good high-speed drag characteristics (Figure 2.4). This is an area of potential application for flow control; modifying the 'engine-out' performance of the lip, so that the lip could be designed for cruise efficiency. During the landing procedure, when the engine throttle may be set at idle, the intake may be operating at an even lower mass-flow ratio, $A_O/A_C=0.2$ (Radespiel *et al*, 1990). At this condition, flow separation is predominately a noise issue and likely to increase in priority in the near future.

5.7. Development of three-dimensional external separation

In order to propose flow control systems for manipulating the external separated flow on a nacelle type configuration, it is necessary to develop an understanding of the fundamental fluid mechanics that lead to the occurrence of the separation. As was shown in the literature review, the traditional understanding of external intake separation has been based upon two-dimensional aerofoil analysis, but as other references indicate, this is a three-dimensional problem. Therefore, the three-dimensionality of the problem needs to be considered to truly understand the phenomena. Figure 5-17 shows the pressure distribution on the cowl in three-dimensions for a mass-flow ratio of $A_O/A_C=0.89$ at three incidence angles pictured top to bottom as 7.5° , 15° and 20° . Figure 5-18 shows the same plot layout for the 'engine-out' mass-flow-ratio of $A_O/A_C=0.4$. From Figure 5-17, it can be seen that the effect of an addition of a small incidence angle is to focus the negative pressure on the intake crown ($\theta=0^\circ$). The recompression to freestream static pressure experienced at the aft of the intake occurs smoothly in both the axial (x/D_{MAX}) and circumferential (θ) directions.

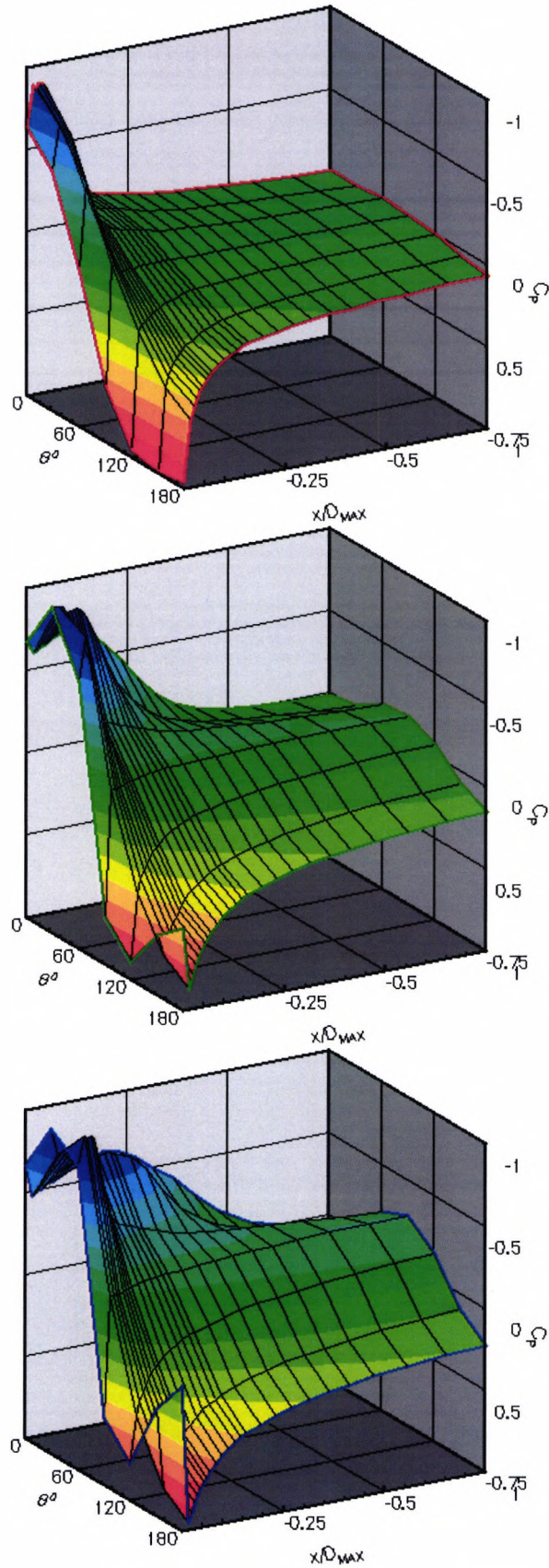


Figure 5-17: External pressures at $A_o/A_c=0.89$ top to bottom, $\alpha=7.5^\circ$, $\alpha=15^\circ$, $\alpha=20^\circ$, contours of pressure coefficient.

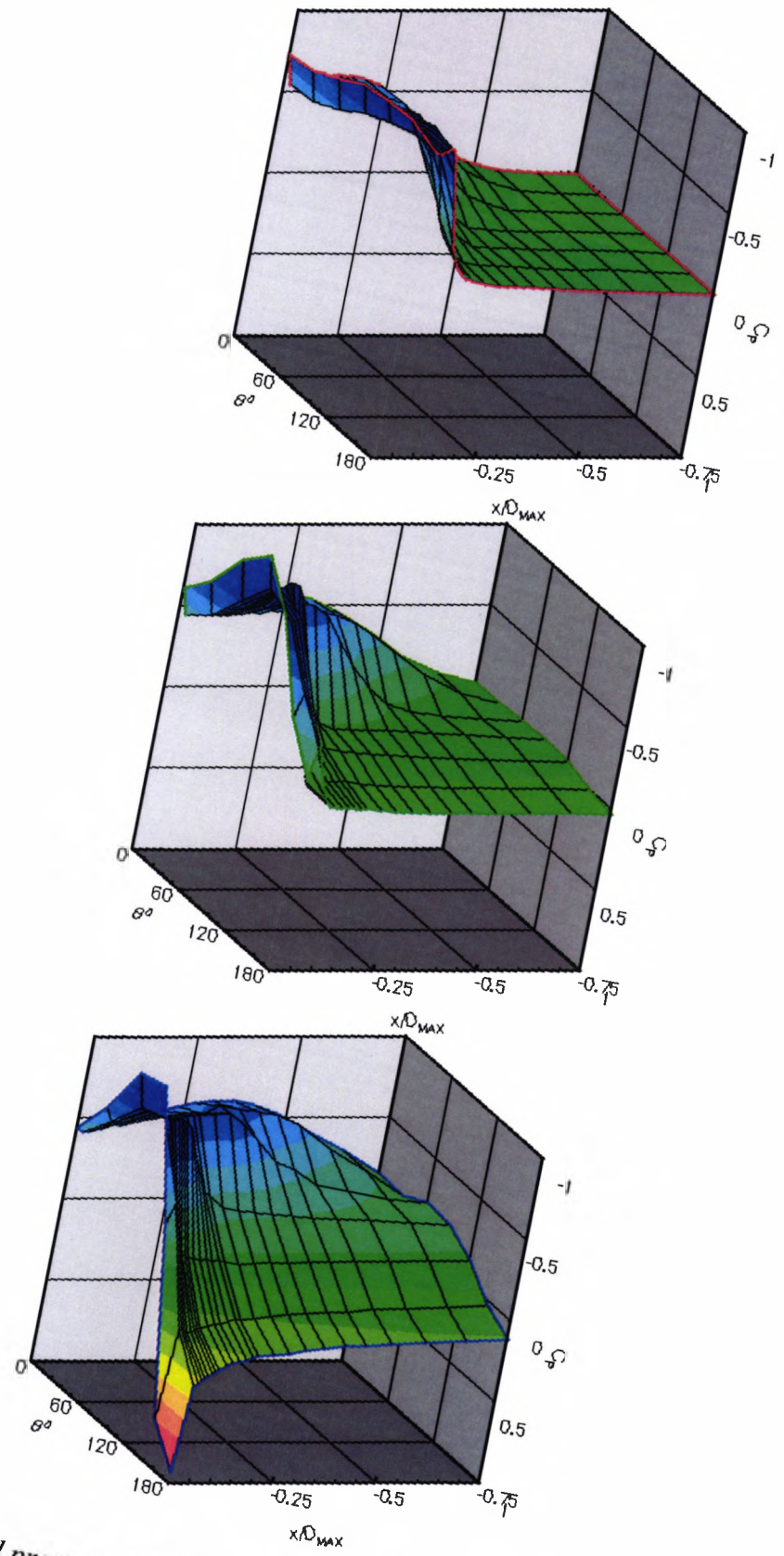


Figure 5-18: External pressures at $Ao/Ac=0.4$ top to bottom, $\alpha=2.5^\circ$, $\alpha=7.5^\circ$, $\alpha=15^\circ$, contours of pressure coefficient.

At $\alpha=15^\circ$, the plot becomes more complex, because the streamtube attachment line now crosses from the internal surface to the external surface at the keel ($\theta=180^\circ$) and, in doing so, increases the circumferential pressure gradient. At the crown, the stagnation line has moved further inside the duct, increasing the extent of the low pressure region on the cowl. This further increases the circumferential pressure gradient as well as the axial pressure gradient.

At the relatively low mass-flow ratio of $A_O/A_C=0.4$, separation is already present on the external cowl at zero incidence. Thus, a slightly smaller incidence range is used to show the development of the separation in Figure 5-18. The images represent 2.5° , 7.5° and 15° . At $\alpha=2.5^\circ$, the separation is still distributed around the circumference of the cowl and is due primarily to the low mass-ratio. At $\alpha=7.5^\circ$, the incidence has focused the separation towards the crown, but a further increase causes the circumferential extent of the separation to extend, so that it covers most of the upper cowl.

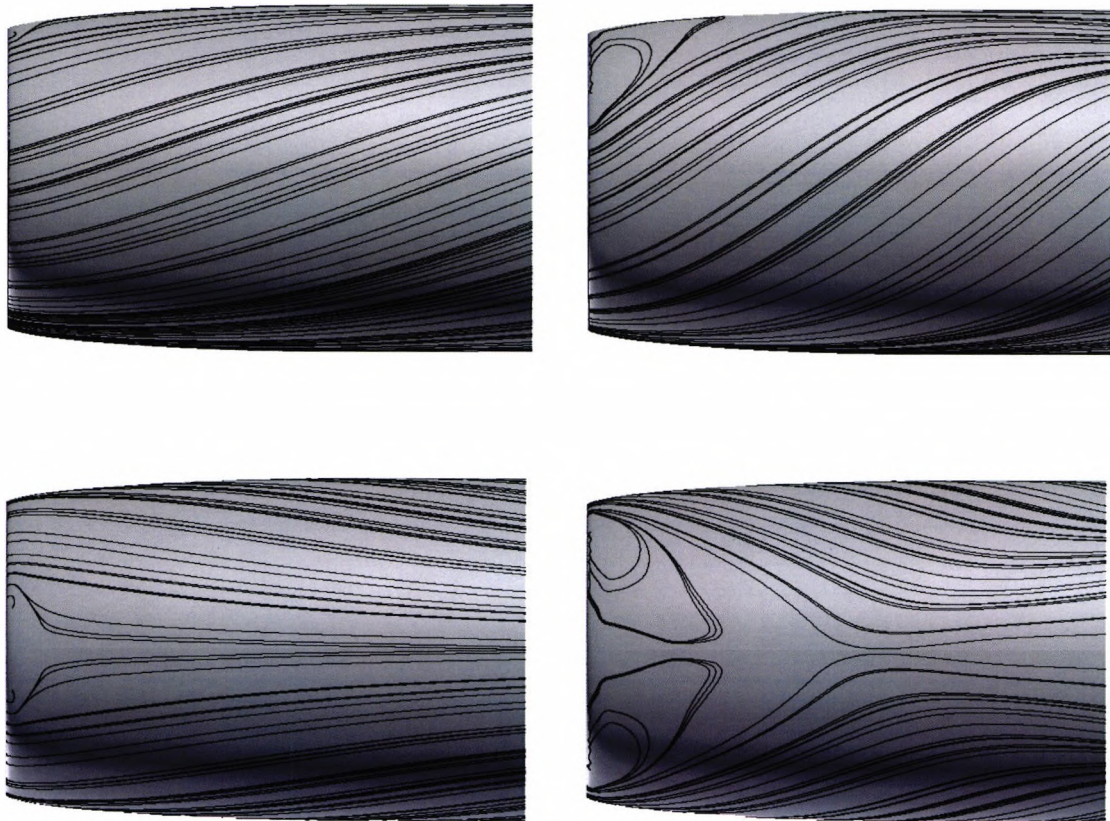


Figure 5-19: Computed surface streamlines on cowl side (top) and cowl top (bottom) for $\alpha=10^\circ$ (left) & $\alpha=20^\circ$ (right)

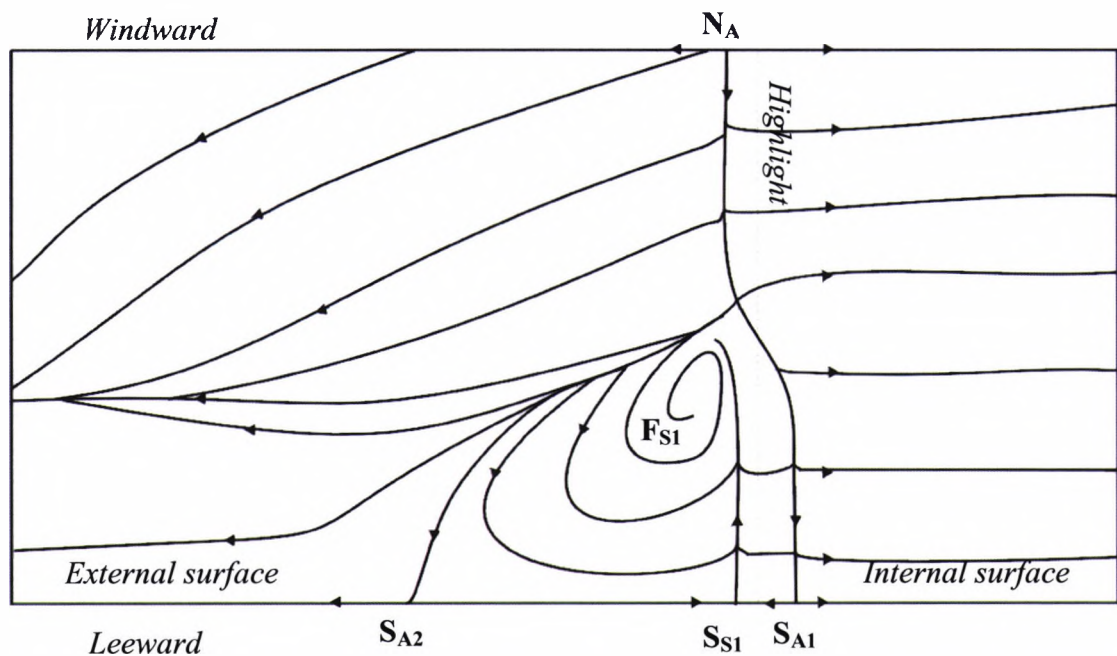


Figure 5-20: Schematic of external flow separation at incidence

Figure 5-20 presents a schematic of the skin-friction lines for external flow separation about a pitot intake at incidence with a mass-flow ratio small enough to cause external separation. In this case, the model is split at the windward generator, with leeward being the symmetry plane. Generally, the topology is similar to that discussed for internal flow separation, particularly with regard to the relationship between nodal points and saddle points; but with an additional separation line. The convergence of the streamlines on the external surface implies a separation surface leaving the body (*Maskell, 1955.*) This separation is not related to the lip flow, but due to the cross-flow pressure gradient on the cylindrical cowl. This was only evident at high incidence. The external flow is very similar to that recorded by *Dobson and Goldsmith (1970)* on rectangular fuselage mounted intakes (Figure 2.6). From Figure 5-20 the number of saddle points and nodes sum to satisfy Equation 5-3. Pictured is the node of attachment (N_A) and one of a pair of foci (F_{S1}). Out of picture is the second foci (F_{S2}) and the final separation node (N_S), this is a total of four nodes. Likewise for the saddle points, pictured are the two saddle points enclosing the separation (S_{S1} and S_{S2}) and the primary saddle point of attachment (S_{A1}). Out of picture is the saddle of separation corresponding to the stream tube leaving the duct, giving a total of four saddle points. Because of the nature of the relationship between the pair of spiral nodes and pair of saddle points and the attachment and separation

nodes and saddles, equation 5.3 holds true for combined internal and external separated flow.

5.8. More appropriate intake mass flows

The maximum intake mass-flow ratio achieved in the experiment is somewhat smaller than that with which the intake would be operating at incidence during flight for the same freestream Mach number. This difference may be considered as a form of scale effect. For the particular intake under evaluation, this scale effect only relates to the incidence at which separation occurs. As we have seen from the correlation in *Chapter 2*, the mass-flow ratio and the angle of incidence may be considered a compound variable. At this sub-scale mass flow, a higher angle of incidence for separation may be reached, but this can be corrected for. The assumption for this hypothesis is that this interchange of mass-flow ratio and incidence does not change the separation type. In this evaluation, at the test Mach number, the sharp nature of the lip means that flow separation occurs before any compressibility effects become evident. This means that the separation is purely due to the adverse pressure gradients at the lip.

The internal lip separation analysis has been carried out at what may be considered as either the wrong Mach number but correct freestream to throat Mach number ratio for combat operation; or a too low mass-flow ratio for the take-off condition, but correct Mach number. To assess the validity of this analysis, CFD is used to expand the envelope to higher mass flows and Mach numbers. It is hypothesised that as long as the separation is not shock-induced, it is the freestream-to-throat Mach number ratio that is the important scaling parameter.

The intake was sized to accommodate the mass-flow required by single-engine combat aircraft with supersonic capability such as the Lockheed Martin F-16 or SAAB JAS 39 Gripen. This class of combat aircraft is configured with pitot intakes of similar overall portions (area ratios) to the relatively sharp m742L Cowl 9 that was used for this study. Another similarity is that these aircraft have no auxiliary inlets to aid mass-flow capability. Mass-flow variation with Mach number has been calculated from the specific engine demand and plotted below in Figure 5.21.

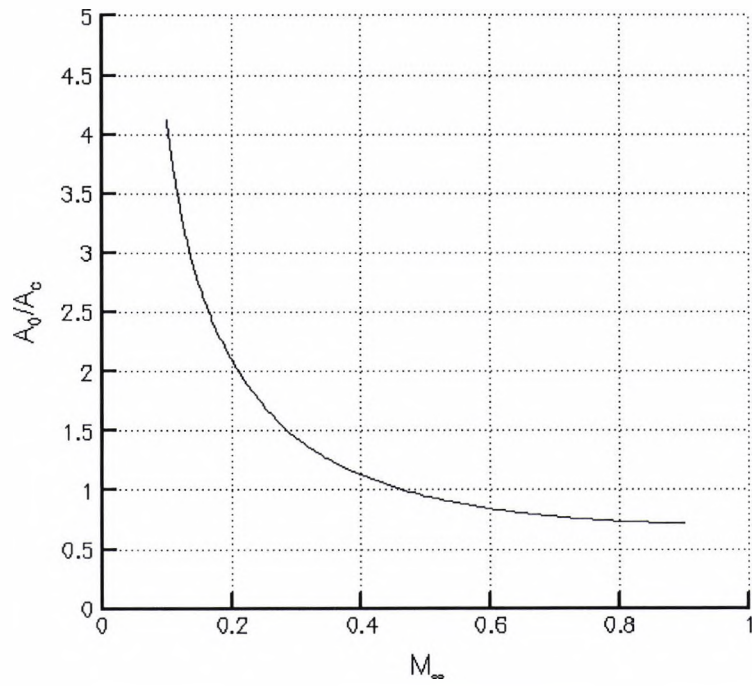


Figure 5-21: Mass-flow demand for assumed engine

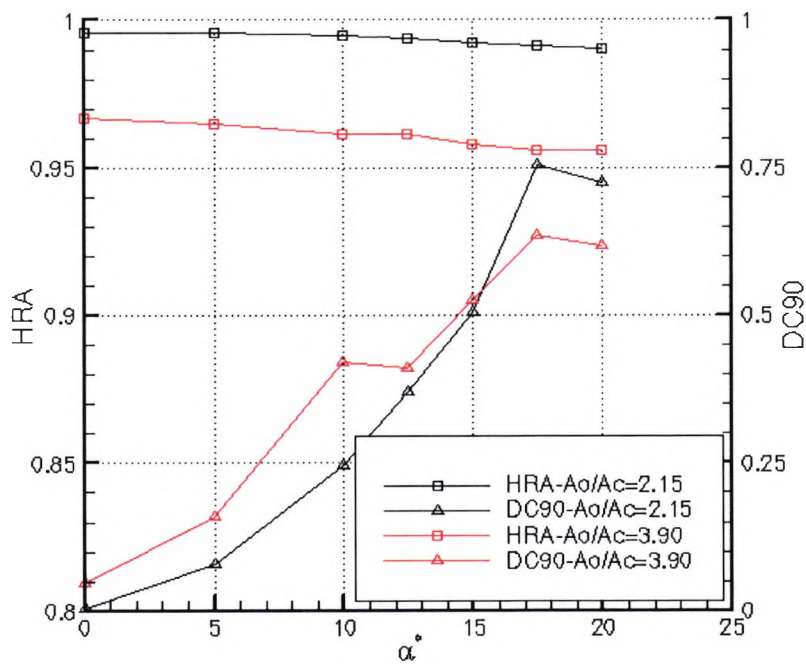


Figure 5-22: Total pressure recovery and distortion for high-mass-flow computations

Incidence sweeps for two additional mass-flow ratios were performed using CFD methods. This expanded the test envelope to provide throat Mach numbers not possible with the available experimental facility and equipment, with the aim of assessing the effect of mass-flow on lip separation. Results are presented for an intermediate mass-flow ratio of $A_O/A_C=2.10$ and the fully representative mass-flow ratio of $A_O/A_C=4.0$. In addition, a higher Mach number calculation was performed at similar mass flow to that achieved in the wind tunnel, $A_O/A_C=0.76$, to provide some understanding into the occurrence of lip separation during air-combat manoeuvring (ACM).

Figure 5.22 show the total pressure recovery and distortion with increasing incidence angle for the two new mass-flow ratios, $A_O/A_C=2.10$ and $A_O/A_C=4.0$. Firstly, the values of DC90 are much higher than for the low mass-flow-ratio case (Figure 5.1). This is primarily due to increased dynamic pressure in the duct. It appears that for this intake, the distortion scales with the square root of engine-face dynamic pressure, until the separation becomes large, i.e. $\alpha > 12^\circ$ (Figure 5.23). That is the scaled DC90 value is obtained by multiplying a non scaled value by the ratio of the scaled to un-scaled square root of engine-face dynamic pressure. This relationship is an indication that the effect of compressibility is small and that the flow mechanics at the low mass flow are representative of those at the higher mass flows. This indicates that applying flow-control techniques at the low mass flow is an acceptable practice, as the separation types are similar to those at high mass flows.

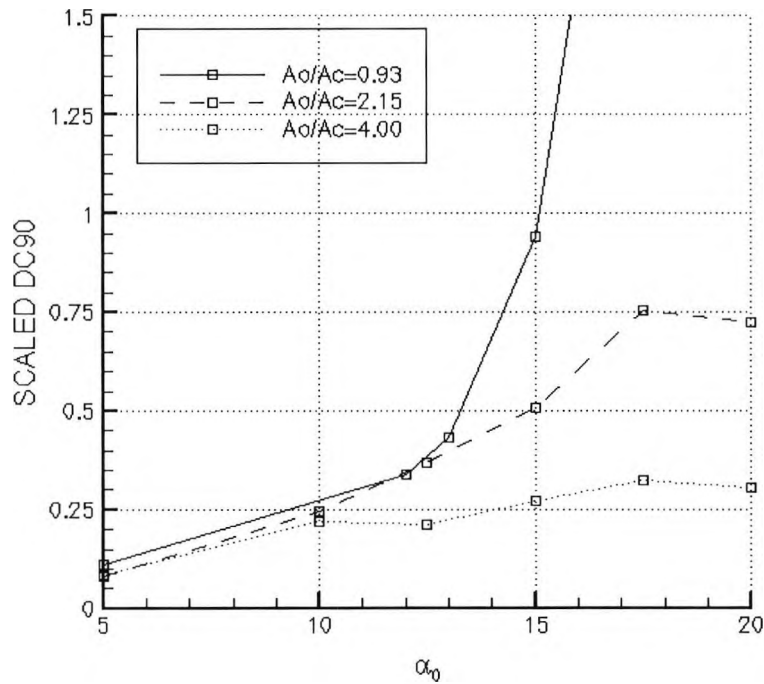


Figure 5-23: DC90 for range of mass-flows scaled to $Ao/Ac=4.0$

Figures 5.24 and 5.25 show Mach number contours for the two additional mass-flow-ratios calculated using CFD to expand the database of flow conditions. The contour levels used in each Figure are independent, the contour key is printed in the $\alpha=0^\circ$ plot in each figure. The visualisation of the development of the separated flow should be compared with the variation of distortion as the incidence angle is increased. The two mass flows represent an intermediate condition (Figure 5.24) between the test value and a ‘full’ value and a ‘full’ value consistent with the freestream Mach number (Figure 5.25). Increasing the mass-flow ratio moves the streamline dividing the internal and external flow aft along the lower cowl. This effect is amplified on the windward lip as the angle of incidence is increased. The first noticeable effect of this movement is an increase in the peak velocity at the internal lip. However, for the intermediate case, it is still well subsonic, with $M_{PEAK} < 0.4$. At the higher mass-flow ratio, the peak surface Mach number at the lip does just reach sonic conditions at $\alpha=0^\circ$, although the addition of a 5-degree positive incidence forces separation to occur with a much lower peak Mach number. The maximum value reaches approximately $M=0.8$ in the separated shear layer. A further increase in incidence brings the separation point nearer the leading edge, with a further reduced peak Mach number. This is similar behaviour to that recorded by *Hurd (1976)*. He noted that

above certain incidence angles the lip separation occurred at subsonic peak Mach numbers, where at lower incidences, it appeared related to the development of supersonic flow on the lip. Because of this occurrence, he doubted the quality of his data. This has been discussed in Section 5.4, where the three-dimensional nature was proposed as an additional mechanism leading to lip separation.

A close up view of the Mach number contours around the windward lip at $\alpha=0^\circ$ and at $\alpha=10^\circ$ is shown in Figure 5.26. This explains the result of the reduced peak Mach numbers when incidence is increased. At zero incidence, the flow is similar to that proposed by *Jakubowski & Luidens (1975)* for larger contraction ratio intakes (*Figure 2.9*) and it composed of a mildly supersonic region, followed by a thickened boundary layer. At ten degrees incidence, the flow has separated from very close to the leading edge and the flow in the entire lip region remains subsonic.

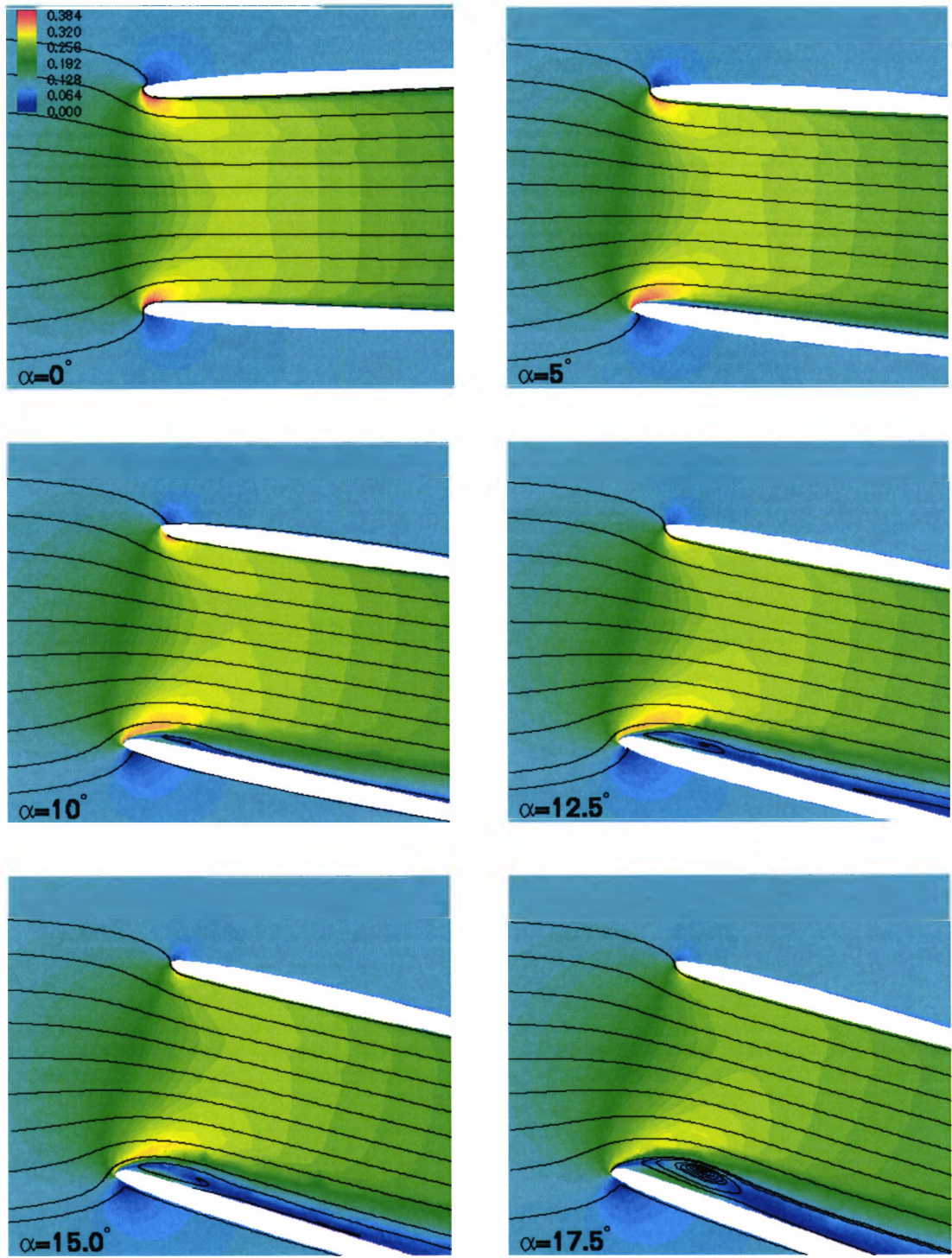


Figure 5-24: Symmetry plane Mach number contours for $Ao/Ac=2.15$

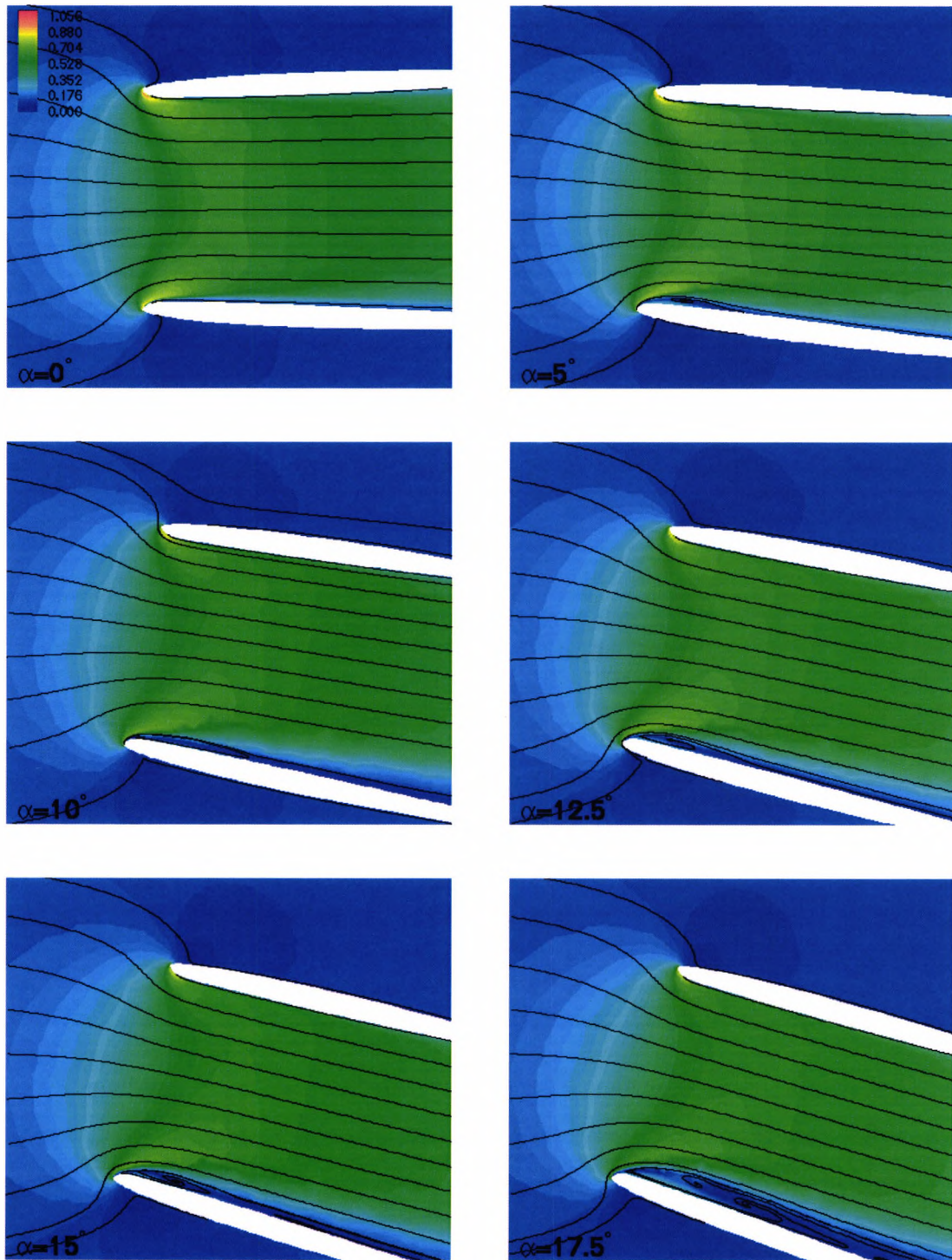


Figure 5-25: Symmetry plane Mach number contours for $Ao/Ac=4.00$

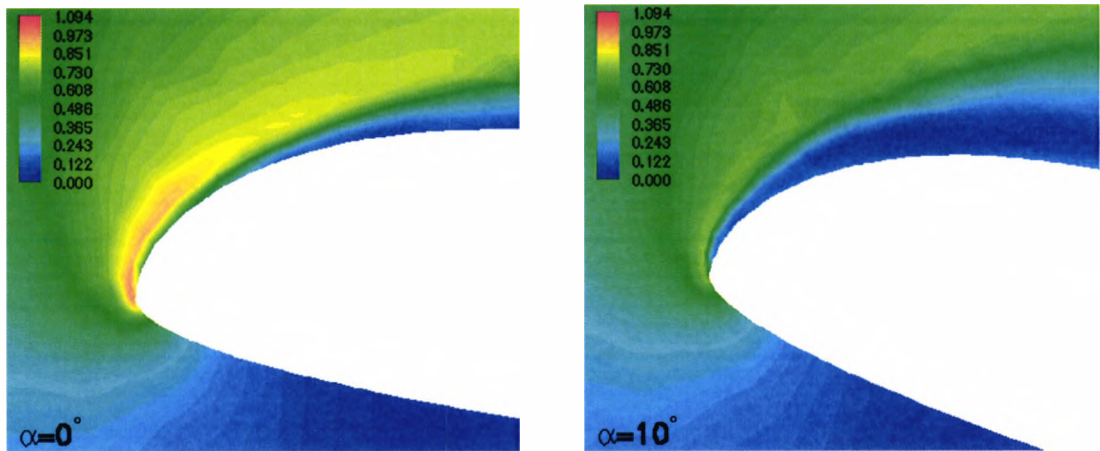


Figure 5-26: Mach number contours at windward lip for $\alpha=0^\circ$ and $\alpha=10^\circ$

The second feature of increasing mass-flow ratio is to suppress the development of the separated flow region that originated at the lip. This is because the higher mass flow reduces the magnitude of the adverse pressure gradient within the diffusing duct. Thus, for the higher mass flows, the flow appears to reattach for a larger range on incidences than the lower experimental mass flow, although the cropped images presented make this a difficult conclusion for the reader to draw.

5.9. Higher Mach numbers

To investigate the development and type of lip separation at higher Mach numbers representative of combat, where eliminating lip separation on a manoeuvring aircraft will be beneficial in maintaining carefree handling and maximising engine thrust, a CFD analysis was performed. A Mach number of $M=0.8$ was chosen and a scaled mass-flow ratio of $A_0/A_C=0.76$ from Figure 5.21. The Reynolds number based on intake diameter was 2.2×10^6 for aircraft scale at an altitude of 11km. Symmetry-plane Mach number contours are shown in Figure 5.27 for a range of incidence angles. This figure shows qualitative agreement with the anomaly of *Hurd (1976)* which has already been discussed in several different contexts. At incidence angles less than or equal to 10° , the flow on the windward lip reaches supersonic conditions. The adverse pressure gradient at the termination of the supersonic region causes a thickening of the boundary layer at 5° . At 10° the flow separates just upstream of the throat. The grid in this region is perhaps too coarse for accurate assessment of the interaction between the supersonic flow and the boundary layer. At 15° the flow separates

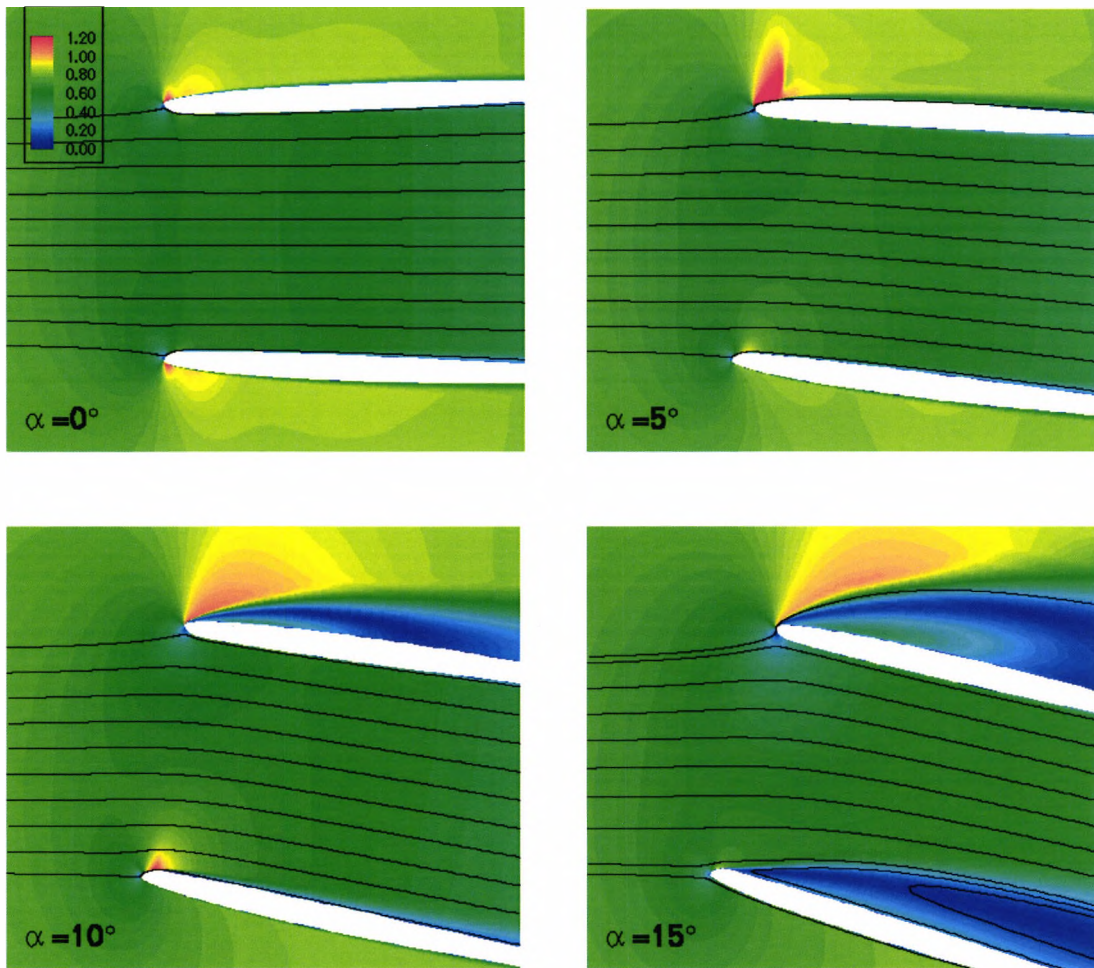


Figure 5-27: Symmetry plane Mach number contours for $Ao/Ac=0.76$, $M=0.8$

further upstream of the throat and the flow remains entirely subsonic. Additional incidence forces the lip separation to move forward and the peak local Mach number at the windward lip to reduce further. A close-up of the supersonic and subsonic lip separation is shown in Figure 5.28, which clearly displays the reduction in the peak local Mach numbers.

At $\alpha=5^\circ$ (Figure 5.27) a slightly different form of lip separation is evident on the external lip. Supersonic flow, which has expanded around the leeward lip to reach a peak Mach number greater than $M=1.4$, is characterised by a region that terminates with a shock wave sitting on the external cowl. The rapid pressure gradient in the subsonic boundary layer below the shock causes the boundary layer to separate. At this flight condition, a separation located so near to the leading edge would provide a significant increase in spillage drag.

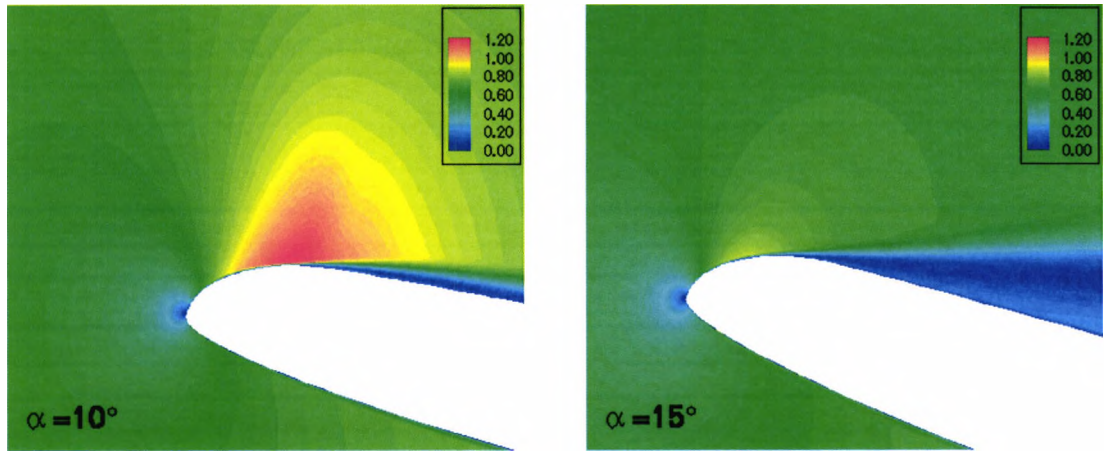


Figure 5-28: Change in separation type as incidence increases, $Ao/Ac=0.76$, $M=0.8$

A detailed view of the external separation is presented in Figure 5.29, which shows density and Mach number contours. The flow physics presented are an accurate representation of the classical interaction between a turbulent boundary layer and a normal shock wave (Seddon, 1967), in which the normal shock is bifurcated due to the thickening of the boundary layer ahead of the shock, giving a three-legged shock of lambda shape. The grid density is perhaps too coarse to accurately resolve the rear foot of the lambda shock but this feature may easily be determined from the contours.

The consideration of the shock wave on the cowl has so far been only in a two-dimensional context; of course the incidence of the cowl, although only 5° , provides a three dimensional element to the flow. Figure 5.30 shows an iso-surface of sonic conditions indicating the distribution of supersonic flow around the cowl.

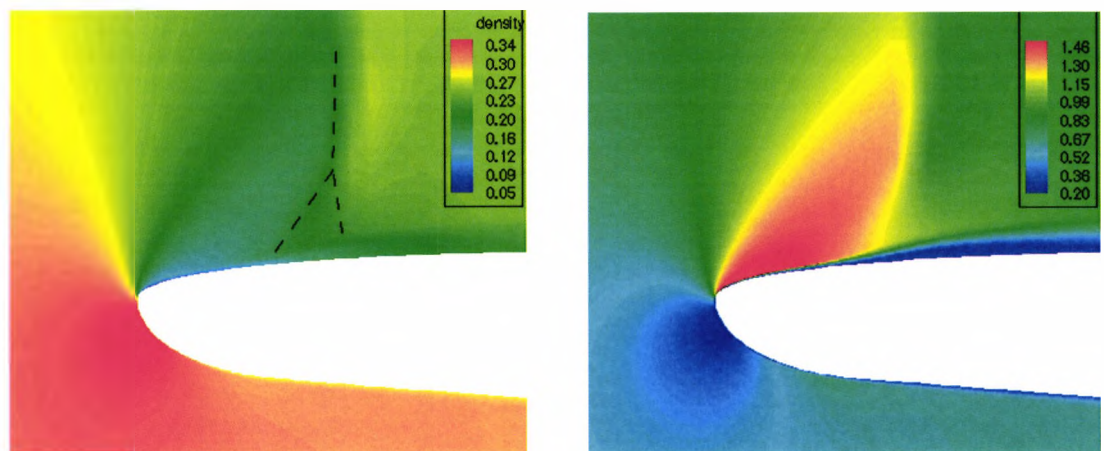


Figure 5-29: Low incidence external cowl separation, $Ao/Ac=0.76$, $M=0.8$, showing shock/boundary layer interaction, density contours (left) and Mach number (right)

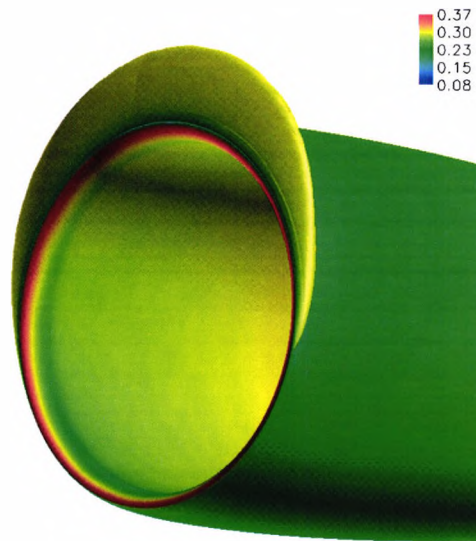


Figure 5-30: Iso-surface of $M=1.0$ enclosing supersonic region on external cowl (contours of density)

The variation in the size of the enclosed region, large at the crown and smaller at the sides, implies a variation in the peak Mach number around the cowl circumference, with the largest value present at the crown. The small region enclosed by the iso-surface at the side suggests the flow returns to subsonic conditions just downstream of becoming supersonic.

5.10. Summary of results concerning intake lip separation

Experimental results collected on an intake model in the wind tunnel have enabled a picture of the three-dimensional nature of intake lip separation to be established. An interactive computational and experimental technique has been used to develop the understanding of these flows. Previous research has focused on trying to understand intake lip separation as analogous to two-dimensional aerofoil separation. The results presented here suggest that the cross-flow components in the pressure gradients need to be considered, as they will influence the onset of the separation. They undoubtedly influence the flow path of low-momentum flow within the intake.

For low contraction-ratio intake lips, the separation is only affected by the adverse pressure gradient at the lip. This is true, except for very high-mass flow at transonic

Mach numbers, where the onset of diffusion at the throat station causes the mildly supersonic region over the lip to be terminated abruptly, resulting in a shock-induced separation. Otherwise, the separation is seen to occur at the keel between the leading edge and throat stations. An increase in incidence or mass flow forces the separation point toward the leading edge, lowering the peak velocity at the lip.

5.11. References

Dobson, M.D., Goldsmith, E.L., 'The external drag at subsonic and supersonic speeds of fuselage-side air intakes for strike fighter aircraft', RAE Tech. Memo Aero 1259, 1970.

Hoelmer, W., Youngmans, J.L., Raynal, J., 'Effect of Reynolds number on upper cowl flow separation' Journal of Aircraft, Vol.24, No.3., March 1987, pp161-169.

Hacker, I.G., Hirst, W., Hayward, R., Hyde, D., Goldsmith E.L., 'Results from tests on a series of axisymmetric pitot intakes at Mach numbers from 0.21 to 2.0', ARA Model test note M163, 1985.

Hurd, R., 'Subsonic pitot intake-high speed performance', Rolls-Royce (Bristol) Report PD 2029, 1976.

Maskell, E.C., 'Flow separation in three dimensions', RAE Report No: Aero.2565, 1955.

Peake, D.J., Tobak, M., 'Three dimensional interactions and vortical flows with emphasis on high speeds', NASA TM 81169, 1980.

Radespiel, R., Horstmann, K.H., Redeker, G., 'Feasibility study on the design of a laminar flow nacelle', J. Aircraft, pp959-965. Vol.27, No. 11, November 1990.

Seddon, J., 'The flow produced by interaction of a turbulent boundary layer with a normal shock wave of strength sufficient to cause separation', ARC R&M No. 3502, HMSO, 1967.

6. Control of lip separation using Air Jet Vortex Generators

6.1. Reasoning

The prospect of using thin or sharp intake lips, i.e. those with a very small leading-edge radius, is attractive in terms of drag reduction and saving structural weight. For military aircraft, the additional requirement of a low radar cross-section (RCS) dictates a sharp intake leading edge. In terms of propulsion system performance, the use of sharp intake lips is not a desirable solution, as the losses induced at high mass flow and, depending on the configuration, incidence, are unacceptably high. Even if the excess thrust of the vehicle were sufficiently large to be able to tolerate this total pressure loss, it is likely that the total pressure distortion would be too great to enable surge-free engine operation across the flight envelope. This is particularly so in the case of civil turbofans, where the distortion tolerance may be very low, typically $DC60 < 0.1$. For military engines, which usually have a higher distortion tolerance, the lip losses will be augmented by the complex flow path to the engine. This will often include a highly offset serpentine diffuser that, even in isolation, will deliver highly distorted flow to the engine.

It is proposed that flow control may be used to improve the off-design performance at take-off and climb, as well as during manoeuvre. The experimental and numerical investigations into the development of separation on an intake lip reported in the previous chapter indicate the complex three-dimensional nature of the problem. This is so even when considering a simple intake geometry in isolation, such as that used in the course of this investigation. This complex flow makes air-jet vortex generators (AJVGs) the most appropriate form of flow control for this problem. This was shown analytically in *Chapter 2*. The primary justification for this outcome is the flexibility of the AJVG system. In theory, a relatively simple control system can be used to relate the air-jet blowing pressure to flow conditions at the intake lip. The placement of the air jets has also been shown to be fairly flexible with regard to the clean flow separation line. It is not as important to locate the jets upstream of a potential separation as is the case with vane vortex generators. As the separation line will move with mass flow and flow onset angle, this flexibility is a very important consideration

that raises the appeal of AJVGs when considered against other active flow control types.

6.2. System Design

6.2.1. Initial thoughts on AJVG system design

The application of AJVGs for controlling flow separation in the region of the intake lip is a new technology development. Thus, the design of the jet layout must be derived from other applications. The two most applicable uses of AJVGs are to delay separation on a three-element aerofoil (*Lewington, 2001*), and to manage engine-face distortion in offset diffusing ducts (*Gibb & Anderson, 1995*), which is a speciality of QinetiQ and its predecessor organisations. These two applications encompass two different approaches. The aerofoil application uses the AJVGs to re-energise the boundary layer, mixing higher energy freestream air into the boundary layer, reducing its tendency to separate. The diffuser distortion-management technique uses a global approach, whereby arrays of AJVGs are used to redistribute the secondary flow to give a more even circumferential distribution of total pressure. It is proposed that the design of an AJVG system to control lip separation requires a combination of the mixing and secondary-flow redistribution techniques. The s-duct described by *Gibb & Anderson (1995)*, uses the distortion management approach to improve the flow quality at the engine-face, even if a separation is present at the lip, although the AJVG control system would have to be designed to cater for this occurrence. The advantage of using AJVGs at the lip, either in addition to, or at the expense of those in the duct, is that the removal or reduction of the lip separation will result in increased total pressure at the engine face. In addition, the low-momentum air from the separation, which is the source of total pressure distortion, will be reduced. It is important that the AJVG system is designed to manipulate the intake boundary layer, so that distortions are not propagated within the diffusing duct.

The spacing for the AJVGs was primarily based upon experience of AJVGs applied to offset ducts. Here, the philosophy is to minimise the volume of blowing air required. It is assumed that the high-pressure air used for blowing is extracted from the engine which will result in a thrust loss (*Section 6.8*), and minimising this is of particular concern. The optimum AJVG arrangement for the m2129 diffusing s-duct is 11

AJVGs located either side of the symmetry plane. The pitch and skew angles are 45° and 45° respectively, orientated such that they point away from the centreline. The circumferential extent on each side is 157.5° .

For the present investigation, the axial location of the AJVG array was fixed upstream of the clean intake separation location at the keel and was based on the methodology for the three-element aerofoil. The separation location was determined from the experimental data described in Chapter 5. Each centre of the AJVG exits was fixed 4mm aft of the lip leading edge on the internal surface. This distance was fixed for all AJVGs. This was done to reduce the number of design variables, because distance of the AJVG from the attachment line varies with circumferential location, mass flow and incidence.

Due to the availability of only a single wind tunnel model in which an AJVG system could be installed, it was decided to conduct a computational study to remove some of the risk associated with the experiment. The complex nature of this problem, both in terms of flow and geometry modelling and grid generation, makes this a big task. CFD methods have been validated for separated lip flows (*see Chapter 3*) and have shown reasonable accuracy in the prediction of AJVG flows (*Lewington, 2001*). Thus a number of aims were identified for the computational study:

- Determine a modelling approach for AJVGs
- Design an AJVG system to be tested experimentally
- Build an understanding of the lip flow in the presence of AJVGs

These three points are discussed in the Sections 6.3-6.5.

6.2.2. Ram Air jet vortex generators

Ram Air Jet Vortex Generators (RAJVGs) were proposed for application to intake lip control by *Peake (2001)*. In this form, the AJVGs are created by ducting the pressure side of the lip to the suction side, the jet being formed from the resulting pressure difference. This approach would be advantageous both in the weight of installation and in not removing any air from the propulsion stream tube. It is, however,

dependent upon the pressure gradient across the lip. A theoretical analysis was conducted to determine if sufficient pressure differential could be generated across the lip before separation occurred.

Using the standard definition of pressure coefficient described in *Chapter 3*, and the isentropic flow relations, the total pressure required to achieve a given jet velocity ratio can be calculated for a specified pressure-coefficient at the location of the jet exit:

$$\frac{H_{Jet}}{H_{\infty}} = \frac{\left(\frac{\gamma}{2} C_{p,Jet} M_{\infty}^2 + 1\right) \left(1 + \frac{\gamma-1}{2} M_{Jet}^2\right)^{\frac{\gamma}{\gamma-1}}}{\left(1 + \frac{\gamma-1}{2} M_{\infty}^2\right)^{\frac{\gamma}{\gamma-1}}} \quad \text{Equation 6-1}$$

$C_{p,Jet}$ is the pressure coefficient at the jet exit and M_{JET} is the jet Mach number derived from the pressure coefficient and prescribed jet velocity ratio. This function is plotted in Figure 6.1 for a range of exit pressure coefficients.

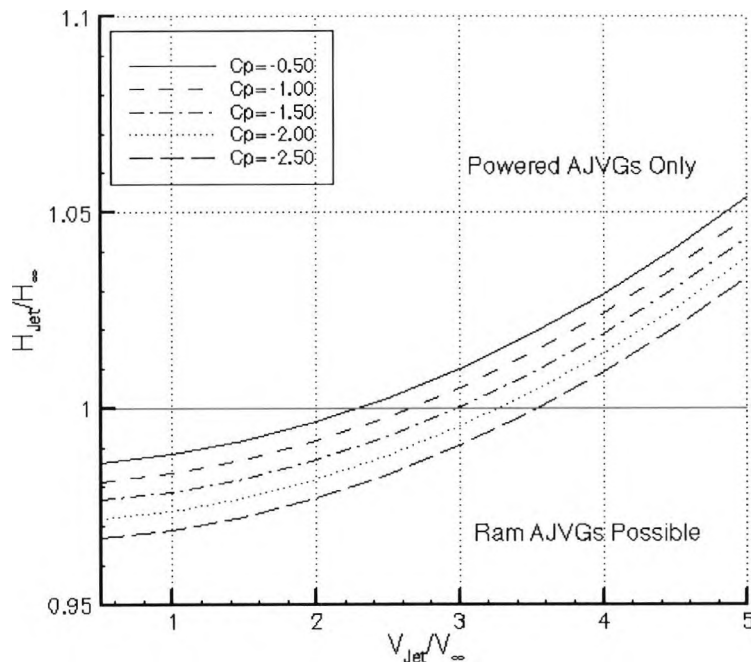


Figure 6-1: AJVG blowing requirements

The expression used to generate Figure 6.1 makes no assumption for the pressure loss the jets may experience. This loss will take three forms, an intake loss due to the inlet shape of the AJVG on the pressure side of the lip, an exit loss and a loss in the ducting

through the lip. The largest of the three by a considerable margin will be the intake loss. If assumptions are made for the loss in the system, RAJVGs still seem feasible. The degree of pressure loss is critical to the performance of the RAJVG system. The horizontal line in Figure 6.1 represents the total pressure available from the freestream. Below this line, ram operation is possible, above this line, powered blowing is required. It can be seen that only a very small range of velocity ratios is theoretically feasible for ram operation. The minimum pressure coefficient recorded in the first phase of testing (Chapter 5) was approximately $C_p = -1.7$.

For further assessment, a CFD simulation was conducted where the RAJVGs were modelled directly. An unstructured Prism/Tetrahedral mesh was used. A test case was selected from the experimental database in which the flow was well separated. This was at $\alpha = 20^\circ$ at a freestream Mach number of $M = 0.1$. The mass-flow was the maximum obtainable in the wind tunnel, $A_o/A_c = 0.98$. For consistency, the RAJVGs calculation was compared to CFD simulation on the clean intake model at the same data point.

The solution procedure with this problem raises issues on the application of CFD. If a RAJVG system such as this was used in the wind tunnel, or in flight, the chosen test point, for which separated flow occurs in the clean case, is reached with a gradual variation in incidence and mass flow. In this case, the RAJVG will start to work gradually as the pressure differential at the lip is increased with positive incidence. A similar procedure must be followed with the CFD to enable the correct flow development. If this is not done, a non-physical solution may develop in which the flow separates from the lip before the RAJVG flow has been resolved. To eliminate this possibility, converged solutions were obtained at low incidence with attached flow and the incidence increased gradually until the correct test conditions were reached. This procedure is obviously computationally intensive and must, therefore, be used selectively.

The initial RAJG installation was based around that described by *Lewington(2001)* for powered jets. The bore diameter, D was fixed as 0.75mm. This is larger than ideal, but is compromised by the need to maintain an acceptable size of computational mesh.

Small geometry components can increase the size of mesh drastically. The spacing was fixed at approximately 12D between RAJVG centrelines giving an angular separation of 20 degrees. A co-rotating array either side of the centreline permitted the use of symmetry in the model. The spanwise or circumferential extent of the jets covered the lower half of the model, i.e. 180°, when considering the reflection of the half model.

The RAJVGs were created by rotating a cylindrical geometry of the specified diameter to the correct orientation and intersecting through the intake geometry. The surfaces were then trimmed to create the finished component. No attempt was made to shape the intake or outlet or to manipulate the AJVG duct area distribution. This is because the small physical scale of the model would make this not possible in the experiment. The pitch and skew angles were set as 30° and 60°. The skew angle was based on previous work at City University, but the pitch angle was constrained by fixing the RAJVG duct across the highest pressure differential at the lip.

The results from this computation did not provide any noticeable improvement at the specified test condition. Although vortices were generated, the mixing was not of sufficient strength to suppress the separation. The jets were being washed to the side of the separation. So the spanwise spacing was halved to 10°, doubling the number of RAJVGs. Again at the test point, the RAJVGs were providing no benefit. It appears that the losses through the RAJVG system, particularly the intake, were larger than expected. This is primarily illustrated by the jet velocity ratio ($V_{\text{Jet}}/V_{\infty}$) which was recorded as being 0.9. The theoretical, (no loss) value for this problem, was approximately 2.75, illustrated by Figure 6.1.

Because of the large losses, it was decided to model a powered system. A computational model of a powered system has more flexibility than a RAJVG system in that the blowing pressure can be changed by manipulating a boundary condition, without having to re-grid the model.

6.3. Computational modelling of vortex generators

6.3.1. Vane Vortex Generator models

The intricacy of modelling vane vortex generators (VVGs) has led to the development of VG models in CFD codes. The problem is predominately one of resource. The application of VVGs is often by trial and error approach. Experimentally, the adjustment of the number and location of VVGs is simple and cost effective. The VVGs are bonded on to the model, and when required, they are simply unstuck and then reattached in a different location. Computationally, a similar exercise becomes expensive. The underlying geometry must be adjusted for the new VVG locations. The mesh must be recreated on the new geometry and the solver run. To reduce the pre-processing time associated with additional geometry and mesh manipulation, VVG models have been designed in the USA and UK. These models replicate the effect of the VVG on the flow by the addition of source terms to the Navier-Stokes equations, whilst eliminating the need to mesh the geometry of each VVG. An additional side effect of these VVG models is the generation of coarser grids than would be expected, if each individual VVG was meshed.

The method developed in the USA by NASA is described in detail by *Bender, Anderson & Yagle (1999)*. This model adds source terms to the momentum and energy equations. The source term models the side force (lift), which is generated by the VVG. This is dependent upon local flow conditions, which are extracted from the flow field during calculation and vane geometry, which is supplied via an additional input file. The disadvantage of this model is that the user must specify the cells in which the source term is to be added. i.e. the cells that would enclose the vortex generator, if it were present. *Waithe (2003)* provides FORTRAN subroutines for calculating the source terms.

A more user-friendly model is proposed by *May (2001)*. This model requires the user to specify only the centre of the vortex along with the dimensions of the VVG. The number of cells in which the source term is applied is then calculated automatically. May's model uses source terms to add vorticity to the flow, to replicate the secondary flow vector created by the VVG. Although this model is perhaps the easier to use of

the two, the results are not as accurate as those from Bender's model, when compared against a fully-gridded solution.

This process of using models to replicate the VVGs allows an optimisation of large parametric data sets to be created economically using Design of Experiments (DOE) methodology. This has been described by *Anderson et al (2003)* for the m2129 s-duct. DOE is a statistical technique that can be used to reduce the number of test points (experiments) in a parametric study by eliminating higher order interactions between design variables.

6.3.2. Modelling of AJVGs

For this study, powered AJVGs were modelled using the approach specified in Chapter 3. This required the exit of the jet to be specified on the cowl surface. Surface grids are then generated for all AJVG exits and the intake surface. Pressure-inlet boundary conditions were then used at the jet exit. This method is more efficient than modelling the complete jet geometry and plenum as had been done by earlier researchers such as *Lewington (2001)* and *Kupper (1999)*, but allowances must be made for the loss of total pressure that may be experienced by the jet. An empirical relationship for the loss of total pressure in a sudden contraction and expansions is presented by *Miller (1990)*.

Despite the relative simplicity of using the pressure-inlet model, a new grid must be made for each different configuration. A more feasible approach for the analysis of AJVGs during the initial phases of a study may be to use a model for AJVGs similar to that for VVGs. This would require only the specification of the centre of the AJVG exit aperture, the bore diameter and a measure of blowing. Momentum components could then be added to the source terms to replicate the jet. This is perhaps a more realistic approach than the VVG model, because the vortex is generated around the jet, and, therefore would still develop naturally. For a jet it is even more realistic; it would be possible to prescribe a velocity distribution across the jet exit, such as that measured experimentally by *Bray (1998)*.

6.3.3. Implications of modelling vortices with CFD

The modelling of small discrete vortices with CFD methods raises a number of issues regarding validity. Predictions of individual vortices arising from a single vortex generator appear to require very fine grids for accurate prediction of the downstream flow properties. This of course leads to very large meshes for full VG arrays. Contrary to this, global influence of the arrays in eliminating separation or managing engine-face distortion can be predicted on a much-reduced computational mesh.

6.4. Design of an installation for experimental validation

The most appropriate form of boundary condition for modelling the AJVGs was the pressure outlet. Using this boundary condition enabled the pitch and skew angles to be varied without re-meshing the entire configuration. This is done by changing the unit vector that describes the streamwise direction of the jet at the boundary (jet exit). Other boundary condition types were tried for this application, such as a velocity-inlet and a mass-flow inlet but they proved impractical, either in the required properties at the boundary, or achieving convergence.

Initially, the pitch angle of the jet was set at 30° , partly to maintain comparison with the RAJVG work described above and partly because this pitch angle seemed the most promising when analysing previous work conducted at City University. The skew angle was set at 60° for the same reasons. The initial development was based on the spanwise spacing used for the RAJVG example. The blowing pressure was incrementally increased to try to eliminate the separation from the lip, but the separation remained. Upon inspection of the CFD flowfield, it became apparent that the flow is strongly dominated by the initial occurrence of the separation on the inner keel, the leeward side of the windward lip. The spacing of the AJVGs at this location was too coarse to remove the separation. By the time the separation interacted with the AJVGs, it was large enough to be the dominant flow feature, thus suppressing the vortices originating from the AJVGs. This can be seen in Figure 6.2, which shows the separation pushing aside the vortices from the AJVGs. In an attempt to try to counter this problem, the sign of the skew angle was reversed so that the AJVGs pointed towards the symmetry plane of the duct. This approach was successful in delaying the separation, but the development of the separation on the inside of the lip was still causing a problem. In addition, the direction of the vortex generators washed the low

momentum flow toward the bottom of the duct. This led to unsatisfactory levels of distortion at the engine face, although the extent of the separation had been reduced.

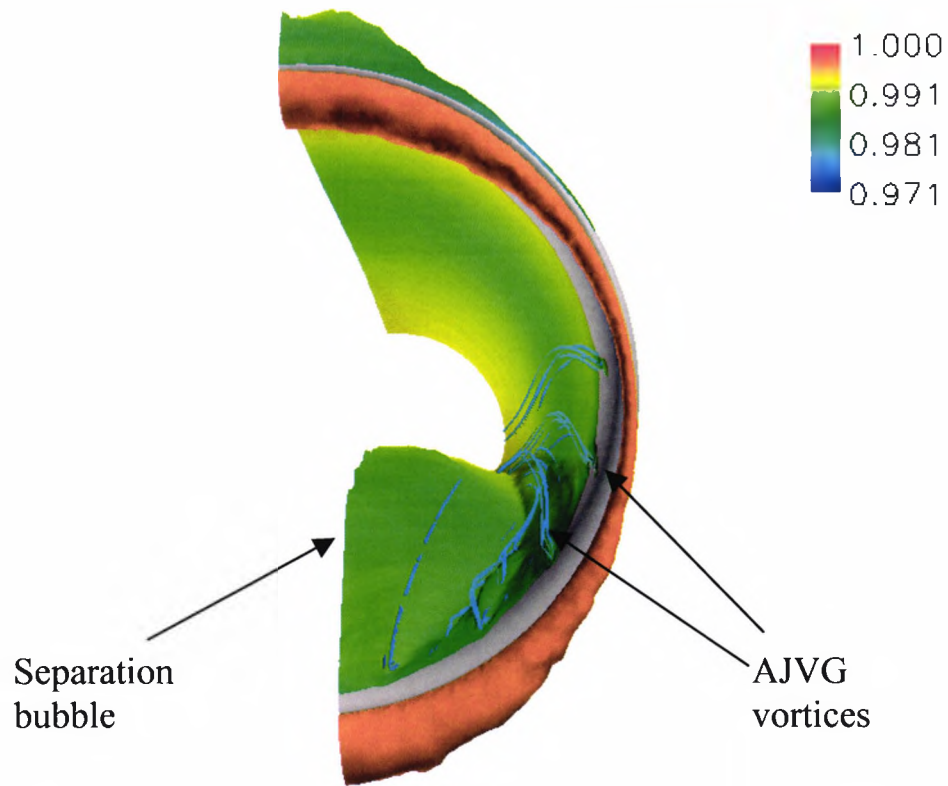


Figure 6-2: Iso surface of $M=0.07$ coloured by p/H showing separation dominance over AJVGs

At this point, the application of AJVGs was showing promise in eliminating the separation, so the evaluation was carried further. For this next step, the AJVGs were rotated around the intake axis toward the centreline. The spacing between all the jets remained equal, other than for those two immediately either side of the intake symmetry plane, where the spacing was half that between the other AJVGs. The reason was to try to suppress the development of the separation that occurs in this region. The skew angle was returned to the initial value of 60° , directed away from the centreline to counter the natural secondary-flow direction in the intake when at incidence.

This approach was successful in both eliminating the separation and reducing engine-face distortion at the test point; and so performance improvement over a full incidence range was evaluated (See Section 6.5 for discussion). The final arrangement is shown

schematically in Figure 6.3. To assess the validity of this approach for modelling the AJVGs and to investigate whether the predicted performance improvement could be replicated experimentally, it was decided to modify the intake wind tunnel model to introduce a powered AJVG array. These modifications to the model are described in *Chapter 4*.

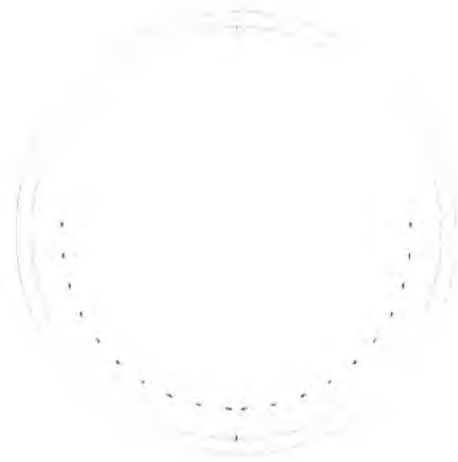


Figure 6-3: Schematic of final AJVG location (viewed from front)

The proposal to conduct experiments to validate the methods impacted on the future direction of the CFD. Because of the small scale of the intake model, the insertion of the compound angle air-jets into the cowl would be problematic and would risk the structural integrity of the model. Previous work at City University (*Peake et al, 1998*) suggested that AJVGs could prove effective, although not optimum, over a large range of skew angles up to 90° from the local flow direction. A skew angle of 90° would be most practical from a manufacturing perspective, as a pure pitch angle is needed for the drilling of the air-jets (jet direction parallel to leading edge). Further calculations were then performed on the successful AJVG arrangement, firstly, with a modified skew angle of 45° and then with a 90° skew angle. In all cases, the pitch angle remained constant at 30° . The effect of the different skew angles on engine-face distortion is plotted in Figure 6.4. All three skew angles are successful in reducing the distortion by eliminating the separation, but the optimum blowing pressure is a function of skew angle. As has already been stated, the actual skew angle differs from the geometric skew angle because of the three-dimensional nature of the flow. Figure 6.4 gives the first indication that a blowing pressure too large in magnitude will cause

the distortion to increase above its optimum level. This is discussed further in the next section.

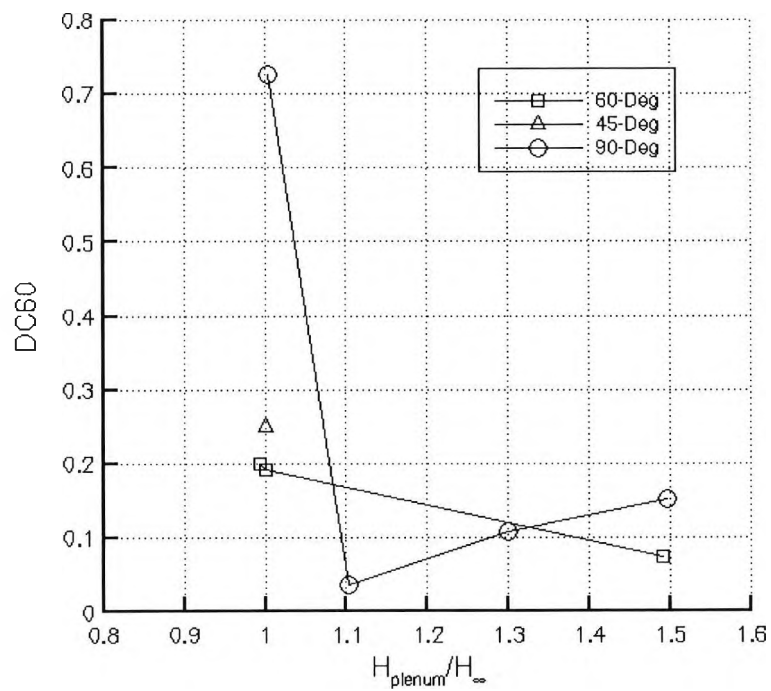


Figure 6-4: Effect of AJVG skew angle on engine-face distortion, $\alpha=20^\circ$

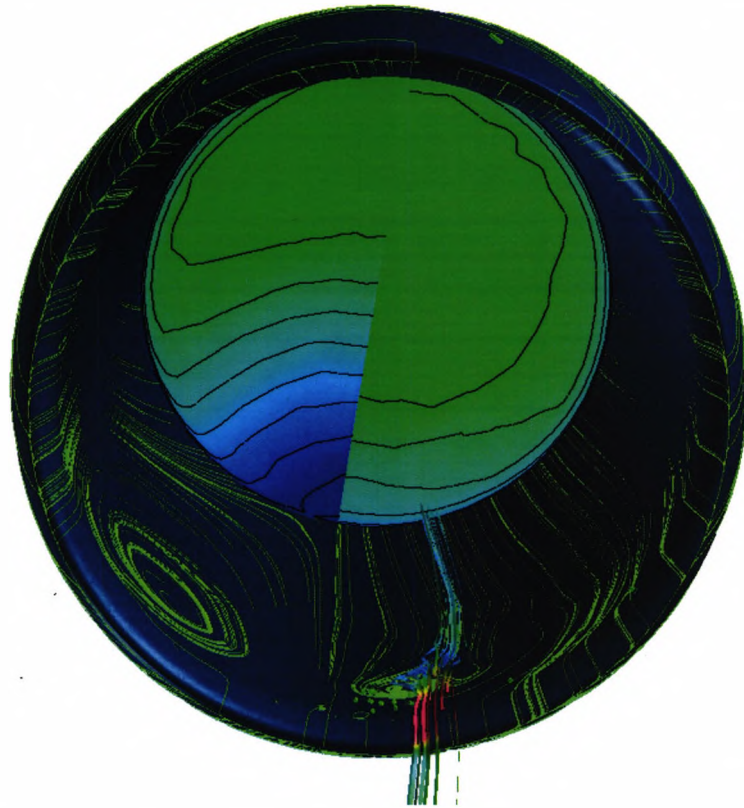


Figure 6-5 : Comparison between clean (left) and 60-Deg skew (right) - surface limiting streamlines and engine-face contours of Mach number- blue is low, red is high - viewed looking down duct

Figure 6.5 shows a comparison of surface limiting streamlines and engine-face contours for the clean intake and AJVGs with a skew angle of 60° with an air-jet plenum pressure equal to freestream stagnation pressure. Streamlines seeded from the core of the spiral node on the AJVG calculation track the small separation. The effect of the AJVGs in removing the large separation inside the lip is evident at the engine-face and on the surface skin-friction lines. In addition to the separation being much reduced, the AJVGs are also successful in maintaining an even circumferential distribution of the low-momentum boundary-layer air.

6.5. Interactive analysis

6.5.1. Experimental results

The major advantage the wind tunnel holds over computational fluid dynamics is that cost-and-time overhead per data-point reduces as the volume of data acquired increases. The opposite is true of computer simulation. In the case of this investigation, once the model was installed in the wind tunnel, an incidence sweep could be conducted within minutes. To generate an incidence sweep using CFD,

would require approximately one week of wall clock time, using the resources available at the time. In the wind tunnel, it was possible to generate a reasonably large experimental database with variations in intake mass flow and AJVG blowing pressure, as well as off-design performance: for example, in sideslip. After the initial design phase was complete, validated CFD methods could then be used selectively to aid in the interpretation of the data.

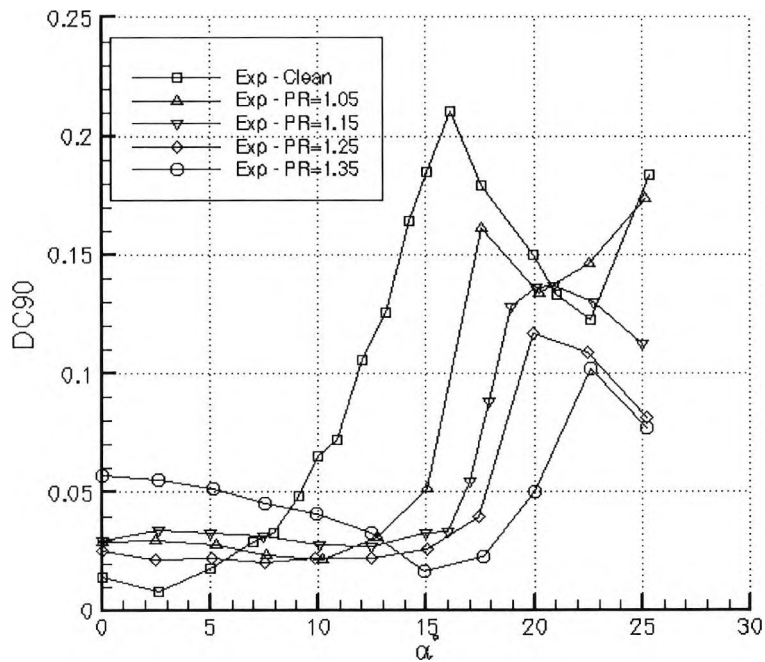


Figure 6-6: Effect of blowing pressure on intake distortion

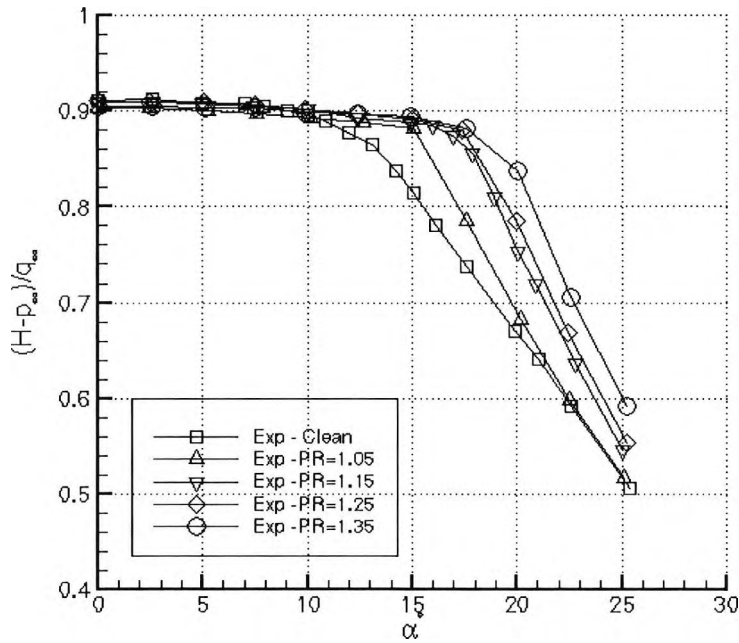


Figure 6-7: Effect of blowing pressure ratio on recovery

Figures 6.6 and 6.7 show the variation of distortion (DC90) and performance (dynamic pressure recovery) for the clean intake and a range of blowing pressures for the maximum intake mass flow that could be achieved experimentally, $A_0/A_c=0.96$. Both these charts can be used to infer the development of the separation. Where the curves are horizontal or of small gradient, the flow within the intake may be considered to be attached; the small performance degradation with increased incidence is due to thickening of the boundary layer. The point where the magnitude of the slope increases sharply is where lip separation occurs. This is true for both distortion and recovery. A point of interest on the distortion plots is a reduction in distortion after a peak value. This may be considered an artificial result, in that although the distortion is low, this condition is not a practical operating point for an engine. Its most likely cause is that the separated region becomes so large that the difference in total pressure between the worst 90° and the mean value is small, resulting in a low distortion value. In other words, the engine-face flow is uniformly bad. It is, however, plausible that the relatively coarse nature of the engine-face rake has some influence on this result as well.

The plot of recovery in Figure 6.7 shows a steady increase in the incidence at which internal separation occurs as the blowing mass flow is increased: this should be studied in conjunction with Figure 6.6 which shows the distortion. These figures show how increasing the blowing pressure delays the incidence at which separation occurs. The maximum blowing pressure tested $PR=1.35$, increased the incidence angle at which separation occurred by approximately 10° . The maximum blowing pressure ratio was limited due to concerns over the integrity of the pressurised components of the model. Although s-duct distortion management work had used blowing pressure ratios above 4.0 (*Gibb & Anderson, 1995*), this had been at much higher mass flows. Because of the obvious success of the AJVGs at increasing the incidence angle at which separation occurred, and the definite trend of that improvement with increasing blowing pressure, the maximum blowing pressure was limited to minimise the risk of damage to the model.

A more detailed indication of the relationship between the DC90 distortion parameter, internal lip separation and the pressure distribution at the engine-face is shown in Figure 6.8. This figure plots contours of dynamic pressure recovery alongside distortion for the clean intake, in addition to the results for an intermediate blowing pressure, $PR=1.23$. The relationship between the development of an increasing area of low total pressure on the engine face and an increase in distortion can be seen. The benefit in using AJVGs to eliminate the lip separation and control the secondary flow, and thus maintaining a more even distribution of total-pressure around the circumference of the duct, would be advantageous to the engine on two counts. It would increase the surge margin and provide an additional benefit in reducing the variation in blade loading per cycle and hence increasing the fan blade life. Figure 6.8 illustrates the evolution of the engine-face flow when AJVGs are present. For the corresponding clean duct case, there is a gradual increase in distortion corresponding to a degradation of the engine-face flow. When the AJVGs are operating, the distortion is nearly constant, while the AJVGs are successful in reducing the separation. However, when separation does occur, it appears to be sudden and the slope of distortion with incidences increases much more steeply than for the clean duct case. This means that for a practical application, some form of error margin must be built into the system. This could be in the form of increasing the blowing pressure

with incidence via a control system, to try to protect the engine from a sudden increase in distortion.

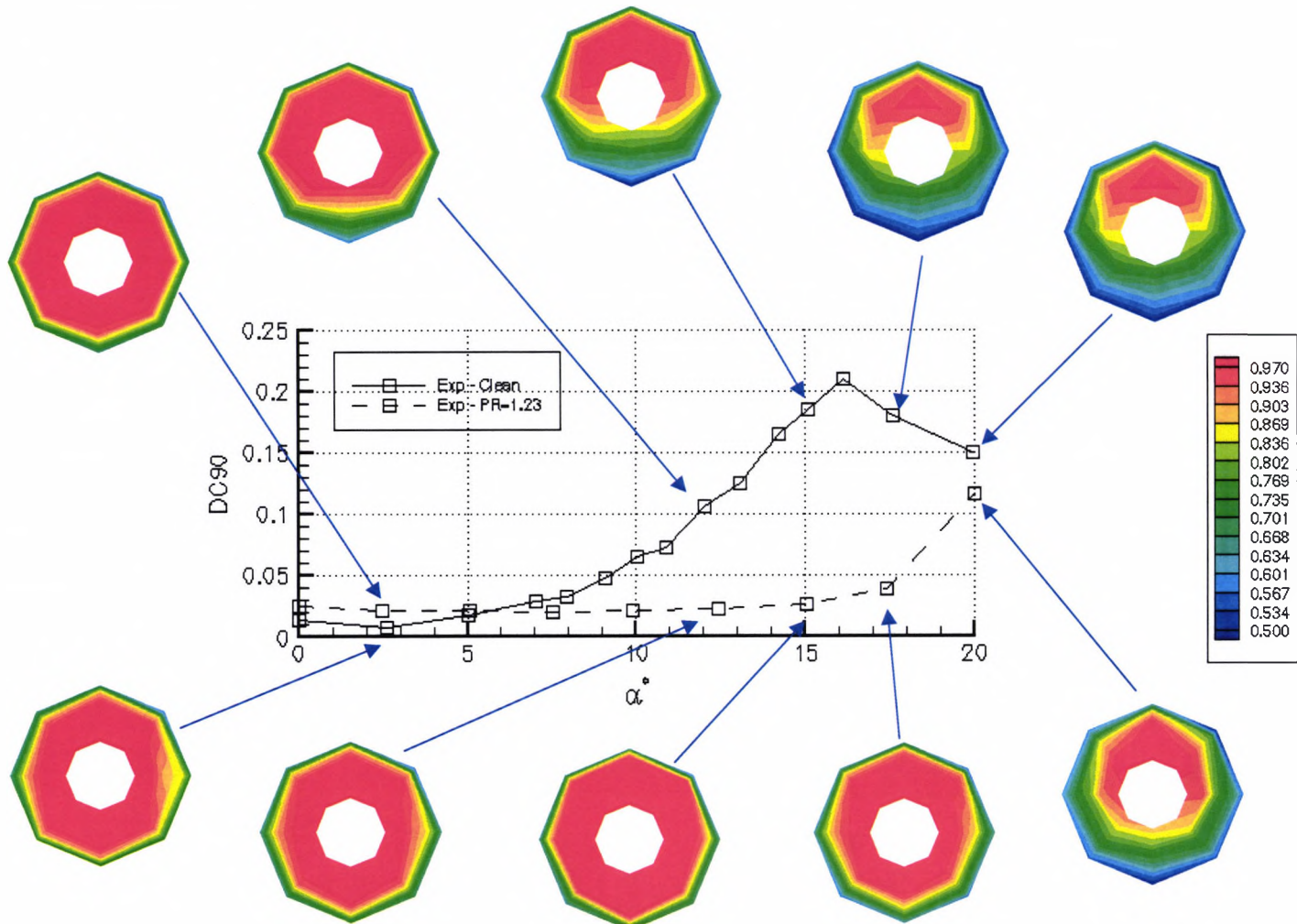


Figure 6-8: Distortion characteristic with engine-face dynamic recovery contours, $A_o/A_c=0.96$

6.5.2. Effects of Intake mass-flow ratio

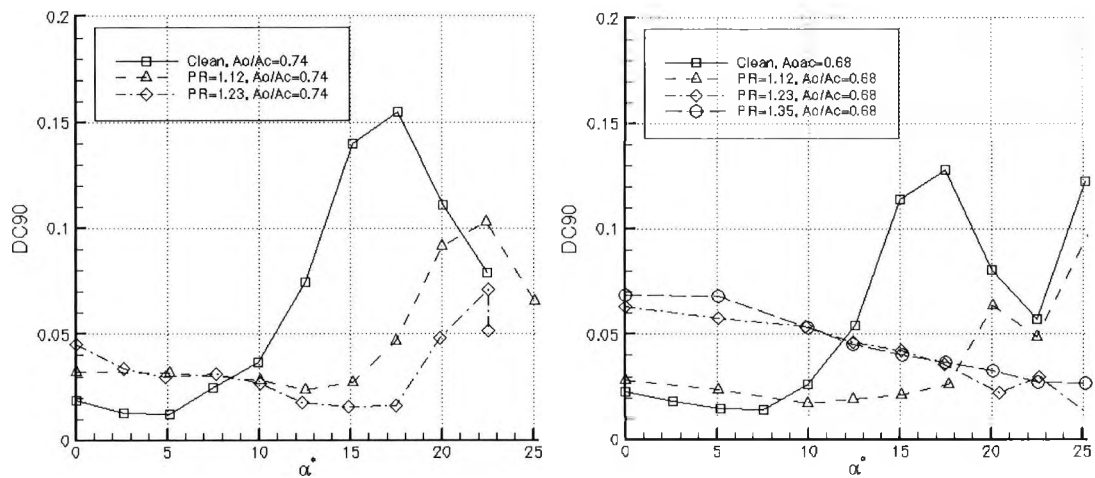


Figure 6-9: Blowing performance at $A_o/A_c=0.74$ (left) and $A_o/A_c=0.68$ (right)

Figure 6.9 shows distortion curves for two further intake mass flows, $A_o/A_c=0.74$ and $A_o/A_c=0.68$. Similar trends are evident to those discussed above; increasing the blowing pressure delays the onset of separation to higher incidence angles. The improved high-incidence performance is compensated by increased distortion at the lower incidence angles, where the influence of the blowing is too dominant. Although this is an acceptable level of distortion, compared to the clean duct, the blowing pressure could be manipulated by a simple control system to provide optimum performance across the intake mass flow and incidence range.

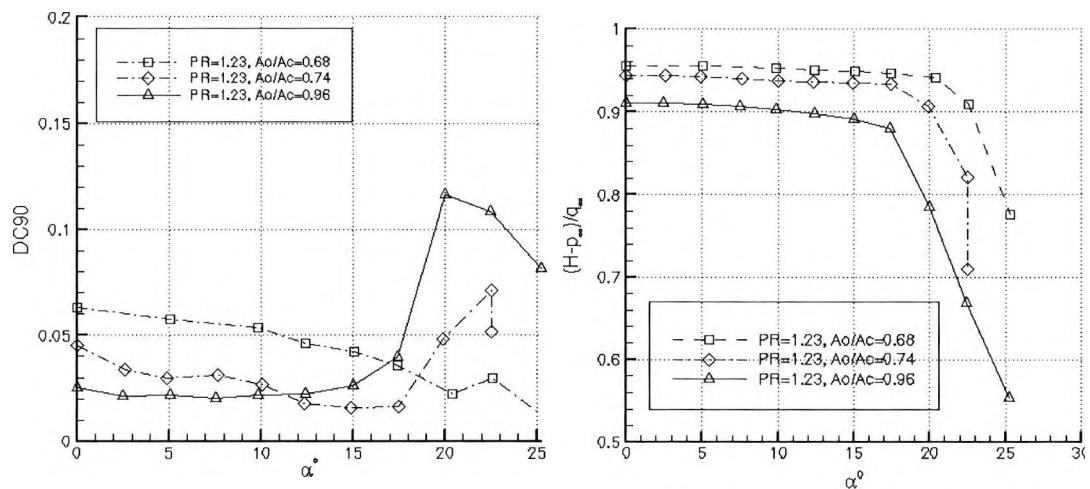


Figure 6-10: Variation of intake mass-flow ratio at constant blowing pressure, $PR=1.23$

Figure 6.10 shows distortion and recovery (total pressure coefficient) curves for a range of intake mass-flow ratios with constant AJVG pressure ratio of $PR=1.23$. This shows that decreasing A_O/A_C has a similar effect to increasing blowing pressure ratio, and indicates that the amount of blowing required is best represented as a fraction of the total intake mass-flow ratio.

Figure 6.11 is performance map linking blowing pressure ratio (PR), intake mass-flow ratio (A_O/A_C) and air-jet mass flow normalised by total intake mass flow (m_j/m_{ef}) with the incidence angle at which separation occurs. This has been constructed from the complete database of experimental results. As would be expected, it shows how the blowing pressure ratio must increase to achieve a particular fraction of overall intake mass flow as A_O/A_C increases. The AJVGs are most effective using a low blowing pressure, as this rapidly increases the angle of attack at which separation occurs. To achieve benefits beyond a 3 or 4 degree increase, the return for increased blowing pressure is not as large, but is still significant. After the blowing air requirement passes 0.5% of total intake mass flow, additional benefits are very small and possible not worth the additional loss in engine power.

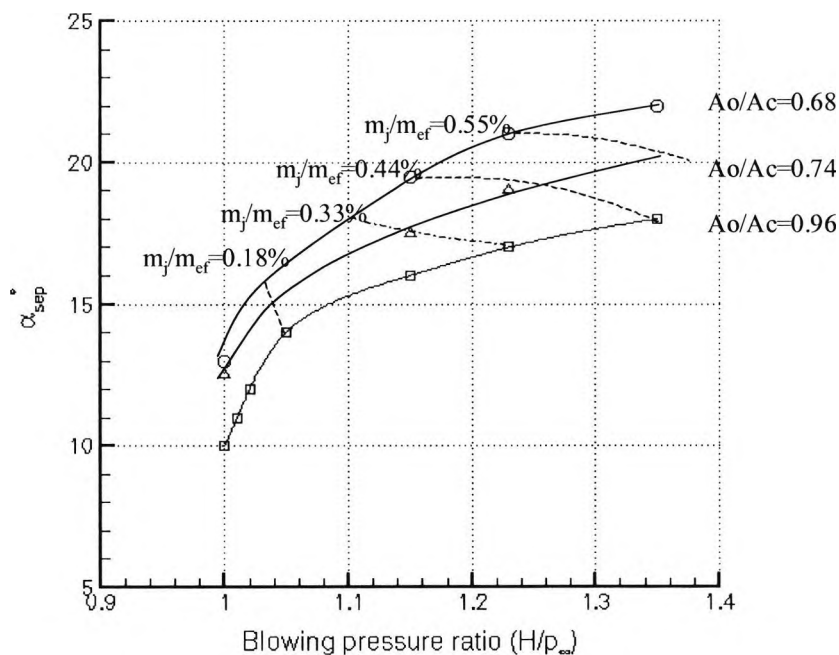


Figure 6-11: AJVG performance map

6.5.3. Validation of CFD methods

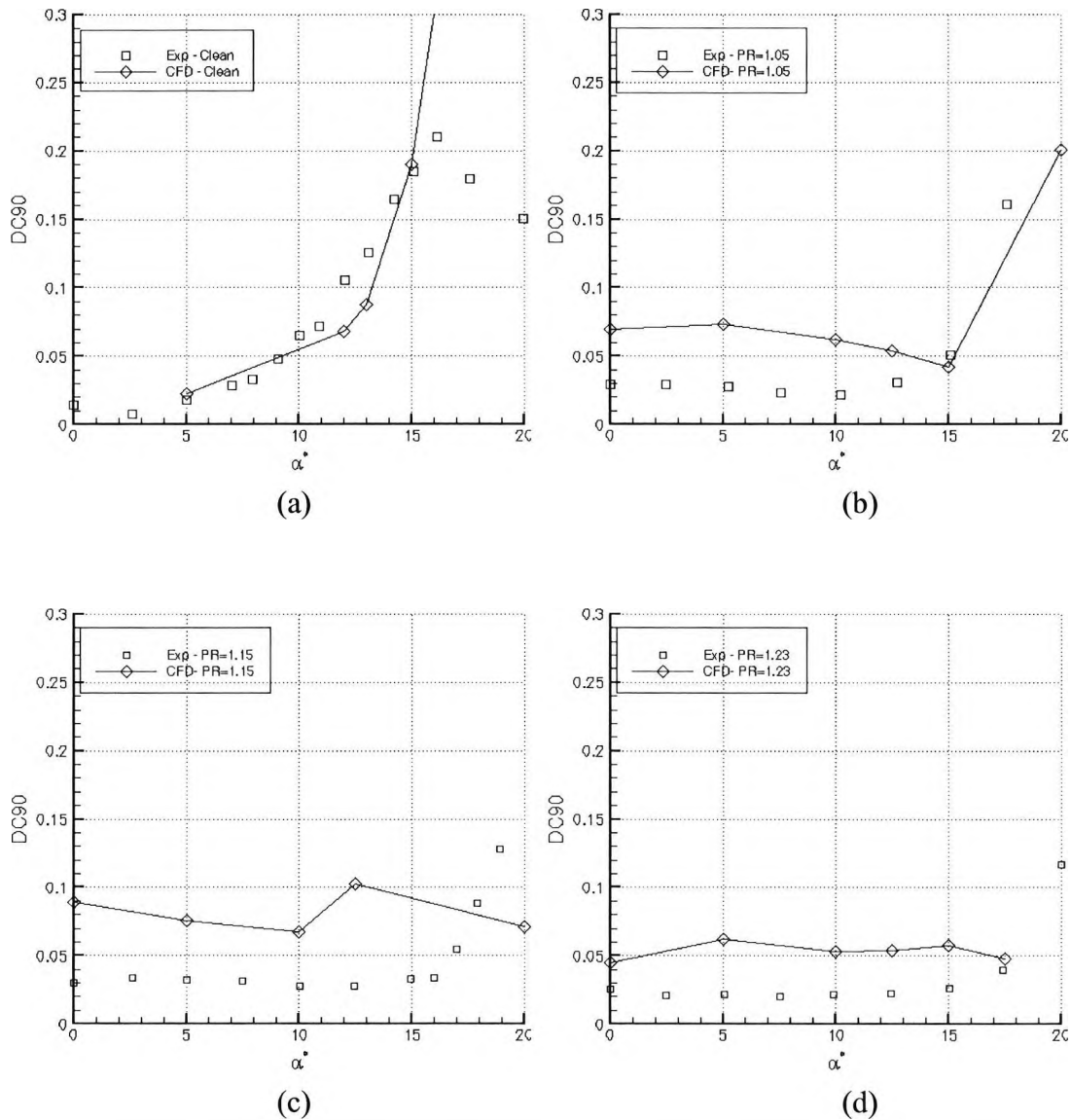


Figure 6-12: CFD validation for a range of jet mass-flows, $Ao/Ac=0.96$

Figures 6.12 (a–d) show experimental and CFD comparisons for four different blowing pressure ratios at $Ao/Ac=0.96$. Figure 6.12a shows the clean duct comparison. This is reasonably good, although the inflexion point in the curve occurs perhaps two degrees too high in the CFD prediction. The overall trend, however, is excellent. Both total pressure and total pressure distortion are notoriously difficult to predict accurately even when the wall static pressures appear to match exactly. There

are several reasons for this. The first is related to turbulence modelling; both total-pressure recovery and total-pressure distortion are dominated by viscous effects at subsonic conditions. The boundary layer is the primary source of total pressure loss when the flow is fully attached, and accurate prediction of both recovery and distortion are dependent upon the prediction of the thickness of three-dimensional boundary layers. This can lead to errors even in the simplest of attached flow trends. Secondly, the enhancement of these total pressure losses is associated with off-surface three-dimensional, possibly time dependent motions across a large-scale range. Hence, issues arise again relating to solution technique, grid density, turbulence models, etc. Current UK state of the art for propulsion applications is to use RANS CFD methods for concept development to assess trends, whilst using experimental or higher order CFD methods, perhaps DES, for detailed design studies. It is important, however, that in any particular study, the purpose of the CFD is understood. Here, CFD is being used to predict trends, to help interpret and understand the flow field and to design a system that was tested experimentally. Because of the complex nature of the flow field and the assumptions used in modelling the flow physics, a correct solution is not expected. However, we are looking to validate the models in such areas as delaying separation onset and predicting overall distortion trends. The purpose of validating a model, in this context, is to know its inadequacies and be able to account for them in the design process.

In all cases, convergence difficulties were encountered when the separated region in the intake became very large. The lower mass-flow AJVG blowing pressure cases were well predicted, but the predictions for the jet pressure ratio of $PR=1.15$ appear quite strange. For neither $PR=1.55$ nor $PR=1.23$ is the rapid increase in DC90 associated with separation (that is observed at $\alpha=16^\circ$ and 17.5° respectively) predicted.

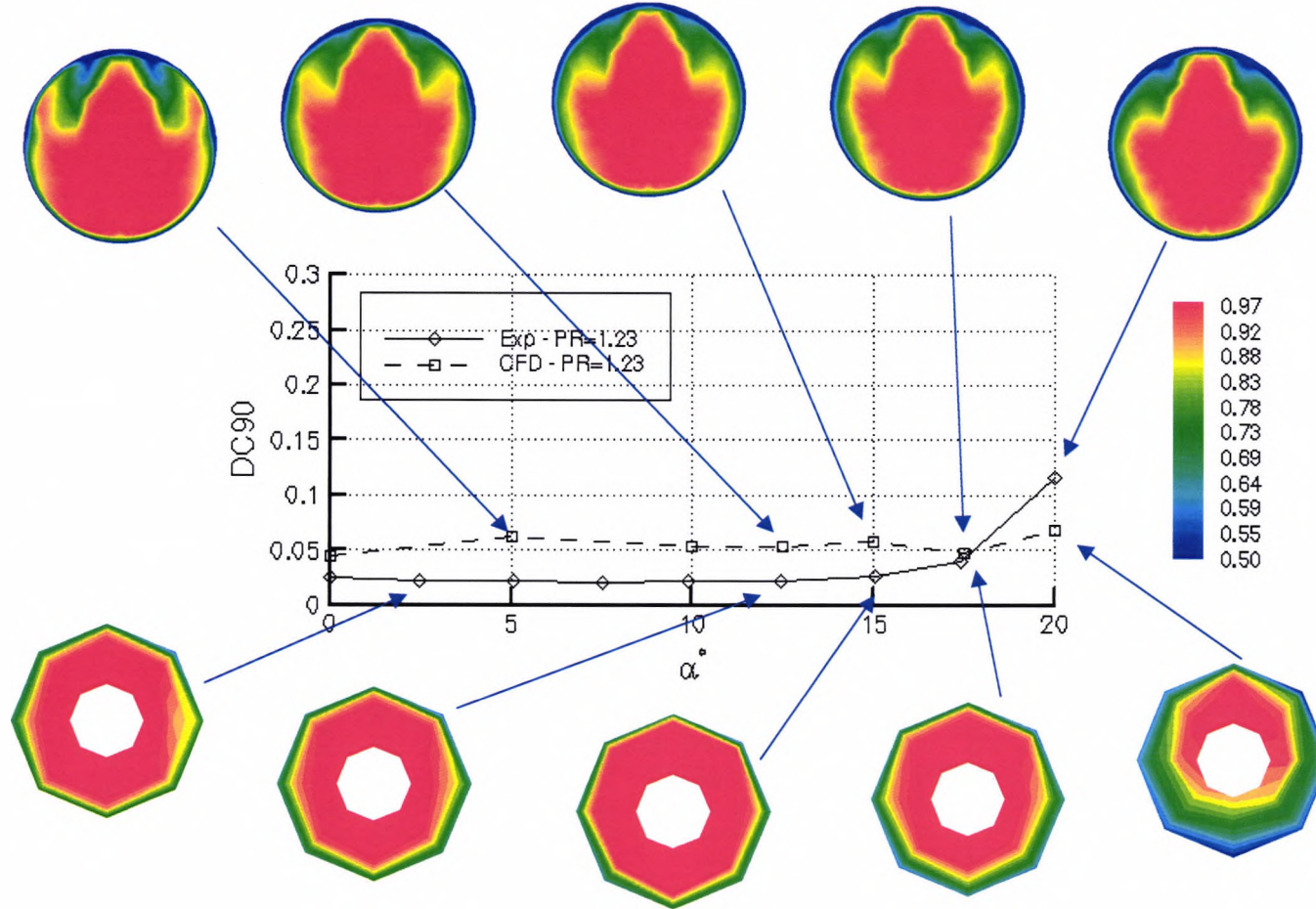


Figure 6-13: Comparison of CFD and experiment, $Ao/Ac=0.89$, $PR=1.23$

The use of a tetrahedral surface mesh may also influence the accurate prediction of separation at the lip. Because tetrahedral cells maintain an aspect ratio of close to unity, high fidelity modelling of high curvature regions such as intake leading edges results in very large computational meshes. Reducing the mesh to a useable size often requires a compromise in the replication of the geometry. On the other hand, tetrahedral meshes may be more advantageous when modelling three-dimensional flows, as they are less sensitive to the local flow direction.

Figure 6.13 shows a comparison of CFD and experiment with AJVGs installed in the intake lip and blowing at a pressure ratio of $PR=1.23$. Although the distortion comparison is good, there are some differences in the engine-face contours. This is partly due to the fact that the computational contours are plotted on the CFD mesh whilst the experimental contours are based purely on the discrete rake measurements. The experimental contours are from the full rake and are not constructed using a half reflection of the model. The main difference in the contours seems to be that there is a small area of increased loss predicted by the CFD in the top section of the contours. This feature is often present in VVG simulation in offset-ducts. It is related to the downstream, dominating influence of the air-jet vortices on the secondary flow in the duct. The implication is that the CFD is at an effectively higher blowing pressure than the experiment, probably due to the losses in air-jet exit ducting. This is also evident in the slight over-prediction for separation incidence.

Because the computational modelling appears to predict the overall trend in separation onset and distortion variation with incidence, computational predictions of the flow field can be used to complement the experimental data. Figure 6.14 shows the influence of AJVGs on the symmetry plane Mach number contours. The picture on the left has AJVGs at a pressure ratio of 1.23, while the picture on the right is the clean intake. Both images are plotted using the same Mach number scale and are at 15° incidence. At this condition, the separation inside the windward lip has been completely removed by the AJVGs. Figure 6.8 illustrates this in terms of DC90, which is reduced by up to one tenth of the clean lip value by the AJVGs. The AJVGs successfully re-energise the boundary layer inside the lip and this results in much higher local Mach numbers, although at this mass-flow condition, the flow remains

subsonic. The higher Mach number is maintained well downstream of the throat. Despite the overall higher throat Mach number and the higher local Mach number at the windward lip, a uniform Mach number gradient is established in a plane normal to the intake centreline in approximately half of a throat diameter. An additional benefit in removing the windward lip separation is the removal of the external separation on the upper cowl. This appears to be because the local flow angle at the upper lip is reduced when the lower lip flow is attached. When the flow on the lower lip separates, the separated flow displaces the main streamtube leading to a larger local incidence at the upper cowl.

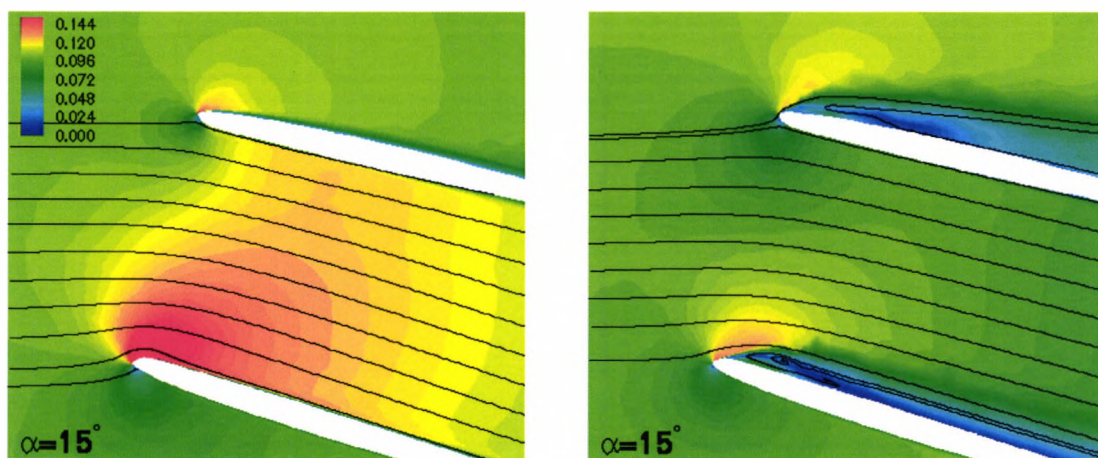


Figure 6-14: Symmetry plane Mach contours at $Ao/Ac=0.90$, $\alpha=15.0^\circ$ with (left) and without (right) AJVGs, $PR=1.23$

Figure 6.15 shows computed pressure distributions over the front portion of the intake inner surface for the clean intake and the intake with AJVGs, at a $PR=1.23$. The shaded surface corresponds to the clean duct, the overlaid wireframe is with the AJVGs. An analysis of the three-dimensional pressure distribution of the clean intake at this condition has been given in the previous chapter. The influence of the AJVGs on the surface pressure distribution is evident. At the lower lip, $x/D_{MAX}=0$, $\theta=180^\circ$, much lower pressures are maintained, and a smooth compression is achieved back to the required duct pressure. In the circumferential direction, the inflection in the leading-edge pressure distribution at approximately 90° corresponds to the end of the AJVG array. It is likely that the AJVGs have an entrainment effect as well as

providing mixing, thus resulting in lower values of pressure coefficient compared to the clean duct, even when the flow is attached in the clean duct case.

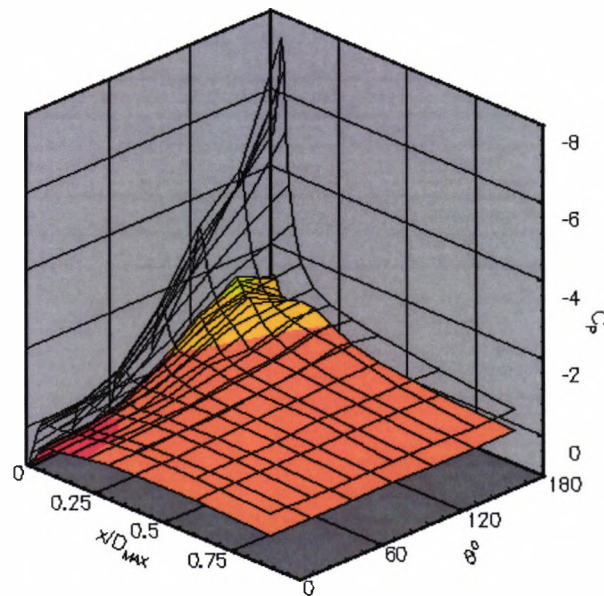


Figure 6-15: Comparison of internal surface pressures, clean (shaded) and $PR=1.23$ (wire) $\alpha=15.0^\circ$, $A_o/A_c=0.89$.

6.6. More Appropriate Intake mass-flows

As was discussed in Chapter 5, the maximum intake mass-flow ratio achieved in the experiment is somewhat smaller than that which the intake would be operating with at incidence during flight for the same freestream Mach number. This difference may be considered as a form of scale effect. For the particular intake under evaluation here, this only relates to the incidence at which separation occurs. As we have seen from the correlation in Chapter 2 the mass-flow ratio and the angle of incidence may be considered a compound variable. At this sub-scale mass flow, a higher angle of incidence for separation may be reached, but this can be corrected for. The assumption for this hypothesis is that this interchange of mass-flow ratio and incidence does not change the separation type. In this evaluation, at the test Mach number, the sharp nature of the lip means that flow separation occurs before any compressibility effects become evident. This means that the separation is purely due to the adverse pressure gradient.

To confirm the validity of AJVGs to real flight mass flows, the CFD method was used to extend the test envelope to higher mass flows. The intake was sized to accommodate the mass flow required by a single-engine combat aircraft with supersonic capability such as the Lockheed Martin F-16 or SAAB JAS 39 Gripen. This class of combat aircraft is configured with pitot intakes of similar overall proportions (area ratios) to the relatively sharp m742L Cowl 9 that was used for this study.

Figure 6-16 presents distortion curves for a CFD analysis of AJVG performance at a higher mass-flow ratio of $A_0/A_c=2.10$ at the test Mach number of $M=0.1$. Engine-face contours of total pressure are also presented. Firstly, because of the higher engine-face Mach number at the higher mass flows, the absolute values of DC90 are much higher, although the curve shapes are similar to those shown in Figure 6.8. It has been proposed in the previous chapter that sub-scale wind tunnel results can be scaled with engine-face Mach number when the separation type is similar. The AJVG curve is for a blowing pressure of $PR=1.23$. This corresponds to 0.7 % of intake mass flow at this condition. The blowing pressure-ratio is normalised by free-stream static pressure and is an indication of the AJVG plenum pressure; thus relating it directly to the off-take requirement from the engine. It is more relevant to this study than the traditional blowing momentum coefficient, $C_{M\mu}$. Blowing momentum coefficient may be calculated from the jet pressure ratio by the following expression derived from the isentropic flow equations:

$$C_{M\mu} = \frac{10p_{Jet}}{p_{\infty}M_{\infty}^2} \left[\left(PR \cdot \frac{p_{\infty}}{p_{Jet}} \right)^{\frac{\gamma-1}{\gamma}} - 1 \right] \quad \text{Equation 6-2}$$

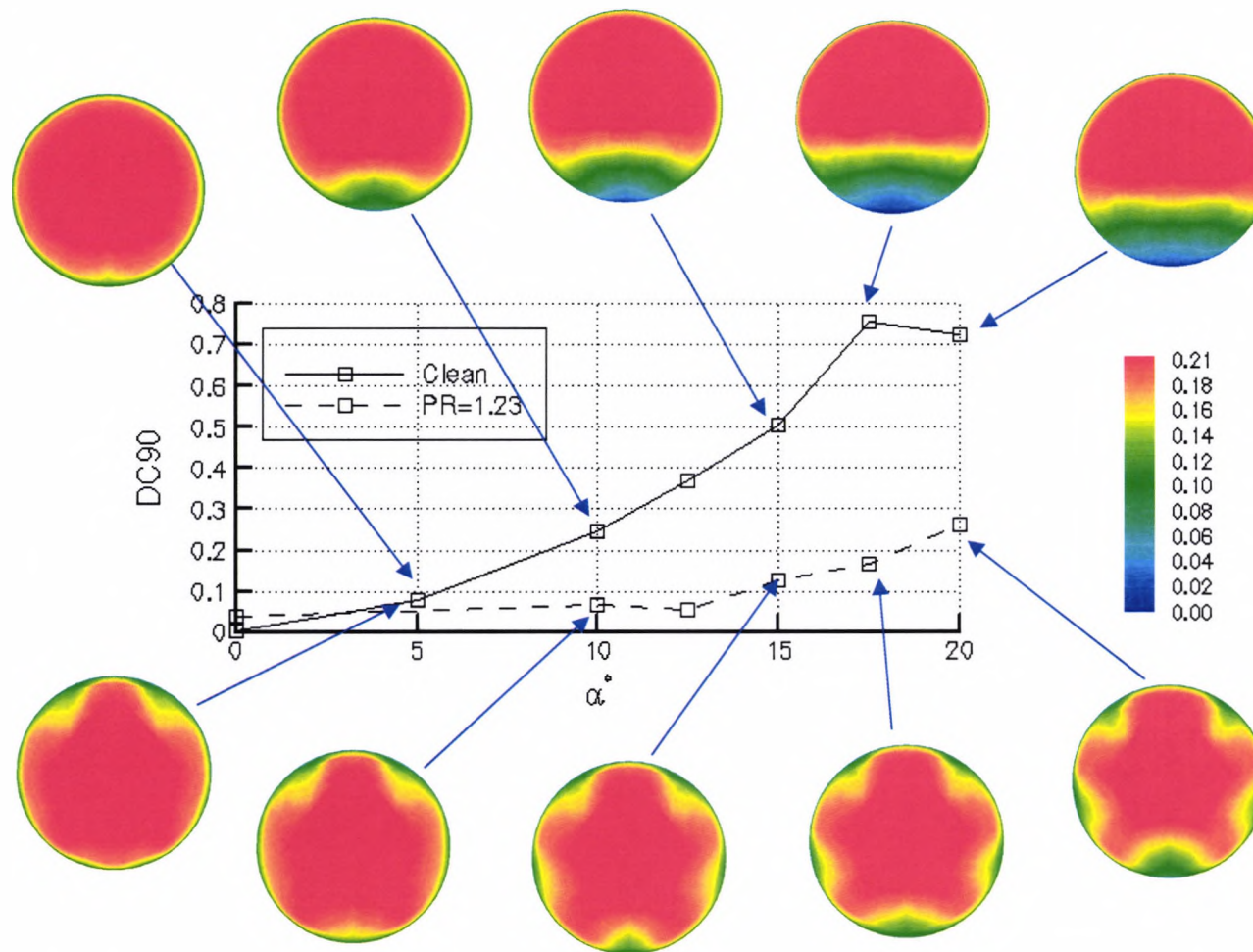


Figure 6-16: Computed distortion characteristic for $Ao/Ac=2.10$, with blowing ($PR=1.23$) and without blowing, contours of Mach number.

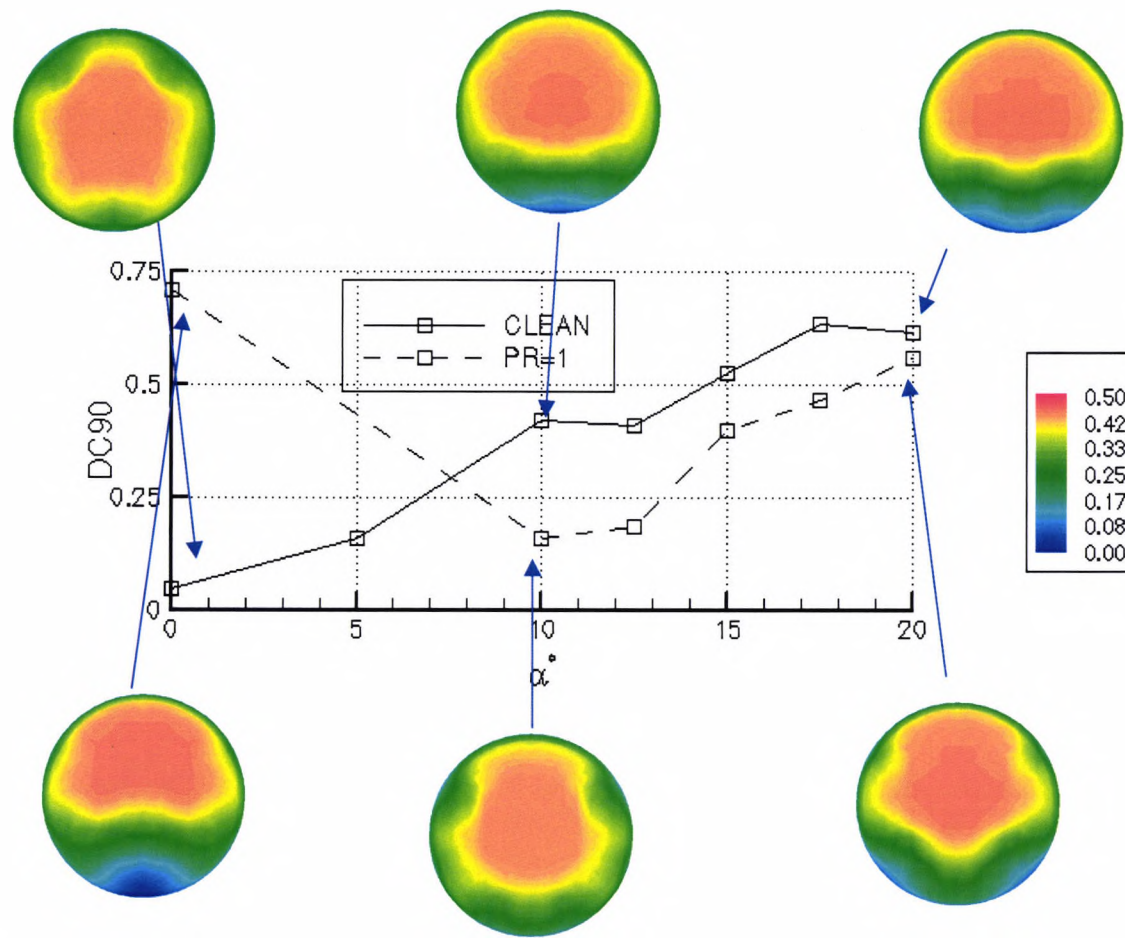


Figure 6-17: Computed distortion characteristic for $Ao/Ac=4.0$, with blowing ($PR=1.00$) and without blowing, contours of Mach number

From Figure 6.16, it can be seen that the AJVGs are still effective in reducing distortion at higher intake mass flows. For the intermediate mass flow, the blowing pressure ratio is somewhat excessive, taking a large fraction of total mass flow. Consequently, a significant reduction in distortion is produced across the incidence range. This highlights the need to control the blowing rate as a function of mass flow, and incidence in a practical application.

Figure 6.17 shows the computed variation of the distortion parameter DC_{90} across the tested incidence range at the full-scale mass-flow ratio of $A_0/A_c=4.0$. Again, the values of DC_{90} are larger due to the higher engine face Mach number. There is a discontinuity in the clean curve at 10-degrees incidence, possibly due to an un converged solution. Also presented is the benefit of using AJVGs. In this case, only a small fraction of the total intake mass flow is being used, 0.2%, but a noticeable benefit is still achieved, particularly at the intermediate incidence angles. The incidence angle for separation is delayed by 5-degrees. The modelling of AJVGs using a pressure-inlet boundary condition at the jet exit proved to be inappropriate for this intake and mass-flow combination using a jet pressure ratio, $PR = 1.0$. This is because the local static pressure at the jet exit is below that which should be required to choke the jet exit. This causes divergence in the flow solver. The evidence presented previously suggests that an optimised AJVG could be designed to achieve the same performance at lower mass-flow ratios or lower blowing pressure at high mass flows, using the modelling approach. A confirmation calculation could then be performed which includes simulating the AJVG ducts and exits in the correct physical manner. Alternatively, it may be tested experimentally in the wind tunnel.

Figures 6.18 and 6.19 show Mach number contours on the symmetry plane for the intermediate mass flow at two different incidence angles with and without AJVGs. At this mass-flow, the AJVGs are successful in eliminating separation and the resulting effects are more localised than for the lower intake mass flows because of the higher Mach number range. The main feature is an increase in the local Mach number on the lower cowl lip. However, the flow remains well subsonic. Aft of the throat, there is a slight thickening of the boundary layer or small separation bubble, most likely due to the axial adverse pressure gradient in the diffuser. This appears to worsen as the incidence angle increases further.

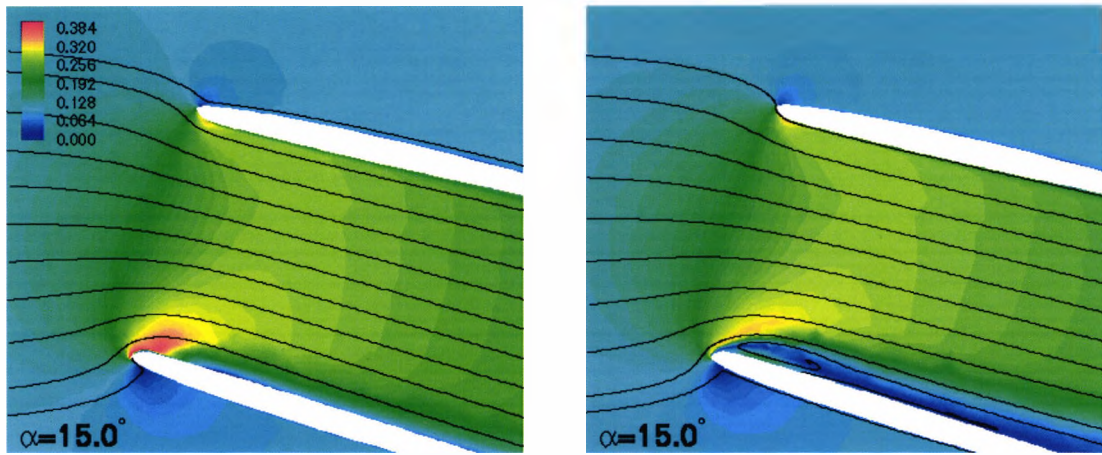


Figure 6-18: Symmetry plane Mach contours at $Ao/Ac=2.10$, $\alpha=15.0^\circ$ with (left) and without (right) AJVGs, $PR=1.23$

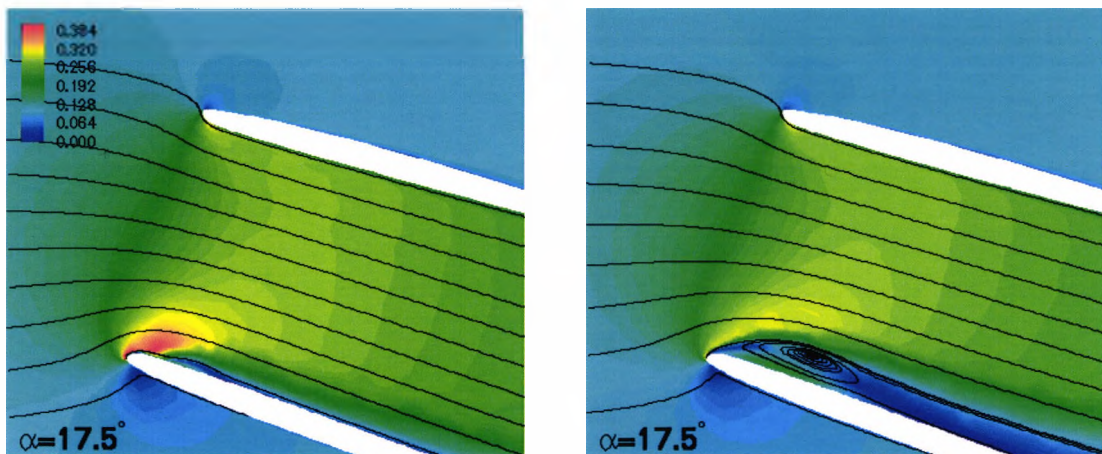


Figure 6-19: Symmetry plane Mach contours at $Ao/Ac=2.10$, $\alpha=17.5^\circ$ with (left) and without (right) AJVGs, $PR=1.23$

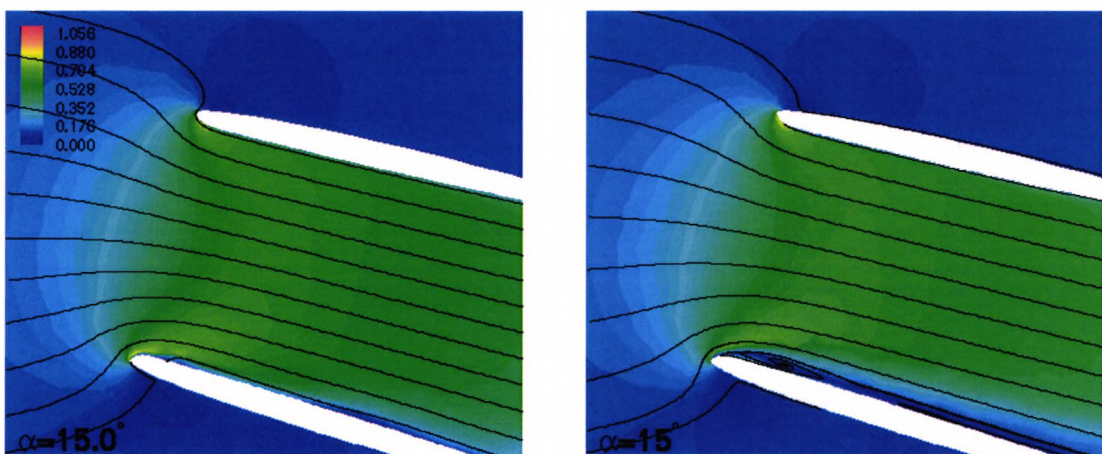


Figure 6-20: Symmetry plane Mach contours at $Ao/Ac=4.00$, $\alpha=15.0^\circ$ with (left) and without (right) AJVGs, $PR=1.00$

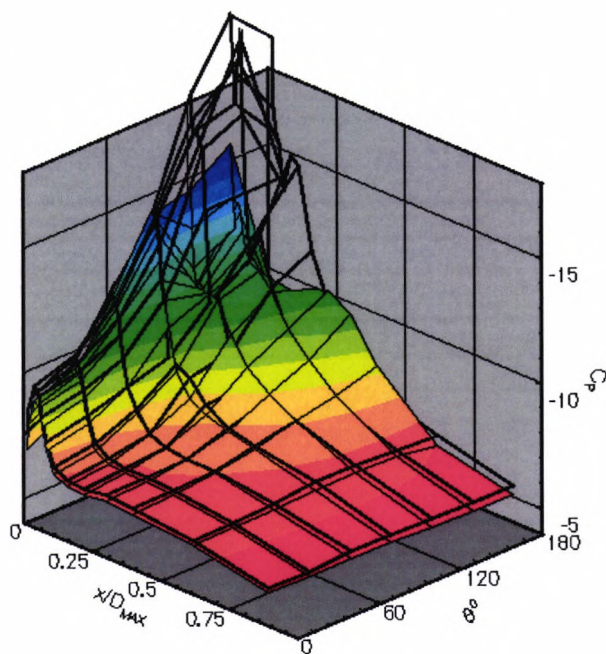


Figure 6-21: Comparison of internal surface pressures, clean (shaded) and $PR=1.23$ (wire) $\alpha=17.5^\circ$, $A_o/A_c=2.10$.

The three-dimensional pressure gradients can be seen in Figure 6.21. This compares computed pressure distributions of the clean intake and intake with AJVGs. These correspond to the shaded surface and the wireframe respectively. With the AJVGs present, the circumferential pressure gradient at the leading edge is much smoother indicating attached flow. The presence of the thickened boundary-layer/separation can be seen by the discontinuity at the windward location, $\theta=180^\circ$, near the leading edge. A similar feature is evident at the full-scale mass flow and is shown in the symmetry plane contours of Figure 6-20, which illustrates the benefit of AJVG at very high mass flow.

6.7. Off-design performance

The vortex generator array was designed to delay internal lip separation in the pure incidence case. The reasoning was firstly, to reduce the complexity of the design process and secondly, a symmetry plane could be used in the computations to keep the mesh down to a usable size. The feature that defines the installed AJVG as being for the pure incidence case is the close proximity of the first air-jet either side of the symmetry plane. A constant AJVG spacing may make the design more applicable for sideslip conditions. The closer spacing on either side of the symmetry plane was

derived during the computational design with the intention of delaying the separation on the internal keel, the region where internal separation first starts to occur during pure incidence. Of course, in reality, aircraft manoeuvres or a crosswind at low-forward speed will induce a compound local flow angle. This may result in an AJVG system such as that discussed here operating at an off-design condition.

The experimental investigation presented the opportunity to derive performance data for the AJVGs during combined incidence and sideslip that could not be obtained using acceptable levels of computational resources. Figures 6-22 and 6-23 show the performance of two different blowing pressure ratios compared to the clean intake as the angle of yaw is increased at fixed incidence. For $\alpha=15^\circ$, shown in Figure 6-22, the effect of sideslip on the clean intake can be seen as slightly increasing the distortion parameter DC90. The influence of blowing in the presence of the combined incidence and sideslip provided a similar reduction in DC90 as for pure incidence. Increased blowing provided further improvements at the higher sideslip angles. Figure 6-23 shows the influence of sideslip at $\alpha=17.5^\circ$. Again, the AJVGs are beneficial providing up to 50% reduction in the clean duct distortion, even at the extreme case.

The sideslip results highlight the flexibility of AJVGs, even at what may be considered significantly off-design conditions and a noticeable reduction in distortion is presented. They also suggest that the close spacing of the jets near the symmetry plane would not be necessary for a more evolved design.

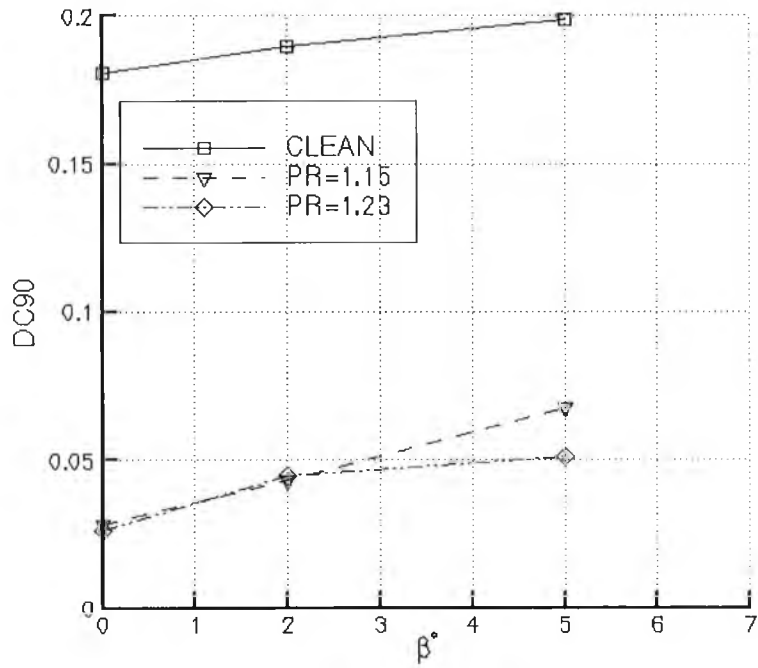


Figure 6-22: Effect of AJVGs during increasing yaw at $\alpha=15^\circ$

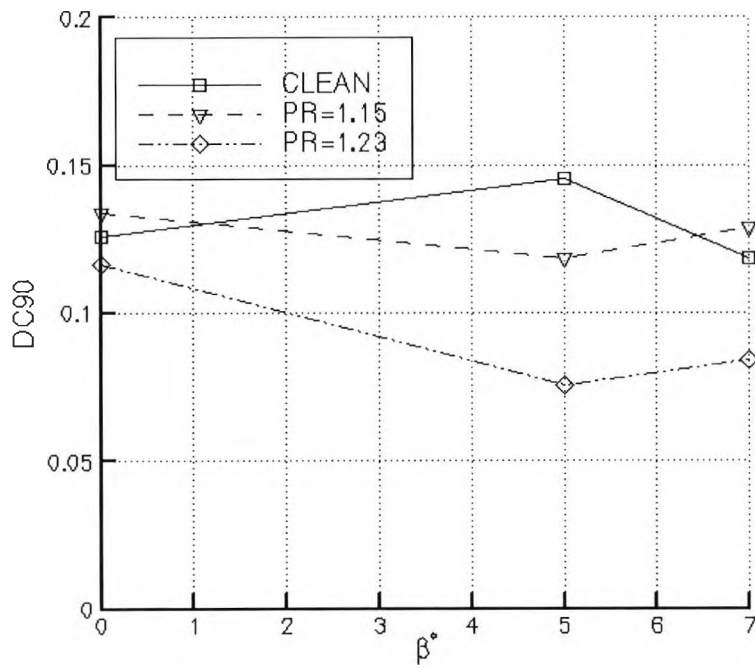


Figure 6-23: Effect of AJVGs during increasing yaw at $\alpha=17.5^\circ$

6.8. Comments regarding further applications and applicability

6.8.1. Application to separation type

Air-jet vortex generators have been shown to be effective in delaying lip separation across a wide range of mass flows on an intake that may be considered to be of relatively sharp proportions. Due to the sharp nature of the lip, the separation is due only to the adverse pressure gradient resulting from the lip geometry and is not influenced by an adverse pressure gradient associated with a shock-induced separation. No results are presented here for AJVGs applied to the shock-induced form of lip separation that may be associated with larger contraction lips. It is argued that using AJVGs may allow the intake designer to use a lower contraction-ratio cowl, as the AJVGs will make up the performance deficit. AJVGs may still have an application on higher contraction ratio intakes, particularly for extreme operations, for example V/STOL. However, AJVGs should be applicable to both forms of separation. *Pearcey (1961)* describes the use of AJVGs for preventing shock-induced separation on aerofoils. The intake application is unique, with the AJVGs filling two roles, firstly the elimination of the separation by increasing the momentum of the boundary layer and secondly, controlling the migration of low-momentum fluid in regions of high circumferential pressure gradients, thus countering the primary mechanism responsible for total-pressure distortion.

6.8.2. Application to external separation

Although this study has examined the occurrence of, and mechanisms behind, both internal and external lip separation, the application of AJVGs has focused on controlling internal lip separation only. This is primarily because performance and compatibility parameters calculated at the engine-face rake provide a direct indication of the improvement in terms of pressure recovery and distortion. The modified cowl could not be pressure plotted without affecting the AJVG installation and the drag measurements from the balance were not accurate enough to determine spillage drag. The application of AJVGs to external intake flow separation would be appealing, particularly for civil cowls which are over-designed for the cruise condition to eliminate flow separation in the event of an engine failure (See Chapter 2). If the cowl could be designed for cruise and the 'engine-out' criteria obtained using AJVGs, both weight and drag savings could be made at the cruise condition, where the aircraft

spends the majority of its time. For this application, it may be possible to design the cowl to achieve an appropriate pressure differential for ram AJVG operating in case of an engine failure. Alternatively, a high-pressure air source may still be available from the failed engine as flow will still be passing through the fan.

6.8.3. Net thrust evaluation

The advantage of AJVGs for intake flows is in reducing the total pressure distortion and providing additional surge margin for the engine. This benefit is hard to assess without considering a particular application. The increase in total pressure recovery due to delaying separation can be evaluated by considering the thrust loss due to AJVG mass extraction from the fan. However, the true benefits of AJVGs go beyond such a simple study because the AJVGs provide additional flight envelope. To fully assess the benefit of AJVGs, a large range of factors needs to be considered that are dependent upon vehicle type and mission requirement. The benefit of the AJVGs is in designing the intake lip contour for a particular application and using AJVGs to maintain flow quality at off-design conditions, thus allowing thrust levels and surge margin to be maintained across a broader envelope.

6.8.4. Thoughts on physical installation

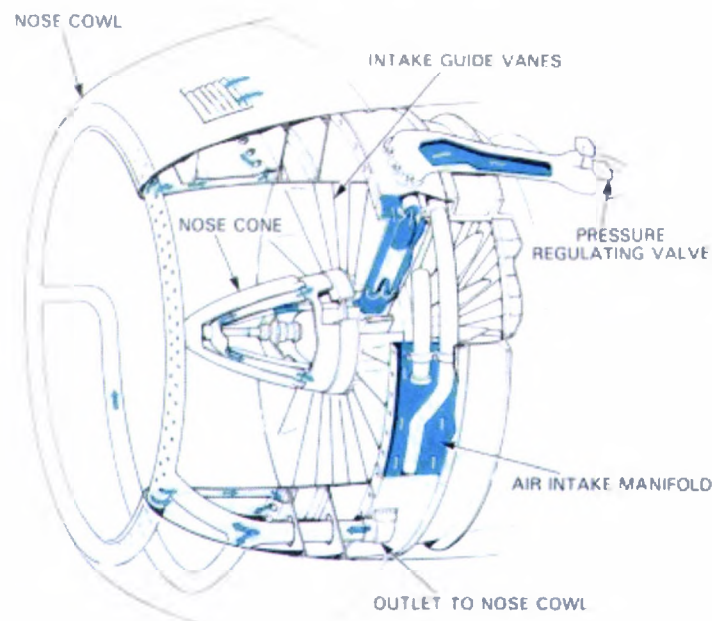


Figure 6-24: Nacelle ice-protection system (Rolls-Royce, 1986)

The primary disadvantage of an AJVG system is the loss in thrust of the propulsion system that is induced because of the mass-flow requirement of the jets. This loss of thrust occurs because mass flow that is passing through the intake and fan is not being expanded through the nozzle. To minimise thrust loss, it is important to both minimise the mass-flow requirement of the jets and minimise the losses in the ducting between the place of air extraction and the air-jet exits. An alternative approach, if the intake was designed with engine growth in mind, would be to increase the intake mass flow to compensate for the AJVG requirement: thus not affecting the exit thrust.

Figure 6.24 shows the air flow through an anti-icing system installed in a turbofan intake. This is an existing pressurised air off-take; air is extracted from the high-pressure compressor and ducted to the lip where it is used to warm the cowl surface to stop ice accretion. This air is then exhausted either into the intake or overboard (Rolls-Royce, 1986). The anti-icing system such as this presents itself as an existing mechanism for extracting high-pressure air from the engine and transporting it to the lip. If it were possible for an AJVG system to 'piggy back' an anti-icing system such as this, then the power loss and weight from AJVG system ducting can be minimised. Obviously, some modification would be required, but in essence, the nacelle structure could be compatible with an AJVG system.

6.9. Summary of AJVG results

Air-jet vortex generators have been shown to be successful in delaying the onset of air intake lip separation as the angle of incidence is increased. A significant improvement of 10 degrees can be achieved for less than 0.5% of intake total mass flow. Further benefits obtained by increasing the air-jet mass flow beyond this level are small. The AJVGs also show significant benefits in delaying intake lip separation when operating in a combination of angle of attack and sideslip. It is recommended that the air-jet mass flow, and hence blowing pressure, is regulated via a simple control system using inputs based on intake operating conditions: mass-flow, Mach number and incidence, for example.

- Ram AJVGs may be improved by the addition of a bellmouth area to the intake. A more elaborate design may improve performance further. It is likely that they could be beneficial on a sharp intake such as m742L cowl 9 at high mass flows.
- AJVGs drastically reduce engine-face distortion by delaying separation onset and controlling the migration of low-momentum flow in the intake.
- AJVGs have been shown to be effective across a large range of mass-flow ratios using an interactive computational and experimental approach.
- It is possible to design an AJVG installation for intake application using a CFD modelling approach, where the AJVG exits are simulated by a pressure-outlet boundary condition located flush with the intake surface. This keeps computational expense low by reducing geometry and mesh construction time and minimising the number of grid points. However, this approach is inappropriate for blowing pressure ratios greater than the critical (based on local conditions).
- Designing at sub-scale intake mass flow or AJVG mass flow is effective in producing an installation for use at full intake mass-flow ratios.

6.10. References

Anderson, B.H., Miller, D.N., Gridley, M.C., Agrell, J. 'The role of design of experiments in managing flow in compact air vehicle inlets' NASA TM-2003-212601, 2003.

Bender, E.E., Anderson, B.H., Yagle, P.J., 'Vortex generator modelling for Navier-Stokes codes' FEDSSM99-6919, 3rd Joint ASME/JSME Fluid Engineering Conference, San Francisco, USA, 1999.

Bray, T.P., 'A parametric study of vane and air-jet vortex generators', Eng.D. Thesis, College of Aeronautics, Cranfield University, UK, 1998.

Gibb, J., Anderson, B.H., 'Vortex flow control applied to aircraft intake ducts', RAeS High Lift & Separation Control Conference Proceedings, Bath, UK, 1995.

Küpper, C., 'A study of the application of air-jet vortex generators to intake ducts' Ph.D. Thesis, City University, UK, 1999.

Lewington, N., 'Enhancing Lift on a Three-element High Lift Aerofoil system by Installing Air-Jet Vortex Generators' Ph.D. Thesis, City University, 2001.

May, N., 'A new vortex generator model for use in complex configuration CFD solvers' AIAA Paper 2001-2434, 19th AIAA Applied Aerodynamics Conference, Anaheim, USE, 2001.

Miller, D.S., 'Internal Flow Systems', Second Edition, BHR Group Limited, 1990.

Peake, D.J., Private Communication, 2001

Peake, D.J., Henry, F.S., Lush, P.A., Pearcey, H.H., 'Flow control with air-jet vortex generators', The RAeS Conference on Passive and Active Flow Control', London, 1998.

Pearcey, H.H., 'Shock induced separation and its prevention by design and boundary-layer control', "Boundary layer and flow control", Ed. Lachman, pp1166-1343, Pergamon Press, 1961.

Rolls-Royce, 'The jet engine', pp 147-151 4th Edition, Rolls-Royce plc. 1986.

Waithe, K.A., 'Source term model for an array of vortex generators', NASA CR-2003-212157.

7. Conclusions

The aim of this research has been to demonstrate the use of AJVGs in controlling air intake lip separation. This has been done successfully using an interactive approach that combined theoretical analysis in the form of computational fluid dynamics (CFD) with experiments performed in the wind tunnel.

An initial wind tunnel test with a highly instrumented intake model enabled a picture of the three-dimensional flow to be established. This was aided by validated CFD methods, to provide additional insight into the nature of the flow field.

A computational method was developed for modelling the AJVG installation within the intake that did not require the detailed design of the installation. This permitted a cost-effective parametric study to be undertaken by varying the AJVG pitch and skew angles. This method was then validated by a further test in the wind tunnel, which enabled a complete picture of the AJVG performance to be built up over a range of conditions. The CFD methods were then used to verify the benefits of the AJVG at intake mass flows not achievable in the wind tunnel.

AJVGs have been shown to delay the angle of incidence at which separation occurs by up to 10 degrees using as little as 0.5% total intake mass-flow. The AJVG installation design for suppressing flow separation due to mass-flow/incidence combinations was also shown effective when substantial sideslip angles were introduced. The delay in separation onset produces a corresponding reduction in engine-face total-pressure distortion.

AJVGs are particularly flexible in that they are less reliant on specific design conditions, for example, local flow angle or velocity. This makes them highly applicable to intake operations where the flow regime in the immediate vicinity of the lip may vary across a wide range of Mach numbers and flow angles. The mass-flow requirement in terms of a percentage of total intake flow needed to power the air-jets is very small compared to other proposed active flow control applications.

8. Suggestions for future research

The study reported here is the first time that AJVGs have been applied to the control of the separations at intake lips. The design of the installation was completed using a parametric study and experience derived from researchers in other fields; wing and diffuser aerodynamics for example. As this AJVG application has been so successful, a path has been opened for the further refinement of this system.

The small physical nature of the intake model used in this study resulted in a number of assumptions and simplification measures being incorporated. For example, no detail could be applied to the AJVG inlets or exits. The potential benefits of AJVGs to intake performance are enormous. It is strongly suggested that the demonstration presented here should be followed by a larger scale model with a 6-inch or larger engine-face diameter, which could be tested at up to full-scale mass flows. A model of this size would allow a greater level of detail to be prescribed in the AJVG installation and allow a parametric assessment using interchangeable lips.

The use of the AJVG raises some issues concerning the cowl design. It is proposed that a series of cowl profiles could be designed with integral air-jets taken into consideration. The cowl contour is specified for the range of pressure and Mach numbers expected when the AJVGs maintain attached flow. This condition has been shown to produce high local Mach numbers, which could possibly induce shock-losses at more extreme operating conditions.

For preliminary design studies, an AJVG model which can be specified as a point or region within the mesh and require no re-meshing when the location of the jet orifices changes would provide some measure of time saving. This could be accomplished by the addition of momentum via the source terms.

Appendix A. Glossary of air intake terms

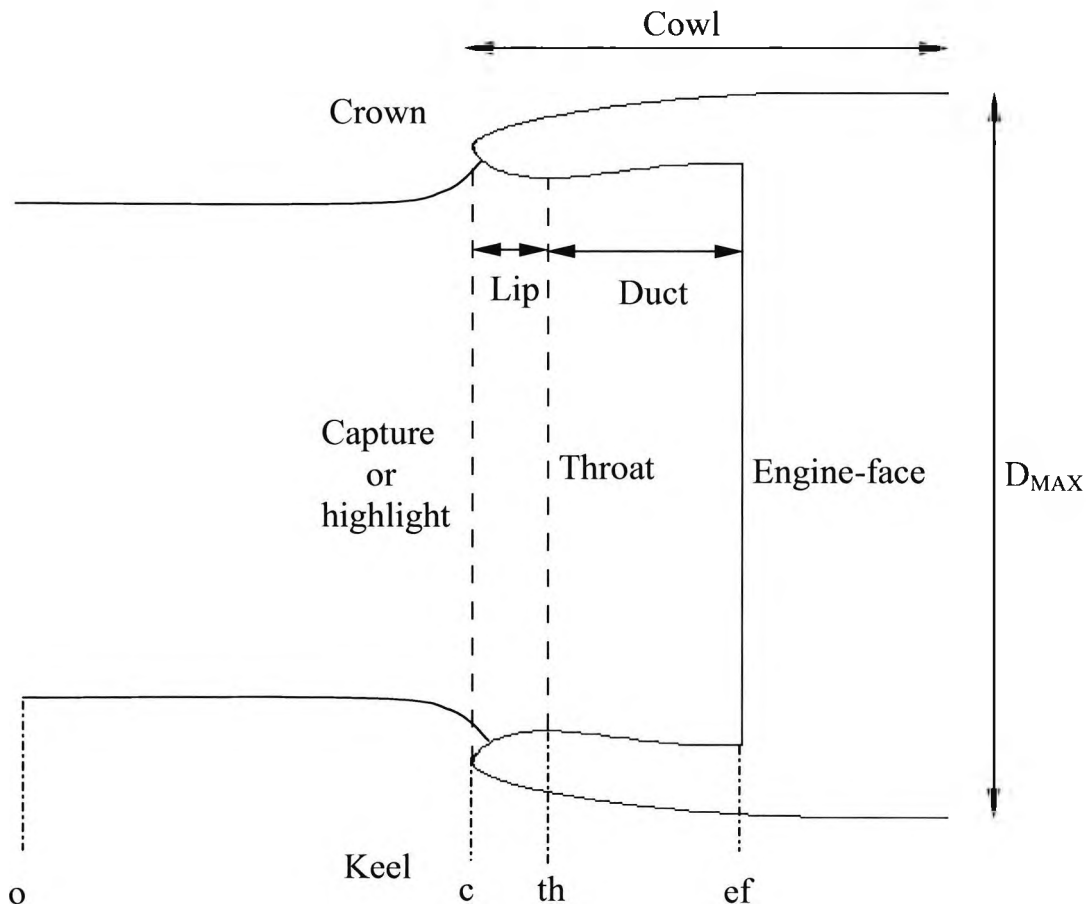


Figure A-1: Intake terminology

AIP	Aerodynamic Interface Plane
Capture Area	forward projected area of highlight
Crown	uppermost lip
Diffuser	diffusing section connecting throat & engine-face
Duct	see diffuser
Highlight	locus of intake leading edge
Keel	lowermost lip
Lip	leading-edge region
Throat	smallest geometric area
Engine-face	station corresponding to engine fan or AIP.

Appendix B. Model 742L geometric definition

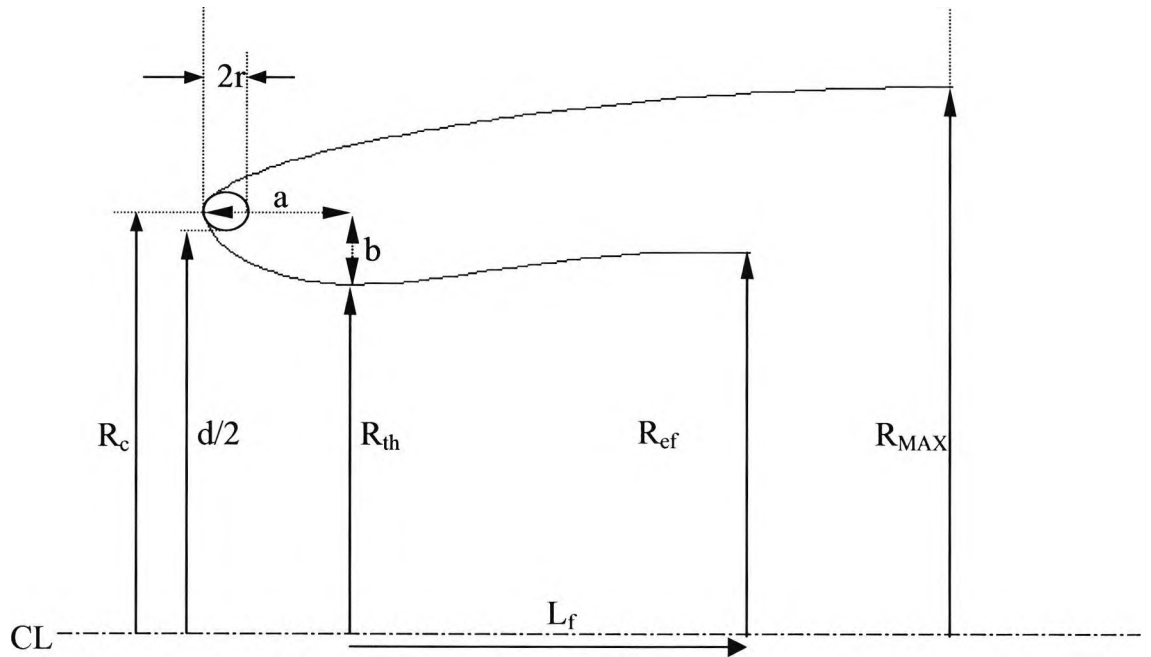


Figure B-1: Intake lip geometry

COWL

M742L cowl 9 is a NACA-1-85-100 Intake of the following proportions:

$$\frac{d}{D_{MAX}} = 0.85$$

$$\frac{L}{D_{MAX}} = 1.0$$

where $D_C = d + 2r$

LIP

The lip is defined by a super ellipse:

$$\left(\frac{x}{a}\right)^p + \left(\frac{y}{b}\right)^q = 1$$

where for cowl 9, $p=q=2$

DIFFUSER

$$\left(\frac{D - D_{th}}{D_{ef} - D_{th}}\right) = 3\left(1 - \frac{x}{L_f}\right)^4 - 4\left(1 - \frac{x}{L_f}\right)^3 + 1$$

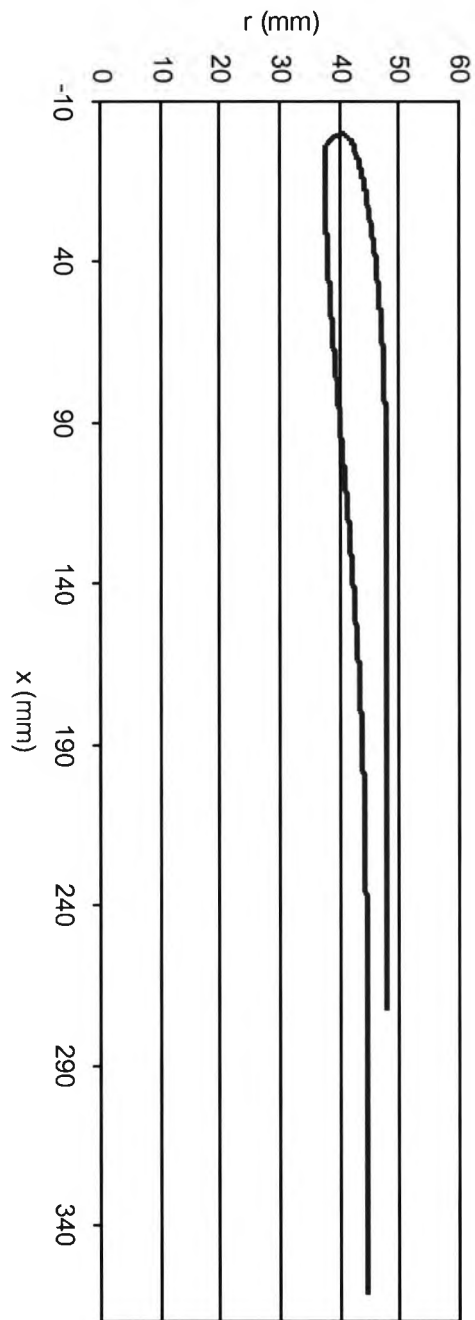


Figure B-2: M742L cowl 9 profile

Appendix C. Model instrumentation

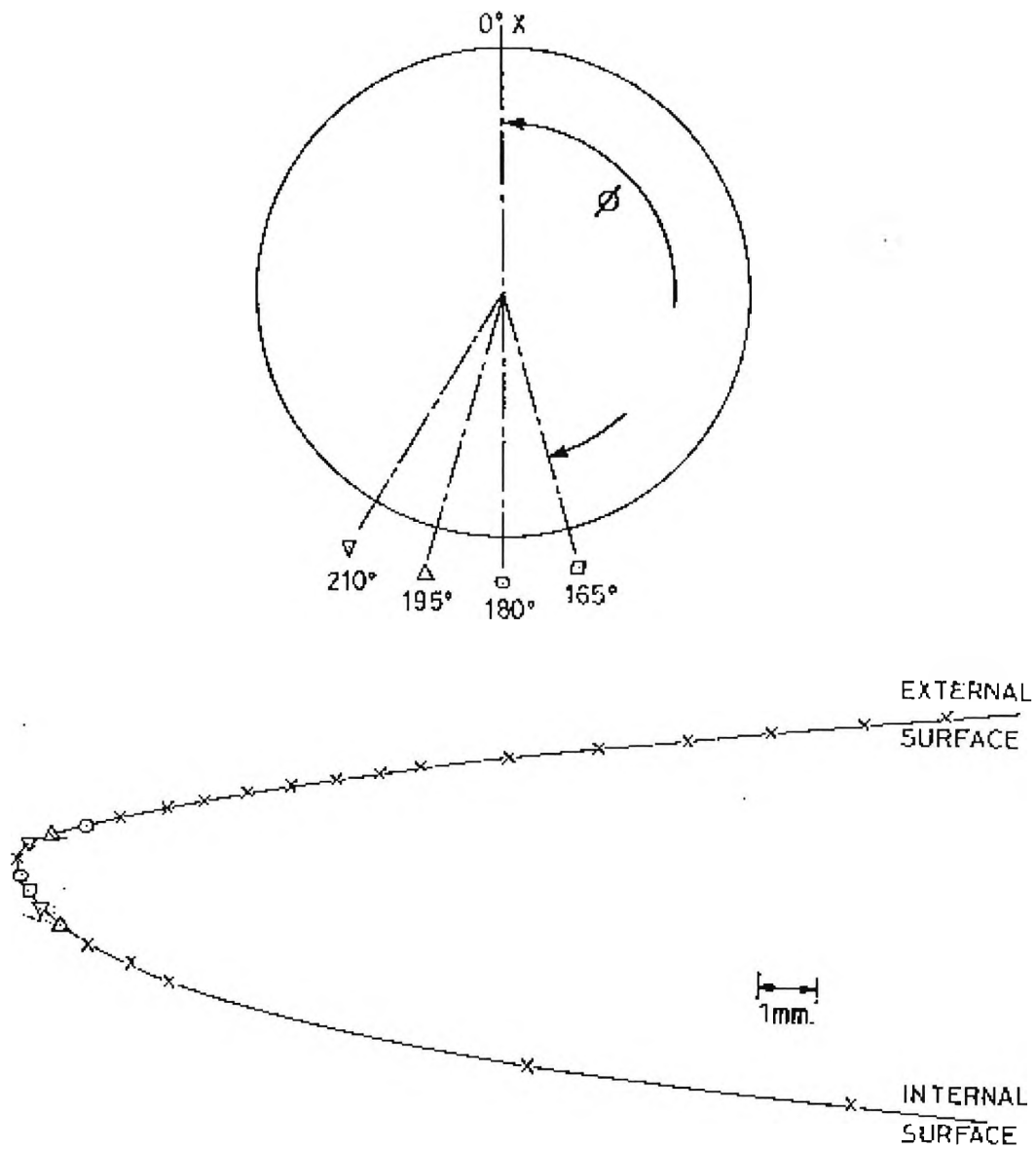


Figure C-1: M742L lip pressure tap detail (leading edge) – see Figure C-3 for co-ordinates

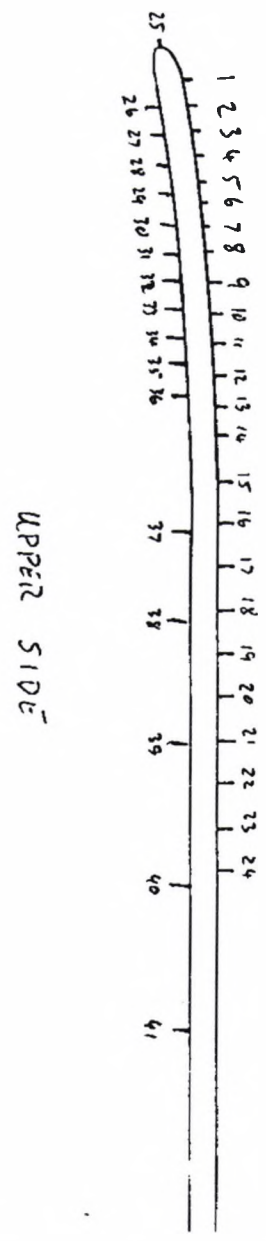


Figure C-2: M742L pressure tap detail (cowl & lip) – see Figure C-3 for coordinates

External			
Hole No.	x (mm)	r(mm)	ϕ (degrees)
24	71.88	47.45	0
23	62.48	47.17	0
22	53.09	46.79	0
21	45.34	46.40	0
20	39.62	46.06	0
19	34.95	45.75	0
18	30.20	45.41	0
17	25.98	45.06	0
16	22.23	44.73	0
15	18.57	44.38	0
14	15.19	44.02	0
13	13.92	43.87	0
12	12.45	43.68	0
11	10.97	43.48	0
10	9.47	43.26	0
9	8.03	43.04	0
8	6.58	42.79	0
7	5.84	42.66	0
6	5.16	42.53	0
5	4.42	42.37	0
4	3.73	42.23	0
3	3.02	42.07	0
12*	3.02	42.07	165
11*	3.02	42.07	180
3*	3.02	42.07	195
8*	3.02	42.07	210
2	2.31	41.88	0
1	1.55	41.67	0
5*	0.81	41.42	165
4*	0.43	41.24	180
9*	0.16	41.09	195
1*	0.04	40.90	210
25	0.00	40.75	0

Internal			
Hole No.	x (mm)	r(mm)	ϕ (degrees)
6*	0.04	40.38	165
2*	0.17	40.03	195
7*	0.37	39.68	210
10*	0.87	39.15	180
26	0.94	39.08	0
27	1.63	38.62	0
28	2.34	38.28	0
29	3.28	39.96	0
30	4.27	37.74	0
31	5.05	37.63	0
32	6.04	37.57	0
33	7.54	37.57	0
34	10.39	37.57	0
35	15.09	37.61	0
36	20.75	37.68	0
37	28.32	37.81	0
38	37.74	38.05	0
39	58.78	38.77	0
40	85.45	39.92	0
41	138.79	42.26	0
42	192.1	43.85	0

* Displaced from main station

Figure C-3: M742L pressure tap stations

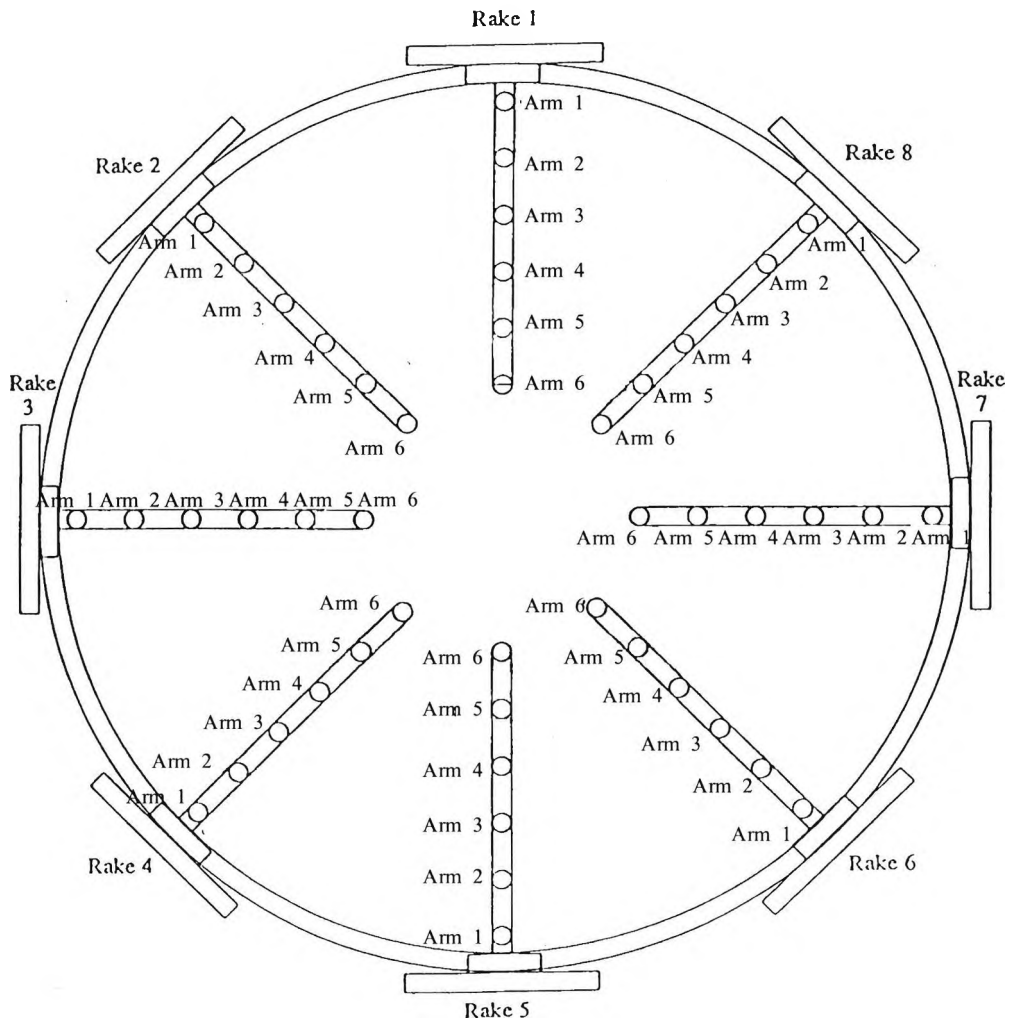


Figure C-4: Engine-face rake schematic

Hole No.	S-v 1	S-v 2	S-v 3
0	Cowl 42	R1A1	R8A1
1	Cowl 42	R1A1	R8A1
2	Cowl 41	R1A2	R8A2
3	Cowl 40	R1A3	R8A3
4	Cowl 39	R1A4	R8A4
5	Cowl 38	R1A5	R8A5
6	Cowl 37	R1A6	R8A6
7	Cowl 36	R2A1	UV1
8	Cowl 35	R2A2	UV2
9	Cowl 34	R2A3	UV3
10	Cowl 33	R2A4	UV4
11	Cowl 32	R2A5	UV5
12	Cowl 31	R2A6	UV6
13	Cowl 30	R3A1	UV7
14	Cowl 29	R3A2	UV8
15	Cowl 28	R3A3	
16	Cowl 27	R3A4	
17	Cowl 26	R3A5	
18	Cowl 25	R3A6	
19	Cowl 24	R4A1	
20	Cowl 24	R4A2	
21	Cowl 23	R4A3	
22	Cowl 22	R4A4	
23	Pref	Pref	Pref
24	Pref	Pref	Pref
25	Pcal	Pcal	Pcal
26	Cowl 21	R4A5	DV1
27	Cowl 21	R4A5	DV1
28	Cowl 20	R4A6	DV2
29	Cowl 19	R5A1	DV3
30	Cowl 18	R5A2	DV4
31	Cowl 17	R5A3	DV5
32	Cowl 16	R5A4	DV6
33	Cowl 15	R5A5	DV7
34	Cowl 14	R5A6	DV8
35	Cowl 13	R6A1	Cowl 1*
36	Cowl 12	R6A2	Cowl 9*
37	Cowl 11	R6A3	Cowl 4*
38	Cowl 10	R6A4	Cowl 12*
39	Cowl 09	R6A5	Cowl 13*
40	Cowl 08	R6A6	Cowl 5*
41	Cowl 07	R7A1	Cowl 2*
42	Cowl 06	R7A2	Cowl 6*
43	Cowl 05	R7A3	Cowl 10*
44	Cowl 04	R7A4	Cowl 8*
45	Cowl 03	R7A5	Cowl 7*
46	Cowl 02	R7A6	Cowl 11*
47	Cowl 401		Cowl 3*

Cowl Cowl pressures
 R Rake
 A Arm
 UV Upstream venturi
 DV Downstream venturi

Figure C-5: Tubing layout

Appendix D. Derivation of equations in text

This appendix provides derivation of equations used in this document, the equation number in the titles of each derivation refers to its chapter of origin.

D.1. Calculation of jet blowing total pressure ratio (Equation 6.1)

The jet pressure ratio, from isentropic flow relations is:

$$\left(\frac{H}{p}\right)_{Jet} = \left(1 + \frac{\gamma - 1}{2} M_{Jet}^2\right) \quad \text{Equation D-1}$$

Rearranging the expression for pressure coefficient for jet static pressure:

$$p_{Jet} = q_{\infty} C_p + p_{\infty} \quad \text{Equation D-2}$$

Expressing the dynamic pressure in terms of static pressure and Mach number:

$$p_{Jet} = p_{\infty} \left(\frac{\gamma}{2} M_{\infty}^2 C_p + 1\right) \quad \text{Equation D-3}$$

Substituting Equation A-3 in to Equation A-1, and normalising by free stream total pressure, H_{∞} :

$$\frac{H}{H_{\infty}} = \frac{p_{\infty} \left(\frac{\gamma}{2} C_{p_{Jet}} M_{\infty}^2 + 1\right) \left(1 + \frac{\gamma - 1}{2} M_{Jet}^2\right)^{\frac{\gamma}{\gamma - 1}}}{H_{\infty}} \quad \text{Equation D-4}$$

Finally expressing freestream total pressure as a function of Mach number in the form of Equation D-1 and substituting into Equation A-4 to give:

$$\frac{H}{H_{\infty}} = \frac{\left(\frac{\gamma}{2} C_{p_{Jet}} M_{\infty}^2 + 1\right) \left(1 + \frac{\gamma - 1}{2} M_{Jet}^2\right)^{\frac{\gamma}{\gamma - 1}}}{\left(1 + \frac{\gamma - 1}{2} M_{\infty}^2\right)^{\frac{\gamma}{\gamma - 1}}} \quad \text{Equation D-5}$$

D.2. Relationship between jet momentum coefficient and jet pressure ratio (Equation 6.2)

Defining the jet momentum pressure coefficient as:

$$C_{M\mu} = \frac{\dot{m}V_{Jet}}{q_{\infty}A_{Jet}} \quad \text{Equation D-6}$$

and expanding to give:

$$C_{M\mu} = \frac{(\rho A)_{Jet} V_{Jet}^2}{q_{\infty} A_{Jet}} = \frac{(\rho A)_{Jet} \gamma R T M_{Jet}^2}{q_{\infty} A_{Jet}} \quad \text{Equation D-7}$$

Replacing ρ and q using the ideal gas equation and isentropic flow relations respectively we have:

$$C_{M\mu} = \frac{2p_{Jet}M_{Jet}^2}{p_{\infty}M_{\infty}^2} \quad \text{Equation D-8}$$

Replacing the jet Mach Number with the jet pressure ratio $(H/p)_{Jet}$ gives:

$$C_{M\mu} = \frac{10p_{Jet}}{p_{\infty}M_{\infty}^2} \left[\left(PR \cdot \frac{p_{\infty}}{p_{Jet}} \right)^{\frac{\gamma-1}{\gamma}} - 1 \right] \quad \text{Equation D-9}$$

Where PR is the overall jet pressure ratio:

$$PR = \frac{H_{Jet}}{p_{\infty}} \quad \text{Equation D-10}$$

Appendix E. Assessment of experimental and numerical errors

This section provides an assessment of the potential sources of error in both the experimental and computational aspects of this investigation. Where appropriate, estimates are made for the actual value of the error components.

E.1. Experimental Errors

An overview of error analysis for the experimental work is given in Section 4.2.5 in Chapter 4. In the section, the AIAA Standard for assessment of uncertainty in wind tunnel testing (AIAA, 1999) is quoted, defining error as the difference between the true value and an experimentally measured value. The error is a measure of the accuracy of a measurement. The error may be considered to consist of two components, a precision or random error and a bias or systematic error.

Precision or random errors arise from non repeatable sources and contribute towards the scatter of the experimental data. These sources cannot be controlled in the experiment; for example humidity, or variation of ambient temperature that may influence the transducer measurements. Systemic errors arise from consistent errors in the measurements due to the measurement system itself, for example the influence of the measuring device on the flow.

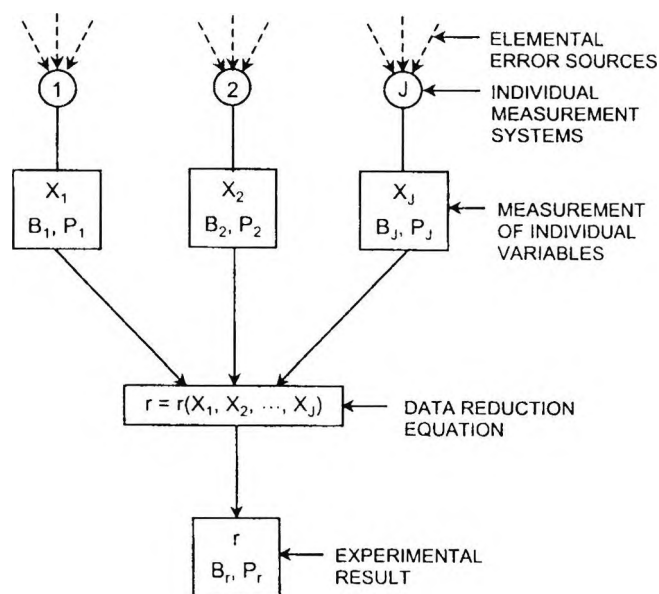


Figure E-1: Propagation of experimental errors (AIAA, 1999)

Figure E-1 shows how errors may propagate through a system designed to measure a particular flow variable. At every level in the process an additional set of bias and precision errors is introduced. The AIAA recommends that the most cost-effective way to evaluate precision errors on such a system is to do so at the highest possible level, for example: the precision of the whole system. Equally, calibrating the measurement system in as large units as possible alleviates the need to estimate the individual bias components (AIAA, 1999). Estimates for the systematic error for the primary measurements are described below.

E.1.1. Surface Static pressure coefficients

For surface static pressure measurement, the magnitude of the random errors is shown to be small in Figure 4-7 in Chapter 4 which illustrates the repeatability of these measurements in the wind tunnel.

In the data reduction procedure for the T2 wind tunnel, the pressure coefficients are calculated based on pressure differentials measured along the contraction. The wind tunnel is calibrated to relate the static pressure in the centre of the working section (p_o) to the wall static pressure. The pressure coefficients are calculated from the following expression (*Innes, 1995*):

$$C_p = \frac{(P - P_o) - (P_2 - P_o)}{K_1(P_1 - P_2)} + \frac{K_3}{K_1} \quad \text{Equation E-1}$$

Where K_1 relates the contraction pressure drop to the dynamic pressure:

$$K_1 = \frac{q_\infty}{P_1 - P_2} = 1.073 \quad \text{Equation E-2}$$

K_2 relates the centreline dynamic pressure to the contraction pressure drop:

$$K_2 = \frac{P_1 - P_3}{P_1 - P_2} = 1.0368 \quad \text{Equation E-3}$$

K_3 is the ratio of the difference between wall and centreline pressures and the contraction pressure drop.

$$K_3 = \frac{P_2 - P_3}{P_1 - P_2} = 0.036575 \quad \text{Equation E-4}$$

This gives the expression for pressure coefficient as a function of the pressure differentials measured when the transducers are referenced to atmosphere:

$$C_p = \frac{(P - P_o) - (P_2 - P_o)}{1.073(P_1 - P_2)} + 0.034 \quad \text{Equation E-5}$$

Three potential errors can be defined in the pressure measurement system; these are the accuracy of the transducer, the digitisation of the transducer output and the effect of the static pressure measurement orifice. The last source of error occurs because the orifice which is used to measure the static pressure produces some local curvature of the streamlines because of the absence of the constraining boundary of the wall.

An expression for the error in static pressure due to the orifice Reynolds number is given by *Ower & Pankhurst (1977)*. A relationship perhaps more applicable to aeronautical flows is given by the US Navy (*Volluz, 1961*) which presents corrections for a range of Mach numbers. From this relationship the orifice diameter of 0.1mm gives an error of 0.1% of the dynamic head. To assess the overall uncertainty in the pressure measurement system the method of *Kline & McClinton (1953)* is used as presented by *Doebelin (1996)*. Here, the error in a measured variable which itself is a function of any number of independent variables, is evaluated by using a Taylor series expansion, in which terms of second order or higher are neglected. This truncated Taylor series approximates the measured value as the sum of the true value and the errors due to each independent variable. Subtracting the true value from the Taylor series, we can calculate the root-sum-square of all the error sources:

$$u_{rms} = \sqrt{\left(\Delta u_1 \frac{\partial f}{\partial u_1}\right)^2 + \left(\Delta u_2 \frac{\partial f}{\partial u_2}\right)^2 + \dots + \left(\Delta u_n \frac{\partial f}{\partial u_n}\right)^2} \quad \text{Equation E-6}$$

For the pressure coefficient, using equation E-5 this expression becomes:

$$u_{Cp} = \sqrt{\left(u_1 \frac{\partial C_p}{\partial (p - p_o)}\right)^2 + \left(u_2 \frac{\partial C_p}{\partial (p_2 - p_o)}\right)^2 + \left(u_3 \frac{\partial C_p}{\partial (p_1 - p_o)}\right)^2} \quad \text{Equation E-7}$$

The individual uncertainties, u_2 and u_3 , of the pressure differentials are evaluated from the transducer accuracy specified by the manufacturer: 0.1% full scale (1.5 psi) and from the data acquisition system, which yields an accuracy of $\pm 0.025\%$, at full scale (Innes, 1995) the square root of the sum of these values is then taken to give:

$$u_2 = u_3 = \sqrt{(0.001 * 1.5 \text{ psi})^2 + (0.00025 * 1.5 \text{ psi})^2} = 10.66 \text{ Pa} \quad \text{Equation E-8}$$

The error in the measurement of a particular static pressure, $p-p_o$, is a combination of the errors due to the measurement orifice, the transducer and the data acquisition system, these values are then root-sum-squared to give:

$$u_1 = \sqrt{(10.66 \text{ Pa})^2 + (0.001 q_\infty)^2} = 10.69 \text{ Pa} \quad \text{Equation E-9}$$

The partial derivatives of Equation E-5 become:

$$\frac{\partial C_p}{\partial (p - p_o)} = \frac{1}{k_1 (p_1 - p_o)} \quad \text{Equation E-10}$$

$$\frac{\partial C_p}{\partial (p_2 - p_o)} = \frac{-1}{k_1 (p_1 - p_o)} \quad \text{Equation E-11}$$

$$\frac{\partial C_p}{\partial (p_1 - p_2)} = -\frac{(p - p_o) - (p_2 - p_o)}{k_1 (p_1 - p_2)^2} \quad \text{Equation E-12}$$

Substituting into equation E-7, the error may be calculated for each pressure tap location. These are plotted as error bars on the pressure distribution of Figure E-2. The mean pressure tap error, as a percentage of pressure-coefficient at stagnation conditions is $\pm 1.41\%$.

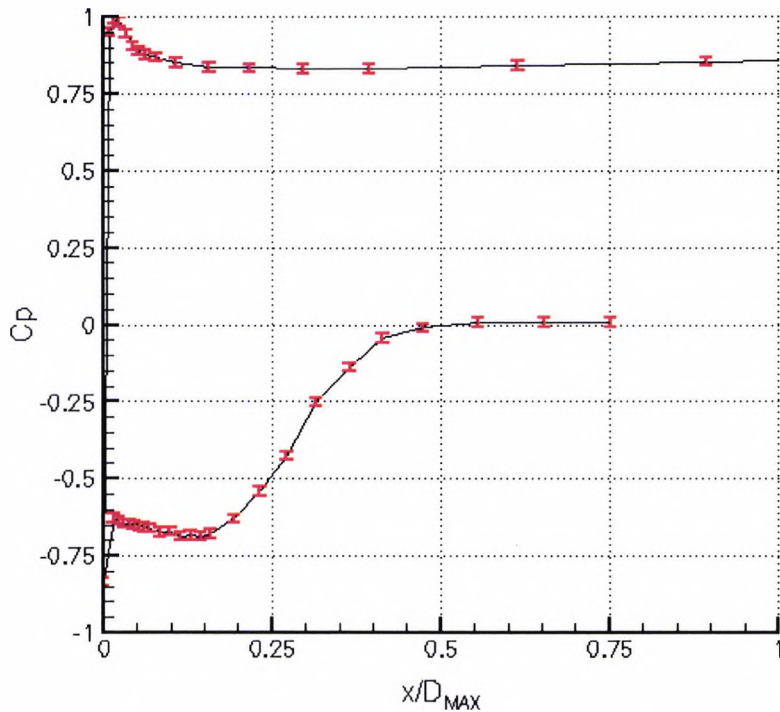


Figure E-2: Indication of experimental error in pressure coefficient at mass-flow ratio of $A_0/A_C=0.33$

E.1.2. Intake dynamic pressure recovery

The precision error sources can be evaluated by assessing the repeated data points in a statistical manner. A mass-flow sweep of the clean model was taken every day during tunnel running for assessment of data repeatability. For a mass-flow ratio $A_0/A_C=0.74$ the standard deviation was 0.00045. An example of data repeatability for dynamic pressure recovery and distortion is shown in Figure 4-11 in Chapter 4.

The measurement accuracy for the intake dynamic pressure may be calculated in a similar manner as for the static pressure presented above with the exception that the orifice correction must be changed. In the case of the pitot probes, the influence of the probe nose is assumed negligible. However, a wall proximity correction may be applied to the pitot probe measurements from the outer ring of the rake, nearest to the wall to account for the reduced values of total pressure measured in the boundary layer due to the total pressure gradient in the normal to the wall. A relationship presented by *Bryer and Pankhurst (1971)* for wall proximity corrections as a function of distance from the wall normalised by tube diameter suggests that a correction of the

order 0.6% of the dynamic pressure should be added to the total pressure readings measured in the outer ring. Using the procedure described in section E.1.1, the dynamic pressure recovery is measured in the same way as pressure coefficient, and the wall proximity correction applied to the outer most tubes. Taking the square root of sums of the contributions of all tubes gives an uncertainty of 1.46% in dynamic recovery at a mass-flow ratio of $A_o/A_c=0.3$. The variation with incidence is plotted in the form of error bars in Figure E-3.

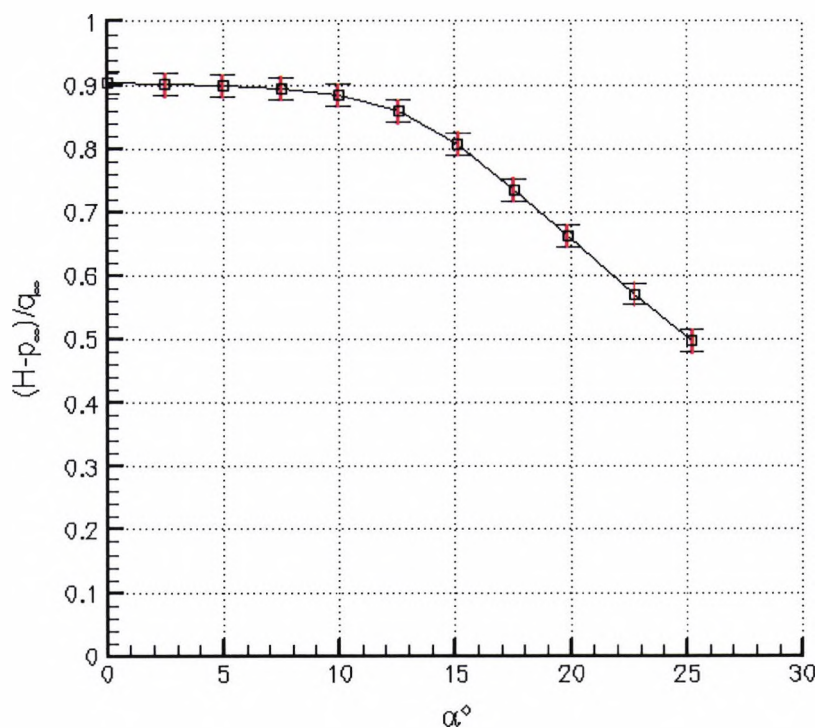


Figure E-3: Error in dynamic pressure recovery

E.1.3. Incidence angle

The model incidence was varied by rotating the roof turntable, a potentiometer providing digitised voltage values on the tunnel control panel. A calibration was determined to provide values of incidence angle in degrees from the control panel reading. The calibration gives a 3 standard deviation precision error of $\pm 0.025^\circ$. The bias error, which is removed by the calibration, is -7.23° .

The change in incidence angle from one data point to another during the course of the test was 2.5° , this increment is large enough that the errors due to the measurement of

incidence angle are negligible. The incidence imprecision is plotted with that of dynamic pressure recovery in Figure E-3.

E.1.4. Intake mass flow

The intake mass-flow cells were previously calibrated to relate the measured mass-flow to the actual mass-flow as discrepancies may occur due both to the distribution of the total pressure probes and the influence on the flow at the measuring station. This process gave a mass flow accuracy of between half and one percent (*McGregor, 1971*).

E.1.5. Errors in measurement introduced by unsteady flow

At high angles of incidence and/or high mass-flow ratios when the flow separation is large it is also most likely unsteady. In this case, the measurement system used to record static and total pressures on the model will be insufficient as no time-averaging is applied to the data (instantaneous measurements are taken). This condition, when large separation has occurred, may be considered to correspond to the point at which the value of distortion coefficient DC90 starts to fall, despite the increase in the extent of the separation. This is, however, a condition of secondary interest of which only qualitative comparisons are made between CFD and experiment in Chapter 5. The flow of interest corresponds to the onset of separation at the lip, any unsteadiness due to the small localised separation near the lip will not influence the global mass-flow measurement made at the engine face.

E.1.6. Wind tunnel velocity

Although not explicitly used in the calculation of intake performance, the wind tunnel working section velocity is presented in output from the data acquisition system. The velocity is not used in the calculation of pressure coefficient values as these are obtained directly from the pressure measuring system. The working section velocity is obtained directly from the measurement of q_∞ using the pressure differentials along the contraction (equation E.2), and the ambient pressure and tunnel total temperature. These are measured to accuracies of ± 1.0 Pa and ± 0.5 °K respectively. Assuming the flow to be incompressible, the density may be expressed as:

$$\rho_{\infty} = \frac{P_a}{RT_o} \quad \text{Equation E-13}$$

Using equation E.6 and substituting ISA sea level conditions for ambient pressure and 40° C for the working section stagnation temperature, the error in the calculated density may be expressed as:

$$u_{\rho} = \sqrt{\left(u_1 \frac{\partial \rho}{\partial p_a}\right)^2 + \left(u_2 \frac{\partial \rho}{\partial T_o}\right)^2} = \sqrt{\left(0.5 \frac{1}{RT_o}\right)^2 + \left(1.0 \frac{P}{RT_o^2}\right)^2} = 0.002 \text{ kg/m}^3$$

$$\text{Equation E-14}$$

The working section velocity is obtained from:

$$V_{\infty} = \sqrt{\frac{2K_1(p_1 - p_2)}{\rho_{\infty}}} \quad \text{Equation E-15}$$

As before, the error in velocity may be obtained from the individual variable errors using equation E.6.

$$u_{V_{\infty}} = \sqrt{\left(u_{(p_1 - p_2)} \frac{\partial V_{\infty}}{\partial (p_1 - p_2)}\right)^2 + \left(u_{\rho} \frac{\partial V_{\infty}}{\partial \rho_{\infty}}\right)^2} = \sqrt{\left(10.37 \sqrt{\frac{2K_1}{\rho_{\infty}(p_1 - p_2)}}\right)^2 + \left(0.004 \sqrt{\frac{2K_1(p_1 - p_2)}{\rho_{\infty}^3}}\right)^2}$$

$$\text{Equation E-16}$$

This gives an error in the calculated velocity of ± 0.53 m/s which equates to $\pm 1.3\%$ of the calculated value at the nominal testing condition of 40m/s.

E.1.7. Error Summary

Table E-1 below lists the magnitude of precision errors for primary variable used to describe the flow in this document for a mass-flow ratio of $A_o/A_c=0.3$ and at a working section velocity of 40m/s.

Variable	Error Magnitude	Source
C_p	1.43% of measured value	Error analysis
$(H-p)/q$	1.78% of measured value	Error analysis
α	$\pm 0.025^\circ$	Tunnel calibration
A_o/A_c	1% of measured value	RAE calibration
V_∞	1.3% of calculated value	Error analysis

Table E-1: Magnitudes of error in measured variables

E.2. Computational Errors

E.2.1. Geometric fidelity and surface finish

A potential source of discrepancy between the computational and experimental results arises from the fidelity of the representation of the intake geometry. The profile may be described as a series of curves; the NACA profile, the lip and the diffuser. However, manufacturing tolerances may mean that the intake tested may differ slightly from the geometric definition. An accurately measured profile, taken from the wind tunnel model was used to construct the CFD geometry. This was done by fitting splines through the inspected points; the cowl surface was then lofted from these splines. When the surface model is discretised in the grid generation process, further variation from the geometric definition may occur. This will primarily be in the area of the leading edge where the high curvature lip is represented by a series of straight lines. Due to the fine nature of the grid, this difference in representation is perceived to be small. The grid dependency presented in Figure 3-11 shows the results are not influenced by the discretisation in the leading edge region when using grid densities greater than the ‘medium’ described in section 3.7.1 of Chapter 3.

In addition to potential difference in the surface shape of the model, the computational model assumes the intake surface to be perfectly smooth. In reality, the model will contain some degree of surface roughness although the model surface is polished to minimise this discrepancy.

E.2.2. Modelling of AJVGs

The use of pressure-inlet boundary conditions to model the effect of the AJVGs is a compromise between computational efficiency and accuracy. Therefore, there may be differences in the detailed flow when comparing experimental and computational results. Although there may be some effect on the vorticity generation from the AJVG orifice itself this is unlikely to be captured by the grid density used even if the orifice itself was replicated in the computation. The primary difference between the calculation and the experimental values will be due to the discharge coefficient of the AJVG holes. In the experiment, pressure readings were taken from the lip plenum. These values were matched for the computations. However, because of the sharp edged nature of the AJVG holes, particularly on the inflow side the total pressure of the jets maybe below that measured in the plenum. Consequently, the CFD results may be at higher jet pressure ratios that those in the experiment to which they are compared. This is not of major concern, as the CFD modelling is intended to be used to aid in the design of wind tunnel tests. Because of the small mass-flows involved the AJVG arrays were not calibrated. This mismatching of boundary conditions is a general problem with viscous intake system calculations. Ideally, we are interested in matching the pressure, Mach number and mass-flow at some boundary condition, but because of the complexity of the loss inducing mechanism in the flow, and the requirement to maintain a correctly posed problem, it is usual to accept a single measure of the flow quantity. In the case of the AJVG model, the plenum pressure has been chosen as this was measured directly (Figure E-4 shows the calibration curve for the transducer). However, it is possible to make an estimation of the influence the AJVG orifice discharge coefficient will on the AJVG system. This is done by using the AJVG performance map of Figure 6-11 to obtain a relationship between incidence angle for separation and the blowing mass-flow to intake mass-flow for a particular condition. A linear 'best fit' is applied as an approximation; this is shown in Figure E-5. Then by applying different discharge coefficients (assuming discharge coefficient of unity, $C_D=1.0$, corresponds to the data of Figure 6-11) to the relative jet mass-flow, the error in incidence angle for separation due to discharge coefficient can be calculated. This is shown for a range blowing pressure ratios in Figure E-6.

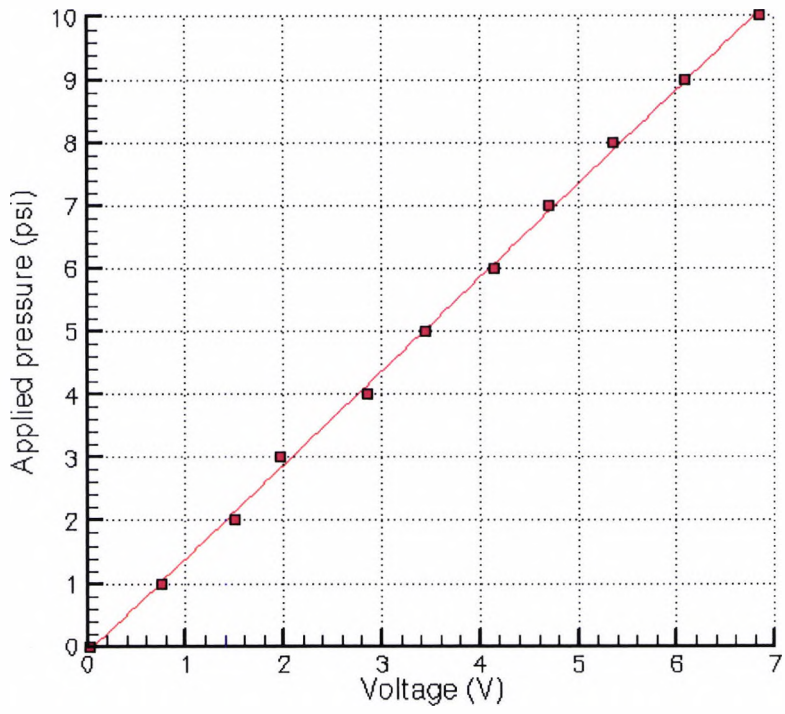


Figure E-4: Calibration of transducer in intake lip plenum

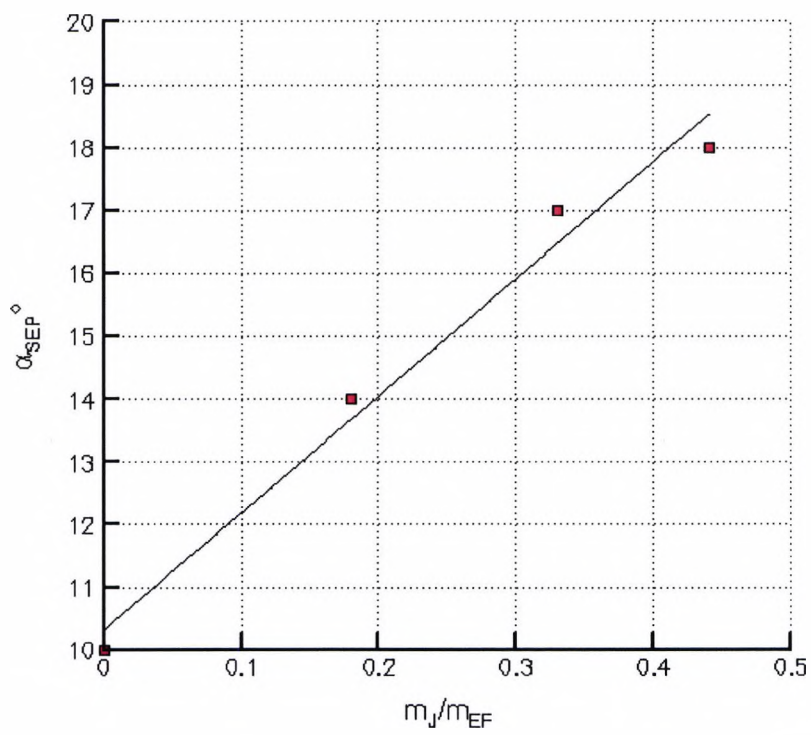


Figure E-5 Best linear fit for angle-of-attack at separation with blowing mass-flow ratio

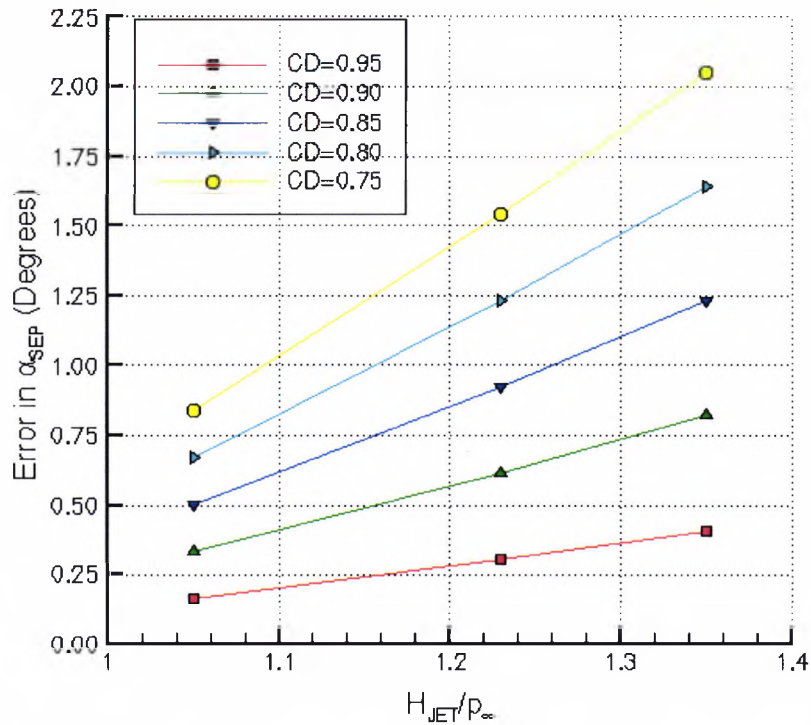


Figure E-6 Estimated error in angle-of-attack at separation, for a range of AJVG discharge coefficients for $Ao/Ac=0.78$

E.2.3. Transition modelling

All computations were performed using turbulence models that assumed that the intake boundary layers were fully turbulent. In RANS CFD methods, there is currently no suitable way to predict transition location during the course of a calculation. With the Fluent commercial CFD software, it is possible to define a transition location by partitioning the computational domain into laminar and turbulent regions but this method is ungainly and inefficient and as a result, not particularly attractive when the details of the transition are not known or potentially vary with the onset flow conditions.

Experimental work completed by *Wilmer et al (1981)* concluded that specifying transition on intake lip flows at low speed made no difference to the critical incidence at which separation occurs. Although post separation performance was better in terms of lower distortion when transition was fixed at the highlight. It is likely that the acceleration of the flow around the lip when the intake is at incidence forces transition

of the flow very close to the leading edge. The wind tunnel model had a transition trip on the internal lip at $x/D_{MAX}=0.12$. This is aft of the location of the separation on the windward lip at moderate incidences as described in section 5.4.2 in Chapter 5, and is used primarily to stabilise the duct flow in the event that the flow is still laminar, as may be the case for the more benign flow conditions.

The validation of the CFD methods (Chapter 3) showed that of the turbulence models evaluated, the Spalart-Allmaras model made a very good approximation of replicating the external cowl laminar separation in which transition occurred over the separation in terms of surface pressure coefficient, as suggested in the literature (no transition trip was applied to the external surface). However, questions are raised regarding how well this replicates the flow physics of the separated three-dimensional boundary layer, and perhaps a more fundamental study is required to compare boundary layer profiles and off surface flow information.

For most cases examined in this study, the flow is three-dimensional and although limitations in turbulence modelling may lead to errors in the prediction of the actual incidence at which separation occurs, qualitatively, the flow physics in terms of separation location, extent and roll-up will be the same. The flexibility of AJVG in terms of their placement with regard to the separation line also alleviates some of the necessity for accurate prediction of the boundary layer when designing the flow control installation. For a practical application of this technology, at full scale Reynolds number, the flow is likely to be turbulent and RANS CFD methods more appropriate.

Appendix F. A note on the correlations of intake lip separation

Figure 2-13 in Chapter 2 shows a correlation that collapses experimental results found in the open literature for internal separation into two primary groups corresponding to take-off conditions and cruise conditions respectively.

The wide range of operating conditions that an air intake must experience which corresponds to different types of flow physics leading to different forms of separation. Although correlations exist in the literature, they are mainly for a particular parametric series of intakes, see for example that by *Wilmer (1981)*. Most of these correlations generally plot lip-loss coefficient or peak surface Mach number, which both correlate well with the flow and geometry parameters for thick lip intakes, up to the point that the flow separates before a strong shock is formed.

In terms of geometry, contraction ratio is the governing parameter; more subtle adjustments to the lip curvature by means of modifying the proportion of a super ellipse are consumed within the scatter of the data. The primary flow parameters that influence the separation are the free stream Mach number, the mass-flow (or similar indicator, for example throat Mach number) and the angle of incidence.

Examples of the variation of the incidence angle at which separation occurs with respect to different flow and geometric variables are plotted in Figure F-1 and F-2 which contain a number of intakes tabulated in Table 2-1. Figure F-1 shows how free stream Mach number and lip contraction ratio influence the onset of separation. At low throat Mach numbers the incidence angle at which separation occurs, increases with increasing mass-flow. This is due to the beneficial affect of the favourable pressure gradient. At a critical value of throat Mach number, the angle decrease due to a shock induced separation on the windward lip.

An alternative presentation of results is shown in Figure F-2, where the data is plotted against mass-flow ratio which is linked to free stream Mach number by the engine demand. On this figure, the solid lines represent the boundary layer separation for

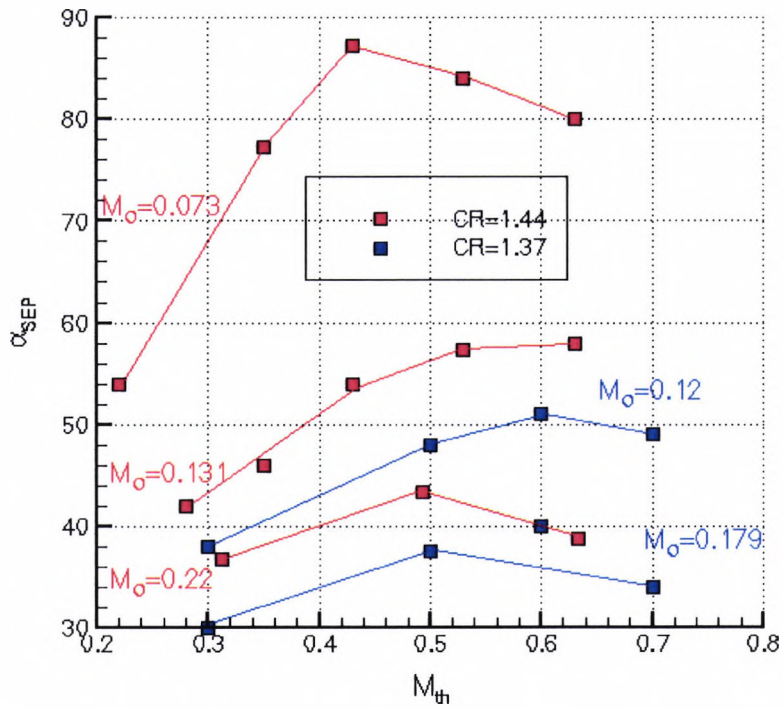


Figure F-1: Angle of attack at separation against throat Mach number for different contraction ratio intakes at low speed

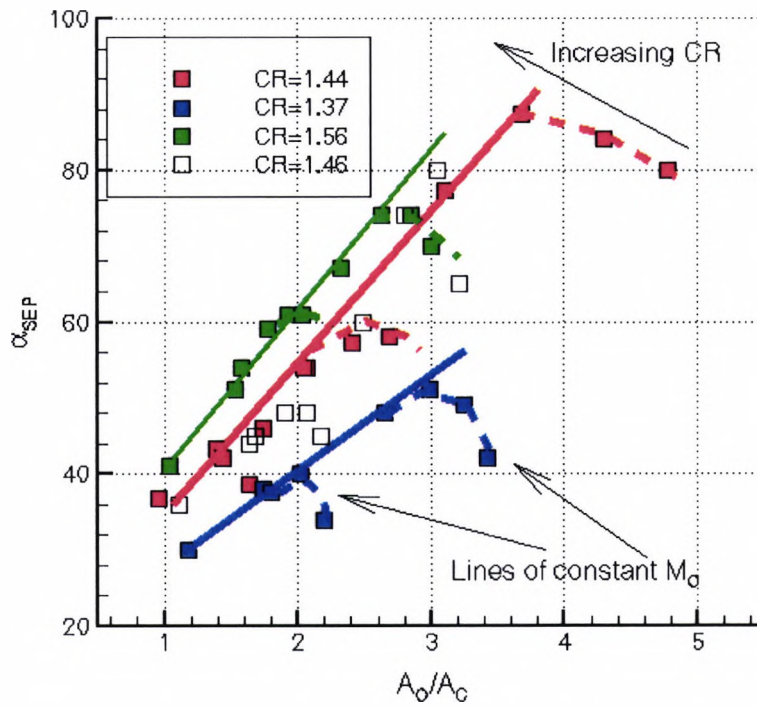


Figure F-2: Angle of attack at separation against mass-flow ratio for different contraction ratio intakes at low speed

each contraction ratio, and the dashed lines, the shock induced separation for a particular Mach number at that contraction ratio.

The results plotted here are of high contraction ratio and discussions in Chapter 5 indicate that lower contraction ratio intakes at higher Mach number exhibit the opposite behaviour. At low or moderate incident and mass-flow combinations, the onset of lip separation is a function of the strength of the shock at the lip, as incidence of mass-flow is increased beyond a critical level, the separation occurs due to the adverse pressure gradient, before a shock can form.

References

American Institute of Aeronautics and Astronautics, 'Assessment of experimental uncertainty with application to wind tunnel testing', AIAA Standard S-071A-1999, 1999.

Doebelin, E.O., 'Measurement systems – application and design' 4th Edition, McGraw-Hill, pp58-73, 1996.

Innes, F, 'An experimental investigation in to the use of vortex generators to improve the performance of a high lift system,' Ph.D. Thesis, City University, 1995.

Kline, S.J., McClintock, F.A., 'Describing uncertainties in single sample experiments' Mech. Eng., Vol75, p3, 1953.

McGregor, I., 'The characteristics and calibration of two types of air-flow metering device for investigation the performance of model air intakes', RAE TR 71212, 1971.

Ower, E., & Pankhurst, R.C., 'The measurement of air flow' 5th Edition, Pergamon Press, 1977.

Volluz, R.J., 'Handbook of supersonic aerodynamics, section 20, wind tunnel instrumentation and operation', NAVORD Report 1488 (Vol. 6), US Navy Ordnance Aerophysics Laboratory, 1961.

Wilmer, A.C., Brown, T.W., Goldsmith, E.L., 'Effects of intake geometry on circular pitot intake performance at zero and low forward speed', Paper 5, AGARD-CP-301 "Aerodynamics of Powerplant Installation", 1981.